CLICKABLE POLY(PROPARGYL METHACRYLATE) PREPARED BY ATOM TRANSFER RADICAL POLYMERIZATION AND ITS DERIVATIVES AS ENZYME STABILIZERS

By

Po-Jen Hsiao

A DISSERTATION

Submitted to
Michigan State University
in partial fulfillment of the requirements
for the degree of

Chemistry — Doctor of Philosophy

2022

ABSTRACT

CLICKABLE POLY(PROPARGYL METHACRYLATE) PREPARED BY ATOM TRANSFTER RADICAL POLYMERIZATION AND ITS DERVIATIVES AS ENZYME STABILIZERS

By

Po-Jen Hsiao

Enzymes are nearly perfect catalysts with excellent selectivity and high turnover frequencies. A long-standing goal has been enabling enzymes to operate ex vivo in nonaqueous solvents, but the structures of native enzymes are typically compromised under these conditions. Polymer-enzyme bioconjugates have shown some promise—albeit limited—in this regard. The clickable poly(propargyl methacrylate) (PPMA) was proposed as a platform to enhance different polymer structures versus the residual enzymatic activities. The degree of polymerization and polydispersity are two factors that affect the polymer properties and can affect the enzymatic activities of the polymer-enzyme bioconjugates. The literature examples of PPMA with degree of polymerization greater than 200 are limited. In the atom transfer radical polymerization (ATRP) conditions we discovered, the degree of polymerization and the polydispersity of poly(trimethylsilylpropargyl methacrylate) (PTMSPMA) can be precisely adjusted by the initiator and monomer ratio, the copper catalyst loading, and the reducing agent loading (copper wire).

After deprotection, PPMA is further reacted with different mole fraction compositions of hydrophilic triethylene glycol monomethyl ether (mDEG) azide and hydrophobic dodecyl azide to prepare amphiphilic polymers as enzyme stabilizers. The activities of the model enzyme, *Subtilisin Carlsberg (SC)*, and polymer-*SC* bioconjugates

were determined by 4-nitrophenolate and 4-thiopyridone assays, and the polymer-enzyme bioconjugate SC@82%mDEG-PPMA was found to be more active than SC alone in toluene. The SC@82%mDEG-PPMA is also more active than SC@100%mDEG-PPMA in 4-nitrophenolate assay, proving that the side chain structure of the polymer micelles can affect the polymer-enzyme bioconjugates. The micelle 80%mDEG-PPMA may isolate the enzyme from the bulk toluene better than 100%mDEG-PPMA.

Deprotonated amino acid salts are great alternatives to the synthesized alkylamines as post-combustion CO₂ absorbents due to their non-toxic and low volatile nature. For CO₂ capture, gas uptake was measured when solutions of monodeprotonated amino acids were sparged with CO₂. The speciation between dissolved CO₃²⁻, HCO₃⁻, and CO₂(aq), and CO₂ captured as carbamates of the deprotonated amino acids, was quantified by ¹³C{¹H} and ¹H NMR spectroscopy. Less hindered amino acids like glycine tend to have faster CO₂ absorption kinetic and higher carbamate concentrations due to the formation of relatively stable carbamates. One equivalent of carbamate forms requires one equivalent of amino acid as sacrificial base. Therefore, the formation of carbamate decreases the total CO₂ absorption capacity and is an unfavorable pathway for CO₂ capture. While the amino acids containing substituents at the α carbon atom adjacent to the amino group, like alanine and proline, destabilize their carbamates by unfavorable steric interaction and lead to carbamate hydrolysis to CO₃²⁻/HCO₃⁻ and enhance the CO₂ capture capacity. Therefore, mixing different amino acids can have the fast absorption kinetics and higher absorption capacity. Based on the results, the mixture amino acid solutions were observed to have higher CO₂ absorption capacity than the single amino acid counterparts.

This thesis is dedicated to my dear grandpa, Jin-Yi Lin. Thank you for always believing in me.

ACKNOWLEDGMENTS

I would like to thank my advisor Dr. Mitch Smith for his guidance and support during my graduate study. I appreciate the opportunities of participating on a variety of projects to broaden my knowledge. Mitch not only taught me how to perform research projects but also train me to be a better presenter. Thanks to Dr. Xuefei Huang for meaningful conversations and encouragement. Thanks to Dr. Wei Liao for the intriguing collaboration and support. Thanks to Dr. Robert Maleczka for helpful discussions and suggestions.

Thanks to Dan Holmes, Xie Li, Kathy Severin, Ardeshir Azadnia, Ed Drown, and Lars Peereboom for teaching me various characterization techniques and troubleshooting skills. I would also like to thank past and current Smith group members: Dmitry, Behnaz, Kristin, Tim, Yu-Ling, Olivia, Reza, Seokjoo, Alex, Ryan, Mona, Pin, Cash, Pauline, Chris, Anshu, and Suzi. Thank you for your support throughout my graduate study. Special thanks to Dmitry, Reza, Seokjoo, Alex, and Pin for the valuable discussion and suggestions.

I would like to thank all the friends from MSU, including Aliakbar, Pin, Louis, Kuang, Pei Jun, Pohan, Shih-Chang, Chi-Fang, Nicky, Karen, Hsien-Yung, and En-Chih. You made my life at MSU memorable.

I would like to thank my family for their endless encouragement and support. Finally, I would like to thank my girlfriend, Tina, for her patience, support, and love. This journey would not be the same without you.

TABLE OF CONTENTS

LIST OF TABLES	viii
LIST OF FIGURES	X
LIST OF SCHEMES	XX
KEY TO ABBREVIATIONS	xxii
Chapter 1. Introduction	1
Overview of atom transfer radical polymerization (ATRP)	1
Overview of preparing comb-like copolymers	8
Overview of post polymerization modification	10
Overview of polymers as enzyme stabilizers	14
Overview of enzyme polymer interactions	17
Overview of post combustion CO ₂ capture	20
Conclusion	26
Chapter 2. Clickable poly(trimethylsilylpropargyl methacrylate) with narr	row
polydispersity prepared by Atom Transfer Radical Polymerization	
Introduction	
Polymerization of TMSPMA by ATRP	
Polymerization of TMSPMA by Activator ReGenerated by Electron Transfe	
(ARGET) ATRP	
Effects of deactivator (Cu ^{II} Br ₂ /ligand) loading	35
Effects of copper wire loading	
Effects of targeted degrees of polymerization	
Effects of induction periods	
Conclusion	
Experimental section	
Chapter 3. Post-polymerization Modification and polymeric micelle forma	ation63
Introduction	
Deprotection of Poly(trimethylsilylpropargyl methacrylate)	66
Functionalizing poly(propargyl methacrylate) by CuAAC	
Kinetic Study of CuAAC	
Characterizing the hydrodynamic radius of amphiphilic polymers with differ	
compositions	
Lower critical solution temperature	
Conclusion	
Experimental section	
Chapter 4. Polymeric Micelles as Enzyme Stabilizers in Organic Solvents.	111111

Introduction	111111
Enzymatic activity of Subtilisin Carlsberg using 4-nitophenolate as chromop	hore (4-
NP assay)	111111
Enzymatic activity of Subtilisin Carlsberg using 4-thiopyridone as chromoph	nore (4-TP
assay)	120120
Conclusion	125125
Experimental Section	126126
Chapter 5. Amino acids solution as CO ₂ capturing absorbents and NMR st	udv of
the CO ₂ adducts	
Introduction	
Cultivating microalgae for post-combustion capture	
Amino acid salts as CO ₂ absorbents for post-combustion capture	
Characterization of the CO ₂ capturing intermediates by ¹³ C{ ¹ H} NMR	
Quantitative ¹³ C{ ¹ H} NMR study with different relaxation delays (d1)	
Assigning ¹³ C{ ¹ H} NMR signals of the amino acid sample after CO ₂ absorpt	
Assigning ¹³ C{ ¹ H} NMR signals of the lysine sample after absorption	
Determination of initial concentration of amino acid solutions	
Determination of CO ₂ adduct by ¹³ C{ ¹ H} NMR integral ratio (primary method	
Verifying the primary method by ¹³ C{ ¹ H} NMR experiment with external sta	
Comparing different amino acid solutions as CO ₂ absorbents	
Mixture solutions containing two amino acids as CO ₂ absorbents	
Mixture solutions containing three and four amino acids as CO ₂ absorbents	
Conclusion	
Experimental section	
	1/11/1
Chapter 6. Amino acid derived polyurea materials	
Introduction	
Synthesis of symmetric diamine monomers from amino acids	
Assigning ¹ H NMR signals of the polyureas	
Thermal analysis of polyureas	
Study the effect of spacer length	
Study the effect of side chain structure	
Conclusion	
Experimental Section	180180
APPENDIX	189189
REFERENCES	264264
INDICATE DE LA CALLA CONTRACTOR DE LA CO	**** #UT#UT

LIST OF TABLES

Table 1. Summary of coupling partners in the commonly used post-polymerization modification methods
Table 2. Effective CO ₂ loading of 30 mass% Aqueous Solutions of monoethanolamine (MEA) and sodium glycinate in different CO ₂ sources. Table from reference 7025
Table 3. Polymerization of TMSPMA by conventional ATRP with different ligands32
Table 4. ARGET ATRP of PTMSPMA with different deactivator loadings and copper wire surface areas. ^a
Table 5. ARGET ATRP of TMSPMA with different targeted degrees of polymerization. ^a
Table 6. Comparison of the mole fraction of mDEG in the reactant azide mixtures with the functionalized x%mDEG-PPMA products71
Table 7. Comparing the theoretical molecular weight (calculated from the degree of polymerization of PPMA) and the experimental molecular weight (determined by GPC) of xx%mDEG-PPMA
Table 8. Integration value of CO ₂ adducts in a mixture of proline, alanine, and lysine solution after CO ₂ absorption obtained by ¹³ C{ ¹ H} NMR experiments with different relaxation delay (d1). The integration value of proline was set as 1.00
Table 9. Average pH values of the amino acid salt solution at 298 K before CO ₂ absorption, after CO ₂ absorption, and after CO ₂ desorption. The synthetic gas used in CO ₂ absorption process contains 10% CO ₂ and 90% air. The pH value was measured by pH meter
Table 10. Volume normalized integration ratio over different glycine concentration determined by 1H NMR. Known concentration of glycine (600 μ L in outer tube) and 2 M of disodium maleate (60 μ L in inner tube) in H_2O : $D_2O = 5$: 1 (v/v)
Table 11. Initial concentration of amino acid samples before absorption. (G: glycine, A: alanine, P: proline, and L: lysine)
Table 12. Glycine sample after absorption characterized by different methods (primary method versus external standard method)
Table 13. Summary of CO ₂ adducts of single amino acid solutions. AA is amino acid and AA-CO ₂ is amino acid carbamate.

Table 14. CO ₂ adducts of solutions containing two amino acids. (G: glycine, A: ala P: proline, and L: lysine)	,
Table 15. CO ₂ adducts of solutions containing three or four amino acids. (G: glycir alanine, P: proline, and L: lysine)	
Table 16. Amino acid profile of the algal biomass (g per 100 g crude protein). Only top 7 abundant amino acids are included	
Table 17. The summary of thermal analysis results of polyurea containing different spacer lengths and side chain structures.	

LIST OF FIGURES

Figure 1. ATRP equilibrium constants K_{ATRP} for nitrogen-based ligands determined with the initiator EtBriB in the presence of Cu ^I Br in MeCN at 22°C. ³
Figure 2. Plot of K_{ATRP} (measured with the initiator EtBriB in acetonitrile, structure shown in Figure 1, versus $E_{1/2}$ for different Cu ^{II} Br ₂ /L complexes (ligand structures show in Figure 1). ³
Figure 3. Activation rate constant (k_a) of various initiators were determine with [Initiator] $_0 = 1 \text{mM}$, [Cu ^I Br/PMDETA] $_0 = 20 \text{ mM}$, at 35°C in MeCN except for EBPA and BrPN. ⁵ The k_a of EBPA is determined by Cu ^I Br/NPPMI. The k_a of EBPA is determined by Cu ^I Br/ HMTETA. ⁵
Figure 4. The ATRP equilibrium constant and activation rate constant of initiator bearing different transfer groups. K_{ATRP} values for various initiators were determined with Cu ^I X/TPMA in MeCN at 22 °C. 3 k_{a} values for various initiators were determined with Cu ^I X/PMDETA in MeCN at 35 °C. 5
Figure 5. The CuAAC modifiable polymer examples
Figure 6. Historical carbon dioxide record from the Vostok Ice core21
Figure 7. The monthly mean direct measurement of carbon dioxide concentration at Mauna Loa Observatory, Hawaii. Data was collected from 1958 to present. 62
Figure 8. The total U.S. greenhouse gas emissions by economic sector in 2019. Note: total emissions in 2019 is 6,558 million metric tons of CO ₂ equivalent. Percentages may not add up to 100% due to independent rounding. ⁶⁵
Figure 9. Molecular weight (left Y axis) and polydispersity (right Y axis) versus the polymerization conversion plot. Copper wire surface area = 39 mm^2 (black square), copper wire loading = 79 mm^2 (red circle), and copper wire loading = 236 mm^2 (blue triangle). [Cu ^{II} Br ₂] = 6.1 mM
Figure 10. First-order kinetic plot of different copper wire loadings ($[Cu^0]$). $[Cu^0] = 39$ mm ² (red dot), $[Cu^0] = 79$ mm ² (blue triangle), and $[Cu^0] = 236$ mm ² (black square) 39
Figure 11. First-order kinetic plot for determining initial polymerization rate of different copper wire surface area = 39 mm ² (orange), 79 mm ² (blue), and 236 mm ² (grey)41
Figure 12. First-order kinetic plot of ARGET ATRP of TMSPMA with monomer and initiator added at $t=0$ h (black dots) and with monomer and initiator added at $t=2.5$ h (red dots). [TMSPMA]: [EBPA]: [Cu ^{II} Br ₂]: [dNbpy] = 200: 1: 0.6: 1.2 and copper wire surface area = 39 (mm ²)

Figure 13. First-order kinetic plot of with constant copper wire surface area = $24 \text{ (mm}^2\text{)}$ at $[Cu^{II}Br_2] = 1.0 \text{ mM}$ (blue square) and at $[Cu^{II}Br_2] = 6.1 \text{ mM}$ (black dot)46
Figure 14. Overlapped ¹ H NMR spectra of the PTMSPMA (top) and PPMA (middle) and 100% mDEG-PPMA (bottom) in CDCl ₃
Figure 15. The GPC trace of PTMSPMA (black) and after removing TMS protecting group, PPMA (red)
Figure 16. The ¹ H NMR of reactant azide mixture (mDEG-N ₃ and C10-N ₃) for preparing 80% mDEG-PPMA in CDCl ₃
Figure 17. The ¹ H NMR of 82% mDEG-PPMA in CDCl ₃
Figure 18. Overlapped GPC traces of PPMA (dark red), 100% mDEG-PPMA (cyan), 82% mDEG-PPMA (purple) and 71% mDEG-PPMA (orange) in THF
Figure 19. The CuAAC mechanism involving binuclear copper intermediate proposed by Worrell and Fokin
Figure 20. ¹ H NMR spectra as a function of time for the CuAAC of PPMA-88.9 kDa and benzyl azide
Figure 21. Conversion versus time plot for the CuAAC reaction of benzyl azide with EMP, PPMA-88.9 kDa (Mn = 88,900, PDI = 1.30), PPMA-34.0 kDa (Mn = 34,000, PDI = 1.12), and PPMA-co-PMMA-29.1 kDa { Mn = 29,100, PDI = 1.20, [PMMA]:[PPMA] = 10: 1 (mol%)}. Reaction progression was monitored by 1H NMR. ([alkyne] = 0.1 M, [azide] = 0.1 M, [Cu ^I Br/PMDETA] = 2 mM, DMF, 25 °C)
Figure 22. ¹ H NMR spectrum of the PPMA- <i>co</i> -PMMA ([PPMA]: [PMMA] = 1: 10 (mol%)) in CDCl ₃
Figure 23. The overlapped 1 H NMR of crude material at 20 h (a) PPMA-34.0 kDa ($M_{\rm n}$ = 34,000, PDI = 1.12, top) and (b) PPMA-co-PMMA-29.1 kDa { $M_{\rm n}$ = 29,100, PDI = 1.20, [PMMA]:[PPMA] = 10: 1 (mol%), bottom}. ([alkyne] = 0.01 M, [azide] = 0.01 M, [Cu ^I Br/PMDETA] = 0.2 mM, DMF, 25 °C)
Figure 24. Recovered and purified PPMA- co -PMMA-29.1 kDa after 20 h reaction time under CuAAC condition ([alkyne] = 0.01 M, [azide] = 0.01 M, [Cu ^I Br/PMDETA] = 0.2 mM, DMF, 25 °C).
Figure 25. The hydrodynamic radius as a function of 100% mDEG-PPMA concentration from 10 to 0.15 mg/mL in MilliQ water
Figure 26. The hydrodynamic radius as a function of 82% mDEG-PPMA concentration from 10 to 0.15 mg/mL in MilliQ water

Figure 27. The hydrodynamic radius as a function of 71% mDEG-PPMA concentration (mg/mL) in MilliQ water. 9494
Figure 28. Schematic phase diagram of a polymer with LCST behavior9595
Figure 29. Cloud point determination by variable temperature-UV/Vis spectroscopy. The turbidity was determined by absorbance at 450 nm and all the polymer concentration is 3 mg/mL in MilliQ water. All the polymers have $M_{\rm n} \sim 90$ kg/mol
Figure 30. Cloud points versus different mole% of mDEG side chain along different polymer backbones: PPMA (green), PMGE (orange), and PPGE (black). 117
Figure 31. Overlapped UV-Vis spectra of variable 4-nitrophenolate concentration in 0.1 N NaOH _(aq) . The wavelength of maximum absorbance is at 400 nm
Figure 32. Determination of extinction coefficient of 4-nitrophenolate in 0.1 N NaOH _(aq) by UV-Vis spectroscopy
Figure 33. Mole of enzymatic assay product (4-nitrophenolate) versus reaction time plot of different biocatalysts: $SC@82\%$ mDEG-PPMA (magenta diamond), $SC@100\%$ mDEG-PPMA (blue triangle), SC (red dot), control (substrate only, black square). Assay was used z-Ala-ONp as substrate in toluene. [substrate] = 0.01 M, [n -BuOH] = 1 M, [SC] = 0.2 mg/mL, [SC]: [xx%mDEG-PPMA] = 1: 2 (mol ratio). Aliquots (50 μ L) were taken periodically, mixed with 500 μ L of 0.1 N NaOH _(aq) , and vortexed for 30 s before determining the aqueous layer by UV-Vis spectroscopy
Figure 34. Triplicate of enzymatic assay of $SC@82\%$ mDEG-PPMA using z-Ala-ONp as substrate in toluene. [substrate] = 0.01 M, [n -BuOH] = 1 M, [SC] = 0.2 mg/mL, [SC]: [mDEG-PPMA] = 1: 2 (mol ratio). Aliquots (50 μ L) were taken periodically, mixed with 500 μ L of 0.1 N NaOH _(aq) , and vortexed for 30 s before determining the aqueous layer by UV-Vis spectroscopy
Figure 35. Triplicate of enzymatic assay of SC using z-Ala-ONp as substrate in toluene. [substrate] = 0.01 M, [n-BuOH] = 1 M, [SC] = 0.2 mg/mL, [SC]: [mDEG-PPMA] = 1: 2 (mol ratio). Aliquots (50 μ L) were taken periodically, mixed with 500 μ L of 0.1 N NaOH _(aq) , and vortexed for 30 s before determining the aqueous layer by UV-Vis spectroscopy
Figure 36. The enzymatic assay results of different order of reagent addition. Standard procedure: in a vial containing biocatalyst $SC@82\%$ mDEG-PPMA, adding n -butanol and substrate solution, respectively (black square). Control procedure: in a vial containing biocatalyst $SC@82\%$ mDEG-PPMA, adding substrate solution and n -butanol, respectively (red dot).
Figure 37. Mole of enzymatic assay product (4-nitrophenolate) versus reaction time plot of different biocatalysts: $SC@82\%$ mDEG-PPMA (magenta diamond), $SC@82\%$ mDEG-PPMA-25 min incubation time (blue triangle), $SC@82\%$ mDEG-PPMA-5 min incubation time (red dot), SC (black square)

Figure 38. Calibration curve of variable concentration of thiophenol reacting with DTDP. $[DTDP] = 1 \times 10^{-4} \text{ M}$ in DMSO solution containing 0.12% (v/v) triethylamine 122122
Figure 39. Calibration curve of UV-Vis absorption@352 nm versus variable thiophenol concentration. [DTDP] = 1×10^{-4} M in DMSO solution containing 0.12% (v/v) triethylamine
Figure 40. Enzymatic assay result using 4-thiopyridone (4-TP) as chromophore. $SC@82\%$ mDEG-PPMA (red dot) and SC (black square) were tested using APTE as substrate in toluene. [APTE] = 1 mM, [n -butanol] = 0.1 M
Figure 41. Initial rate of biocatalysts in 4-TP assay. <i>SC</i> @82%mDEG-PPMA (blue) and <i>SC</i> (red)
Figure 42. Microalgae photobioreactor, PHYCO2 APB unit. Diagram of the photobioreactor (left) and the photobioreactor at the MSU. T.B. Simon power plant (right). 124, 130130
Figure 43. The CO ₂ absorption experimental setup. From reference
Figure 44. The CO ₂ absorption (blue circle and orange triangle) and desorption (green star and red cross) progression plot using potassium glycinate solution as absorbent.
Figure 45. The mole fraction of potassium glycine and its protonated form (KG/KGH ⁺ , black square), potassium glycine carbamate (KG-CO ₂ ⁻ , red dot), and bicarbonate and carbonate ions (HCO ₃ ⁻ /CO ₃ ²⁻ , blue triangle) versus the CO ₂ loading, characterized by quantitative ¹³ C{ ¹ H} NMR. CO ₂ loading is calculated by dividing the sum of potassium glycine carbamate and bicarbonate with the initial potassium glycinate concentration. The data are from reference 137.
Figure 46. $^{13}C\{^{1}H\}$ NMR spectrum of alanine absorption sample in H_2O : $D_2O=5$: 1 (v/v)
Figure 47. $^{13}C\{^{1}H\}$ NMR spectrum of alanine desorption sample in H_2O : $D_2O=5$: 1 (v/v)
Figure 48. $^{13}C\{^{1}H\}$ NMR spectrum of proline desorption sample in H_2O : $D_2O=5$: 1 (v/v)
Figure 49. 13 C{ 1 H} NMR spectrum of glycine desorption sample in H ₂ O: D ₂ O = 5:1 (v/v)
Figure 50. $^{13}C\{^{1}H\}$ NMR of lysine sample after absorption (carbonyl region only) in $H_2O: D_2O = 5:1 \ (v/v)$
Figure 51. HMBC spectrum of lysine sample after absorption in $H_2O:D_2O = 5:1$ (v/v).

Figure 52. ¹³ C{ ¹ H} NMR spectrum of lysine sample after absorption in D ₂ O (carbonyl region only)
Figure 53. $^{13}C\{^1H\}$ NMR spectrum of lysine sample after absorption in D_2O (aliphatic region only)
Figure 54. The NMR setup with stem coaxial insert NMR tube. Samples is in the outer tube (green) and the external standard is in the inner tube (red)
Figure 55. The ¹ H NMR calibration curve using external standard (60 µL of 2 M disodium maleate solution)
Figure 56. ¹³ C{ ¹ H} NMR spectrum of glycine sample after absorption
Figure 57. ¹³ C{ ¹ H} NMR calibration curve using external standard (2 M disodium maleate solution)
Figure 58. $^{13}C\{^1H\}$ NMR spectrum of glycine sample after absorption (600 μ L) with 2 M disodium maleate (60 μ L) as external standard
Figure 59. Retrosynthesis of polyurea from aromatic diisocyanate and diamine from amino acids
Figure 60. Overlapped FT-IR spectrum of 4,4′-MDI (green), PU-NH-Leu-C12-Leu-NH (black), PU-NH-Phe-C12-Phe-NH (red), and PU-NH-Ala-C12-Ala-NH (blue) 165165
Figure 61. ¹ H NMR of PU-NH-Phe-C2-Phe-NH in DMSO- <i>d</i> ₆
Figure 62. gCOSY of PU-NH-Phe-C2-Phe-NH in DMSO- <i>d</i> ₆ highlighting the cross-peaks with protons 5
Figure 63. gCOSY of PU-NH-Phe-C2-Phe-NH in DMSO- <i>d</i> ₆ highlighting the cross-peaks between protons 4 and protons 7
Figure 64. gCOSY of PU-NH-Phe-C2-Phe-NH in DMSO- <i>d</i> ₆ highlighting the cross-peaks between protons 3 and protons 10
Figure 65. ¹ H NMR of PU-NH-Phe-C2-Phe-NH in DMSO- <i>d</i> ₆ with all the signals assigned on the polymer chemical structure
Figure 66. Overlapped ¹ H NMR of PU-NH-Phe-C2-Phe-NH (top), PU-NH-Phe-C12-Phe-NH (middle), and PU-NH-Leu-C12-Leu-NH (bottom)
Figure 67. Differential scanning calorimetry (DSC) data for PU-NH-Phe-C2-Phe-NH and the $T_{\rm g}$ was analyzed by TA instruments Universal Analysis 2000 software. The sample was equilibrated at -20 °C and ramp 10 °C/min up to 300 °C

Figure 68. Overlapped differential scanning calorimetry (DSC) data for PU-NH-Phe-C2-Phe-NH (black) and PU-NH-Phe-C12-Phe-NH (red) and the $T_{\rm g}$ was analyzed by TA instruments Universal Analysis 2000 software. Heating rate is 10 °C/min under nitrogen atmosphere
Figure 69. Schematic representation of the free volume in a polymer
Figure 70. The thermogravimetric curve (green) and first derivative weight loss curve (blue) of PU-NH-Phe-C2-Phe-NH. Data are plotted and processed by TA instruments Universal Analysis 2000 software. Heating rate is 10 °C/min under nitrogen atmosphere.
Figure 71. The thermogravimetric curve of PU-NH-Phe-C2-Phe-NH (black) and PU-NH-Phe-C12-Phe-NH (red) and the onset temperatures were analyzed by TA instruments Universal Analysis 2000 software. Heating rate is 10 °C/min under nitrogen atmosphere.
Figure 72. First derivative of the thermogravimetric curve of PU-NH-Phe-C2-Phe-NH (black) and PU-NH-Phe-C12-Phe-NH (red)
Figure 73. The overlapped DSC data of PU-NH-Phe-C12-Phe-NH (red), PU-NH-Ala-C12-Ala-NH (blue), and PU-NH-Leu-C12-Leu-NH (black). The numbers in the Figure are the $T_{\rm g}$ of the corresponded sample. The PU-NH-Ala-C12-Ala-NH data was shifted along the y-axis for clarity. Heating rate is 10 °C/min under nitrogen atmosphere. 176176
Figure 74. The thermogravimetric curve of PU-NH-Ala-C12-Phe-NH (blue), PU-NH-Leu-C12-Leu-NH (black), and PU-NH-Phe-C12-Phe-NH (red). The onset temperatures were analyzed by TA instruments Universal Analysis 2000 software and shown on the figure. Heating rate is 10 °C/min under nitrogen atmosphere
Figure 75. First derivative of the thermogravimetric curve of PU-NH-Ala-C12-Phe-NH (blue), PU-NH-Leu-C12-Leu-NH (black), and PU-NH-Phe-C12-Phe-NH (red) 177177
Figure A1. ¹ H NMR spectrum of PMA in CDCl ₃
Figure A2. ¹ H NMR spectrum of TMSPMA in CDCl ₃
Figure A3. ¹³ C{ ¹ H} NMR spectrum of TMSPMA in CDCl3
Figure A4. ¹ H NMR spectrum of PTMSPMA in CDCl ₃
Figure A5. Overlapped GPC traces during ATRP polymerization kinetic reaction. [TMSPMA]:[EBPA]:[$Cu^{II}Br_2$]:[$dNbpy$] = 200:1:0.6:1.2, [Cu^0] = 10 (mm^2) 194194
Figure A6. ¹ H NMR spectrum of PPMA in CDCl ₃
Figure A7. ¹ H NMR spectrum of PMMA-co-PTMSPMA (mol ratio = 10 : 1) in CDCl ₃ .

Figure A8. ¹ H NMR spectrum of PMMA-co-PPMA (mol ratio = 10 : 1) in CDCl ₃ .197197
Figure A9. ¹ H NMR spectrum of mDEG-azide in CDCl ₃
Figure A10. ¹³ C{ ¹ H} NMR spectrum of mDEG-azide in CDCl ₃
Figure A11. ¹ H NMR spectrum of dodecyl azide in CDCl ₃
Figure A12. ¹³ C{ ¹ H} NMR spectrum of dodecyl azide in CDCl ₃
Figure A13. ¹ H NMR spectrum of 100% mDEG-PPMA in CDCl ₃
Figure A14. ¹ H NMR spectrum of 90% mDEG-PPMA in CDCl ₃
Figure A15. ¹ H NMR spectrum of 80% mDEG-PPMA in CDCl ₃
Figure A16. ¹ H NMR spectrum of 70% mDEG-PPMA in CDCl ₃
Figure A17. ¹ H NMR spectrum of 60% mDEG-PPMA in CDCl ₃
Figure A18. Overlapped ¹ H NMR spectrum of CuAAC kinetic result between EMP and benzyl azide
Figure A19. ¹ H NMR spectrum of N-acetyl-L-phenylalanine S-thiophenyl ester (APTE) in CDCl ₃
Figure A20. ¹³ C{ ¹ H} NMR spectrum of alanine sample after CO ₂ absorption in D ₂ O
Figure A21. ¹³ C{ ¹ H} NMR spectrum of alanine sample after CO ₂ desorption in D ₂ O
Figure A22. ¹³ C{ ¹ H} NMR spectrum of glycine sample after CO ₂ absorption in D ₂ O
Figure A23. ¹³ C{ ¹ H} NMR spectrum of glycine sample after CO ₂ desorption in D ₂ O
Figure A24. ¹³ C{ ¹ H} NMR spectrum of proline sample after CO ₂ absorption in D ₂ O
Figure A25. ¹³ C{ ¹ H} NMR spectrum of proline sample after CO ₂ desorption in D ₂ O
Figure A26. $^{13}C\{^{1}H\}$ NMR spectrum of lysine sample after CO ₂ absorption in D ₂ O (aliphatic region only)
Figure A27. ¹³ C{ ¹ H} NMR spectrum of lysine sample after CO ₂ absorption in D ₂ O (carbonyl region only)

Figure A28. ¹³ C{ ¹ H} NMR spectrum of lysine sample after CO ₂ desorption in D ₂ 0	
Figure A29. ¹³ C{ ¹ H} NMR spectrum of GA sample after CO ₂ absorption in D ₂ O (carbonyl region only).	. 218218
Figure A30. ¹³ C{ ¹ H} NMR spectrum of AP sample after CO ₂ absorption in D ₂ O (carbonyl region only).	. 219219
Figure A31. ¹³ C{ ¹ H} NMR spectrum of GP sample after CO ₂ absorption in D ₂ O (carbonyl region only).	. 220220
Figure A32. ¹³ C{ ¹ H} NMR spectrum of GL sample after CO ₂ absorption in D ₂ O (carbonyl region only).	. 221221
Figure A33. ¹³ C{ ¹ H} NMR spectrum of GL sample after CO ₂ absorption in D ₂ O (carbonyl region only).	. 222222
Figure A34. ¹³ C{ ¹ H} NMR spectrum of AL sample after CO ₂ absorption in D ₂ O (carbonyl region only).	. 223223
Figure A35. ¹³ C{ ¹ H} NMR spectrum of GAP sample after CO ₂ absorption in D ₂ C (carbonyl region only).	
Figure A36. ¹³ C{ ¹ H} NMR spectrum of GAL sample after CO ₂ absorption in D ₂ C (carbonyl region only).	
Figure A37. ¹³ C{ ¹ H} NMR spectrum of PAL sample after CO ₂ absorption in D ₂ O (carbonyl region only).	
Figure A38. ¹³ C{ ¹ H} NMR spectrum of GPL sample after CO ₂ absorption in D ₂ O (carbonyl region only).	
Figure A39. ¹³ C{ ¹ H} NMR spectrum of GAPL sample after CO ₂ absorption in D ₂ (carbonyl region only).	
Figure A40. ¹ H NMR spectrum of Boc-Phe-OSu in CDCl ₃	. 229229
Figure A41. gCOSY of Boc-Phe-OSu in CDCl ₃ .	. 230230
Figure A42. ¹ H NMR spectrum of Boc-Leu-OSu in CDCl ₃	. 231231
Figure A43. ¹ H NMR spectrum of Boc-Ala-OSu in CDCl ₃	. 232232
Figure A44. Overlapped variable temperature ¹ H NMR spectrum of Boc-Phe-C2-Boc in CDCl ₃ at 25 °C (bottom), at 45 °C (middle), and 65 °C (top)	
Figure A45. 1D NOESY spectrum of Boc-Phe-C2-Phe-Boc in CDCl ₃	. 234234

Figure A46. ¹ H NMR spectrum of Boc-Leu-C2-Leu-Boc in CDCl ₃	235235
Figure A47. ¹ H NMR spectrum of Boc-Leu-C12-Leu-Boc in CDCl ₃	236236
Figure A48. ¹ H NMR spectrum of Boc-Phe-C12-Phe-Boc in CDCl ₃	237237
Figure A49. ¹ H NMR spectrum of Boc-Ala-C12-Ala-Boc in CDCl ₃	238238
Figure A50. ¹ H NMR spectrum of NH-Phe-C2-Phe-NH in CDCl ₃	239239
Figure A51. ¹³ C{ ¹ H} NMR spectrum of NH-Phe-C2-Phe-NH in CDCl ₃	240240
Figure A52. ¹ H NMR spectrum of NH-Leu-C2-Leu-NH in CDCl ₃	241241
Figure A53. $^{13}C\{^1H\}$ NMR spectrum of NH-Leu-C2-Leu-NH HCl salt in D2O	242242
Figure A54. ¹ H NMR spectrum of NH-Phe-C12-Phe-NH in CDCl ₃	243243
Figure A55. ¹³ C{ ¹ H} NMR spectrum of NH-Phe-C12-Phe-NH in CDCl ₃	244244
Figure A56. ¹ H NMR spectrum of NH-Ala-C12-Ala-NH in CDCl ₃	245245
Figure A57. ¹³ C{ ¹ H} NMR spectrum of NH-Ala-C12-Ala-NH in CDCl ₃	246246
Figure A58. ¹ H NMR spectrum of NH-Leu-C12-Leu-NH in CDCl ₃	247247
Figure A59. ¹³ C{ ¹ H} NMR spectrum of NH-Leu-C12-Leu-NH in CDCl ₃	248248
Figure A60. ¹ H NMR spectrum of polyurea-NH-Leu-C2-Leu-NH in DMSO-d ₆	249249
Figure A61. ¹ H NMR spectrum of polyurea-NH-Phe-C2-Phe-NH in DMSO-d ₆	250250
Figure A62. ¹ H NMR spectrum of polyurea-NH-Phe-C12-Phe-NH in DMSO- <i>d</i> ₆ .	251251
Figure A63. ¹ H NMR spectrum of polyurea-NH-Leu-C12-Leu-NH in DMSO-d ₆ .	. 252252
Figure A64. ¹ H NMR spectrum of polyurea-NH-Ala-C12-Ala-NH in DMSO- <i>d</i> 6.	253253
Figure A65. DSC data for polyurea-NH-Phe-C2-Phe-NH.	254254
Figure A66. DSC data for polyurea-NH-Leu-C2-Leu-NH.	255255
Figure A67. DSC data for polyurea-NH-Leu-C12-Leu-NH.	256256
Figure A68. DSC data for polyurea-NH-Phe-C12-Phe-NH.	257257
Figure A69. DSC data for polyurea-NH-Ala-C12-Ala-NH.	258258

Figure A70. The thermogravimetric curve (green) and first derivative weight loss (blue) of polyurea-NH-Phe-C2-Phe-NH.	
Figure A71. The thermogravimetric curve (green) and first derivative weight loss (blue) of polyurea-NH-Leu-C2-Leu-NH.	
Figure A72. The thermogravimetric curve (green) and first derivative weight loss (blue) of polyurea-NH-Ala-C12-Ala-NH.	
Figure A73. The thermogravimetric curve (green) and first derivative weight loss (blue) of polyurea-NH-Phe-C12-Phe-NH	
Figure A74. The thermogravimetric curve (green) and first derivative weight loss (blue) of polyurea-NH-Leu-C12-Leu-NH.	

LIST OF SCHEMES

Scheme 1. The ATRP mechanism
Scheme 2. Three different synthetic routes to comb-like copolymers. (a) grafting to method. (b) grafting through method. (c) grafting from method. The scheme is from reference 14
Scheme 3. The post-polymerization modification using methacrylate bearing a selective handle as an example. Different functional groups (FGs) can be introduced to the same polymer backbone.
Scheme 4. The sol-gel method for enzyme entrapment
Scheme 5. Alkyne-containing polymer prepared by esterification. 15,77
Scheme 6. Poly(trimethylsilyl propargyl methacrylate) examples reported by various polymerization conditions
Scheme 7. Polymerization of TMSPMA by conventional ATRP
Scheme 8. The ARGET ATRP mechanism
Scheme 9. Lipid bilayer formation by hydrophilic hydrophobic interactions65
Scheme 10. Formation of micelle from block copolymer65
Scheme 11. The deprotection of poly(trimethylsilylpropargyl methacrylate)68
Scheme 12. Post-polymerization modification of PPMA with mDEG-N3 by CuAAC 70
Scheme 13. CuAAC reaction rate of poly(3-azidopropyl methacrylate) (top) and 3-azidopropyl methacrylate (bottom) reacting with propargyl alcohol
Scheme 14. Reactivity of diazide toward phenylacetylene and mechanism proposed by Fokin and Finn
Scheme 15. Synthesis of copper iminophosphorane triazole complex reported by Venderbosch and coworkers. 108
Scheme 16. Reactivity of dialkyne toward benzyl azide and mechanism proposed by Fokin and Finn
Scheme 17. CuAAC reaction of benzyl azide with ethynyl-2-methylpropanoate (EMP), poly(propargyl methacrylate) (PPMA), and poly(propargyl methacrylate)-co-poly(methyl methacrylate) (PPMA-co-PMMA)

Scheme 18. Reaction scheme of cross-linking three different poly(propargyl acrylate- co - n -butyl acrylate)s (PPA- co -PBAs) ($M_n = 9,600, 12,000, $ and 19,100) with three-arm-star
azido-telechelic poly(isobutylene) reported by Döhler8787
Scheme 19. Formation of unimolecular micelle by amphiphilic comb polymer9292
Scheme 20. Colorimetric enzymatic assay using z-Ala-ONp as a substrate in toluene. [substrate] = 0.01 M, [n -BuOH] = 1 M, [SC] = 0.2 mg/mL, [SC]: [mDEG-PPMA] = 1: 2. Aliquots (50 μ L) were taken periodically, mixed with 500 μ L of 0.1 N NaOH _(aq) , and vortexed for 30 s before measuring the UV-Vis of the aqueous layer
Scheme 21. Mechanism of 4,4′-dithiodipyridine (DTDP) reacting with a thiol to release a 4-mercaptopyridine and then tautomerizing into 4-thiopyridone chromophore 121121
Scheme 22. The design of enzymatic assay using 4-thiopyridone as chromophore. 124124
Scheme 23. Ionization states of amino acid in different pH value
Scheme 24. MEA carbamate formation via zwitterion mechanism
Scheme 25. Formation of bicarbonate ion by reaction between hydroxide ion with dissolved CO ₂ (aq)
Scheme 26. Formation of bicarbonate ion by carbamate decomposition
Scheme 27. Formation of amino acid carbamate and amino acid zwitterion 134134
Scheme 28. Chemical structures of lysine CO ₂ adducts after absorption
Scheme 29. The steric effect to the amino acid-CO ₂ intermediate stability
Scheme 30. Synthesis of symmetric diamine monomers from different amino acids (phenylalanine, leucine, and alanine) and two different spacer lengths (C2 and C12).
Scheme 31 Polymerization of symmetrical diamine monomers with 4.4' -MDI 165165

KEY TO ABBREVIATIONS

18-Crown-6 ether 1,4,7,10,13,16-hexaoxacyclooctadecane

AA Amino acid

ARGET ATRP Activator ReGenerated by Electron Transfer ATRP

ATRP Atom Transfer Radical Polymerization

br Broad

Bz Benzyl

BzBr Benzyl α-bromoisobutyrate

cmc Critical micelle concentration

Conv. Conversion

C_p Cyclopentadiene

CuAAC Copper-catalyzed alkyne-azide cycloaddition

Cu^IBr Copper(I) bromide

 $Cu^{II}Br_2$ Copper(II) bromide

d Doublet

δ Chemical shift

Da Dalton

DCM Dichloromethane

DLS Dynamic light scattering

DMF *N,N*-Dimethylformamide

DMSO Dimethyl sulfoxide

dNbpy 4,4-Dinonyl-2,2'-bipyridine

dN5bpy 4,4'-Di(5-nonanyl)-2,2'-bipyridine

DTDP 4,4'-Dithiodipyridine

EBPA Ethyl α-bromophenylacetate

EtBriB Ethyl α-bromoisobutyrate

FG Functional group

gCOSY Gradient-selected Correlation Spectroscopy

GPC Gel permeation chromatography

h Hour

HMBC Heteronuclear multiple bond coherence

HMTETA 1,1,4,7,10,10-hexamethyltriethylenetetramine

HSQC Heteronuclear single quantum coherence

Hz Hertz

IR Infrared spectroscopy

J Coupling constant

 K_{ATRP} ATRP equilibrium constant

LCST Lower critical solution temperature

m Multiple

M Molar

MALS Multiangle light scattering detector

mg Milligram

MHz Megahertz

min Minute

mL Milliliter

*M*_n Number-average molecular weight

M_w Weight-average molecular weight

NHS *N*-hydroxysuccinimide

NOE nuclear Overhauser effect

PBS Phosphate buffered saline

PDI Polydispersity index

mDEG Triethylene glycol monomethyl ether

NMR Nuclear magnetic resonance

PEG Poly(ethylene glycol)

PMMA Poly(methyl methacrylate)

ppm Parts per million

PPM Post-polymerization modification

PPMA Poly(propargyl methacrylate)

ppmv Parts per million by volume

PTMSPMA Poly(trimethylsilyl propargyl methacrylate)

q Quartet

RAFT Reversible-addition fragmentation chain transfer

*R*_H Hydrodynamic radius

rt Room temperature

s Singlet

SC Subtilisin Carlsberg

SPAAC Strain promoted alkyne-azide cycloaddition

t Triplet

t Time

 $T_{\rm g}$ Glass transition temperature

THF Tetrahydrofuran

UV-Vis Ultraviolet-visible

Chapter 1. Introduction

Overview of atom transfer radical polymerization (ATRP)

In conventional radical polymerizations, an initiator reacts with an atom in a closed-shell monomer to make a new covalent bond, while creating unpaired electron spin density—a radical—on the initiated monomer. The chains grow through subsequent reactions of the radical chain and the monomer. Chain growth terminates when the radical at the chain terminus is quenched. The molecular weight distribution of the polymer chains is broadened when (i) chain initiation is slow relative to chain propagation, (ii) two radical chains react to generate two new radical chains via chain transfer, and/or (iii) two chain ends couple in a radical chain termination event. If the goal of a radical polymerization is to produce a material where the range of chain molecular weights is narrow, the three events noted above must avoided.

Atom transfer radical polymerization (ATRP), was independently developed by $Sawamoto^{1} \text{ and Matyjaszewski.}^{2} \text{ In the ATRP mechanism,}^{2} \text{ the initiator was initiated by}$ the activator ($Cu^{I}X/L_{n}$) to generate an initiator radical ($In\cdot$) and a deactivator ($Cu^{II}X_{2}/L_{n}$), shown in Scheme 1.

Scheme 1. The ATRP mechanism

The first step in initiating the polymerization is the reaction between Cu^I–X/L_n with In-X to generate two species—Cu^{II}-X₂/L_n and In⋅. These radicals can either recombine to their dormant states, Cu^I–X/L_n and In–X, or In· can react with a monomer to initiate the radical chain. The initiated monomer $In-P_1$ can react in an analogous fashion. Reaction with one (or more) monomers extends that radical chain, forming In-P_n, while reaction with the deactivating Cu radical, Cu^{II}–X₂/L_n, returns both radicals to their dormant states, Cu^{I} – X/L_n and In– P_1 –X. The propagation rate is determined by the monomer structure and the concentration of the radical. The termination rate is affected by the concentration of radical. Therefore, the termination rate can be decreased by lowering the radical concentration, leads to overall a lower propagation rate for ATRP than conventional free radical polymerization. With sufficient deactivator concentration, the radical concentration is suppressed by the equilibrium between the higher oxidative state deactivator ($Cu^{II}X_2/L_n$) and the lower oxidative state activator (Cu^IX/L_n). With much lower radical concentrations during polymerization, side reactions like chain transfer and chain termination can be minimized. The vast majority of the chains are in the dormant state (R-X), and only a small

fraction exist as free radicals react with monomers to propagate with chain before returning to their dormant state after a few monomer additions.

Finding the proper condition with optimal balance between k_a and k_d is the key to well-control polymerization with a reasonable polymerization rate. Factors affect k_a and k_d of a polymerizing a specific monomer include: (1) Ligand structures on the copper center (2) initiator structures (3) transfer atom groups (4) polymerization solvents.

The first factor is the activator ($Cu^{I}X/L_n$) and deactivator ($Cu^{II}X_2/L_n$) activities can be modified by the ligand structures on the copper centers. The activities of the copper complexes are defined by the ATRP equilibrium constant (K_{ATRP}), shown in Eq 1Eq 1, i.e., the ratio of the rate constants for activation (k_a) and deactivation (k_d) . The K_{ATRP} of ATRP catalysts is small to ensure most of the radicals are in the dormant state. The complex with higher K_{ATRP} drives the equilibrium toward radical side and the higher radical concentration leads to faster polymerization rate. The Figure 1 shows various ligand structures and the K_{ATRP} of the corresponding copper complexes in acetonitrile.³ The activities of catalysts bearing different ligand structures decrease in the following trend: alkyl amine ~ pyridine > alkyl imine. Since the ATRP equilibrium is governed by the redox properties between Cu(I) and Cu(II), cyclic voltammetry data can help illustrate the activities of different catalyst complexes. A linear correlation of $E_{1/2}$ of different copper complexes with their K_{ATRP} is reported by Tang and coworkers,³ shown in Figure 2. The more reducing complexes (with lower $E_{1/2}$ value) are the more active ATRP catalyst with higher K_{ATRP} , which drives the equilibrium toward the radical side. The polymerization control and polymerization rate rely on finding the proper copper catalyst structure for the corresponded monomer.

Figure 1. ATRP equilibrium constants K_{ATRP} for nitrogen-based ligands determined with the initiator EtBriB in the presence of Cu^IBr in MeCN at 22°C.³

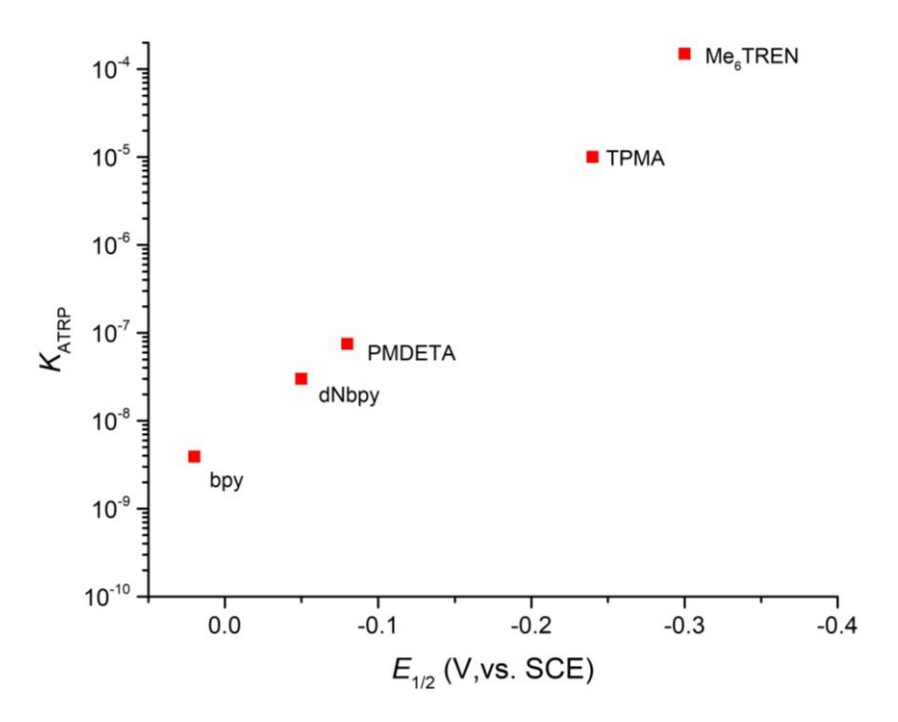


Figure 2. Plot of K_{ATRP} (measured with the initiator EtBriB in acetonitrile, structure shown in Figure 1, versus $E_{1/2}$ for different Cu^{II}Br₂/L complexes (ligand structures show in Figure 1).³

The second factor that can affect the k_a and k_d at the early stage of polymerization is the initiator structure. As we mentioned above, to obtain polymer with narrower PDI, the initiation rate must be faster than the propagation rate. Therefore, the k_a plays an important role in keeping PDI narrow. The different initiator structures lead to different stabilities of the corresponding radicals and different k_a values. The k_a and k_d of a specific initiator were determined by trapping the generated radicals by TEMPO and the resulting In–TEMPO products were quantified by HPLC or GC.^{4,5} The k_a values for primary, secondary, and tertiary alkyl halide follow the order: $1^{\circ} < 2^{\circ} < 3^{\circ}$, shown in Figure 3. The k_a of the tertiary alkyl bromide initiator MBriB is 8 times higher than the secondary initiator MBrP, and 87 times higher than the primary counterpart MBrAc.⁵ The size of the alkyl ester group also found to affect the k_a values of initiators. The k_a of the initiator containing methyl ester group MBrP is 4 times higher than the counterpart with t-butyl ester group t-brown in Figure 3.

The α -substituent of the radical also affects the k_a value of the initiator. Substituents with π -accepting functional groups can stabilize the radical by delocalizing the unpaired electron onto the π^* -orbital. Most of the k_a values for the initiators listed in the Figure 3 were determined by reacting 1 mM of different initiators with 20 mM of Cu^IBr/PMDETA and trapped the radical by TEMPO. However, for the active initiators like EBPA and BrPN, less active catalysts like Cu^IBr/NPPMI and Cu^IBr/HMTETA, respectively were used to obtain accurate k_a values. By assuming Cu^IBr/PMDETA (more reactive catalyst) and Cu^IBr/HMTETA (less reactive catalyst) have the same selectivity toward different initiators, the k_a values determined from the less active catalysts can be extrapolated using an initiator with k_a that has been accurately determined in both catalysts (more reactive and

less reactive catalysts). k_a (BrPN, Cu^IBr/PMDETA) = k_a (BrPN, Cu^IBr/HMTETA) × k_a (EtBriB, Cu^IBr/PMDETA) / k_a (EtBriB, Cu^IBr/HMTETA). The k_a (Cu^IBr/PMDETA) of initiator bearing substituents follow this order: ester and phenyl (EBPA, $5.3 \times 10^3 \,\mathrm{M}^{-1} \mathrm{s}^{-1}$) > cyano (BrPN, $2.3 \,\mathrm{M}^{-1} \mathrm{s}^{-1}$), ester (MBrP, $0.33 \,\mathrm{M}^{-1} \mathrm{s}^{-1}$) > phenyl (PEBr, $0.17 \,\mathrm{M}^{-1} \mathrm{s}^{-1}$) > amide (DEBrPA, $0.040 \,\mathrm{M}^{-1} \mathrm{s}^{-1}$). Due to the dual stabilization effect from ester and phenyl groups, the k_a of EBPA is 132,500 times higher than the amide bearing initiator DEBrPA.

Primary, secondary, tertiarty alkyl bromide:

O Br O Br O Br MBrAc MBrP MBriB
$$k_a = 0.030 \text{ M}^{-1}\text{s}^{-1}$$
 $k_a = 0.33 \text{ M}^{-1}\text{s}^{-1}$ $k_a = 2.6 \text{ M}^{-1}\text{s}^{-1}$

Size of the alkyl ester group:

α -Substituent effect:



Figure 3. Activation rate constant (k_a) of various initiators were determine with [Initiator]₀ = 1mM, [Cu^IBr/PMDETA]₀ = 20 mM, at 35°C in MeCN except for EBPA and BrPN.⁵ The k_a of EBPA is determined by Cu^IBr/NPPMI. The k_a of EBPA is determined by Cu^IBr/HMTETA.⁵

The third factor that can affect the k_a and k_d during ATRP is the transfer group, X, which is typically halogen. The K_{ATRP} for the Br-based initiators are almost 10 times higher than their Cl-based counterparts.³ Under the same condition (Cu^IX/PMDETA in acetonitrile), the k_a of initiator bearing bromo MBrP is 0.33 M⁻¹s⁻¹ 22 times higher than the chloro-containing initiator MClP because the C–Br bond is weaker than the C–Cl bond.⁵ The iodo-containing initiator, MIP has a k_a that is higher than the bromo-containing counterpart MBrP but due to the low stability of Cu^{II}–I bond, the K_{ATRP} of MIP is ~ 15 times smaller than MBrP. The alkyl iodides are not common choices as ATRP initiators.

MIP MCIP MBrP

$$K_{ATRP} = 2.2 \times 10^{-8}$$
 $K_a = 0.53 \text{ M}^{-1}\text{s}^{-1}$
 $K_a = 0.33 \text{ M}^{-1}\text{s}^{-1}$

Figure 4. The ATRP equilibrium constant and activation rate constant of initiator bearing different transfer groups. K_{ATRP} values for various initiators were determined with Cu^IX/TPMA in MeCN at 22 °C.³ k_{a} values for various initiators were determined with Cu^IX/PMDETA in MeCN at 35 °C.⁵

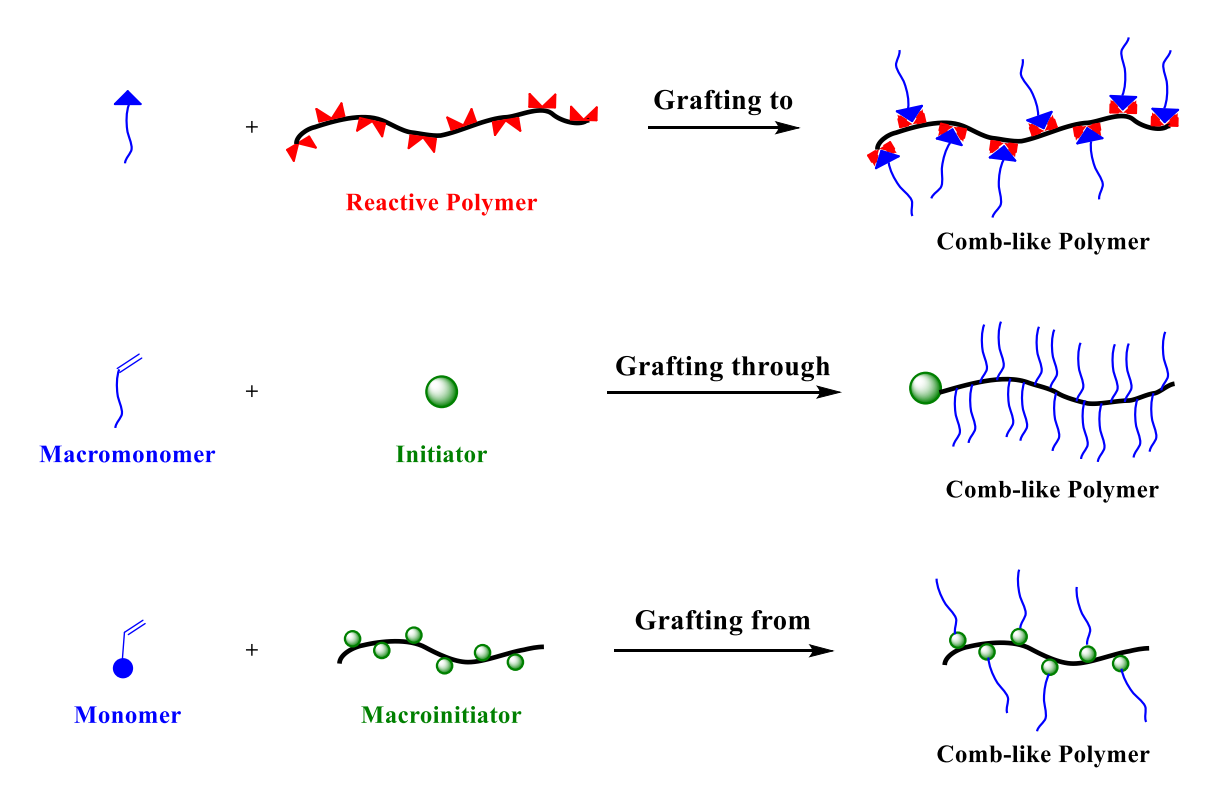
The last factor that affects the k_a and k_d during ATRP is the solvent. The polar solvent accelerates the activation process and decreases the rate of deactivation leading to higher $K_{\rm ATRP}$. Under the same condition (EtBriB as the initiator and Cu^IBr/HMTETA as the catalyst), 14 different solvents were tested and discovered that the k_a in DMSO (k_a = 1.30 M⁻¹s⁻¹) is roughly 31-fold higher than in butanone, the one with the lowest k_a (k_a = 0.0417 M⁻¹s⁻¹). In the same condition, formamide has the highest $K_{\rm ATRP}$ (2.83×10⁻⁶) followed by DMSO ($K_{\rm ATRP}$ = 2.59×10⁻⁹) and butanone ($K_{\rm ATRP}$ = 1.55×10⁻⁹).

With the versatile reactivity of different ligand and initiator structures, ATRP has successfully been applied to polymerize various monomers, including styrene,⁸ acrylate,⁹ methacrylate,⁹ acrylonitrile,¹⁰ acrylamide,¹¹ 4-vinyl pyridine,¹² and methacrylic acid.¹³

Overview of preparing comb-like copolymers

Comb-like copolymers are the polymers containing one or more than one chemically different polymer structures connected to the main polymer backbone. The synthetic methods of comb-like copolymers can be categorized into three types: grafting-to, grafting-through, and grafting-from.¹⁴ These three synthetic routes are summarized in Scheme 2Scheme 2.

Scheme 2. Three different synthetic routes to comb-like copolymers. (a) grafting to method. (b) grafting through method. (c) grafting from method. The scheme is from reference 14.



The grafting-to method uses polymer backbones bearing reactive groups where sidechains can be installed through chemical reactions with another functional polymer shown in Scheme 2Scheme 2a. One advantage of the grafting-to approach is that the side

chains with diverse structures can be installed on the same batch of polymer backbone. This allows for the side chain structure—property studies since the grafted polymer products have the same backbone length and polydispersity but different side chain structures and grafting density. The grafting density of the polymer product is determined by the density of the functional group on the reactive polymer backbone, the size of the functional polymer, and the chemical structure of the functional polymer. Gao and Matyjaszewski ¹⁵ studied the effect of the size and the chemical structure of the functional polymer. They grafted different azide functionalized polymers, such as poly(ethylene glycol)-N₃, polystyrene-N₃, poly(n-butyl acrylate)-N₃, and poly-(n-butyl acrylate)-b-polystyrene-N₃, to reactive polymer bearing alkyne groups. Among all the side chain structures, they found the poly(ethylene glycol)- N_3 with $M_n = 750$ g/mol reached the highest grafting density (88%) when 8 equivalents of azide to alkyne group was used. The grafting density dropped when grafting longer side chains onto the polymer backbone or the side chains containing bulkier groups like polystyrene. The concept of grafting-to is a form of post-polymerization modification and will be further discussed in the following section.

Grafting-through is polymerizing the macromonomer that contains the desired side chain structure with a reactive end group, the "monomer," from which the polymer backbone of the comb is grown by polymerization at one terminus. Grafting through does not have the incomplete grafting conversion issue. Polymerization of the macromonomer with high molecular weight is challenging due to the increasing viscosity after each macromonomer is added to the chain. It can be explained by the Mark-Houwink Sakurada equation (Eq 2Eq 2), which is an empirical relationship between molecular weight (M) and intrinsic viscosity ([η]):

 $[\eta] = KM^a$ Eq 2

where K and a are empirically determined constants for a polymer-solvent system.

If a monomer with a small molecular weight was added to the polymer chain, it has a limited impact on the intrinsic viscosity of the system per monomer addition. While polymerizing a macromonomer with much higher molecular weight, the significant increase of molecular weight per monomer addition can significantly alter the intrinsic viscosity of the system. Therefore, the solubility can drop quickly even at low polymerization conversion. The phase separation of the growing chain to the bulk polymerization media decreases or halts the polymerization. For growing side chains with high molecular weight, grafting-from can be a better choice.

Grafting-from uses polymer backbones bearing initiating sites and the polymer chains are grown from the initiator sites. With the advent of the control/living radical polymerization, grafting from method can prepared comb-like copolymers with high grafting density and narrow polydispersity. Beers and colleagues¹⁶ prepared poly-(2-(2-bromoisobutyryloxy)ethyl methacrylate)-*graft*-polystyrene by atom transfer radical polymerization (ATRP) with M_n up to 4,980,000 and PDI = 1.20. While the free radical polymerization counterpart only resulted in polymer with $M_n = 90,800$ and PDI = 2.20. Suppressing the cross-coupling between polymer chains is critical in grafting from method.

Overview of post polymerization modification

There are two general approaches for synthesizing polymers having one or more functional groups along the chain: (i) Polymerizing monomers containing the desired functional group(s) (i.e., functionalized monomers) or (ii) post-polymerization

modification (PPM). For the functionalized monomer strategy, altering the polymer structure requires the synthesis and polymerization of new functionalized monomers. While the requirement that functional groups must be compatible with polymerization conditions can restrict the scope of polymer functionality, multiblock co-polymers can be synthesized via the functionalized monomer approach. In the PPM method, a polymer is synthesized from a monomer that contains functionality retained in the resulting polymer. What sets PPM apart from the functionalized monomer strategy is that the functionality in the polymer is easily and reliably transformed by chemical reactions with both exceptional substrate scope and cross-compatibility. PPM can enable rapid synthesis of polymers with diverse combinations of functionalities, including groups that cannot be installed using the functionalized monomer approach due to their incompatibility with the polymerization conditions. The PPM approach is illustrated in Scheme 3. The ideal PPM process should include the following: (1) the reaction should be highly selective, and it should not react with the polymer chain, (2) it should not be prone to crosslinking, and (3) it should exhibit a high functional group tolerance and yield.¹⁷ Common PPM reactions include thio-ene, thio-yne, Michael addition, copper(I)-catalyzed alkyne-azide cycloaddition (CuAAC), Strain promoted alkyne-azide cycloaddition (SPAAC), etc. The coupling partners of the PPM methods are summarized in Table 1.

Scheme 3. The post-polymerization modification using methacrylate bearing a selective handle as an example. Different functional groups (FGs) can be introduced to the same polymer backbone.

Table 1. Summary of coupling partners in the commonly used post-polymerization modification methods.

Post-polymerization modification method	Coupling partner	Coupling partner
CuAAC	R _{N3}	R'
Strain promoted alkyne- azide cycloaddition (SPAAC)	R _{N3}	N R'
Michael addition	R _S	N R'
Radical-mediated thiol-ene addition	R _{`SH}	⊗ R'
Radical-mediated thiol-yne addition	R _{\SH}	R'
Diels-Alder	RO	N R'

CuAAC was independently introduced by Sharpless, Fokin, ¹⁸ and Meldal ¹⁹ groups. Due to the high selectivity, broad functional group tolerance, and mild reaction conditions, CuAAC has been found as a powerful tool for post polymerization modification (PPM) and was applied to various polymer backbones: polyester, 20 polyurethane, 21 poly(2oxazoline), ²² polycarbonate, ²³ and poly(p-phenylene ethynylene) ²⁴, as shown in Figure 5Figure 5. The PPM approach obviates the synthesis of individual monomers each time a new structural feature is to be introduced, as a parent polymer bearing azide or alkyne groups can be modified by grafting side chains along the polymer chain with CuAAC reactions of alkyne or azide molecules. CuAAC introduces the functional groups that are not compatible with the polymerization conditions and is a useful tool for studying structure-property relationship since all the modified polymer products are made from the same parent polymer, which has the same chain length and polydispersity. However, the requirement of copper catalyst in CuAAC can be problematic in electronic applications, ²⁵ and Cu toxicity can arise in bio-applications in vivo. 26,27 The other limitation is that CuAAC, like other grafting to methods, usually does not reach complete conversion if the polymer backbone was coupled with high molecular weight side chains, due to the grafted chains blocking the neighboring modifiable sites.¹⁵

Figure 5. The CuAAC modifiable polymer examples.

Overview of polymers as enzyme stabilizers

Through billions of years of evolution, enzymes have adapted and become excellent catalysts capable of converting a wide spectrum of substrates into metabolites with high efficiencies and high chemo-, regio-, and enantioselectivities under mild conditions. ^{28,29,30} Enzymatic catalysis has gained more attention due to the need for enantiomerically pure chemicals for pharmaceutical and agrochemical uses. There are two candidates suitable for this purpose: whole cells (from microbial, plant, or animal) and isolated enzymes. To keep cells alive, the reactions are run under aqueous condition. However, there are several challenges of using living cells as biocatalysts for unnatural transformation: (i) the desired

substrates or products can be toxic to cell, causing the inhibition of the further reactions, (ii) the substrates or products might have poor cell permeability, (iii) living cells need to be cultured and fed to precede the reactions, (iv) limited substrate solubility in water leads to low reagent concentrations in biocatalytic reactions and complicated product recovery process, and (v) the substances from cell or cell-growth medium might contaminate products.

Applying isolated enzymes as biocatalysts can solve the cell permeability issue, prevent the product contamination from cell-growth medium, and circumvent the need for cell culture. Unfortunately, the poor substrate solubility in water remains unsolved. To solve the solubility issue, organic solvents as reaction media were considered to be implausible because enzymes were evolved in organisms where water is the "solvent." Their structural integrity is compromised in mixtures of organic solvents that are miscible in water, and their catalytic activity in organic media is typically destroyed. This conventional wisdom started to change when Klibanov and co-workers found that two lyophilized enzymes, Bovine pancreatic α -chymotrypsin (α -chymotrypsin) and Bacillus subtilis protease (subtilisin Carlsberg), could act as heterogenous catalysts in nearly anhydrous, hydrophobic organic solvents.²⁹ Klibanov and co-workers also established three key factors, which greatly affect the enzymatic activities: (1) solvent effects (2) pH memory effect (3) effects of additives during lyophilization. In the first case, higher enzymatic activity was observed in hydrophobic solvents, as hydrophilic solvents were prone to remove vital protein-bound water, which is critical for maintaining protein structure and activity.³¹ In the second case, the "pH memory effect" was observed by Zak and colleagues 32 that enzymatic activity in nearly anhydrous organic media greatly depends on the pH environment of the enzyme precipitated or lyophilized from. The porcine pancreatic lipase precipitated from the optimal pH (8.4) has the highest activity in 2 M heptanol in the tributyrin (containing 0.02% water). While the pH memory effect is not observed in the aqueous media due to the fast equilibrium with the bulk aqueous media. Zacharis and colleagues further found out that the pH memory effect in organic media can be altered if the organic-extractable weak acid or base was used as buffer. The *subtilisin* lyophilized from ammonium formate buffer, which both ions can be removed by hexane (the assay media), did not have the pH memory effect, and have lower activity than the counterpart lyophilized from sodium phosphate buffer.³³ The third case is the effect of additives during lyophilization. Khmelnitsky and co-workers showed that the catalytic activity of subtilisin Carlsberg in dry hexane was 3750-fold higher when it was lyophilized in 98% KCl aqueous buffer solution compared to the salt-free lyophilized counterpart.³⁴ Several additives, such as sorbitol, poly (ethylene glycol), and glycerol, could also enhance the enzymatic activity.³⁵

Reaction media other than organic solvents have been studied in the realm of enzymatic catalysis, including water-miscible organic solvents, ³⁶ water-immiscible organic solvents, ³⁷ and biphasic systems. ³⁸ In anhydrous organic media, water-dependent side reactions, such as hydrolysis, ³⁹ were suppressed. In some cases, the product selectivity can be altered or even inversed when switching from aqueous media to organic solvent. ²⁸ However, most isolated enzymes are not sufficiently stable and often exhibit low catalytic activity in organic media. There are several methods to increase enzymatic activity in organic solvents: (i) directly suspending a lyophilized enzyme in an organic solvent, (ii) finding a solvent or solvent mixtures to create a more favorable environment for enzymes

(solvent engineering), (iii) immobilization or stabilization of enzymes by synthetic macromolecules, (iv) chemical modification on the surface of enzymes to increase stability, (v) genetic modification of enzyme structures to make them remain active in unconventional media.

Overview of enzyme polymer interactions

Different kinds of enzyme polymer interactions are utilized to stabilize enzymes: (1) covalent binding, (2) physical adsorption, (3) affinity binding, and (4) entrapment. For covalent binding, the chemical reaction is either site-specific or non-specific between with functional groups on the enzyme surfaces and on the polymers to form an enzyme polymer bioconjugates. One of the popular polymers to covalently bind to enzyme is poly(ethylene glycol) (PEG). In 1977, Abuchowski and co-workers^{40,41} reported the first PEG enzyme bioconjugate, bovine serum albumin (BSA)–PEG bioconjugate, which has reduced immunogenicity due to the incorporation of PEG polymer. Now PEG is frequently attached to therapeutic proteins and enzymes to prolong circulation time of the biopharmaceuticals and enhance solubility and stability due to the steric shielding effect provided by the synthetic polymer.⁴²

Another type of polymer enzyme interaction is physical adsorption, where enzymes interact with carriers, from silica, polymer resins, to modified surfaces, through weak interactions like Van der Waals forces, hydrogen bonds, ionic interaction, and hydrophobic interactions. Physical adsorption methods are widely used due to their simplicity, but they are also highly environmentally dependent and can lead to protein leakage due to the weak interaction between protein and the matrix.⁴³

Affinity interaction requires installing an affinity handle on the enzyme to interact with the carrier bearing the corresponding tag. The most common affinity interactions are metal ion-polyhistidine and Streptavidin-biotin interactions.⁴⁴ The metal ion-polyhistidine interaction are commonly used in protein purification, known as immobilized metal affinity chromatography. The bivalent metal ions (Co²⁺, Ni²⁺, Cu²⁺, Fe²⁺ or Zn²⁺) are chelated to the supporting materials including ligands like nitrilotriacetic acid (NTA) or iminodiacetic acid. The desired enzymes need to have six histidine tags at either N- or C-termini to coordinate to the metal ions. Metal ion-polyhistidine interaction has been used to immobilize green fluorescent protein, 45 horseradish peroxidase, 46 ferredoxin-NADP+ reductase, 46 NADH oxidase 47 onto various surfaces. The streptavidin-biotin interaction is a non-covalent interaction between a water-soluble vitamin B complex, biotin, and the homotetrameric protein streptavidin. It is one of the tightest non-covalent protein ligand interactions where the dissociation constant K_d is 10^{-15} . As Each streptavidin has four biotinbinding sites. ⁴⁹ To immobilize proteins through streptavidin–biotin interaction, there are two possible routes: (1) biotinylation of the protein; or (2) attaching streptavidin to the target protein. The biotinylation of protein can be site-specifically catalyzed by E. coli biotin ligase.⁵⁰ The biotin can also be introduced onto protein by *N*-hydroxysuccinimide (NHS) chemistry.⁵¹ Catalase,⁵¹ glucose oxidase,⁵² and horseradish peroxidase⁵³ have been immobilized onto different materials via streptavidin-biotin binding.

Enzymes can be entrapped within gel or polymer matrixes either by the sol-gel method or by polymerization around the enzymes.⁵⁴ The entrapped enzymes experience minimum conformational change during the entrapping process and have high operational stability. The drawbacks of the entrapment process are the potential enzyme leakage if the

supporting carriers decompose and the deactivation of enzymes by the reagents used in the entrapping process. The sol-gel method involves two steps: (1) generation of silanol group by acidic condition and (2) the gel formation by condensation, shown in Scheme 4Scheme 4. The first step (Scheme 4Scheme 4a) is acid catalyzed hydrolysis of alkylsilanes RSi(OCH₃)₃ and Si(OCH₃)₄ to form the silanol group (Si-OH, the "sol"). In the second step (Scheme 4Scheme 4b), the reaction mixture contains freshly prepared "sol" and the enzyme is adjusted to mildly basic condition to promote condensation between two silanol groups to form the Si–O–Si network (gel), trapping the desired enzyme within the gel.⁵⁵ The pH condition of the second step is crucial since strong basic conditions can lead to enzyme deactivation. The gels are then washed and dried to remove the free enzyme and reaction media to form a xerogels containing entrapped enzymes. The drying conditions determine the pore sizes of the enzyme-xerogel conjugates, which directly affect the substrate and product diffusion rate.⁵⁴ Alkaline phosphatase, ⁵⁶ glucose oxidase, and peroxidase ⁵⁷ have been entrapped by the sol-gel method. The entrapped alkaline phosphatase was found to have 30% of the initial enzymatic activity but better thermal stability at 70 °C than the free enzyme. The entrapped glucose oxidase and peroxidase have similar activities as their free enzyme counterparts.

Scheme 4. The sol-gel method for enzyme entrapment.

(a) Formation of silanol group (Si-OH):

OR
ROUSI OR
$$OH$$
H

Notice
 OH

ROUSI OH

H

Notice
 OH

ROUSI OH

ROUSI OH

Sol

Polymeric entrapment is conducted by initiating polymerization around the desired enzyme and trapping the enzymes within the polymer matrixes. The enzyme entrapped by the polymer is described as enzyme@polymer. Glucose isomerase@poly(acrylamide),⁵⁸ laccase@poly(acrylamide-N-isopropyl-acrylamide), ⁵⁹ and α-glucosidase@poly(2-hydroxyethyl methacrylate) ⁶⁰ have been prepared and the enzyme-polymer conjugates were reusable and retained 50% to 98% of their initial enzymatic activities after 10 to 25 cycles.

Overview of post combustion CO₂ capture

The historical atmospheric CO₂ concentration can be determined by the air trapped within the ice-core obtain from Vostok, Antarctica. Carbon dioxide concentrations in the atmosphere, expressed as part per million by volume (ppmv), for the past 420,000 years are shown in Figure 6. ⁶¹ Scientists discovered that the CO₂ level in the air fluctuated between 180 to 300 ppmv the peak CO₂ concentration is 300 ppm at 3 million years ago. However, after the industrial revolution, the utilization of the fossil fuels for electricity generation and transportation caused CO₂ levels to rise to an historic high of 414 ppmv in

the 2021 shown in Figure 7.62 The higher CO₂ concentration in the atmosphere traps more heat and causes global warming. Higher temperature leads to faster moisture evaporation rate, rapid drying of soil, and drier climate condition. The warmer air can also hold more moisture than cooler air. The extra water vapor in the atmosphere is available to storm systems, leading to heavier rainfalls. The extreme climate pattern can cause food security problem, loss of life and properties. The urgent need to reduce CO₂ emission and increase CO₂ capture have brought attention to governments, industry leaders, and scientific communities. Scientists from different fields are working together to tackle this task. According to the United States Environmental Protection Agency, the transportation, electricity, and industry are the three top greenhouse gas emitters by economic sector in the 2019, shown in Figure 8.65

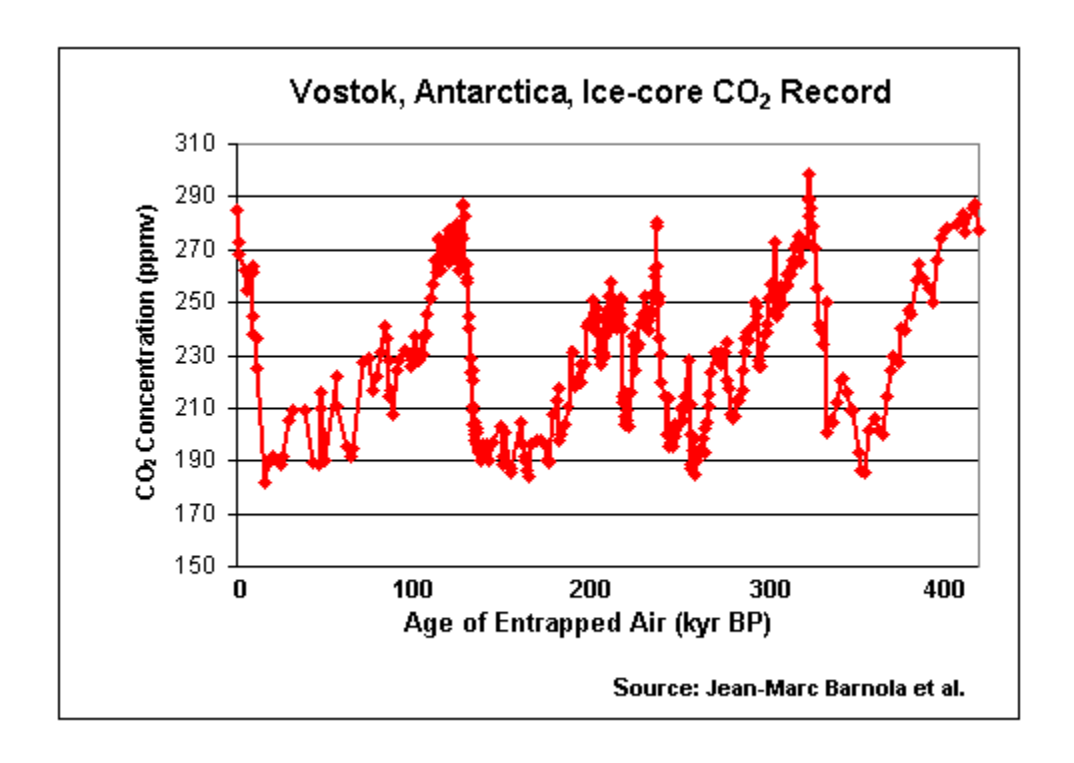


Figure 6. Historical carbon dioxide record from the Vostok Ice core. 66

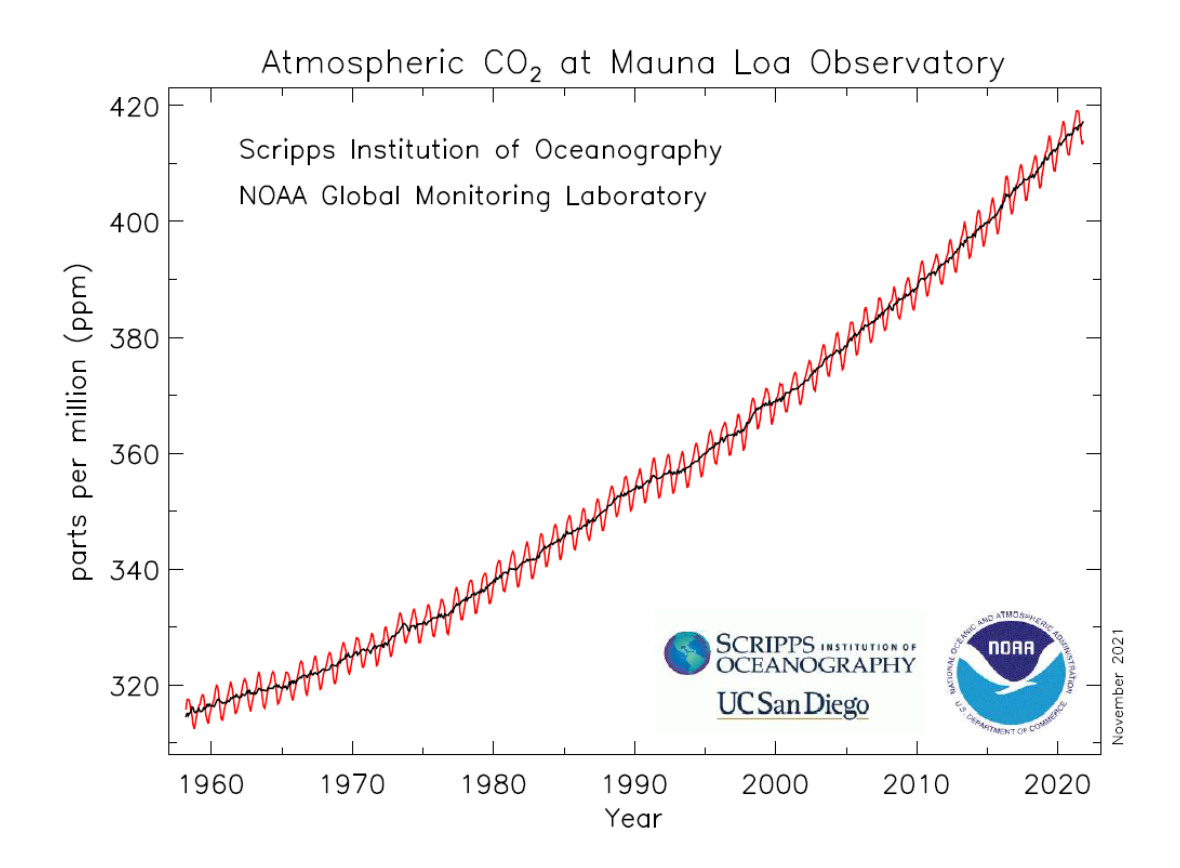


Figure 7. The monthly mean direct measurement of carbon dioxide concentration at Mauna Loa Observatory, Hawaii. Data was collected from 1958 to present. ⁶²

Several ways to reduce CO₂ emissions from the fossil fuel-fired power plants include: (i) enhancing the efficiency of the power generation process (1% increase in coalfired power plant efficiency reduces CO₂ by 2-3%)⁶⁷, (ii) partially or completely switching to low carbon-content fuels or to carbon neutral fuels, and (iii) capturing CO₂ from the flue gas to recycle or store it. For the latter strategy, the three main approaches available for capturing CO₂ from the fossil fuel-fired power plants are post-combustion capture, precombustion capture, and oxy-fuel combustion. In the post-combustion capture, the CO₂ can be chemically absorbed into amine solutions or onto solid sorbents or separated from the flue gas by membranes and captured before the balance of the flue gas is discharged to the air. In the pre-combustion capture, the coal gasification process converts coal to CO₂,

which is captured with similar methods used in post-combustion capture, and hydrogen gas that remains is converted to electricity. In the oxy-fuel capture, pure or enriched O_2 that has been separated from air is used for combustion, so the flue gas is comprised of CO_2 and H_2O that can be stored or recycled. This eliminates the need for post-combustion separation of N_2 form CO_2 , but the oxy-fuel capture is expensive due to cryogenic extraction O_2 , which is energy intensive. The separated CO_2 is then transported to storage sites or utilized as a chemical feedstock.

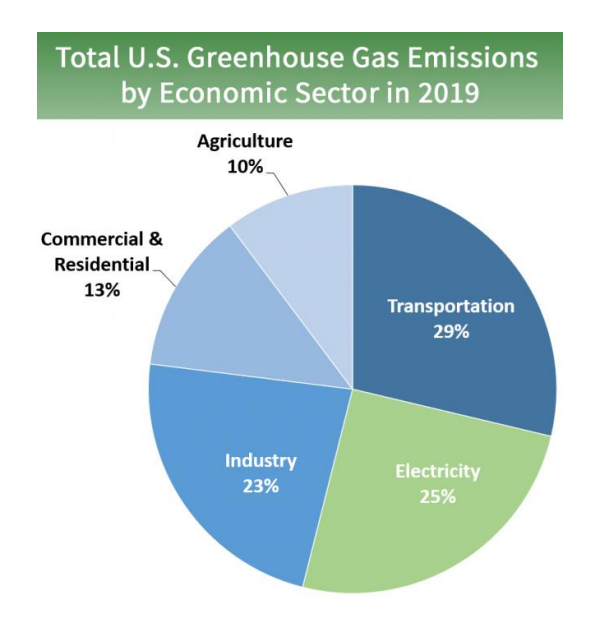


Figure 8. The total U.S. greenhouse gas emissions by economic sector in 2019. Note: total emissions in 2019 is 6,558 million metric tons of CO₂ equivalent. Percentages may not add up to 100% due to independent rounding.⁶⁵

Among different post-combustion capture technologies, aqueous monoethanolamine (MEA) solution is the most common alkanolamine chemical absorbent and has been industrially employed for 50 years due to its fast absorption rate and low material costs. However, the MEA solution also suffers from several limitations includes high energy consumption for MEA regeneration (4 GJ/ton CO₂ released),⁶⁸ poor thermal and oxidative stability, volatility, and its toxic nature.⁶⁹

Like MEA, amino acid alkali metal salts, $[NH_2C(R)CO_2][M^+]$ (M = Na or K), are amine chemical absorbent candidates for post-combustion capture. Compared to MEA solutions, amino acid salts are non-volatile and non-toxic, and their solutions are less corrosive. If the amino acids can be efficiently and sustainably obtained from sources like microalgae biomass, some CO_2 capture can be accomplished during algal growth, and production of amino acid salts may be more economical than chemically synthesized MEA and related absorbents. To prove the viability, Song and colleagues compared the effective CO_2 loading of 30 mass% MEA solution with 30 mass% sodium glycinate solution. The effective CO_2 loading of the absorbent is defined by Eq 3Eq 3, where α_{rich} is the moles of CO_2 absorbed per mol of absorbent. The lean CO_2 loading, α_{lean} , is determined by the solubility of CO_2 (aq) at the desorption temperature.

Effective
$$CO_2$$
 loading = $\alpha_{rich} - \alpha_{lean}$ Eq 3

The effective CO_2 loading of 30 mass% sodium glycinate solution is comparable to the 30 mass% aqueous MEA solution in different CO_2 sources, shown in Table 2. However, the higher CO_2 solubility of sodium glycinate solution at the desorption temperature (120 °C) leads to the slightly higher α_{lean} and lower effective CO_2 loading than MEA solution.

Table 2. Effective CO₂ loading of 30 mass% Aqueous Solutions of monoethanolamine (MEA) and sodium glycinate in different CO₂ sources. Table from reference 70.

CO ₂ source	M	30 mass% IEA soluti		30 mass% Na glycinate solution			
CO2 source	α_{rich}	αlean	effective loading	α_{rich}	α_{lean}	effective loading	
Natural gas power plant $(P_{CO2} = 3.5 \text{ kPa})$	0.489	0.132	0.357	0.538	0.243	0.295	
Coal-fired power plant $(P_{\text{CO2}} = 12 \text{ kPa})$	0.525	0.241	0.284	0.584	0.333	0.251	
Iron and steel industry ($P_{\text{CO2}} = 25 \text{ kPa}$)	0.549	0.299	0.250	0.613	0.382	0.231	

The regeneration energy for 30 mass% sodium glycinate solution is 5.2 GJ/ton CO₂ released and it is slightly higher than its 30 mass% MEA solution counterpart (4.3 G GJ/ton CO₂ released).⁷⁰ Despite having a higher regeneration energy, amino acid salts could still be viable for post-combustion capture due to its lower toxicity, corrosivity, and volatility.

Another emerging post-combustion capture method is cultivating microalgae to capture and directly utilize the CO₂ in the flue gas. Microalgae are naturally abundant unicellular photosynthetic microorganisms and have five main classes: Chlorophyceae (green algae), Rhodophyceae (red algae), Phaeophyceae (brown algae), Cyanophyceae (blue-green algae) and Bacillariophyceae (diatoms). Under favorable conditions, some microalgae are fast-growing and can divide their cells within 3–4 h while most microalgae divide every 1–2 days.⁷¹ The CO₂ enriched flue gas can be a great carbon source for the photosynthesis of microalgae, which converts CO₂ to carbohydrates, the building blocks for nucleic acids, lipids, and proteins. Due to the fast-growing rate, the biomass productivity of microalgae could be 50 times more than the fastest growing terrestrial plant,

switchgrass.⁷² Photosynthetic microalgae CO₂ capture is a sustainable post-combustion capture method with great potential.

Conclusion

With the equilibrium between Cu^I and Cu^{II} catalysts, the radical concentration during ATRP is minimized by the reversible activation and deactivation process. In Chapter 2 ATRP of trimethylsilylpropargyl methacrylate with different chain length and narrow polydispersity, and the poly(propargyl methacrylate) functional monomer by removing the trimethylsilyl protecting groups, will be presented. In Chapter 3, the design of macromolecular micelles is described, where the properties of amphiphilic polymers can be tuned by varying mole fractions of hydrophilic and hydrophobic sidechains installed along the polymer backbone using CuAAC. In Chapter 4, the structure–property relationship of polymeric micelles as enzyme stabilizers is presented.

Carbon dioxide capture is the topic of Chapters 5 and 6. In Chapter 5, Amino acid salts are shown to be better CO₂ absorbents than commonly used alkanolamine chemical absorbents like MEA, with the added benefit of eliminating the toxicity associated with MEA. The CO₂ absorption efficiency of single amino acid solutions and mixture solutions of several amino acids are described. In Chapter 6, synthetic of amino acid-derived polyureas is developed, and the influence of the amino acid structures on the resulting polyureas is presented.

Chapter 2. Clickable poly(trimethylsilylpropargyl methacrylate) with narrow polydispersity prepared by Atom Transfer Radical Polymerization

Introduction

Azide- and alkyne-containing polymers are the two parent polymer candidates that are amenable to CuAAC modification. Azide functionalized polymers can be prepared by direct polymerization of azido-containing monomers but monomers bearing the shocksensitive azides can pose safety hazards during handling or purification by distillation or recrystallization. 73 The azido-containing polymethacrylate with the highest degree of polymerization was prepared by reversible addition–fragmentation chain transfer (RAFT) polymerization of 2-azidoethyl methacrylate (DP = 322, PDI = 1.13).⁷⁴ Another azidocontaining polymer, poly(3-azidopropyl methacrylate) (DP=109, PDI = 1.33), was prepared via atom transfer radical polymerization (ATRP).⁷³ To avoid safety hazards of shock-sensitive monomers, azido-containing polymers can be synthesized by polymerizing monomers with groups that can be readily displaced by azide after polymerization. Poly(glycidyl methacrylate)⁷⁵ and poly(2-chloroethyl methacrylate)⁷⁶ are examples where reaction with sodium azide affords azido polymers. A significant drawback to modifying azido polymers with CuAAC is that the scope of methods for alkyne synthesis are limited when compared to ease with which azides can be synthesized from a vast array of commercially available starting materials. Consequently, alkyne-containing polymers are the preferred synthons for post-polymerization modification with CuAAC.

Alkyne functional polymers can be prepared by grafting an alkyne onto a functional polymer or polymerizing an alkyne containing monomer. Gao and coworkers grafted

pentynoic acid onto poly(2-hydroxyethyl methacrylate) by esterification (DP = 217 and PDI = 1.22), shown in Scheme 5.¹⁵ The esterification was judged to be quantitative, positioning alkynes on side chains nine atoms away from the polymer backbone. The molecular weight variation between hydroxy-containing polymer and alkyne-containing polymer is caused by the hydrodynamic volume difference in the DMF GPC. Gan and colleagues reported grafting two alkyne groups per monomer unit onto the poly(2-hydroxyethyl methacrylate) backbone by esterification. The modification was quantitative based on the disappearing hydroxy proton NMR signal on the poly(2-hydroxyethyl methacrylate).⁷⁷

Scheme 5. Alkyne-containing polymer prepared by esterification. ^{15,77}

Gao and coworkers:

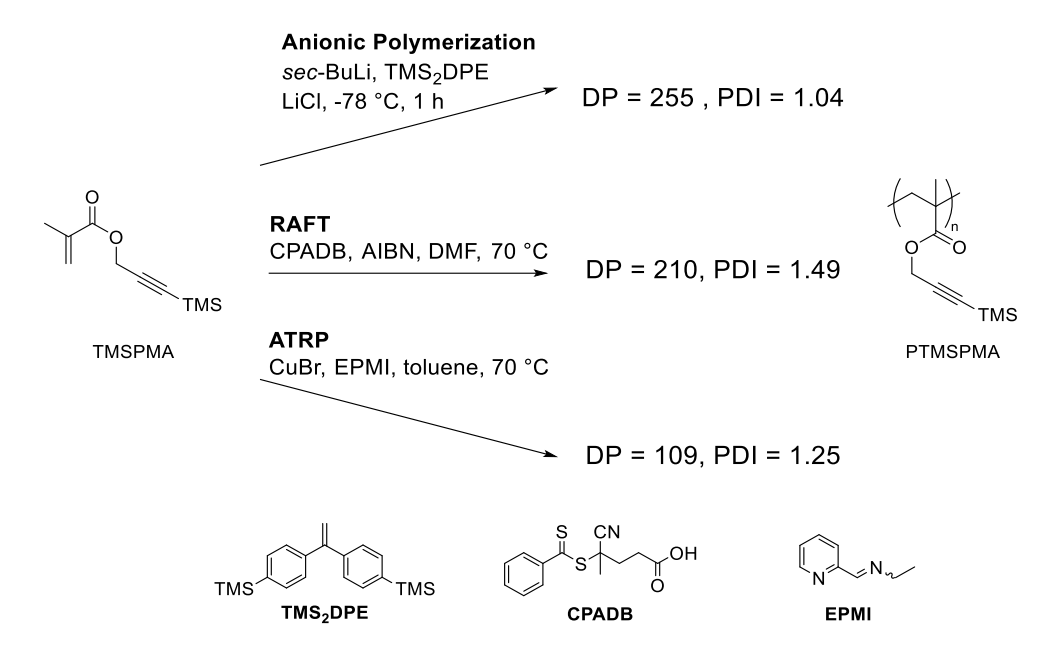
Gan and coworkers:

Direct polymerization of alkyne-modified acrylates and methacrylates are less prevalent. In radical polymerizations like ATRP the alkyne groups can intercept the chain propagating radicals, which creates crosslinks between chains. This becomes more problematic as the monomer is consumed and the [alkyne]:[alkene] ratio increases.

Consequently, the control of molecular weight distribution (MWD) is lost. Alkyne protecting groups can greatly alleviate this problem.

Trimethylsilyl propargyl methacrylate (TMSPMA, Scheme 6) is a protected alkyne monomer that has been polymerized to poly(trimethylsilyl propargyl methacrylate) (PTMSPMA). Examples of PTMSPMA with the highest DP by different polymerization methods are summarized in Scheme 6. Anionic polymerization under anhydrous conditions at -78 °C affords the highest molecular weight polymer with a narrow PDI (DP = 254, PDI = 1.04),⁷⁸ while controlled radical polymerizations yield the poly(trimethylsilyl propargyl methacrylate) (PTMSPMA) with PDI < 1.5 and DP up to 210 were synthesized by RAFT polymerization under less stringent conditions.⁷⁹ The longest homopolymer of TMSPMA prepared by another atom transfer radical polymerization (ATRP), has DP = 109 and a narrow PDI (1.25).⁸⁰

Scheme 6. Poly(trimethylsilyl propargyl methacrylate) examples reported by various polymerization conditions.



Atom transfer radical polymerization (ATRP) is a controlled/living polymerization method that can tailor the length of the polymer chain, control the molecular weight dispersity, and keep the chain end fidelity for efficient block copolymer preparation. More details about ATRP will be introduced in the following section. The combination of ATRP and copper-catalyzed azide-alkyne cycloaddition (CuAAC) has allowed chemists to tailor polymers with fine-tuned structures such as block copolymer, 81,82 star polymers, 83 graft polymers, ^{73,84,85} polymer brushes, ¹⁵ and polymer networks. ⁸⁶ However, most of the alkynecontaining polymethacrylate chains reported either require demanding polymerization conditions like anionic polymerization 87 or result in relatively small degree of polymerization^{79,80} [DP < 210 for reversible addition–fragmentation chain transfer (RAFT) or ATRP]. Here we reported ATRP conditions that control the molecular weights of poly(trimethylsilylpropargyl methacrylate) over a broader range while keeping polydispersity narrow. This protocol will enable chemists to make alkyne-functionalized polymers with controlled molecular weights that can be easily functionalized by CuAAC with azide-bearing molecules.

Polymerization of TMSPMA by ATRP

Several terms will be defined first. $M_{n,theo}$ is defined by Eq 4Eq 4. The $M_{n,theo}$ can be calculated by the monomer to initiator ratio at t = 0, $[M]_0/[I]_0$, molecular weight of monomer and initiator, and conversion of the polymerization.² When the experimental molecular weight is close to the $M_{n,theo}$, indicating the efficient initiation occurs and the termination event is not significant during the polymerization. If only fraction of the initiator is initiated, the experimental molecular weight determined by GPC ($M_{n,GPC}$) will be higher than the $M_{n,theo}$ due to higher actual monomer to initiator ratio than $[M]_0/[I]_0$. If

termination is significant in the polymerization, $M_{n,GPC}$ will be higher than the $M_{n,theo}$ and higher polydispersity will be observed as well.

$$M_{n,theo} = \frac{[M]_0}{[I]_0} \times MW_{monomer} \times conversion + MW_{initiator}$$
 Eq 4

The commonly used ATRP catalyst and ligand (Cu^IBr/bpy) was tested first (Table 1Table 1 Entry 1) and showed good PDI control, but the experimental molecular weight determined by GPC $(M_{n,GPC})$ is significantly larger than theoretical molecular weight $(M_{\rm n,theo})$, shown in Table 3Table 3. Matyjaszewski and colleagues 88 showed that a homogeneous polymerization mixture was observed when using the di-n-heptyl substituted bipyridine as ligand (Cu¹Br/dHbpy) in a mixture of styrene at the end of polymerization. However, when replacing ligand bearing shorter di-t-butyl chain (Cu^IBr/dtbbpy), the polymerization media became heterogenous. This result indicates the ligand with longer dialkyl substituents has better solubility in the polymerization media and will ensure the effective concentration of deactivator in the solution to minimize the radical concentration. At targeted DP = 100, both catalysts (Cu¹Br/bpy and Cu¹Br/dtbbpy) have comparable results (Table 1 Table 1 Entry 1 and 2). When the targeted DP = 200, the dtbbpy cannot reach to higher conversion even with longer reaction time (Table 1 Table 1 Entry 3 and 4). With the limited literature precedent for homopolymerization of poly(trimethylsilyl propargyl methacrylate) (PTMSPMA), we turned to ATRP conditions that produce poly(methyl methacrylate) with good control. After testing several polymerization conditions, we found that the Activator ReGenerated by Electron Transfer (ARGET) ATRP using copper wire as a reducing agent gave better results for preparing PTMSPMA.89

Scheme 7. Polymerization of TMSPMA by conventional ATRP.

Table 3. Polymerization of TMSPMA by conventional ATRP with different ligands.

Entry	Cu ^I Br/L	$[M]/[I]/[Cu^IBr]/[L]$	[I] (mM)	Time (h)	Conv. (%)	$M_{\rm n,theo}$ (× 10^{-3})	$M_{\rm n,GPC}$ (× 10^{-3})	PDI	
1	Cu ^I Br/bpy	100/1/1.2/2.5	16	44	98	19.2	29.3	1.16	
2	Cu ^I Br/dtbbpy	100/1/1.1/2.3	17	41	96	18.8	33.0	1.19	
3	Cu ^I Br/dtbbpy	200/1/1.5/3.2	8	23	69	27.1	36.0	1.27	
4	Cu ^I Br/dtbbpy	200/1/1.7/3.5	8	67	65	25.5	49.0	1.21	

Polymerization of TMSPMA by Activator ReGenerated by Electron Transfer (ARGET) ATRP

Activator ReGenerated by Electron Transfer (ARGET) ATRP is a catalytic initiation system that reduces the copper concentrations relative to conventional ATRP, which uses equal concentration of copper catalyst as the initiator concentration. In ARGET ATRP, stable Cu^{II} is replaced the Cu^{I} and the activator Cu^{I} is *in situ* generated by reducing Cu^{II} with various reductants, such as Ag(0), 90,91 Cu(0), 92 $Sn(EH)_2$, 93 or ascorbic acid. 94 The mechanism of ARGET ATRP is shown in Scheme 8. In ARGET ATRP, the Cu^{II} concentration is commonly lower than the initiator concentration ($[Cu^{II}X_2] < [In-X]$). If the low concentration of reductants is added or heterogeneous reductants are used (like copper metal in ARGET ATRP), then $[Cu^{I}X] < [Cu^{II}X] < [P_n-X]$ and [In-X]. Since $[Cu^{I}X]$

<< [P_n-X], most of the chains are in the dormant state and [Cu^{II}X₂] > [P_n·]. This ensures that deactivation rate = k_d [P_n·][Cu^{II}X₂] is significantly greater than the termination rate = k_t [P_n·]² throughout the polymerization. These features of ARGET ATRP enable the synthesis of high molecular weight polymers compared to other ARTP methods.

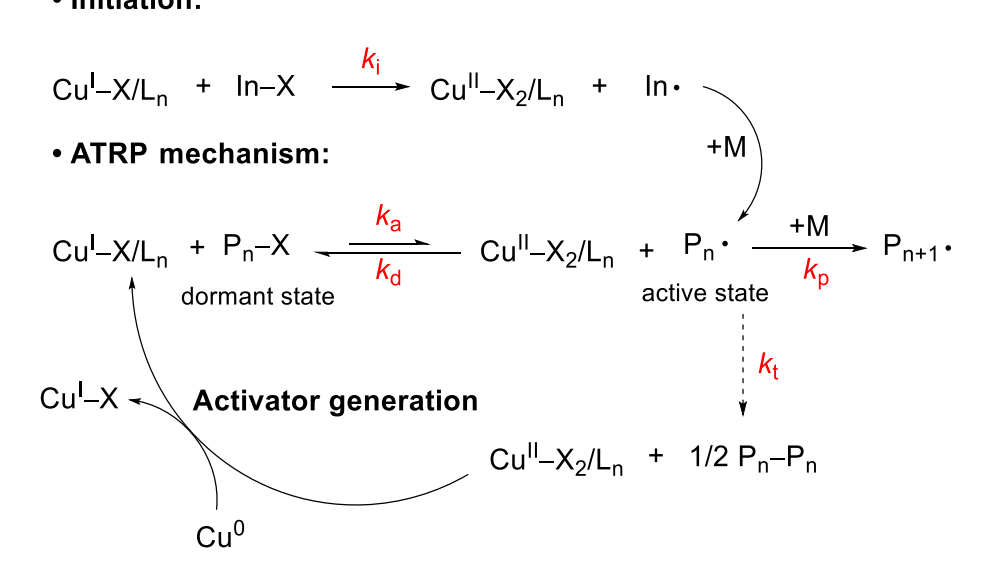
Using Cu(0) as a reductant, the ARGET ATRP polymerization follows the regular ATRP mechanism after generating the activator (Cu^IX_2/L_n). Cu(0) serves two extra functions during polymerization. One is that Cu(0) can scavenge excess deactivators (Cu^IX_2/L_n), regulate the concentration of deactivators, and increase the rate of polymerization while keeping the radical concentration low. The termination events can be minimized but not eliminated during ATRP and one equivalent of deactivator is generated when one termination event occurs. The accumulation of deactivator can decelerate or even halt the polymerization. The adequate amount of Cu(0) reduces the deactivator Cu(II) back to Cu(I) and accelerates the polymerization. The other function is that Cu(0) eliminates the residual oxygen in the system. With an excess amount of copper wire as oxygen scavenger, ATRP without the need for a deoxygenation step has been reported. Avoiding the use of air-sensitive Cu^I catalyst, faster reaction rate, and better oxygen tolerance are the three advantages of ARGET ATRP over conventional ATRP.

Scheme 8. The ARGET ATRP mechanism

Activator generation:

$$Cu^{II} - X_2/L_n + Cu^0 \longrightarrow Cu^I - X/L_n + Cu^I - X$$

Initiation:



Eq 5 defines factors that affect polydispersity (M_w/M_n) in ATRP. These include the targeted degree of polymerization (DP_n) , which is equal to the monomer to initiator ratio, the rate constant for chain propagation (k_p) , the total initiator concentration at t=0 ([In–X]₀), the rate constant for deactivation (k_d) , the deactivator concentration ([Cu^{II}–(Br)₂/L_n]), and conversion of the polymerization (p). Eq 5 can guide us to find the proper polymerization conditions.

$$\frac{M_w}{M_n} = 1 + \frac{1}{DP_n} + \left(\frac{k_p[\ln - X]_0}{k_d[\text{Cu}^{\text{II}} - (\text{Br})_2/\text{L}_n]}\right) \left(\frac{2}{p} - 1\right)$$
 Eq 5

For the polymerization of a specific monomer with the desired targeted degree of polymerization, several strategies can be used to yield polymers with smaller M_w/M_n (or PDI): (1) choosing deactivators with higher k_d values; (2) increasing deactivator

concentration; and (3) driving conversion close to completion. The propagation rate constant (k_p) of the methacrylate derivative monomers increase with the size of the ester group. ⁹⁶ Based on this trend, our targeted monomer TMSPMA should have a higher k_p than methyl methacrylate ($k_p = 648 \text{ mol}^{-1}\text{s}^{-1}$ at 50 °C), ⁹⁶ which is an active monomer in ATRP. We chose a deactivator with high k_d (2×10⁶ M⁻¹s⁻¹), Cu^{II}Br₂/4,4'-dinonyl-2,2'-dipyridyl (dNbpy), to compensate for the active TMSPMA monomer.

To synthesize polymers with M_w/M_n values approaches the minimum value of 1, the initiation rate needs to be faster than the monomer propagation rate so that all the chains are initiated simultaneously. Two initiators with different activation rate constants k_a , ethyl α -bromoisobutyrate (EtBriB) ($k_a = 2.7 \text{ M}^{-1}\text{s}^{-1}$)⁵, benzyl α -bromoisobutyrate (BzBr), and ethyl α -bromophenylacetate (EBPA) ($k_a = 5.3 \times 10^3 \text{ M}^{-1}\text{s}^{-1}$),⁵ were tested for polymerizing TMSPMA. The EBPA has dual stabilization effect from the ester and phenyl groups, which makes the k_a value of EBPA 1963 times higher than EtBriB. EBPA is an efficient initiator for active monomers like acrylonitrile and methyl methacrylate³ and will be used as the initiator for all the polymerization conditions reported in this chapter.

Effects of deactivator (CuIIBr2/ligand) loading

The effect of deactivator loading to polydispersity was investigated by varying concentration of deactivator ($Cu^{II}Br_2/dNbpy$) versus initiator concentration while keeping the targeted degree of polymerization $DP_n = 200$ and copper wire surface area constant (79 mm²) (Table 4Table 4 Entry 1—4). There are two observations from this series of experiments. (1) The polymerization rate increases with deactivator concentration ($Cu^{II}Br_2/dNbpy$) due to the higher concentration of activator (Cu^{II} complex) will be generated by comproportionation of Cu^0 and Cu^{II} . At lower deactivator concentration (1.0

mM, Table 4Table 4 Entry 1) the reaction cannot reach higher conversion even with prolonged reaction times. (2) Among these polymerization conditions, the deactivator concentration mildly affects the PDI but has a strong impact on the initiation efficiency (IE), which is defined by

Eq **6**

Eq **6**. When the initiation efficiency is close to 100%, indicates the initiation is efficient and without significant termination or chain transfer side reactions. The polymerization with deactivator concentration at 6.1 mM (Table 4Table 4 Entry 3) produced the product with the exact molecular weight ($M_{n,GPC}$) as the theoretical molecular weight ($M_{n,theo}$). Under this condition, the activator [Cu^I] and deactivator [Cu^{II}] were in the range that suppressed termination while maintaining a reasonable polymerization rate. We utilized this optimized deactivator concentration (Table 4Table 4 Entry 3) as a model reaction to investigate the effect of copper wire loading.

Initiation Efficiency (IE) =
$$\frac{M_{n,theo}}{M_{n,GPC}}$$
 Eq 6

Table 4. ARGET ATRP of PTMSPMA with different deactivator loadings and copper wire surface areas.^a

Entry	[TMSPMA]/[EBPA] /[Cu ^{II} Br ₂]/[dNbpy]	[Cu ^{II}] (mM)	Cu ⁰ surface area (mm ²) ^b	Time (h)	Conv. (%) ^c	$M_{\rm n,theo}^d (\times 10^{-3})$	$M_{\rm n,GPC} \ (\times 10^{-3})$	DP	IE^e	PDI
1	200/1/0.1/0.2	1.0	79	42	44.0	18.7	28.2	144	66%	1.26
2	200/1/0.4/0.8	3.9	79	17	79.4	33.8	40.5	206	83%	1.27
3	200/1/0.6/1.2	6.1	79	10	80.2	34.2	34.2	174	100%	1.27
4	200/1/1.0/2.0	9.5	79	13	93.4	39.8	44.4	226	90%	1.29
5	200/1/0.6/1.2	6.1	39	11	78.5	33.4	34.8	177	96%	1.26
6	200/1/0.6/1.2	6.1	236	10	85.9	36.6	45.2	230	81%	1.97

^a The ARGET ATRP were set up with [TMSPMA] = 2.0 M, T = $35 \,^{\circ}\text{C}$, $50\% \,(\text{v/v})$ anisole versus TMSPMA, total reaction mixture volume: 7.5 mL, and copper wire (length = 5, 10, or 30 cm, diameter = $0.25 \,\text{mm}$). ^b Calculated by assuming copper wire is a smooth cylinder. ^c Determined by ¹H NMR. ^d Calculated by Eq 4Eq 4^c Calculated by Eq 6Eq 6.

Effects of copper wire loading

In ARGET ATRP, the generation of the activator (Cu^I) occurs on the surface of the copper wire, so the copper wire surface area plays a critical role in controlling the ratio of activator concentration and deactivator concentration ([Cu^I]/[Cu^{II}]), which determines the polymerization rate and regulates the radical concentration. The copper wire was assumed to be a cylinder and its surface area was calculated with the standard formula. The copper wire surface area ranging from 39 to 236 (mm²) was tested while keeping deactivator concentration at 6.1 mM, shown in Table 4Table 4 entries 3, 5, and 6. Several trends were observed: (1) The polymerization rate increased with the copper wire surface area. This tendency can be explained by the generation of higher activator concentration during polymerization and is consistent with the proposed ARGET ATRP mechanism (Scheme 8). (2) The polymerization conditions with smaller copper wire surface areas (39 or 79 mm²), shown in Table 4Table 4 Entry 3 and 5, yielded polymers with narrow PDIs and close to 100 % initiation efficiency.

At much higher copper surface areas (236 mm²), shown in Table 4Table 4 Entry 6, the initiation efficiency dropped to 81 % and yielded the product with broad molecular weight distribution. This consistent generated the activator-radical equilibrium shifting to the radical, P_n , increasing the probability for chain termination relative to propagation, which increases the PDI.

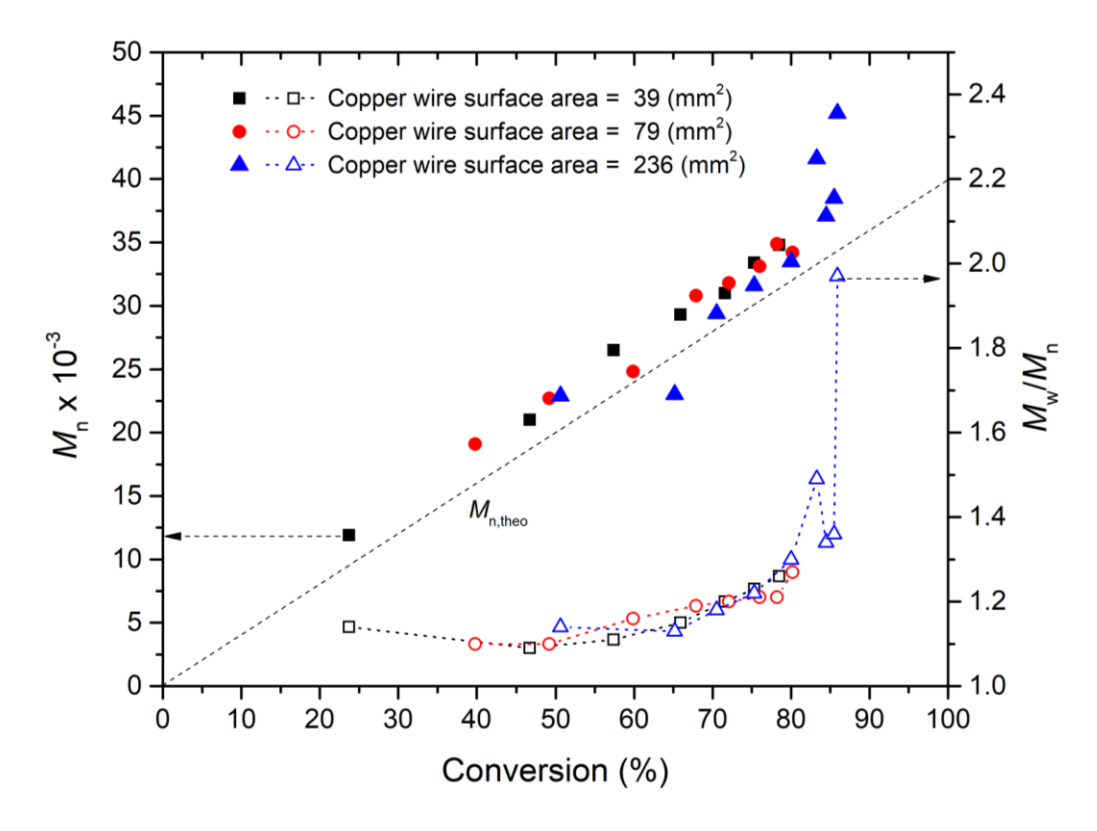


Figure 9. Molecular weight (left Y axis) and polydispersity (right Y axis) versus the polymerization conversion plot. Copper wire surface area = 39 mm^2 (black square), copper wire loading = 79 mm^2 (red circle), and copper wire loading = 236 mm^2 (blue triangle). [Cu^{II}Br₂] = 6.1 mM.

The molecular weight and polydispersity (M_w/M_n) versus the polymerization conversion plot, shown in Figure 9, revealed more details of copper wire surface area effect during the polymerization. At smaller surface area (39 and 79 cm²), the molecular weight $(M_{n,GPC})$ grew linearly and closely to the theoretical molecular weight $(M_{n,theo})$, dashed line in Figure 9) and the M_w/M_n remained less than 1.3 at the end of the polymerization. While

the polymerization with the largest surface area (236 mm², black square), the $M_{\rm n,GPC}$ grew along the $M_{\rm n,theo}$ below 80% conversion, and $M_{\rm n,GPC}$ started deviating from $M_{\rm n,theo}$ and the PDI soared to 2 at above 80% conversion.

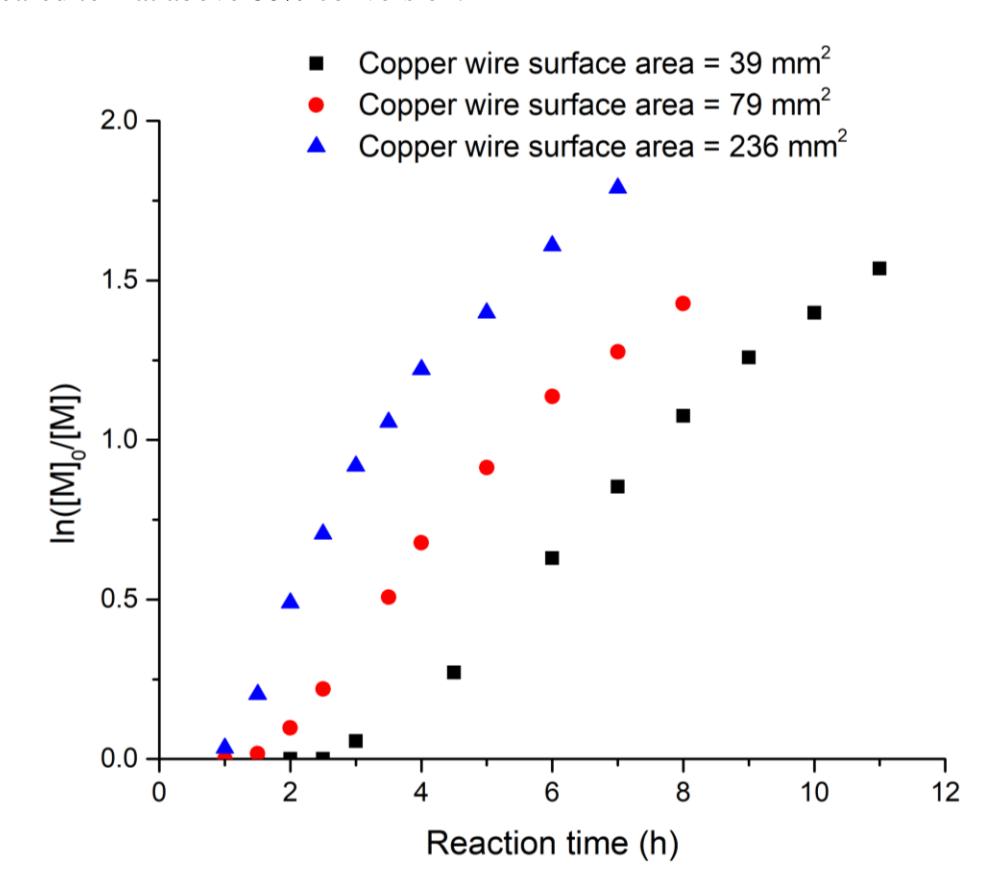


Figure 10. First-order kinetic plot of different copper wire loadings ($[Cu^0]$). $[Cu^0] = 39 \text{ mm}^2$ (red dot), $[Cu^0] = 79 \text{ mm}^2$ (blue triangle), and $[Cu^0] = 236 \text{ mm}^2$ (black square).

In the first-order kinetic plot, shown in Figure 10, we found several general trends. (1) Induction periods were observed for all three entries and the one with larger surface area (236 mm²) has the shortest induction period (1 h). Since comproportionation between Cu^{II} and Cu⁰ involves soluble Cu^{II} species reacting at a metal surface, a larger copper wire surface area accelerates reduction of Cu^{II} by Cu⁰ to generate the Cu^I activator. This will be further discussed in the "Effects of induction periods" section.

- (2) After the induction period, early stages of polymerization, the plot of $ln([M_0]/[M])$ vs. time for polymerization with lowest Cu^0 surface area (39 mm²) had a reasonable linearity from $ln([M_0]/[M]) = 0$ to 1.5, indicating the first-order kinetic behavior—consistent with the concentration of propagation radicals remaining constant. However, the analogous plots for polymerizations with higher Cu^0 surface areas (79 and 236 mm²) started deviating from the linear correlation when $ln([M]_0/[M]) > 1$.
- (3) The rate of polymerization decreased with the copper wire loading [Cu⁰]. The observed rate constant of propagation (k_p^{obs}) is defined by Eq 10, where [M]₀ and [M]_t are the monomer concentration at t=0 and at a specific time, t, during polymerization. Natural logarithm of ([M]₀/[M]) depends on propagation rate constant (k_p) , ATRP equilibrium constant (K_{ATRP}) , initiator concentration ([In–X]), activator concentration ([Cu^I]), and deactivator concentration ([Cu^{II}]). The initial k_p^{obs} of different copper wire surface area is determined by the slope of the first-order kinetic plot, shown in Figure 11. The k_p^{obs} dropped two-fold from k_p^{obs} (236 mm²) = 1.19 × 10⁻⁴ s⁻¹ (0.43 h⁻¹) to k_p^{obs} (39 mm²) = 5.83 × 10⁻⁵ s⁻¹ (0.21 h⁻¹).

$$-\frac{d[M]}{dt} = \frac{k_{p}K_{ATRP}[In-X][Cu^{I}]}{[Cu^{II}]}[M]$$
 Eq 7

$$k_{\rm p}^{\rm obs} = \frac{k_{\rm p} K_{\rm ATRP} [\rm In-X] [\rm Cu^I]}{[\rm Cu^{II}]}$$
 Eq 8

$$-\frac{d[M]}{[M]} = k_{\rm p}^{\rm obs} dt$$
 Eq 9

$$\ln\left(\frac{[\mathsf{M}]_0}{[\mathsf{M}]}\right) = k_{\mathsf{p}}^{\mathsf{obs}}t$$
 Eq 10

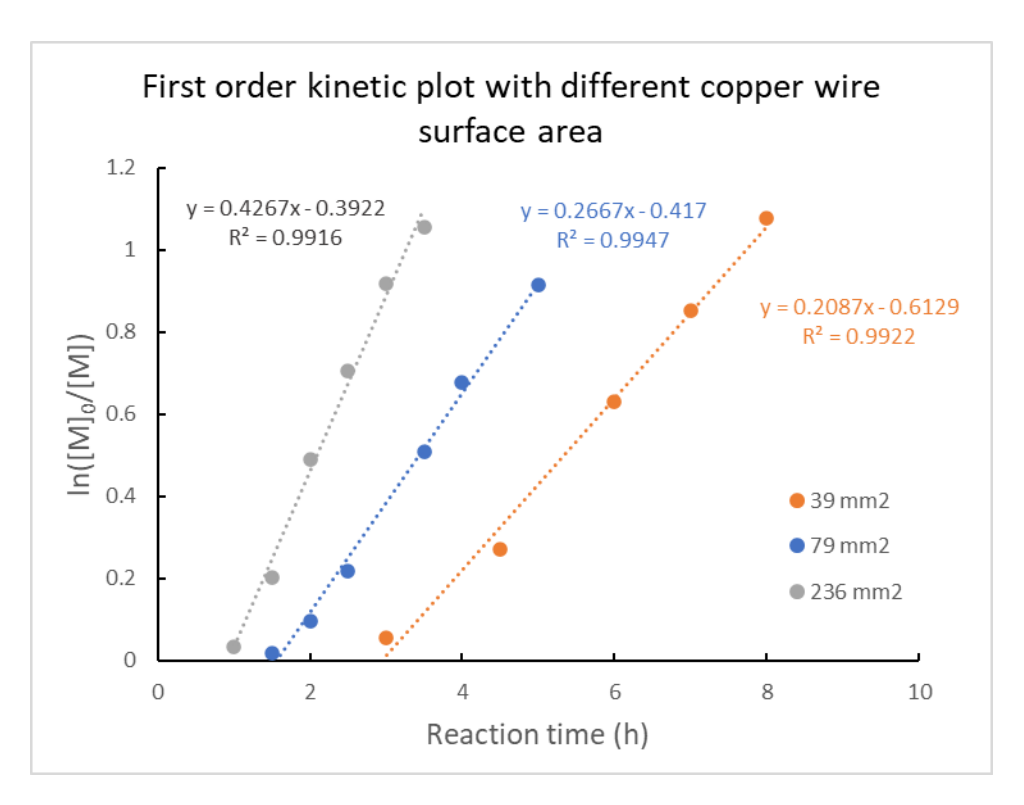


Figure 11. First-order kinetic plot for determining initial polymerization rate of different copper wire surface area = 39 mm² (orange), 79 mm² (blue), and 236 mm² (grey).

Effects of targeted degrees of polymerization

To obtain good control over different targeted degrees of polymerization, two boundary conditions were applied based on findings in the previous section: (1) The initial deactivator concentration, $[Cu^{II}]_0$, was 6.1 mM, and (2) Cu^0 surface areas did not exceed 79 mm². Both conditions were expected to maintain radical chain concentration $[P_n \cdot]$ at levels sufficient for propagating the polymer chain, but sufficiently lower than $[Cu^{II}]_t$ to minimize chain termination.

Table 5. ARGET ATRP of TMSPMA with different targeted degrees of polymerization.^a

Entry	[TMSPMA]/[EBPA] /[Cu ^{II} Br ₂]/[dNbpy]	[Cu ^{II}] (mM)	Cu ⁰ surface area ^b (mm ²)	Time (h)	Conv. ^c (%)	$M_{n,theo}$ (×10 ⁻³)	$M_{n,GPC}$ (×10 ⁻³)	DP	IE^d	PDI
1	200/1/0.6/1.2	6.1	39	24.0	95.7	40.8	40.0	204	102%	1.25
2	200/1/0.3/0.6	3.1	24	16.5	87.1	37.1	36.0	183	103%	1.12
3	100/1/0.3/0.6	6.1	39	23.5	99.6	20.7	21.6	110	96%	1.15
4	100/1/0.3/0.6	6.1	24	23.5	99.3	20.7	22.0	112	94%	1.17
5	600/1/0.6/1.2	2.0	39	18.0	70.1	83.5	78.4	399	107%	1.27
6	600/1/0.6/1.2	2.0	24	24.0	77.8	92.7	83.0	423	112%	1.25
7	600/1/0.3/0.6	1.0	24	41.5	78.6	93.7	98.2	501	95%	1.30

^a The ARGET ATRP were set up with [TMSPMA] = 2.0 M, T = 35 °C, 50% (v/v) anisole versus TMSPMA, total reaction mixture volume: 7.5 mL, and copper wire (length = 3, or 5 cm, diameter = 0.25 mm). ^b Assuming the copper wire is a cylinder. ^c Determined by ¹H NMR. ^d Initiation efficiency (IE) = $M_{n,\text{theo}}/M_{n,\text{GPC}}$

We first used concentrations that mimicked the best polymerization conditions from Table 4Table 4 to determine whether longer reaction times would give higher conversions and molecular weights for targeted DP = 200. Compared to Entry 3 of Table 4, Entry 1 in Table 5 shows that lowering the Cu^0 surface area from 79 to 39 mm² and increasing the reaction time from 10 to 24 h increased conversion (95.7% vs 80.2%) and increased M_n from 34,200 to 40,000 g/mol, while comparable PDIs (1.25 vs. 1.27) are indicate that control of the polymerization is maintained. In several entries, the initiation efficiency is greater than 100%, which may be caused by the $M_{n,GPC}$ is determined by the retention time of the polymer sample against poly(methyl methacrylate) standards. Therefore, the $M_{n,GPC}$ may be underestimated because of the slightly structure difference of the TMSPMA monomer.

Entry 4 of Table 5 shows that ARGET ATRP is well behaved when both [Cu^{II}Br₂] (3.1 vs 6.1 mM) and the Cu⁰ surface area (24 vs 39 mm²) are decreased. Analysis of the resulting polymers showed that control of M_w was maintained and the narrower PDI (1.12)

is consistent with less termination due to lower $[P_n \cdot]$. Thus, lowering both $[Cu^{II}]$ and $[Cu^0]$ can offer better control in polymerization of TMSPMA.

For the lowest targeted DP (100, entries 3 and 4 of Table 5), the impact of lowering the surface area was minimal as conversions were complete and M_n and PDI values were nearly identical. For the highest targeted DP (600, entries 5-7), the best combination of IE and control of $M_{n,GPC}$ and PDI was found for entry 6 where IE = 112%, $M_{n,GPC}$ = 83,000 and PDI = 1.25. While $M_{n,GPC}$ value is less than the $M_{n,theo}$, this is caused by the $M_{n,GPC}$ was determined by using GPC column retention time against poly(methyl methacrylate) standards. When this adjustment is made (entry 6 of Table 5), the value of $M_{n,theo}$ was 92,700 at 77.8% conversion, which is lower than $M_{n,GPC}$. The higher $M_{n,GPC}$ value is consistent with incomplete activation of the initiator and a higher ratio of monomer to growing chains, which leads to higher $M_{n,GPC}$ values than that when the initiator was fully activated. For entry 7, where $[Cu^{II}] = 1.0 \text{ mM}$ vs 2.0 mM in entry 6, and entry 5, where the Cu⁰ surface area is 24 mm² vs 39 mm² in entry 5, the IE (95% for entry 7) were significantly lower than the values for entry 5 and 6. We found that using 0.3 equivalent deactivator versus initiator concentration and copper wire surface area = 24 mm² gave the polymer with highest DP, narrow PDI (Table 5 entry 7).

The most significant outcome of these studies is that ARGET ATRP vastly improves polymerizations of TMSPMA compared to ATRP. This is highlighted by entries 5-7 in Table 5, where much higher molecular weight values were achieved without compromising molecular weight control, as was observed for the polymer with the highest $M_{n,GPC}$ value in Table 5 entry 5, the TMSPMAs can be polymerized up to DP = 500 with PDI =1.30, which is five times higher than the PTMSPMA reported by ATRP (DP = 109)

and two times longer than the PTMSPMA by anionic polymerization (DP = 250). Noteworthily, low or no conversion were observed when the systems were not properly degassed. Thus, the fact that experiments DP_n = 600 gave lower targeted DP_n experiments may be due to trace molecular oxygen.

Effects of induction periods

The induction periods decrease from 2.5 h to 1 h with increasing the copper wire surface area—33 to 198 mm², respectively—as shown in Figure 10. A one-hour induction period was reported in ARGET ATRP of acrylonitrile using CuCl₂ as the deactivator and PMDETA as both the ligand and the reducing agent.⁹⁷ The stronger C–Cl bond breaks slower than the C–Br counterpart leads to the induction period. Moreover, no induction period was reported from Cu⁰-mediated ATRP of MMA utilizing the same deactivator (Cu^{II}Br₂/dNbpy) with 10 mol% copper deactivator versus initiator concentration, which is lower deactivator loading than our study.⁸⁹

Our hypothesis is that the induction period is the time of reducing the Cu(II) deactivator and accumulating the concentration of Cu(I) activator. To evaluate this hypothesis, the copper wire was added to the reaction vessel containing degassed $CuIIBr_2$ solution and stirred for 2.5 h, which was followed by the addition of the degassed initiator and monomer solution to the reaction vessel. In the delayed addition of the monomer and initiator experiment, the induction period was (~30 min) significantly shorter, shown in Figure 12Figure 12 (red dots). After the induction period, the polymerization rates are similar (slope of first-order kinetic plot) for both polymerizations (monomer addition at t = 0 and t = 2.5 h). Another way to test our hypothesis—the induction period is the time of reducing the Cu(II) deactivator and accumulating the concentration of Cu(I) activator—is to

lower the deactivator concentration from 6.1 mM to 1.0 mM, following the standard procedure under the same copper wire loading. No induction period was observed at the lower deactivator loading, shown in Figure 13Figure 13 (blue squares). Both generation of Cu(I) prior to adding the monomer and initiator and lowering the deactivator experiments support our hypothesis and indicate the induction period results from the slow generation of Cu(I) from Cu(0) and Cu(II).

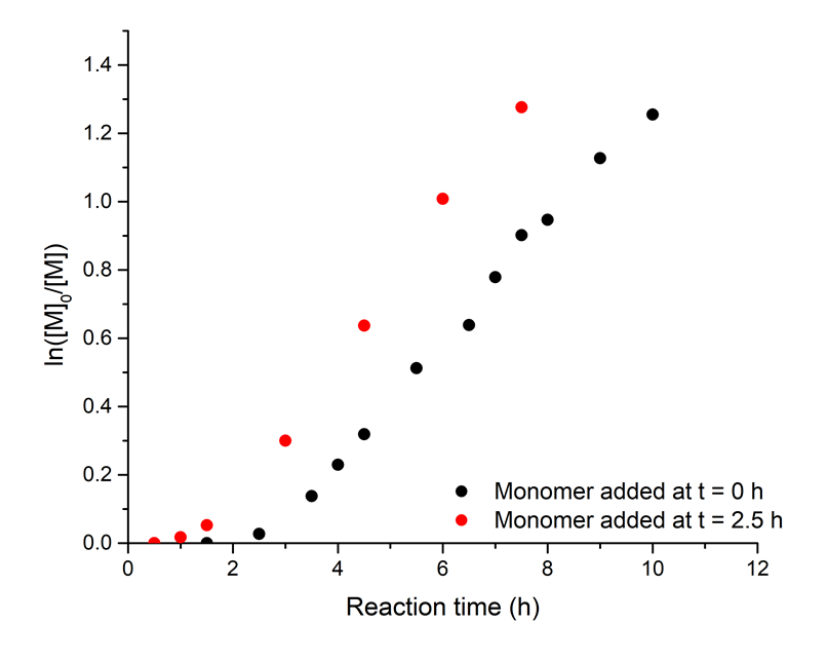


Figure 12. First-order kinetic plot of ARGET ATRP of TMSPMA with monomer and initiator added at t = 0 h (black dots) and with monomer and initiator added at t = 2.5 h (red dots). [TMSPMA]: [EBPA]: [Cu^{II}Br₂]: [dNbpy] = 200: 1: 0.6: 1.2 and copper wire surface area = 39 (mm²)

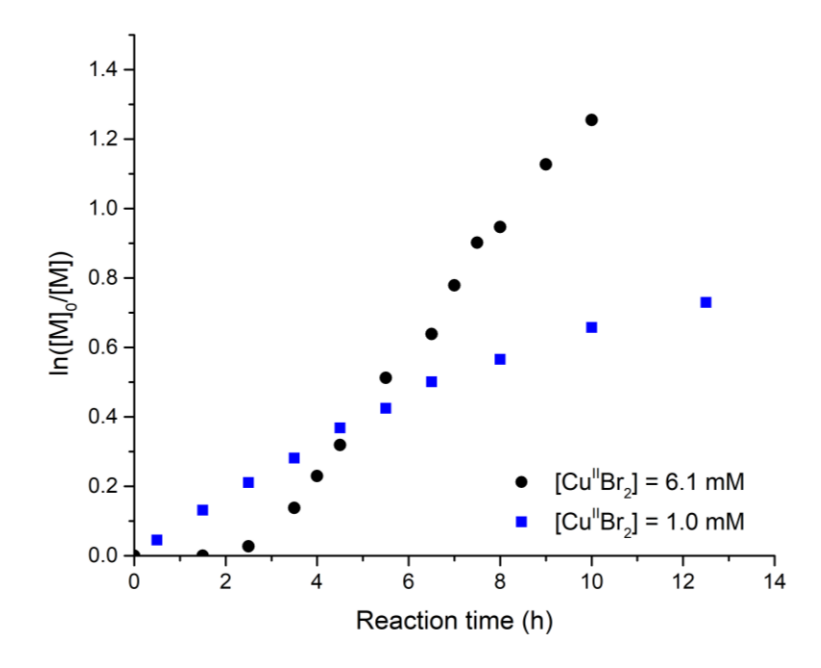


Figure 13. First-order kinetic plot of with constant copper wire surface area = $24 \text{ (mm}^2)$ at $[Cu^{II}Br_2] = 1.0 \text{ mM}$ (blue square) and at $[Cu^{II}Br_2] = 6.1 \text{ mM}$ (black dot).

Conclusion

With the fast initiator EBPA, high k_d deactivator $Cu^{II}Br_2/dNbpy$, and reduced radical concentration by lowering both deactivator concentration and copper wire surface area, the polymerization of clickable TMSPMA can be well-controlled from DP = 100 to 500 with low polydispersity (<1.3). Under the smaller copper surface area, the kinetic data also showed that the radical concentration remains constant throughout the polymerization and the molecular weight grew along the theoretical molecular weight, indicating the well-balance between activator and deactivator concentration. The induction period in ARGET ATRP was the time for reducing Cu(II) to Cu(I), which was supported by delaying monomer addition and lowering the deactivator concentration.

Experimental section

Materials

Unless otherwise specified, ACS reagent grade solvents and starting materials were used as received. Anisole (Aldrich, 99.7%, anhydrous), triethylamine (J.T. Baker, 99.5%), dimethylformamide (Macron fine chemical, 99.8%), 2-propyn-1-ol (Acros, 99%), copper wire (Strem, d = 0.25 mm, 99.99%), 1,8-diazabicyclo[5.4.0]undec-7-ene (DBU) (Oakwood Chemical, 99%), methacryloyl chloride (Aldrich, 97%), silver chloride (American Drug and Chemical Co., reagent grade), chlorotrimethylsilane (Acros, 98%), Ethyl α-bromophenylacetate (EBPA) (Alfa Aesar, 97%), 4,4'-dinonyl-2,2'-dipyridyl (dNbpy) (TCI, 98%), copper(II) bromide (Acros, 99%, anhydrous) was kept in a desiccator with phosphorus pentoxide. Triethylamine was stored over KOH pellets.

Characterization

The molecular weights of polymers were determined by gel permeation chromatography (GPC) at 35 °C using two PLgel 10μ mixed-B columns in series (manufacturer stated linear molecular weight range of 500-10,000,000 g/mol) with THF as the eluent solvent at a flow rate of 1 mL/min. Optilab rEX (Wyatt Technology Co.) differential refractive index (dRI) detector was used as detector. The columns were calibrated by narrow poly(methyl methacrylate) standards ($M_n = 6$, 12, 30, 60, 127, 350 kg/mol). The GPC samples were prepared by dissolving 1-4 mg of polymer in 1 mL of THF and all GPC samples were filtered through a 0.2 μ m Whatman PTFE syringe filter before injecting into GPC.

Synthesis of propargyl methacrylate (PMA)

The procedure reported by the Haddleton group was followed, 98 but reaction solvent was changed to DCM from diethyl ether because the reaction was more easily stirred and the byproduct, triethylammonium chloride, was more soluble in DCM. In a 1 L three neck round bottom flask equipped with a magnetic stirring bar and an addition funnel, the solution of propargyl alcohol (55 mL, 0.963 mol) and triethylamine (150 mL, 1.087 mol) in dry DCM (250 mL) was cooled under ice bath. A solution of freshly distilled methacryloyl chloride (83.42 g, 0.806 mol) in dry DCM (100 mL) was added dropwise over 1 h. The mixture was then stirred at ambient temperature overnight. The crude product was diluted with diethyl ether and the triethylammonium chloride salt was filtered off. The filtrate was then washed with 1 M HCl solution and brine. The organic layer was dried over sodium sulfate and concentrated using rotary evaporator. The product was purified by passing through a silica plug using petroleum ether as an eluent. The solution was concentrated using rotary evaporator, further purified by vacuum distillation (45 °C at 0.02 mmHg). The product is a colorless oil (61.8 g, 62 %). ¹H NMR (500 MHz, CDCl₃, 298 K) δ 6.17 (dd, J = 1.5, 1.0 Hz, 1H), 5.62 (p, J = 1.6 Hz, 1H), 4.75 (d, J = 2.5 Hz, 2H), 2.48 (t, J = 2.5 Hz, 1H), 1.96 (dd, J = 1.6, 1.0 Hz, 3H). ¹³C{¹H} NMR (125 MHz, CDCl₃, 298 K) δ 166.53, 135.58, 126.58, 77.74, 74.76, 52.18, 18.24.

Synthesis of Trimethylsilylpropargyl Methacrylate (TMSPMA)

We followed the procedure reported by Stenzel group. Silver chloride (1.82 g, 12.7 mmol) was suspended in 170 mL of dry dichloromethane. Propargyl methacrylate (15.76 g, 127 mmol) and DBU (24 mL, 160 mmol) were added to this suspension, forming a pale-yellow mixture. The reaction mixture was then heated to 40 °C, chlorotrimethylsilane (24 mL, 189 mmol) was added dropwise, and the mixture was stirred for 24 h. The dark green solution obtained was diluted with hexane (400 mL), and the organic phase was washed with saturated NaHCO₃ solution (2 × 100 mL), 1M HCl solution (2 × 100 mL), DI water (2 × 100 mL), dried over magnesium sulfate, and concentrated by rotary evaporator. The crude product was further purified by flash column chromatography using hexanes/ethyl ether = 25: 1 mixture as eluent. A colorless oil (20.6 g, 82.8 % yield) was obtained. H NMR (500 MHz, CDCl₃, 298 K) δ 6.17 (p, J = 1.1 Hz, 1H), 5.61 (p, J = 1.6 Hz, 1H), 4.76 (s, 2H), 1.96 (dd, J = 1.6, 1.0 Hz, 3H), 0.18 (s, 9H). NMR (125 MHz, CDCl₃, 298 K) δ 166.57, 135.70, 126.40, 99.08, 91.95, 77.00, 76.75, 52.97, 18.30, -0.30.

Monitoring conversion and molecular weight during polymerization

Aliquots (0.4 mL) were removed at specific times using a degassed syringe. The NMR samples were prepared by dissolving 5 drops of crude samples with CDCl₃ without any purification. The molecular weight and PDI were monitored by the following GPC sample preparation procedure. The remaining sample aliquots (~ 0.3 mL) were passed through a flash pipette column packed with activated basic alumina using DCM as eluent.

After evaporating excess DCM, the polymers were precipitated by adding MeOH, the MeOH supernatants were decanted, and the amorphous solids were dried under high vacuum. The GPC samples were prepared by dissolving ca. 4 mg polymer product in 1 mL of THF and filtered through $0.2 \mu m$ Whatman PTFE syringe filters.

ARGET ATRP procedure (entry 1 of Table 4Table 4, [TMSPMA]: [EBPA]: [Cu^{II}Br₂]: [dNbpy] = 200: 1: 0.1: 0.2, copper wire surface area = 79 mm²)

A 10 mL long-necked Schlenk round-bottom flask equipped with a magnetic stir bar was charged with 3.2 mL of anisole, 0.096 mL of a freshly prepared 0.076 M Cu^{II}Br₂ solution in DMF (0.0076 mmol), 6.4 mg of dNbpy (0.02 mmol), 1.004 mL of DMF, and 3.2 mL of 0.022 M EBPA (0.07 mmol) in TMSPMA (15.3 mmol), respectively. The solution was then degassed with three freeze-pump-thaw cycles by liquid nitrogen. After the last freeze cycle, copper wire (length: 100 mm, diameter: 0.25 mm, surface area: 79 mm²) was coiled around a glass pipette and added under a strong nitrogen counterflow, and the frozen mixture was evacuated and backfilled with nitrogen three times. Next, the mixture was thawed and submerged in an oil bath maintained at 35 °C. The reaction was timed after the mixture thawed and samples were withdrawn periodically for conversion determination by ¹H NMR. At the end of the reaction, the crude mixture was diluted with dichloromethane and passed through a short basic aluminum plug to remove the catalyst. The solution color changed from brown to colorless. Excess solvents were removed using rotary evaporator and the polymer product was precipitated by methanol. The product was an amorphous solid. ¹H NMR (500 MHz, CDCl₃, 298 K) δ 4.59 (s, 2H), 1.96 – 1.60 (br, 2H), 1.09 - 0.94 (br, 3H), 0.19 (s, 9H). ⁸⁵ $M_n = 28.2$ kg/mol, PDI = 1.26.

ARGET ATRP procedure (entry 2 of Table 4Table 4, [TMSPMA]: [EBPA]: [Cu^{II}Br₂]: [dNbpy] = 200: 1: 0.4: 0.8, copper wire surface area = 79 mm²)

A 10 mL long-necked Schlenk round-bottom flask equipped with a magnetic stir bar was charged with 3.2 mL of anisole, 0.38 mL of a freshly prepared 0.076 M Cu^{II}Br₂ solution in DMF (0.0289 mmol), 24 mg of dNbpy (0.06 mmol), 0.720 mL of DMF, and 3.2 mL of 0.022 M EBPA (0.07 mmol) in TMSPMA (15.3 mmol), respectively. The solution was then degassed with three freeze-pump-thaw cycles by liquid nitrogen. After the last freeze cycle, copper wire (length: 100 mm, diameter: 0.25 mm, surface area: 79 mm²) was coiled around a glass pipette and added under a strong nitrogen counterflow, and the frozen mixture was evacuated and backfilled with nitrogen three times. Next, the mixture was thawed and submerged in an oil bath maintained at 35 °C. The reaction was timed after the mixture thawed and polymerization progress was analyzed as described above. At the end of the reaction, the crude mixture was diluted with dichloromethane and passed through a short basic aluminum plug to remove the catalyst. The solution color changed from brown to colorless. Excess solvents were removed by rotary evaporator and the polymer product was precipitated by methanol. The product was an amorphous solid. ¹H NMR (500 MHz, CDCl₃, 298 K) δ 4.59 (s, 2H), 1.96 – 1.60 (br, 2H), 1.09 – 0.94 (br, 3H), 0.19 (s, 9H). $^{85}M_n = 40.5$ kg/mol, PDI = 1.27.

ARGET ATRP procedure (entry 3 of Table 4Table 4, [TMSPMA]: [EBPA]: [Cu^{II}Br₂]: [dNbpy] = 200: 1: 0.6: 1.2, copper wire surface area = 79 mm²)

A 10 mL long-necked Schlenk round-bottom flask equipped with a magnetic stir bar was charged with 3.2 mL of anisole, 0.56 mL of a freshly prepared 0.076 M Cu^{II}Br₂ solution in DMF (0.043 mmol), 35 mg of dNbpy (0.086 mmol), 0.540 mL of DMF, and

3.2 mL of 0.022 M EBPA (0.07 mmol) in TMSPMA (15.3 mmol), respectively. The solution was then degassed with three freeze-pump-thaw cycles by liquid nitrogen. After the last freeze cycle, copper wire (length: 100 mm, diameter: 0.25 mm, surface area: 79 mm²) was coiled around a glass pipette and added under a strong nitrogen counterflow, and the frozen mixture was evacuated and backfilled with nitrogen three times. Next, the mixture was thawed and submerged in an oil bath maintained at 35 °C. The reaction was timed after the mixture thawed and polymerization progress was analyzed as described above. At the end of the reaction, the crude mixture was diluted with dichloromethane and passed through a short basic aluminum plug to remove the catalyst. The solution color changed from brown to colorless. Excess solvents were removed using rotary evaporator and the polymer product was precipitated by methanol. The product was an amorphous solid. 1 H NMR (500 MHz, CDCl₃, 298 K) δ 4.59 (s, 2H), 1.96 – 1.60 (br, 2H), 1.09 – 0.94 (br, 3H), 0.19 (s, 9H). 85 $M_{\rm n}$ = 34.2 kg/mol, PDI = 1.27.

ARGET ATRP procedure (entry 4 of Table 4, [TMSPMA]: [EBPA]: [Cu^{II}Br₂]: [dNbpy] = 200: 1: 1.0: 2.0, copper wire surface area = 79 mm²)

A 10 mL long-necked Schlenk round-bottom flask equipped with a magnetic stir bar was charged with 3.2 mL of anisole, 0.94 mL of a freshly prepared 0.076 M Cu^{II}Br₂ solution in DMF (0.071 mmol), 58 mg of dNbpy (0.14 mmol), 0.160 mL of DMF, and 3.2 mL of 0.022 M EBPA (0.07 mmol) in TMSPMA (15.3 mmol), respectively. The solution was then degassed with three freeze-pump-thaw cycles by liquid nitrogen. After the last freeze cycle, copper wire (length: 100 mm, diameter: 0.25 mm, surface area: 79 mm²) was coiled around a glass pipette and added under a strong nitrogen counterflow, and the frozen mixture was evacuated and backfilled with nitrogen three times. Next, the mixture was

thawed and submerged in an oil bath maintained at 35 °C. The reaction was timed after the mixture thawed and polymerization progress was analyzed as described above. At the end of the reaction, the crude mixture was diluted with dichloromethane and passed through a short basic aluminum plug to remove the catalyst. The solution color changed from brown to colorless. Excess solvents were removed using rotary evaporator and the polymer product was precipitated by methanol. The product was an amorphous solid. ¹H NMR (500 MHz, CDCl₃, 298 K) δ 4.59 (s, 2H), 1.96 – 1.60 (br, 2H), 1.09 – 0.94 (br, 3H), 0.19 (s, 9H). ⁸⁵ $M_{\rm n}$ = 44.4 kg/mol, PDI = 1.29.

ARGET ATRP procedure (entry 5 of Table 4Table 4, [TMSPMA]: [EBPA]: [Cu^{II}Br₂]: [dNbpy] = 200: 1: 0.6: 1.2, copper wire surface area = 39 mm²)

A 10 mL long-necked Schlenk round-bottom flask equipped with a magnetic stir bar was charged with 3.2 mL of anisole, 0.56 mL of a freshly prepared 0.076 M Cu^{II}Br₂ solution in DMF (0.043 mmol), 35 mg of dNbpy (0.086 mmol), 0.540 mL of DMF, and 3.2 mL of 0.022 M EBPA (0.07 mmol) in TMSPMA (15.3 mmol), respectively. The solution was then degassed with three freeze-pump-thaw cycles by liquid nitrogen. After the last freeze cycle, copper wire (length: 50 mm, diameter: 0.25 mm, surface area: 79 mm²) was coiled around a glass pipette and added under a strong nitrogen counterflow, and the frozen mixture was evacuated and backfilled with nitrogen three times. Next, the mixture was thawed and submerged in an oil bath maintained at 35 °C. The reaction was timed after the mixture thawed and polymerization progress was analyzed as described above. At the end of the reaction, the crude mixture was diluted with dichloromethane and passed through a short basic aluminum plug to remove the catalyst. The solution color changed from brown to colorless. Excess solvents were removed using rotary evaporator and the

polymer product was precipitated by methanol. The product was an amorphous solid. 1 H NMR (500 MHz, CDCl₃, 298 K) δ 4.59 (s, 2H), 1.96 – 1.60 (br, 2H), 1.09 – 0.94 (br, 3H), 0.19 (s, 9H). 85 $M_{\rm n}$ = 34.8 kg/mol, PDI = 1.26.

ARGET ATRP procedure (entry 6 of Table 4Table 4, [TMSPMA]: [EBPA]: [$Cu^{II}Br_2$]: [dNbpy] = 200: 1: 0.6: 1.2, copper wire surface area = 236 mm²)

A 10 mL long-necked Schlenk round-bottom flask equipped with a magnetic stir bar was charged with 3.2 mL of anisole, 0.56 mL of a freshly prepared 0.076 M Cu^{II}Br₂ solution in DMF (0.043 mmol), 35 mg of dNbpy (0.086 mmol), 0.540 mL of DMF, and 3.2 mL of 0.022 M EBPA (0.07 mmol) in TMSPMA (15.3 mmol), respectively. The solution was then degassed with three freeze-pump-thaw cycles by liquid nitrogen. After the last freeze cycle, copper wire (length: 300 mm, diameter: 0.25 mm, surface area: 79 mm²) was coiled around a glass pipette and added under a strong nitrogen counterflow, and the frozen mixture was evacuated and backfilled with nitrogen three times. Next, the mixture was thawed and submerged in an oil bath maintained at 35 °C. The reaction was timed after the mixture thawed and polymerization progress was analyzed as described above. At the end of the reaction, the crude mixture was diluted with dichloromethane and passed through a short basic aluminum plug to remove the catalyst. The solution color changed from brown to colorless. Excess solvents were removed using rotary evaporator and the polymer product was precipitated by methanol. The product was an amorphous solid. ¹H NMR (500 MHz, CDCl₃, 298 K) δ 4.59 (s, 2H), 1.96 – 1.60 (br, 2H), 1.09 – 0.94 (br, 3H), 0.19 (s, 9H). ⁸⁵ $M_n = 45.2$ kg/mol, PDI = 1.97.

ARGET ATRP procedure (entry 1 of Table 5Table 5, [TMSPMA]: [EBPA]: [$Cu^{II}Br_2$]: [dNbpy] = 200: 1: 0.6: 1.2, copper wire surface area = 39 mm²)

A 10 mL long-necked Schlenk round-bottom flask equipped with a magnetic stir bar was charged with 3.2 mL of anisole, 0.56 mL of a freshly prepared 0.076 M Cu^{II}Br₂ solution in DMF (0.043 mmol), 35 mg of dNbpy (0.086 mmol), 0.540 mL of DMF, and 3.2 mL of 0.022 M EBPA (0.07 mmol) in TMSPMA (15.3 mmol), respectively. The solution was then degassed with three freeze-pump-thaw cycles by liquid nitrogen. After the last freeze cycle, copper wire (length: 50 mm, diameter: 0.25 mm, surface area: 79 mm²) was coiled around a glass pipette and added under a strong nitrogen counterflow, and the frozen mixture was evacuated and backfilled with nitrogen three times. Next, the mixture was thawed and submerged in an oil bath maintained at 35 °C. The reaction was timed after the mixture thawed and polymerization progress was analyzed as described above. At the end of the reaction, the crude mixture was diluted with dichloromethane and passed through a short basic aluminum plug to remove the catalyst. The solution color changed from brown to colorless. Excess solvents were removed using rotary evaporator and the polymer product was precipitated by methanol. The product was an amorphous solid. ¹H NMR (500 MHz, CDCl₃, 298 K) δ 4.59 (s, 2H), 1.96 – 1.60 (br, 2H), 1.09 – 0.94 (br, 3H), 0.19 (s, 9H). 85 $M_n = 40.0 \text{ kg/mol, PDI} = 1.25.$

ARGET ATRP procedure (entry 2 of Table 5, [TMSPMA]: [EBPA]: [Cu^{II}Br₂]: [dNbpy] = 200: 1: 0.3: 0.6, copper wire surface area = 24 mm²)

A 10 mL long-necked Schlenk round-bottom flask equipped with a magnetic stir bar was charged with 3.2 mL of anisole, 0.30 mL of a freshly prepared 0.076 M Cu^{II}Br₂ solution in DMF (0.023 mmol), 18 mg of dNbpy (0.044 mmol), 0.80 mL of DMF, and 3.2 mL of 0.022 M EBPA (0.07 mmol) in TMSPMA (15.3 mmol), respectively. The solution was then degassed with three freeze-pump-thaw cycles by liquid nitrogen. After the last

freeze cycle, copper wire (length: 30 mm, diameter: 0.25 mm, surface area: 24 mm²) was coiled around a glass pipette and added under a strong nitrogen counterflow, and the frozen mixture was evacuated and backfilled with nitrogen three times. Next, the mixture was thawed and submerged in an oil bath maintained at 35 °C. The reaction was timed after the mixture thawed and polymerization progress was analyzed as described above. At the end of the reaction, the crude mixture was diluted with dichloromethane and passed through a short basic aluminum plug to remove the catalyst. The solution color changed from brown to colorless. Excess solvents were removed using rotary evaporator and the polymer product was precipitated by methanol. The product was an amorphous solid. 1 H NMR (500 MHz, CDCl₃, 298 K) δ 4.59 (s, 2H), 1.96 – 1.60 (br, 2H), 1.09 – 0.94 (br, 3H), 0.19 (s, 9H). 85 $M_{\rm n}$ = 36.0 kg/mol, PDI = 1.12.

ARGET ATRP procedure (entry 3 of Table 5, [TMSPMA]: [EBPA]: [Cu^{II}Br₂]: [dNbpy] = 100: 1: 0.3: 0.6, copper wire surface area = 39 mm²)

A 10 mL long-necked Schlenk round-bottom flask equipped with a magnetic stir bar was charged with 3.2 mL of anisole, 0.60 mL of a freshly prepared 0.076 M Cu^{II}Br₂ solution in DMF (0.046 mmol), 37 mg of dNbpy (0.09 mmol), 0.50 mL of DMF, and 3.2 mL of 0.045 M EBPA (0.14 mmol) in TMSPMA (15.3 mmol), respectively. The solution was then degassed with three freeze-pump-thaw cycles by liquid nitrogen. After the last freeze cycle, copper wire (length: 50 mm, diameter: 0.25 mm, surface area: 39 mm²) was coiled around a glass pipette and added under a strong nitrogen counterflow, and the frozen mixture was evacuated and backfilled with nitrogen three times. Next, the mixture was thawed and submerged in an oil bath maintained at 35 °C. The reaction was timed after the mixture thawed and polymerization progress was analyzed as described above. At the end

of the reaction, the crude mixture was diluted with dichloromethane and passed through a short basic aluminum plug to remove the catalyst. The solution color changed from brown to colorless. Excess solvents were removed using rotary evaporator and the polymer product was precipitated by methanol. The product was an amorphous solid. 1 H NMR (500 MHz, CDCl₃, 298 K) δ 4.59 (s, 2H), 1.96 – 1.60 (br, 2H), 1.09 – 0.94 (br, 3H), 0.19 (s, 9H). 85 $M_{\rm n}$ = 21.6 kg/mol, PDI = 1.15.

ARGET ATRP procedure (entry 4 of Table 5, [TMSPMA]: [EBPA]: [Cu^{II}Br₂]: [dNbpy] = 100: 1: 0.3: 0.6, copper wire surface area = 24 mm²)

A 10 mL long-necked Schlenk round-bottom flask equipped with a magnetic stir bar was charged with 3.2 mL of anisole, 0.60 mL of a freshly prepared 0.076 M Cu^{II}Br₂ solution in DMF (0.046 mmol), 37 mg of dNbpy (0.09 mmol), 0.50 mL of DMF, and 3.2 mL of 0.045 M EBPA (0.14 mmol) in TMSPMA (15.3 mmol), respectively. The solution was then degassed with three freeze-pump-thaw cycles by liquid nitrogen. After the last freeze cycle, copper wire (length: 30 mm, diameter: 0.25 mm, surface area: 24 mm²) was coiled around a glass pipette and added under a strong nitrogen counterflow, and the frozen mixture was evacuated and backfilled with nitrogen three times. Next, the mixture was thawed and submerged in an oil bath maintained at 35 °C. The reaction was timed after the mixture thawed and polymerization progress was analyzed as described above. At the end of the reaction, the crude mixture was diluted with dichloromethane and passed through a short basic aluminum plug to remove the catalyst. The solution color changed from brown to colorless. Excess solvents were removed using rotary evaporator and the polymer product was precipitated by methanol. The product was an amorphous solid. ¹H NMR (500

MHz, CDCl₃, 298 K) δ 4.59 (s, 2H), 1.96 – 1.60 (br, 2H), 1.09 – 0.94 (br, 3H), 0.19 (s, 9H).⁸⁵ $M_{\rm n} = 22.0$ kg/mol, PDI = 1.17.

ARGET ATRP procedure (entry 5 of Table 5Table 5, [TMSPMA]: [EBPA]: [Cu^{II}Br₂]: [dNbpy] = 600: 1: 0.6: 1.2, copper wire surface area = 39 mm²)

A 10 mL long-necked Schlenk round-bottom flask equipped with a magnetic stir bar was charged with 3.2 mL of anisole, 0.40 mL of a freshly prepared 0.0385 M Cu^{II}Br₂ solution in DMF (0.015 mmol), 13 mg of dNbpy (0.030 mmol), 0.70 mL of DMF, and 3.2 mL of 0.0079 M EBPA (0.03 mmol) in TMSPMA (15.3 mmol), respectively. The solution was then degassed with three freeze-pump-thaw cycles by liquid nitrogen. After the last freeze cycle, copper wire (length: 50 mm, diameter: 0.25 mm, surface area: 39 mm²) was coiled around a glass pipette and added under a strong nitrogen counterflow, and the frozen mixture was evacuated and backfilled with nitrogen three times. Next, the mixture was thawed and submerged in an oil bath maintained at 35 °C. The reaction was timed after the mixture thawed and polymerization progress was analyzed as described above. At the end of the reaction, the crude mixture was diluted with dichloromethane and passed through a short basic aluminum plug to remove the catalyst. The solution color changed from brown to colorless. Excess solvents were removed using rotary evaporator and the polymer product was precipitated by methanol. The product was an amorphous solid. ¹H NMR (500 MHz, CDCl₃, 298 K) δ 4.59 (s, 2H), 1.96 – 1.60 (br, 2H), 1.09 – 0.94 (br, 3H), 0.19 (s, 9H). 85 $M_{\rm n} = 78.4$ kg/mol, PDI = 1.27.

ARGET ATRP procedure (entry 6 of Table 5, [TMSPMA]: [EBPA]: [Cu^{II}Br₂]: [dNbpy] = 600: 1: 0.6: 1.2, copper wire surface area = 24 mm²)

A 10 mL long-necked Schlenk round-bottom flask equipped with a magnetic stir bar was charged with 3.2 mL of anisole, 0.40 mL of a freshly prepared 0.0385 M Cu^{II}Br₂ solution in DMF (0.015 mmol), 13 mg of dNbpy (0.030 mmol), 0.70 mL of DMF, and 3.2 mL of 0.0079 M EBPA (0.03 mmol) in TMSPMA (15.3 mmol), respectively. The solution was then degassed with three freeze-pump-thaw cycles by liquid nitrogen. After the last freeze cycle, copper wire (length: 30 mm, diameter: 0.25 mm, surface area: 24 mm²) was coiled around a glass pipette and added under a strong nitrogen counterflow, and the frozen mixture was evacuated and backfilled with nitrogen three times. Next, the mixture was thawed and submerged in an oil bath maintained at 35 °C. The reaction was timed after the mixture thawed and polymerization progress was analyzed as described above. At the end of the reaction, the crude mixture was diluted with dichloromethane and passed through a short basic aluminum plug to remove the catalyst. The solution color changed from brown to colorless. Excess solvents were removed using rotary evaporator and the polymer product was precipitated by methanol. The product was an amorphous solid. ¹H NMR (500 MHz, CDCl₃, 298 K) δ 4.59 (s, 2H), 1.96 – 1.60 (br, 2H), 1.09 – 0.94 (br, 3H), 0.19 (s, 9H). 85 $M_n = 83.0$ kg/mol, PDI = 1.25.

ARGET ATRP procedure (entry 7 of Table 5, [TMSPMA]: [EBPA]: [Cu^{II}Br₂]: [dNbpy] = 600: 1: 0.3: 0.6, copper wire surface area = 24 mm²)

A 10 mL long-necked Schlenk round-bottom flask equipped with a magnetic stir bar was charged with 3.2 mL of anisole, 0.20 mL of a freshly prepared 0.0385 M Cu^{II}Br₂ solution in DMF (0.0077 mmol), 7 mg of dNbpy (0.017 mmol), 0.90 mL of DMF, and 3.2 mL of 0.0079 M EBPA (0.03 mmol) in TMSPMA (15.3 mmol), respectively. The solution was then degassed with three freeze-pump-thaw cycles by liquid nitrogen. After the last

freeze cycle, copper wire (length: 30 mm, diameter: 0.25 mm, surface area: 24 mm²) was coiled around a glass pipette and added under a strong nitrogen counterflow, and the frozen mixture was evacuated and backfilled with nitrogen three times. Next, the mixture was thawed and submerged in an oil bath maintained at 35 °C. The reaction was timed after the mixture thawed and polymerization progress was analyzed as described above. At the end of the reaction, the crude mixture was diluted with dichloromethane and passed through a short basic aluminum plug to remove the catalyst. The solution color changed from brown to colorless. Excess solvents were removed using rotary evaporator and the polymer product was precipitated by methanol. The product was an amorphous solid. 1 H NMR (500 MHz, CDCl₃, 298 K) δ 4.59 (s, 2H), 1.96 – 1.60 (br, 2H), 1.09 – 0.94 (br, 3H), 0.19 (s, 9H). 85 $M_{\rm n}$ = 98.2 kg/mol, PDI = 1.30.

Induction period study procedure monomer added at t = 2.5 h ([TMSPMA]: [EBPA]: $[Cu^{II}Br_2]$: [dNbpy] = 200: 1: 0.3: 0.6, copper wire surface area = 39 mm²)

In a 10 mL long neck Schlenk flask charged with a stir bar, 3.2 mL of anisole, 0.56 mL of 0.076 M Cu^{II}Br₂ (0.043 mmol) in DMF, dNbpy (35 mg, 0.086 mmol), 0.54 mL DMF were added respectively. The solution mixture was degassed by three freeze-pumpthaw cycles. The solution was frozen again and backfilled with nitrogen. Under the nitrogen flow, copper wire (length = 50 mm, diameter = 0.25 mm, surface area = 39 mm²) was coiled around a glass pipette and added under a strong nitrogen counterflow. The reaction mixture was allowed to stir at 35 °C for 2.5 h. In another Schlenk flask, 3.2 mL of 0.022 M EBPA in TMSPMA was degassed by three freeze-pump-thaw cycles and added to the reaction mixture at the end of 2.5 h, which is t = 0 h for the polymerization. The

reaction was allowed to stir at 35 °C and the polymerization conversion and molecular weight were monitored by ¹H NMR and GPC as described above.

Induction period study procedure $[Cu^{II}] = 1.0 \text{ mM}$ ([TMSPMA]: [EBPA]: $[Cu^{II}Br_2]$: [dNbpy] = 200: 1: 0.1: 0.2, copper wire surface area = 39 mm²)

A 10 mL long-necked Schlenk round-bottom flask equipped with a magnetic stir bar was charged with 3.2 mL of anisole, 0.1 mL of a freshly prepared 0.076 M Cu^{II}Br₂ solution in DMF (0.0076 mmol), 6.0 mg of dNbpy (0.015 mmol), 1.0 mL of DMF, and 3.2 mL of 0.022 M EBPA (0.07 mmol) in TMSPMA (15.3 mmol), respectively. The solution was then degassed with three freeze-pump-thaw cycles by liquid nitrogen. After the last freeze cycle, copper wire (length: 50 mm, diameter: 0.25 mm, surface area: 39 mm²) was added with a strong nitrogen counterflow, and the frozen mixture was evacuated and backfilled with nitrogen three times. Next, the mixture was thawed and submerged in an oil bath maintained at 35 °C. The reaction was timed after the mixture thawed and samples were withdrawn periodically for conversion determination by ¹H NMR.

Induction period study procedure $[Cu^{II}] = 6.1 \text{ mM}$ ([TMSPMA]: [EBPA]: $[Cu^{II}Br_2]$: [dNbpy] = 200: 1: 0.6: 0.2, copper wire surface area = 39 mm²)

A 10 mL long-necked Schlenk round-bottom flask equipped with a magnetic stir bar was charged with 3.2 mL of anisole, 0.56 mL of a freshly prepared 0.076 M Cu^{II}Br₂ solution in DMF (0.043 mmol), 35 mg of dNbpy (0.086 mmol), 0.540 mL of DMF, and 3.2 mL of 0.022 M EBPA (0.07 mmol) in TMSPMA (15.3 mmol), respectively. The solution was then degassed with three freeze-pump-thaw cycles by liquid nitrogen. After the last freeze cycle, copper wire (length: 50 mm, diameter: 0.25 mm, surface area: 79 mm²) was coiled around a glass pipette and added under a strong nitrogen counterflow, and the

frozen mixture was evacuated and backfilled with nitrogen three times. Next, the mixture was thawed and submerged in an oil bath maintained at 35 °C. The reaction was timed after the mixture thawed and polymerization progress was analyzed as described above.

Chapter 3. Post-polymerization Modification and polymeric micelle formation

Introduction

Modifying the properties of a class of polymers (e.g., polyolefins, polymethacrylates, etc.) can be achieved by using different monomers, including combining them (e.g., copolymerization of ethylene and 1-hexene) or by chemically modifying a polymer—an approach described as post-polymerization modification (PPM). Modification by polymerizing different monomer(s) is preferable when the monomers are commercially available, inexpensive, and compatible with polymerization conditions.

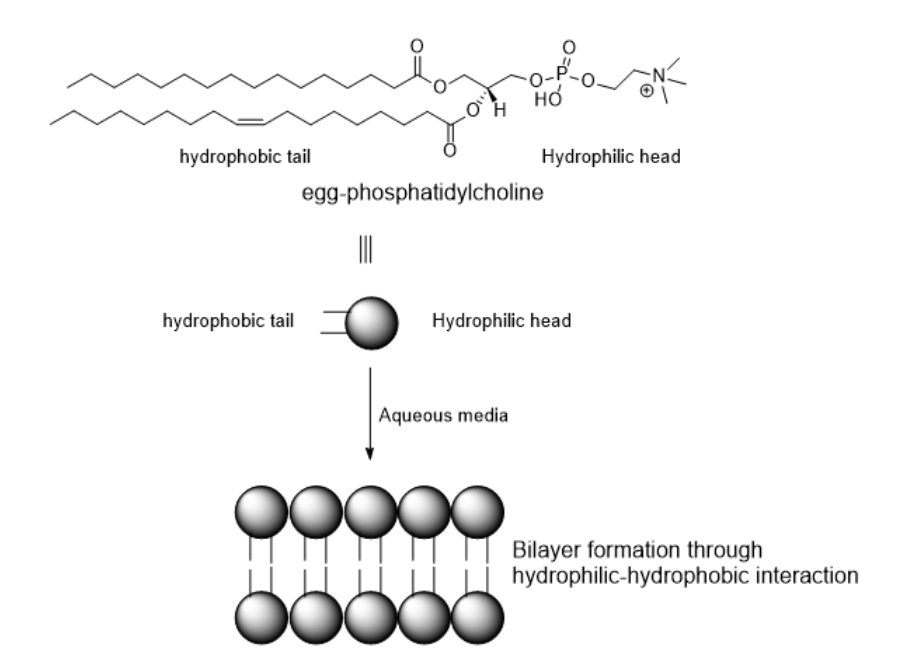
In the PPM approach monomers containing functional groups that (1) can be chemoselectively modified and (2) are compatible with the polymerization conditions are polymerized to yield a functional polymer. By reacting the functional groups along the backbone with suitably functionalized molecules or macromers, new polymers or polymer brushes with a range of chemical and physical properties can be prepared from a common starting material—the functional polymer. An important advantage of the PPM approach is that polymers with functional groups that are incompatible with polymerization conditions can be synthesized. Many reactions have been used as PPMs: esterification, amidation, Michael type addition, Diels -Alder reaction, and copper-catalyzed alkyne azide cycloaddition (CuAAC), etc.

CuAAC is one of the widely used PPM method that exhibits high yield, high chemo-selectivity, broad functional group tolerance, and produce byproducts that can be easily removed without chromatography. CuAAC has been utilized to make various

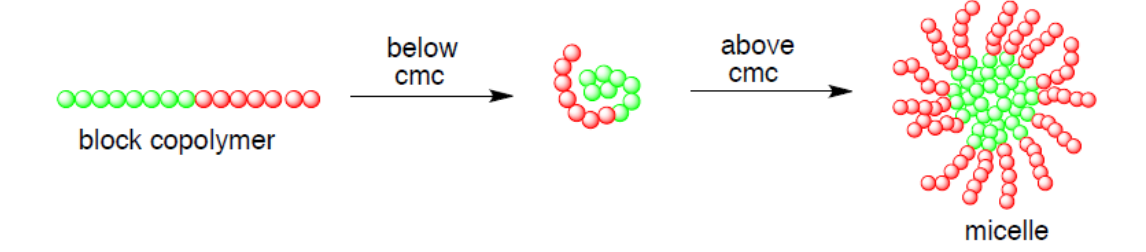
polymer structures: comb-shape polymers, dendrimers, block copolymers. This chapter describes using PPM to synthesize micelles formed from individual polymer chains.

Micelles can form by the hydrophobic interactions between the water molecules, polar functional groups, and nonpolar functional groups on surfactant molecules or amphiphilic macromolecules. In 1950, Walter Kauzmann identified the hydrophobic interactions as a primary source of protein stability. In 1999, Lum, Chandler and Weeks developed a theory of solvation of small and large nonpolar molecules in water. 100 For a small nonpolar solute at low concentration in water, the hydrophobic surface does not form hydrogen bonds with nearby water molecules. Due to the size of the solute molecule, the water nearby can recognize the solute and form hydrogen bonds around the solute. In this situation, the water molecules separate the solute and the hydrophobic interactions between solutes are weak. However, if the length of the hydrophobic solute is greater than 1 nm, the formation of hydrogen bond networks around the hydrophobic solute is geometrically impossible. The two hydrophobic surfaces can push nearby water molecules away to generate a thin vapor layer around the surface. The pressure imbalance leads to the attraction force between two hydrophobic surfaces. Chandler explained the hydrophobicity by "oil and water molecules actually attract each other, but not nearly as strongly as water attracts itself."101 Hydrophobic interactions are also observed in biological systems. One example is the bilayer formation from polar lipid, shown in Scheme 9. The phosphatidylcholine from chicken egg is used as an example. When the phosphatidylcholine dissolved in aqueous media, the aliphatic tails are associated by the hydrophobic interactions and the ionic heads point toward the bulk water solution to stabilize the bilayer structure. 102 The bilayer is the building block to form membranes. Another example of hydrophilic-hydrophobic interaction is the micelle formation from amphiphilic block copolymers containing polar (red) and nonpolar (green) ends, shown in Scheme 10. At lower concentrations, the copolymers exist as single polymer chain, while at concentrations higher than critical micelle concentration (cmc), they self-assemble into micelles with polar (red) ends point toward the bulk aqueous media.

Scheme 9. Lipid bilayer formation by hydrophilic hydrophobic interactions



Scheme 10. Formation of micelle from block copolymer.



The concentration of the surfactant (or block copolymer) plays an important role during this process. The critical micelle concentration (cmc) is defined as the threshold concentration for a specific surfactant to form stable micelles. The critical micelle

concentration (cmc) is defined by the lowest concentrations of molecular surfactants or amphiphilic block copolymers where micelles form. Several methods have been reported to measure cmcs, including pyrene encapsulation, 103 surface tension measurements, 104 and dynamic light scattering (DLS). 105 In these experiments, physicochemical properties are plotted vs surfactant or amphiphile concentrations, and the concentration where the property deviates is the cmc. Unlike traditional micelles formed by aggregation of surfactant molecules or amphiphilic block polymers, "intramolecular" micelle formation is entropically more favorable for polymers chains where hydrophilic and hydrophobic side chains randomly (or approximately randomly) distributed along the polymer backbone. This chapter focuses on whether CuAAC of functional polymers prepared by ARGET ATRP can produce polymers capable of forming single-chain micelles.

Deprotection of Poly(trimethylsilylpropargyl methacrylate)

The first step in testing the above hypothesis is cleaving the trimethylsilyl group of PTMSPMA to prepare poly(propargyl methacrylate) (PPMA), which has terminal alkynes as the partners for azides in CuAACs. As shown in Scheme 11, treating poly(trimethylsilylpropargyl methacrylate) (PTMSPMA) with tetra-*n*-butylammonium fluoride trihydrate (TBAF) under acidic condition, deprotects the terminal alkyne yielding poly(propargyl methacrylate) (PPMA). PMMA was characterized by ¹H NMR spectroscopy and GPC. In the NMR spectrum, , the disappearance of the TMS signal at 0.2 ppm (protons a in Figure 14Figure 14) and appearance of the alkyne signal at 2.5 ppm (proton b in Figure 14Figure 14) indicates complete deprotection. The removal of TMS group leads to a 37% mass loss from each repeating unit on the polymer chain. However, the apparent molecular weight of based on the poly(methyl methacrylate) standards did not

reflect the mass loss of the deprotection process. The similar retention time in THF-GPC system indicates that the deprotected polymer PPMA has similar hydrodynamic radius as the PTMSPMA. Triple detection GPC may give more accurate molecular weight determination of PPMA. The overlapped GPC traces of PTMSPMA and PPMA are, shown in Figure 15Figure 15.

Scheme 11. The deprotection of poly(trimethylsilylpropargyl methacrylate).

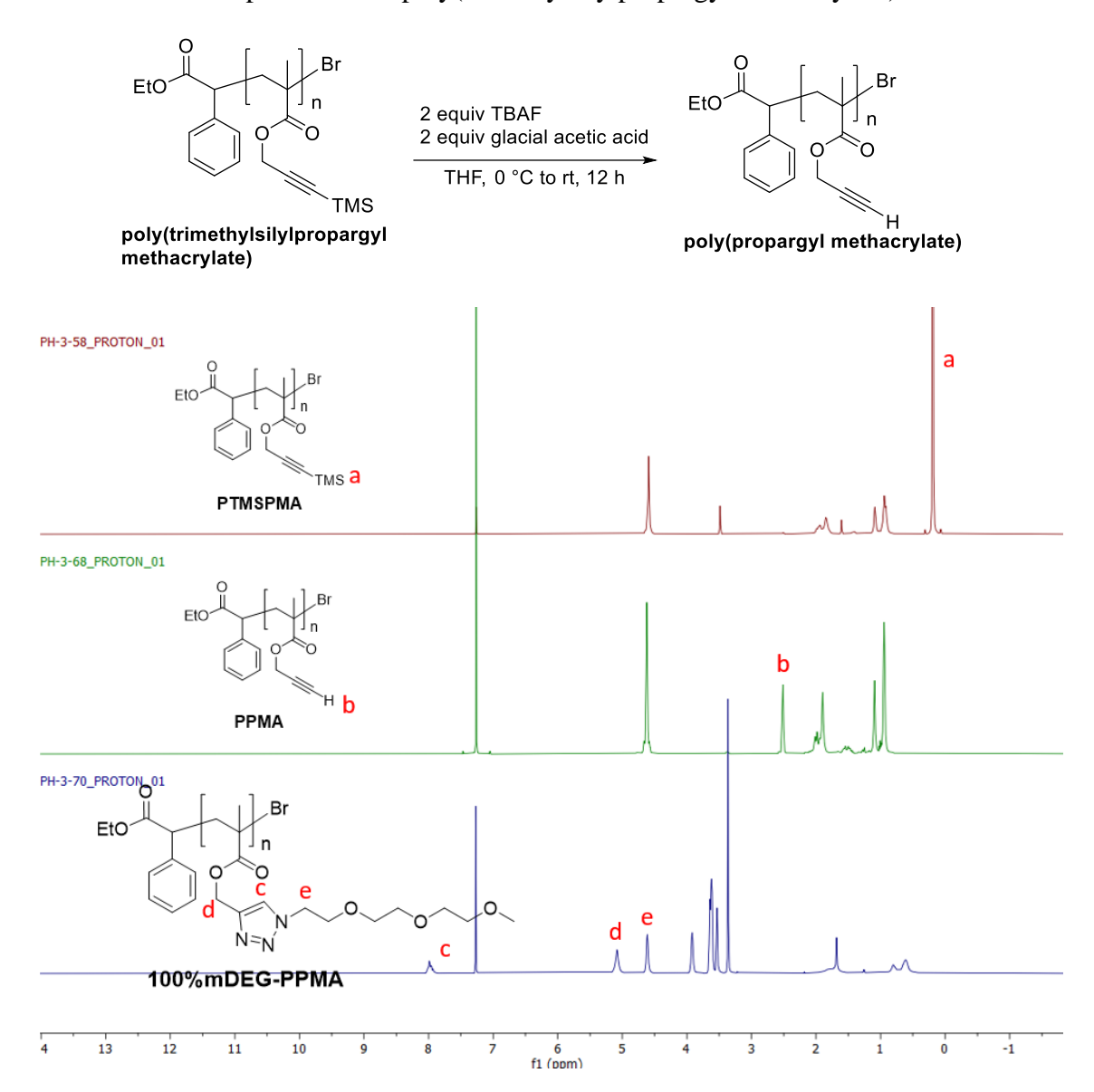


Figure 14. Overlapped ¹H NMR spectra of the PTMSPMA (top) and PPMA (middle) and 100% mDEG-PPMA (bottom) in CDCl₃

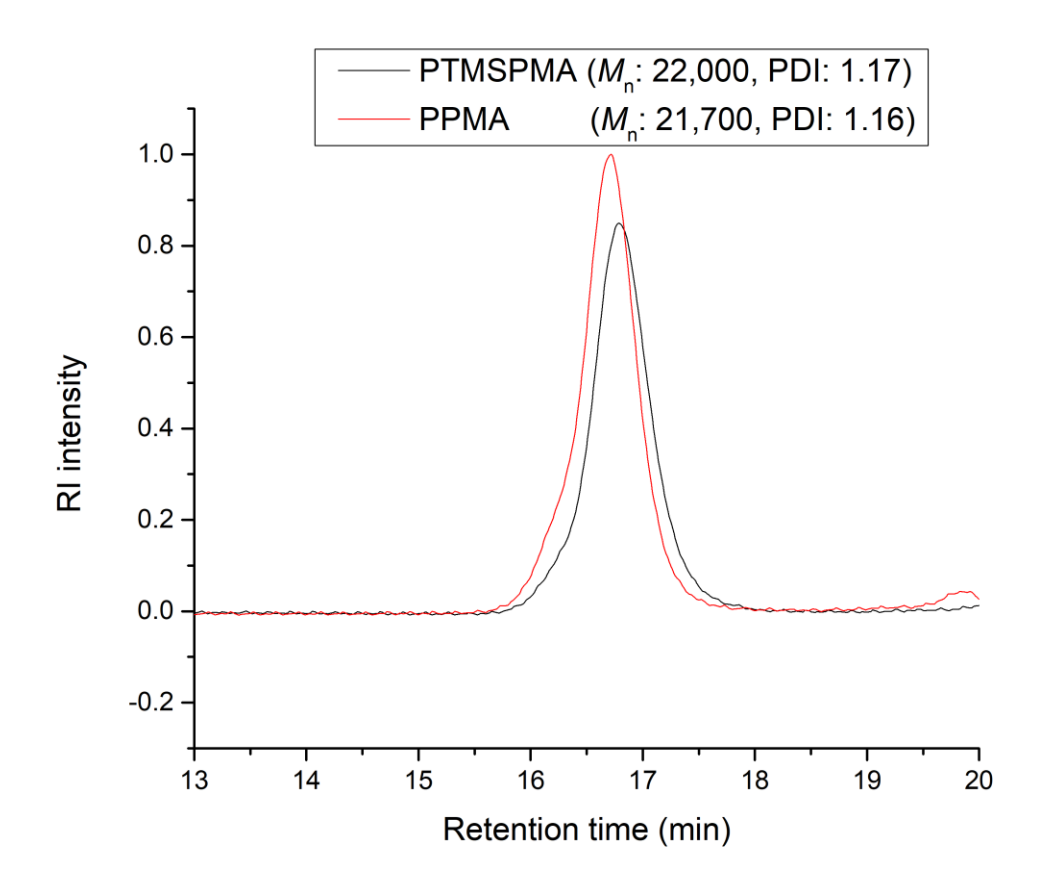


Figure 15. The GPC trace of PTMSPMA (black) and after removing TMS protecting group, PPMA (red).

Functionalizing poly(propargyl methacrylate) by CuAAC

With the alkyne polymer, PPMA, in hand, the viability of CuAAC for PPM with azide bearing molecules was initially tested by reacting PPMA with 3 equiv of methoxy tri(ethylene glycol) azide (mDEG-N3) versus the alkyne concentration catalyzed by 5 mol% CuSO₄ • 5H₂O and 12 mol% sodium ascorbate versus the alkyne concentration in DMF for 3 h at room temperature (Scheme 12). The overlaid ¹H NMR spectra of PPMA and 100% mDEG-PPMA are shown in Figure 14Figure 14. The disappearance of the alkyne signal at 2.5 ppm and the presence of the broad signal from the triazole ring at 7.98 ppm (proton c in Figure 14Figure 14), indicate that the CuAAC reactions is >99% complete.

Scheme 12. Post-polymerization modification of PPMA with mDEG-N3 by CuAAC.

After this success, syntheses of amphiphilic polymers were explored by CuAAC reactions of PPMA was then reacted with mixtures containing different ratios of hydrophilic mDEG-N3 and hydrophobic dodecyl azide (C10-N3) catalyzed by CuSO₄ • 5H₂O and sodium ascorbate in DMF. The polymer with 80% mDEG and 20% C10 groups, 80% mDEG-PPMA, illustrates how the products of CuAAC were synthesized and characterized. The mole fraction of the hydrophilic mDEG-N3 reactant within the azide mixture was 79%, determined by the methylene protons next to the azido group on mDEG- N_3 (protons 2 in Figure 16) and C10- N_3 (protons 5 in Figure 16). The hydrophilic/hydrophobic side chains ratios of CuAAC products were determined by ¹H NMR, using the integration value of the methylene groups next to the nitrogen on the triazole rings. Comparing the integration value of the methylene on the hydrophilic mDEG chain at 4.60 ppm (protons a in Figure 17) and the hydrophobic dodecyl chains at 4.41 ppm (protons b in Figure 17), the hydrophilic/hydrophobic ratio can be precisely determined. The mole fraction of the targeted 80% mDEG-PPMA has 82% hydrophilic mDEG side and will be later referred as 82% mDEG-PPMA. Comparison of the mole fraction of mDEG in reactant azide mixtures and the mole fraction of the mDEG side chains in the functionalized

mDEG-PPMAs are summarized in Table 6. The results indicate the mDEG- N_3 and C10- N_3 have similar reactivity toward alkyne groups on the polymer backbones and shows that mole fraction of the mDEG can be controlled with less than a 3% difference between mole fractions of the reactant and the polymers.

Table 6. Comparison of the mole fraction of mDEG in the reactant azide mixtures with the functionalized x% mDEG-PPMA products.

Sample	Reactant azide ratio (mol% of mDEG)	Polymer side chain ratio (mol% of mDEG)
90% mDEG-PPMA	88.5%	90.1%
82% mDEG-PPMA	78.7%	82.0%
61%mDEG-PPMA	59.9%	61.0%

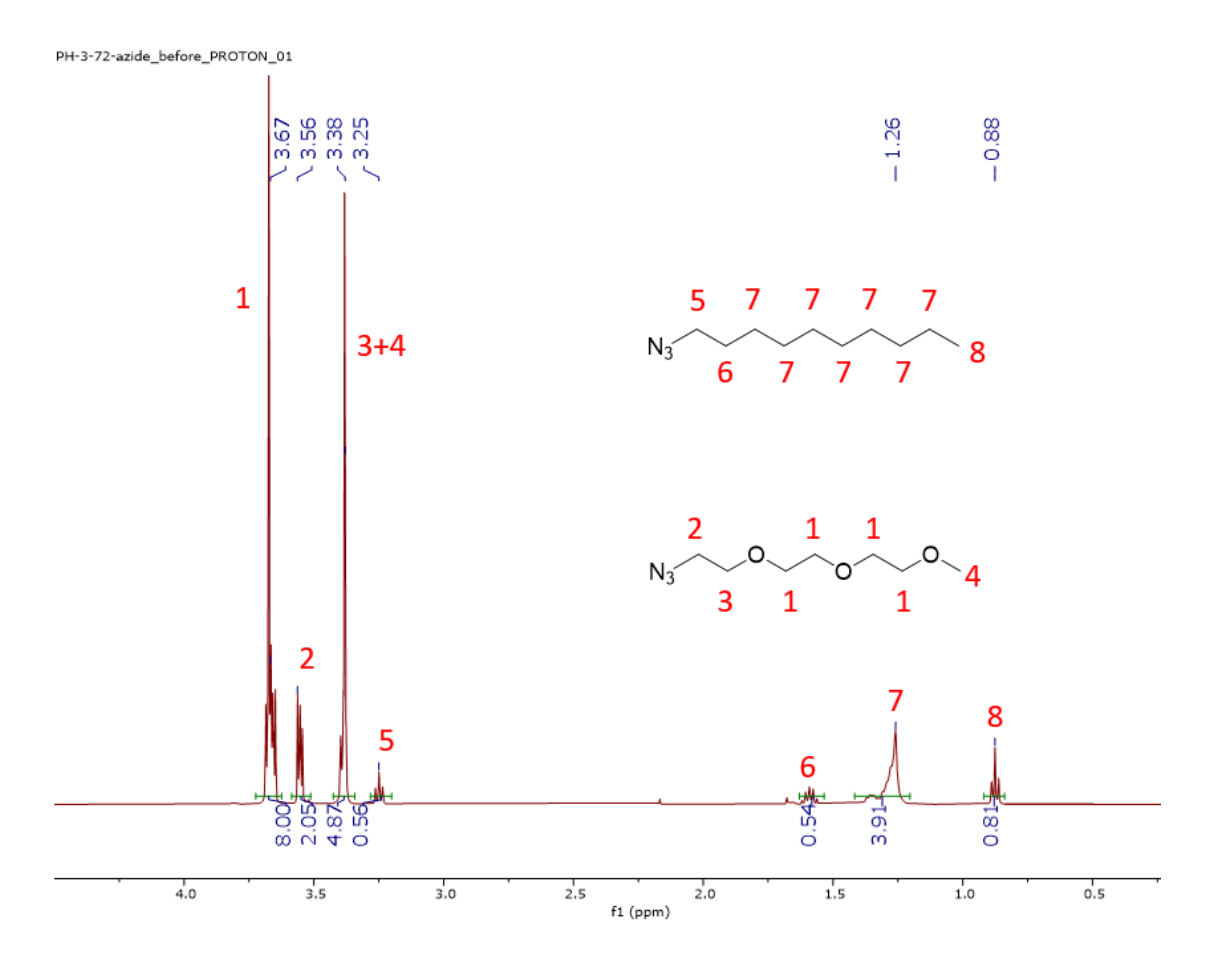


Figure 16. The ^1H NMR of reactant azide mixture (mDEG-N $_3$ and C10-N $_3$) for preparing 80%mDEG-PPMA in CDCl $_3$

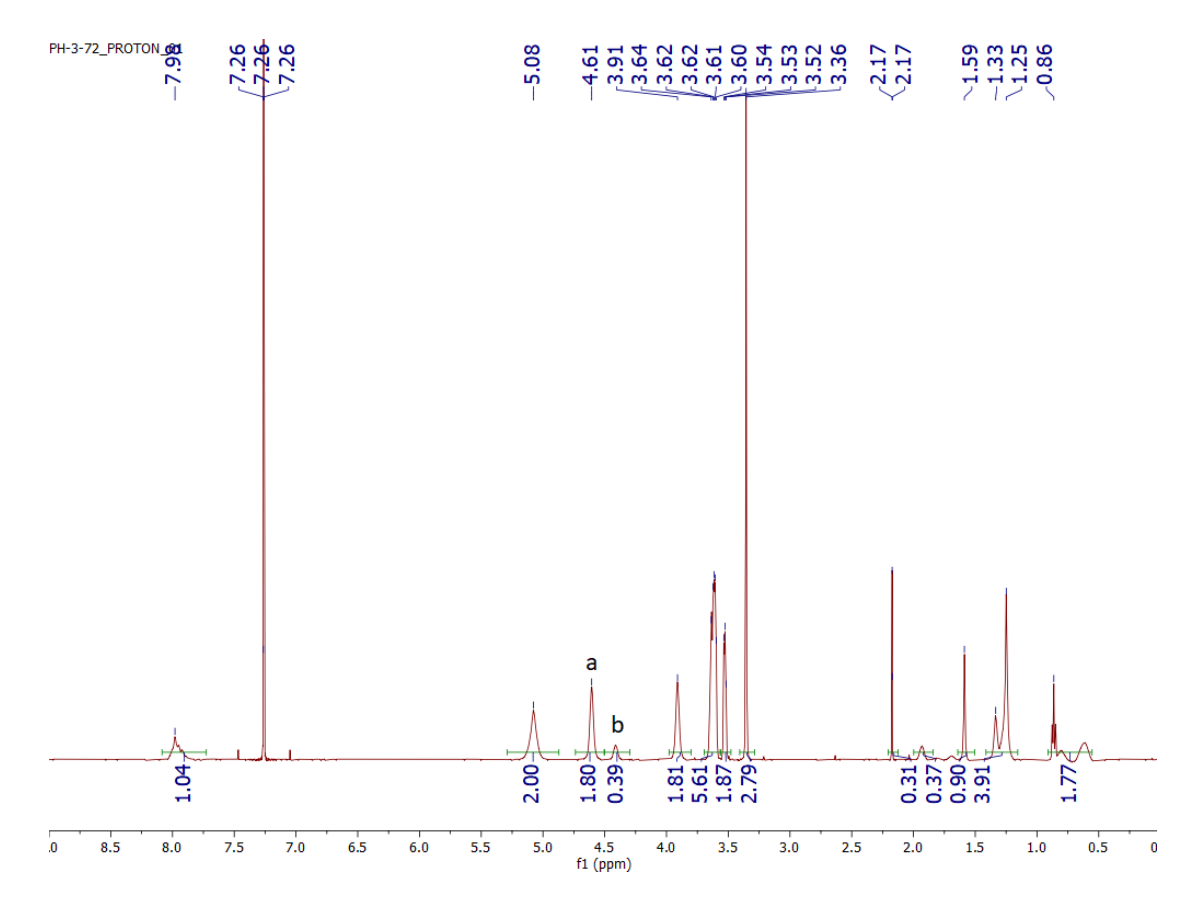


Figure 17. The ¹H NMR of 82% mDEG-PPMA in CDCl₃.

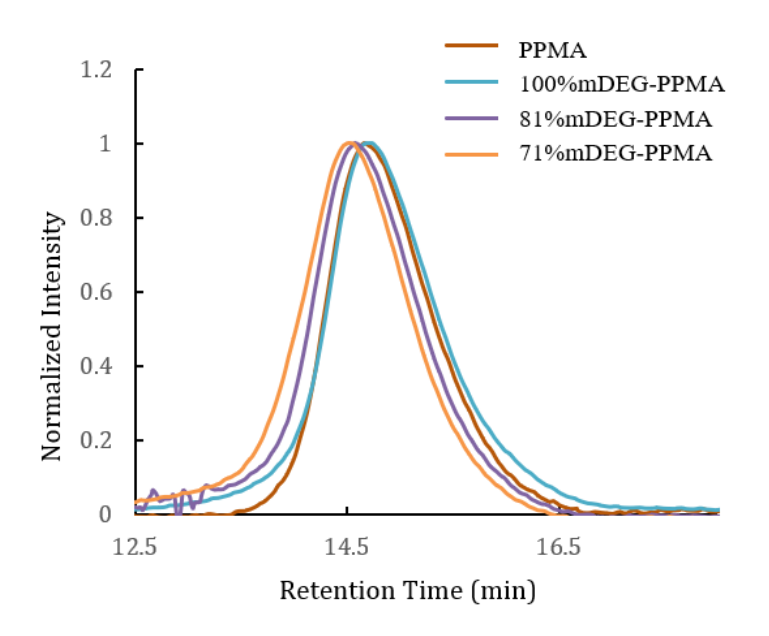


Figure 18. Overlapped GPC traces of PPMA (dark red), 100%mDEG-PPMA (cyan), 82%mDEG-PPMA (purple) and 71%mDEG-PPMA (orange) in THF.

CuAAC modified polymers with different side chain ratios were further characterized by GPC. Theoretically, the molecular weight of the grafted polymers should increase by 2.5 but the GPC results only show slightly higher molecular weight for 82%mDEG-PPMA and 71%mDEG-PPMA. The 100%mDEG-PPMA has roughly the same molecular weight as the PPMA precursor. The theoretical M_n s of CuAAC products were calculated from the degree of polymerization of parent polymer PPMA (DP = 288). The experimental $M_{\rm n}$ s are significantly lower than the theoretical $M_{\rm n}$ s, shown in Table 7Table 7. The CuAAC modified polymer products have similar PDI value to the parent polymer except 100% mDEG PPMA. The underestimating molecular weight of the grafted polymers is due to the GPC calibration method. The GPC columns are calibrated by the retention time of the linear poly(methyl methacrylate) (PMMA) standards within the GPC columns. The molecular weights of the grafted polymer samples were then calculated against the calibration curve. The grafted polymers have compact structure, and their hydrodynamic radius are comparable to the linear PMMA standards with much smaller molecular weight and lead to the underestimate of the molecular weight. The underestimate of molecular weight was also observed by Gao while characterizing polymer brushes using the same GPC calibration method.¹⁵

Table 7. Comparing the theoretical molecular weight (calculated from the degree of polymerization of PPMA) and the experimental molecular weight (determined by GPC) of xx%mDEG-PPMA.

Sample	Experimental M_n	Experimental PDI	Theoretical M_n
PPMA	35,800	1.13	
100% mDEG PMMA	35,300	1.31	90,200
82%mDEG PMMA	43,300	1.17	89,900
71% mDEG PMMA	47,000	1.17	89,700

Kinetic Study of CuAAC

The CuAAC kinetic of the azido-bearing polymer, poly(3-azidopropyl methacrylate) was reported by Matyjaszewski group. They discovered that over 90% of the azido-bearing polymer was functionalized in 150 min when reacts with propargyl alcohol. Under the same condition, 3-azidopropyl methacrylate has around 30 % conversion in 150 min, shown in Scheme 13.

Scheme 13. CuAAC reaction rate of poly(3-azidopropyl methacrylate) (top) and 3-azidopropyl methacrylate (bottom) reacting with propargyl alcohol.

$$0.05 \text{ M}$$
 0.0025 M CuCl
 0.0025 M CuCl

This kinetic result was explained by anchimeric assistance and is supported by the mechanistic study from Fokin and Finn, shown in Scheme 14Scheme 14,¹⁰⁶ who reported that ditriazole **3** was the major product when diazide **1** was coupled with phenylacetylene, even when 10 equivalents of diazide 1 vs phenylacetylene were used. They proposed that

the monotriazole copper complex **4** can recruit another copper—acetylide to form dinuclear copper complex intermediate **5** and intramolecularly couple with the second azide.

Scheme 14. Reactivity of diazide toward phenylacetylene and mechanism proposed by Fokin and Finn.

Proposed Mechanism:

The CuAAC mechanism involving the binuclear copper complex was proposed by Worrell and Fokin, shown in Figure 19. ¹⁰⁷ The formation of binuclear copper complex intermediate was proven by reacting the isotopically pure ⁶³Cu(MeCN)₄PF₆ with Cu acetylide with natural Cu isotope ratio (⁶³Cu: ⁶⁵Cu ratio = 69: 31). After CuAAC, Cu triazole product (⁶³Cu: ⁶⁵Cu ratio = 85: 15) with 50% isotopic enrichment was observed. While reacting Cu triazole complex containing natural Cu isotope ratio with isotopically pure ⁶³Cu(MeCN)₄PF₆, no isotopic enrichment was observed. Based on the evidence, Worrell and Fokin claimed the existence of the binuclear copper intermediate, and the 50%

76

isotopic enrichment happens during the cycloaddition process to form copper triazole complex.

$$R^{1} \xrightarrow{N-R^{2}} R^{1} \xrightarrow{H} E^{2} \qquad E^{1} \xrightarrow{Cu} H$$

$$R^{1} \xrightarrow{H} E^{2} \qquad E^{2}$$

Figure 19. The CuAAC mechanism involving binuclear copper intermediate proposed by Worrell and Fokin.

Venderbosch and coworkers prepared a Cu(I) iminophosphorane triazole complex, shown in Scheme 15, and found it is catalytically active to couple benzyl azide and phenylacetylene. The Cu triazole complex is isolable and characterized by H NMR and cold-spray ionization mass and proposed to be the resting state of the CuAAC catalytic cycle.

Scheme 15. Synthesis of copper iminophosphorane triazole complex reported by Venderbosch and coworkers. ¹⁰⁸

Fokin and Finn suggested the anchimeric assistance of the diazide reacting with phenylacetylene (Scheme 14Scheme 14) is catalyzed by the monotriazole copper complex 4 recruiting another copper—acetylide to form dinuclear copper complex intermediate 5 and intramolecularly coupling with the second azide. Worrell and Fokin have proven the involvement of the dinuclear copper complex during CuAAC catalytic cycle by the copper isotope enrichment experiment. Venderbosch and coworkers identified the copper triazolide complex as the resting state of the catalytic cycle. Both experimental results are consistent with the Fokin and Finn's statement of anchimeric assistance of diazide in CuAAC reaction.

Fokin and Finn also studied reactivity of the dialkyne 6 with benzyl azide and found out that the distinct reactivity of dialkyne 6 from the diazide 1, shown in Scheme 16Scheme 16. The products of dialkyne and benzyl azide are a statistical mixture of monotriazole product 7 and ditriazole product 8. The reaction mechanism was proposed by Fokin and Finn to be stepwise due to the weak interaction between copper-triazole complex intermediate 9 and benzyl azide. Failing to recruit the benzyl azide, the proteolysis of intermediate 9 generates the monotriazole product 7 before the neighbor alkyne groups couple with benzyl azide.

Scheme 16. Reactivity of dialkyne toward benzyl azide and mechanism proposed by Fokin and Finn.

Proposed Mechanism:

Based on Fokin and Finn's result on dialkyne reacting with benzyl azide, we hypothesize that no anchimeric assistance will be observed when reacting alkyl-bearing polymer PPMA with organic azide due to the weak interaction between copper triazole complex and organic azide. To prove the concept, the CuAAC kinetic of the alkyne-bearing polymer PPMA is compared with the monomer containing alkyne. It was known that the vinyl group on the propargyl methacrylate monomer can coordinate to the copper catalysts. ¹⁰⁹ To eliminate the impact of vinyl coordination on copper catalyst activity, ethynyl-2-methylpropanoate (EMP), shown in

Scheme 17

Scheme 17a, was prepared to mimic the propargyl methacrylate monomer. All the kinetic reactions were set up with the same alkyne and azide concentration (0.1 M) and 2 mol% CuBr/PMDETA (N,N,N',N'',N''-pentamethyldiethylenetriamine) catalyst loading (0.002 M) in DMF. The conversion of the reactions was monitored by ¹H NMR spectroscopy. The overlapped NMR spectra as a function of reaction time is shown in Figure 20. For the CuAAC reaction of PPMA, the conversion was determined by the integration value of the benzyl methylene signal on the benzyl azide (protons 1 in Figure 20) and the integration value of the methylene signal on the polymer products (protons 4 in Figure 20).

Scheme 17. CuAAC reaction of benzyl azide with ethynyl-2-methylpropanoate (EMP), poly(propargyl methacrylate) (PPMA), and poly(propargyl methacrylate)-*co*-poly(methyl methacrylate) (PPMA-*co*-PMMA).

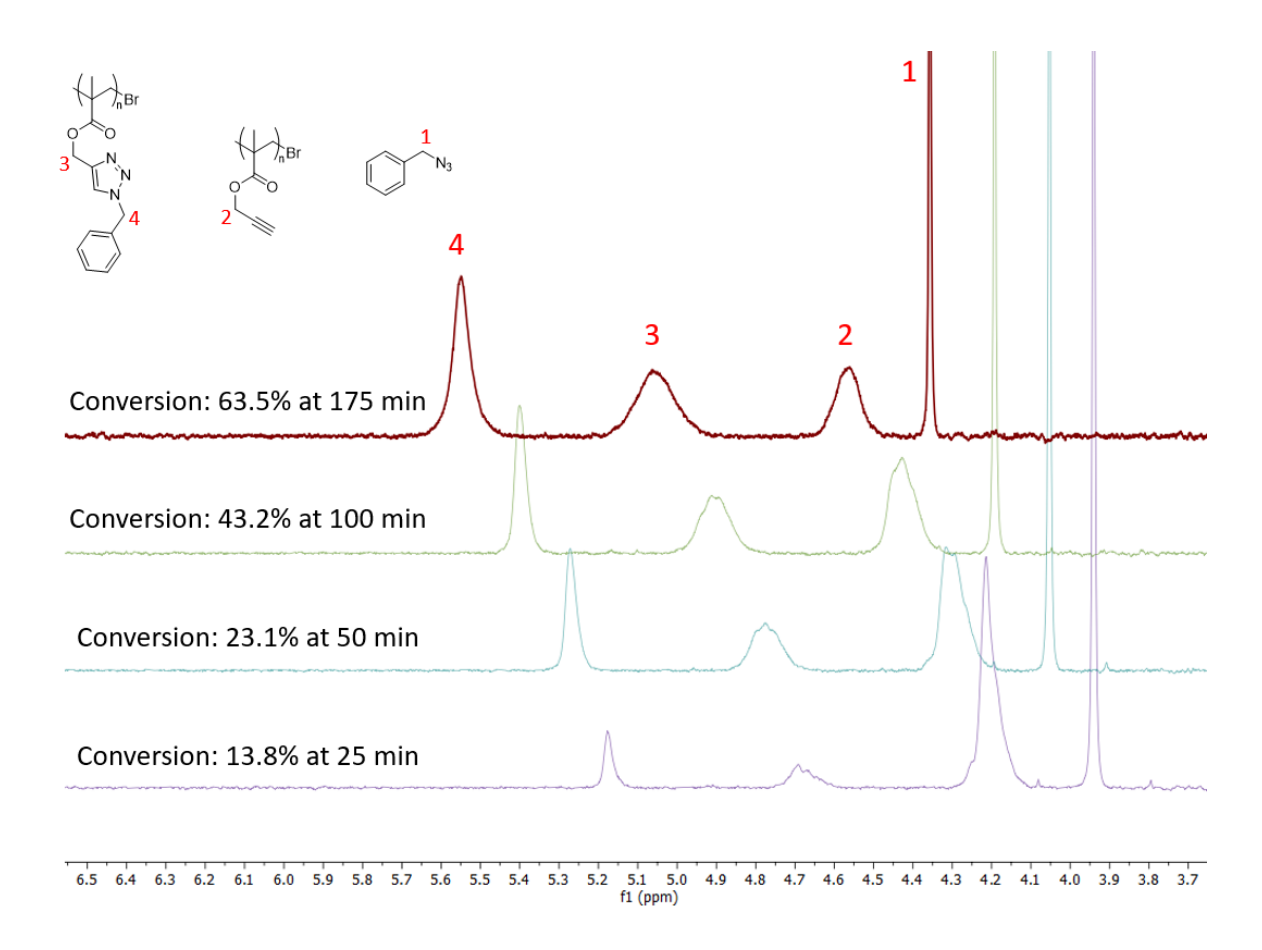


Figure 20. ¹H NMR spectra as a function of time for the CuAAC of PPMA-88.9 kDa and benzyl azide.

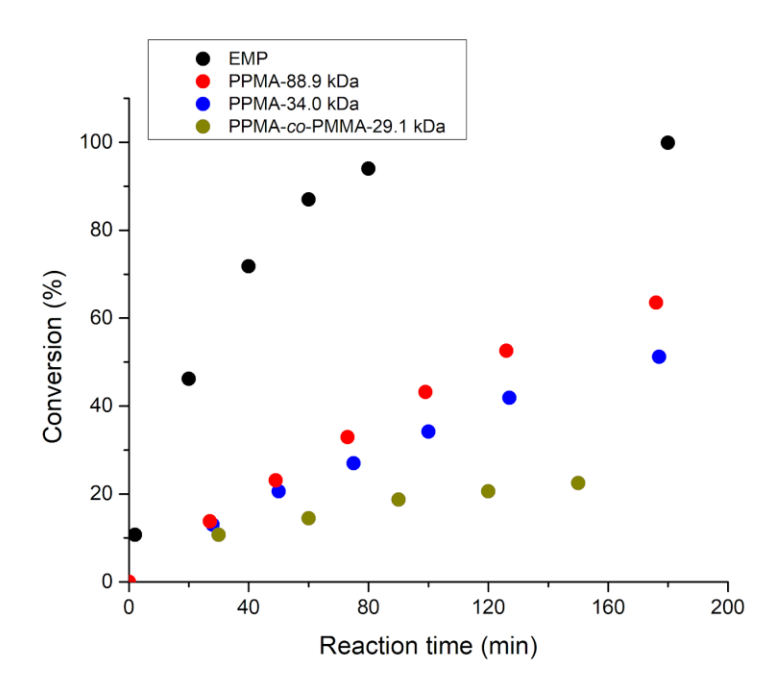


Figure 21. Conversion versus time plot for the CuAAC reaction of benzyl azide with EMP, PPMA-88.9 kDa (Mn = 88,900, PDI = 1.30), PPMA-34.0 kDa (Mn = 34,000, PDI = 1.12), and PPMA-co-PMMA-29.1 kDa { Mn = 29,100, PDI = 1.20, [PMMA]:[PPMA] = 10: 1 (mol%)}. Reaction progression was monitored by 1H NMR. ([alkyne] = 0.1 M, [azide] = 0.1 M, [Cu^IBr/PMDETA] = 2 mM, DMF, 25 °C).

Unlike Matyjaszewski's result of azido-containing polymer, poly(3-azidopropyl methacrylate), the CuAAC reaction rate of poly(propargyl methacrylate) (PPMA) (red and blue dots in Figure 21Figure 21) is roughly four times slower than the small molecule EMP (black dots in Figure 21Figure 21). We found the PPMA with higher M_n (PPMA-88.9 kDa) has similar reaction rate with benzyl azide as the lower molecular weight (PPMA-34.0 kDa).

We had two hypotheses for the slower reaction rates of PPMA-34.0 kDa and PPMA-88.9 kDa compared to the small molecule EMP. One hypothesis is that due to the steric hinderance from the neighboring chains, the alkyne groups on the PPMA are less accessible than those on the small molecules EMP. Another hypothesis is that multiple alkyne groups on the PPMA might coordinate to one copper catalyst and deactivate the

catalyst. To minimize the multiple alkyne group coordinate to the copper center, a copolymer, PPMA-co-PMMA, containing mole ratio of poly(methyl methacrylate) to poly(propargyl methacrylate) 10 to 1 was prepared by ARGET ATRP from the mixture of methyl methacrylate and trimethylsilylpropargyl methacrylate (TMSPMA) at the 10 to 1 mole ratio. The molecular weight of PTMSPMA-co-PMMA was 31.5 kDa and PDI = 1.17, characterized by GPC, and the ratio of PMMA to PTMSPMA segments was 10 to 1, determined by ¹H NMR. The PPMA-co-PMMA for CuAAC kinetic study was obtained by deprotecting the PTMSPMA-co-PMMA. The deprotection process did not vary the mole ratio of PMMA to PPMA segments on PPMA-co-PMMA (10 to 1), characterized by ¹H NMR spectroscopy, shown in Figure 22. The molecular weight of PPMA-co-PMMA is 29,100, characterized by GPC. With the smaller fraction of alkyne groups per polymer chain, PPMA-co-PMMA reduces the chance of copper catalyst deactivation by a multiple alkyne coordination from the same polymer chain. The CuAAC reaction of PPMA-co-PMMA was conducted under the same total alkyne concentration as the homopolymer PPMA experiment (dark green dots in Figure 21Figure 21). The reaction rate of PPMAco-PMMA is slower than the PPMA, indicating the deactivation of the catalyst by multiple alkyne coordination is not the main cause of the slower reaction rate. The CuAAC reaction of PPMA-co-PMMA only reached 25.4 % conversion even after prolonged reaction time (22 h). While the conversion of PPMA-34.0 kDa and benzyl azide was > 99% at 22 h. However, to keep the same initial alkyne concentration, 10 times higher polymer concentration of PPMA-co-PMMA than the homopolymer PPMA is required. The higher polymer concentration leads to more polymer chain entanglement and higher viscosity of the reaction mixture. 110 The slower CuAAC reaction rate was also observed in more

viscous reaction mixture by Döhler and coworkers. They cross-linked the three different poly(propargyl acrylate-co-n-butyl acrylate)s (PPA-co-PBAs) ($M_n = 9,600, 12,000, and 19,100$) with three-arm-star azido-telechelic poly(isobutylene) ($M_n = 6,200$) shown in Scheme 18. Gel time is determined by the reaction time that the shear storage moduli and the shear loss moduli cross. The shear storage modulus shows the elastic character of the material, and the shear loss modulus indicates the viscous response of the material. Under the same alkyne and azide concentration (0.245 M) and copper concentration, increasing gel time (from 213 min to 418 min) was observed on the reaction mixture with higher initial viscosity (from 60 Pa·s to 123 Pa·s). The longer gel time was reported as the molecular weight of PPA-co-PBA increased (from 9,600 to 19,100).

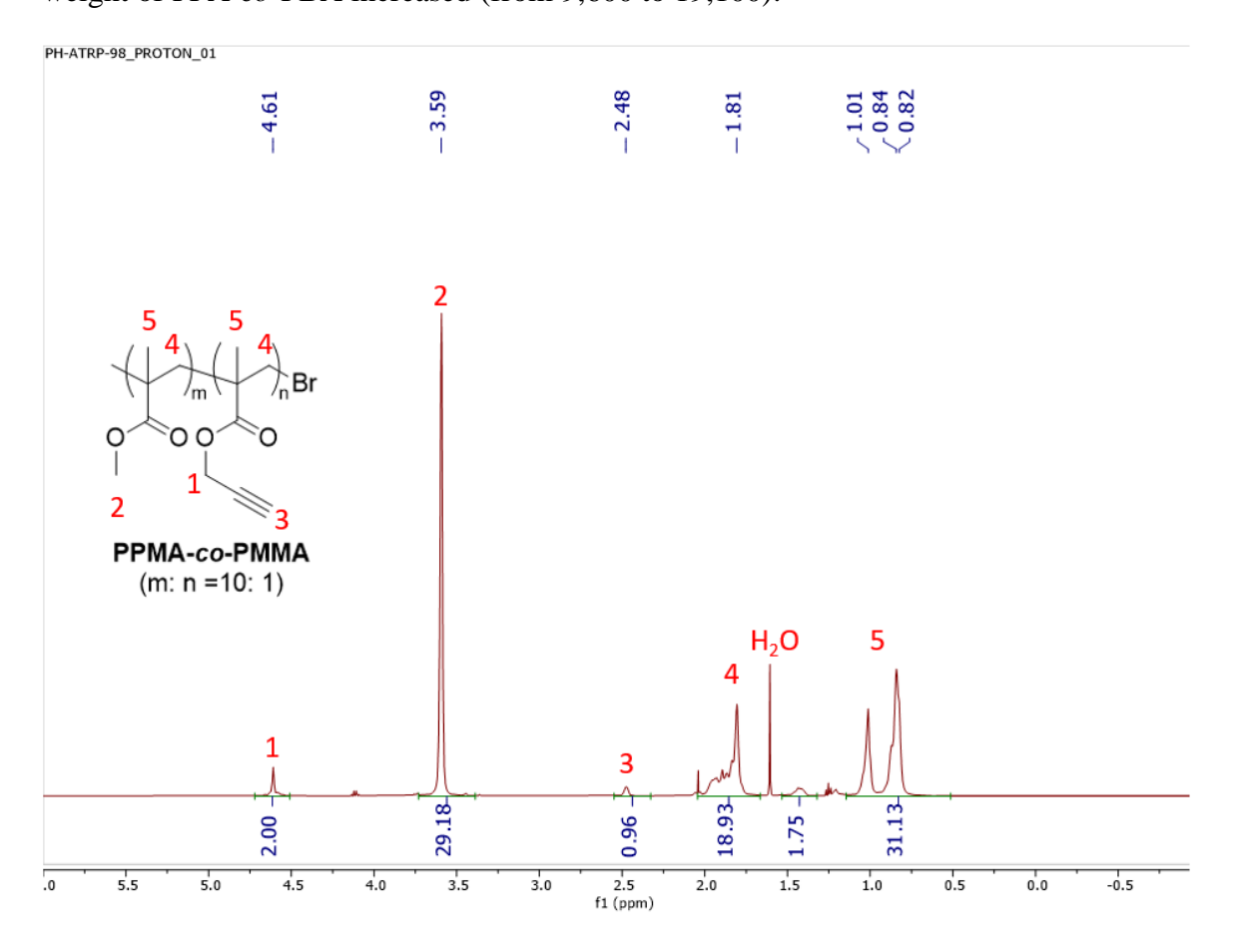
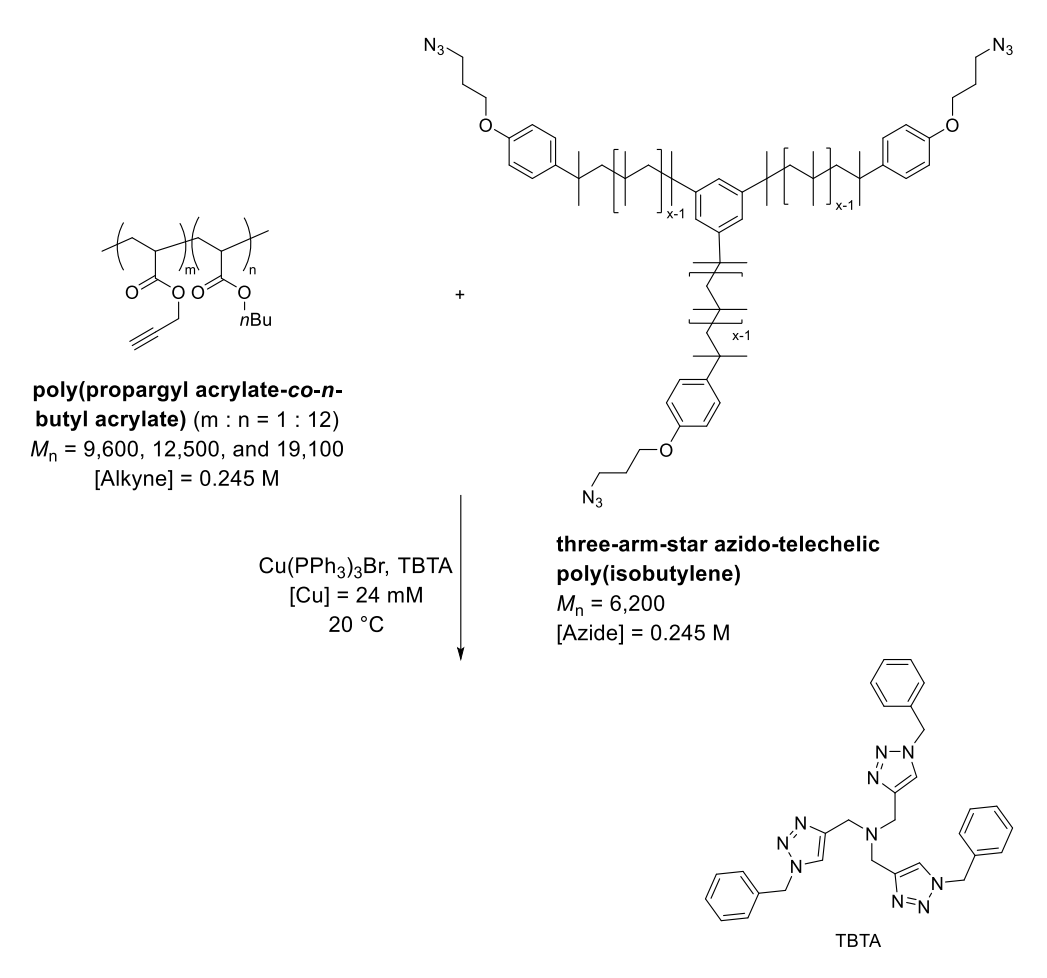


Figure 22. ¹H NMR spectrum of the PPMA-co-PMMA ([PPMA]: [PMMA] = 1: 10 (mol%)) in CDCl₃

Scheme 18. Reaction scheme of cross-linking three different poly(propargyl acrylate-co-n-butyl acrylate)s (PPA-co-PBAs) ($M_n = 9,600, 12,000, and 19,100$) with three-arm-star azido-telechelic poly(isobutylene) reported by Döhler.



To test the effect of the viscosity on CuAAC kinetics, the alkyne concentration was diluted 10 times and PPMA and PPMA-co-PMMA with [alkyne] = 0.01 M were conducted under 2 mol% Cu^IBr/PMDETA catalyst loading (0.2 mM). The CuAAC reaction of PPMA ([alkyne] = 0.01 M) and benzyl azide reached 24.5% conversion at 20 h, which was significantly slower than their higher alkyne concentration counterpart (0.1 M, > 99% conversion at 22 h). Under the same condition ([alkyne] = 0.01 M), no conversion was observed between PPMA-co-PMMA and benzyl azide at 20 h. To confirm that the PPMA-co-PMMA was unreacted, the product was purified and characterized by ¹H NMR

spectrum. The alkyne protons (proton c in Figure 24) were intact. If viscosity is the dominate factor that decrease the reaction rate of copolymer PPMA-*co*-PMMA, the diluted reaction should have faster rate. More data will be needed to address the impact of viscosity on the reaction rate.

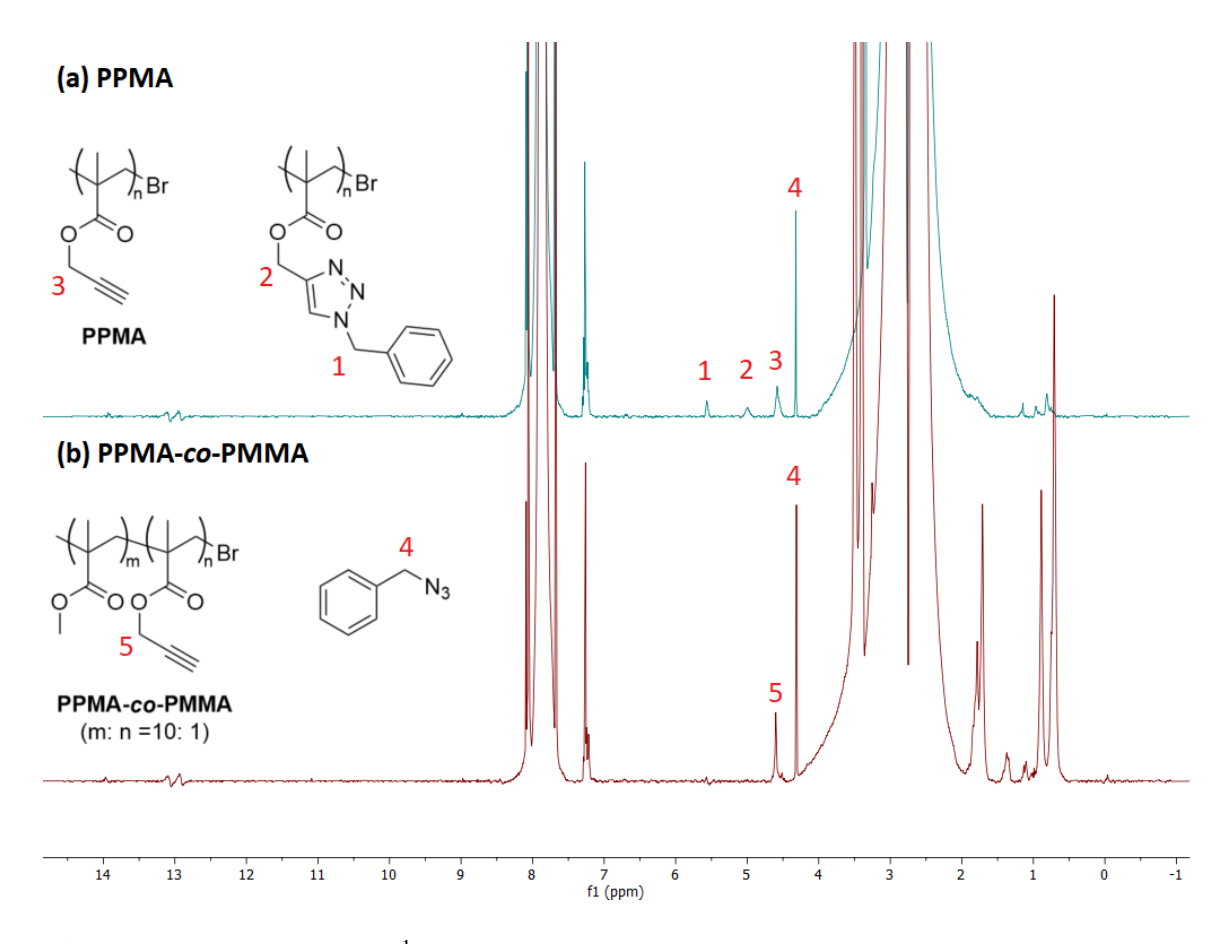


Figure 23. The overlapped ¹H NMR of crude material at 20 h (a) PPMA-34.0 kDa (M_n = 34,000, PDI = 1.12, top) and (b) PPMA-co-PMMA-29.1 kDa { M_n = 29,100, PDI = 1.20, [PMMA]:[PPMA] = 10: 1 (mol%), bottom}. ([alkyne] = 0.01 M, [azide] = 0.01 M, [Cu^IBr/PMDETA] = 0.2 mM, DMF, 25 °C)

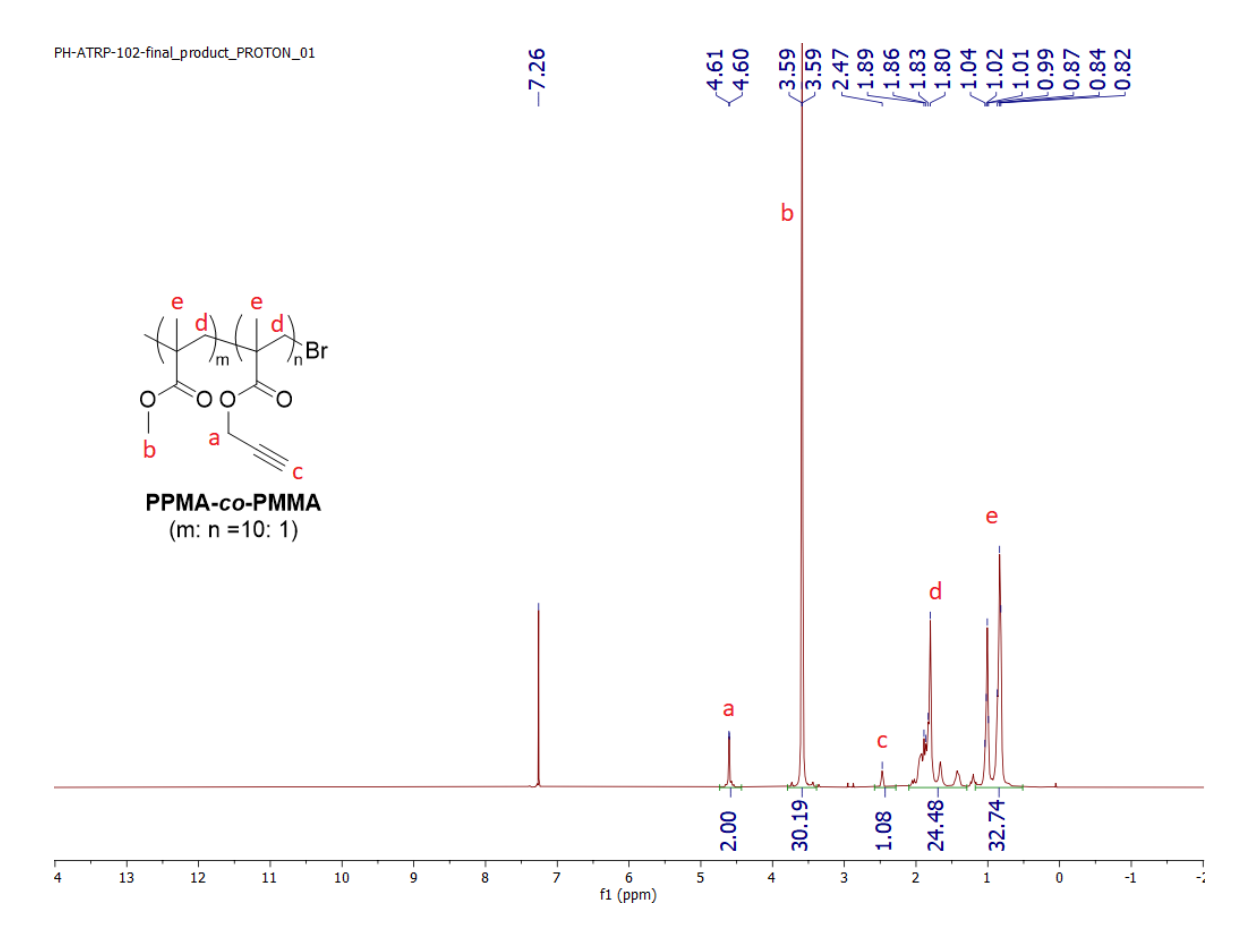


Figure 24. Recovered and purified PPMA-co-PMMA-29.1 kDa after 20 h reaction time under CuAAC condition ([alkyne] = 0.01 M, [azide] = 0.01 M, [Cu^IBr/PMDETA] = 0.2 mM, DMF, 25 °C).

The slower reaction rate observed on PPMA-co-PMMA than homopolymer PPMA indicates that the multiple alkyne coordination to the copper catalyst is unlikely the cause of slower reaction rate of PPMA than small molecule EMP. The slower reaction rate of homopolymer PPMA than small molecule EMP is probably due to the less accessibility of the alkyne on the polymer.

Several trends were observed on the CuAAC kinetic of the alkyne containing polymer PPMA. (1) Our kinetic results support the mechanistic study from Fokin and Finn that the CuAAC on the dialkyne is stepwise without the anchimeric assistance. (2) The

slower reaction rate of polymer PPMA than small molecule EMP is probably caused by the less accessibility of alkyne groups on PPMA.

Characterizing the hydrodynamic radius of amphiphilic polymers with different compositions

Micelles are formed when dissolving functionalized mDEG-PPMAs in water and dynamic light scattering (DLS) is used to characterize the hydrodynamic radius of the micelles. DLS measures the hydrodynamic radius of a particle in solution by monitoring its time-dependent fluctuation in scattering intensity due to Brownian motion. If the particle size is identical, at short time delays, the scattering correlation is high because the particles cannot travel very long distance. The scattering correlation will eventually decay to zero after longer delay time. In the same delay time, bigger particles move slower than smaller particles so that the scattering correlation of bigger particles are higher due to the shorter the distance they travel. Therefore, the dynamic light scattering can be used to predict the particle size by the Stokes-Einstein equation, shown in Eq 11Eq 11, which calculates the size of a particle based on its velocity due to Brownian motion, where D is the diffusion constant, $k_{\rm B}$ is Boltzmann's constant, T is the temperature, η is the viscosity of the solution and $R_{\rm H}$ is the hydrodynamic radius of particles.

$$D = \frac{k_B T}{6\pi \eta R_H}$$
 Eq 11

The comb-shape amphiphilic polymers, prepared by ATRP and CuAAC, contains hydrophilic and hydrophobic side chains attach to the polymer backbones. To determine the cmc, the hydrodynamic radius was plotted as a function of amphiphilic polymer concentration. The hydrodynamic radius of **100%mDEG-PPMA** was determined in

polymer concentration from 0.15 to 10 (mg/mL), which is equal to 1.7×10^{-6} to 1.1×10^{-4} M ($M_n = 90,200$) shown in Figure 25. The hydrodynamic radius remains 6 to 7 nm over two-order polymer concentration range with no drastic change of hydrodynamic radius indicating no cmc observed in this range. The higher concentration cannot be studied due to the limited solubility. The results shows that the size of the micelle is stable during dilution and can be an ideal nanocarrier at low concentration. The Scheme 19 illustrates the amphiphilic comb polymer self-assemble into unimolecular micelle with polar ends (red in Scheme 19) point toward the bulk water and form a hydrophobic micelle core. The covalently bonded polar and nonpolar side chains keep the unimolecular micelles stable even under low polymer concentration.

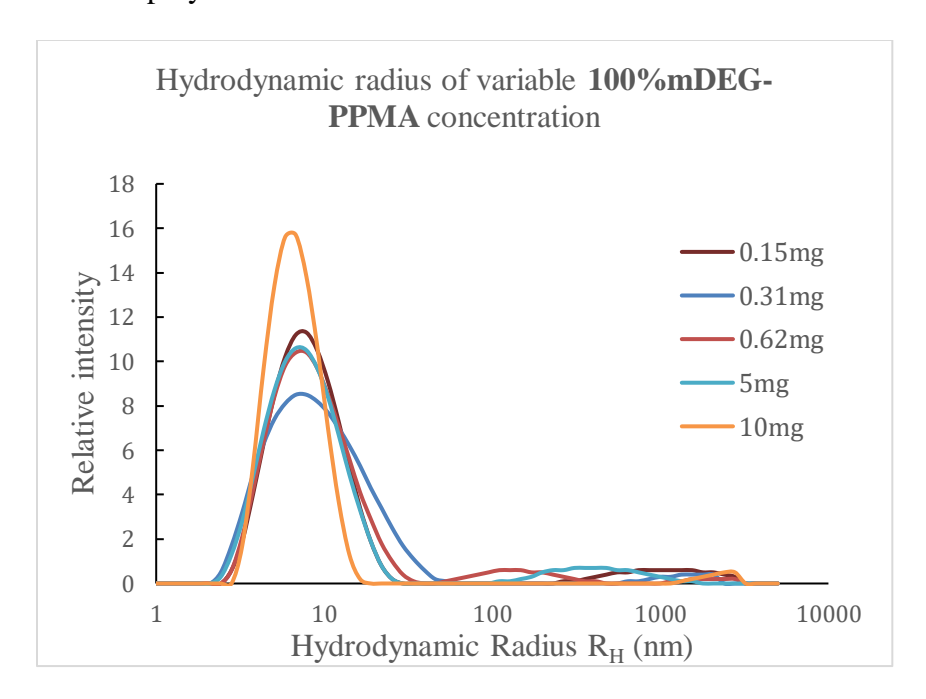
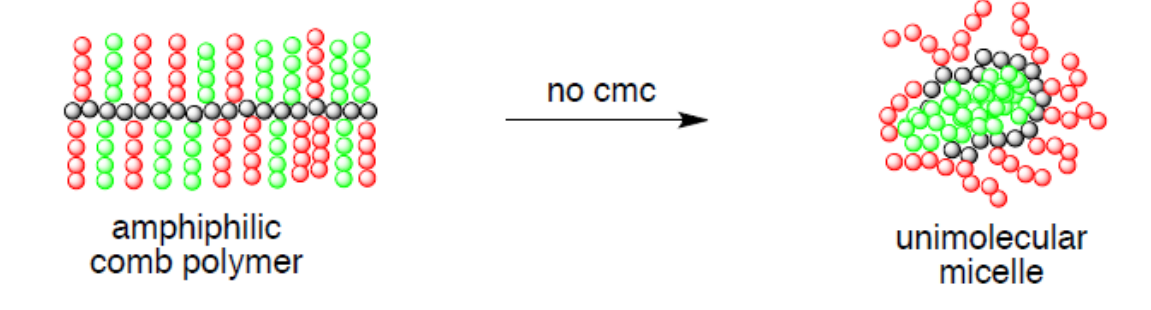


Figure 25. The hydrodynamic radius as a function of **100%mDEG-PPMA** concentration from 10 to 0.15 mg/mL in MilliQ water.

Scheme 19. Formation of unimolecular micelle by amphiphilic comb polymer.



The hydrodynamic radius of variable **82%mDEG-PPMA** concentration is between 5 to 8 nm from 0.15 to 10 (mg/mL), which equal to polymer concentration: 1.7×10^{-6} to 1.1×10^{-4} M ($M_n = 89,900$), shown in Figure 26. The **82%mDEG-PPMA** was observed to have a fraction of bigger aggregation (~170 nm) due to the loose aggregation or large association complexes. Micelles are stable and have similar size across the concentration range tested. The hydrodynamic radius of both **82%mDEG-PPMA** and **100%mDEG-PPMA** is independent to the polymer concentration (0.15 to 10 mg/mL), indicating the micelle formation did not involve multiple polymer chains in this concentration range.

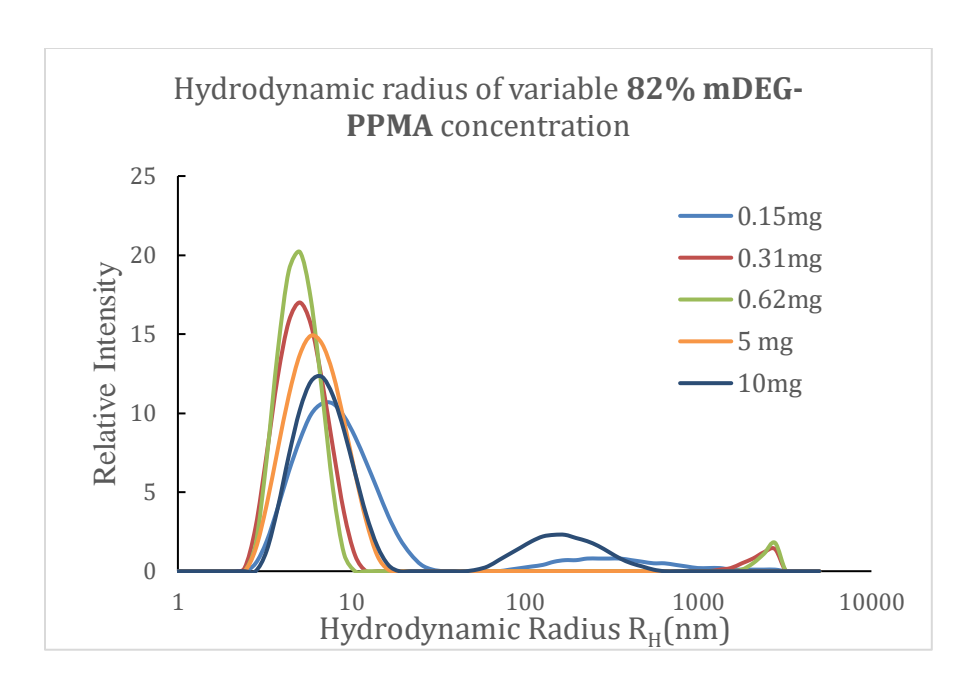


Figure 26. The hydrodynamic radius as a function of **82% mDEG-PPMA** concentration from 10 to 0.15 mg/mL in MilliQ water.

The hydrodynamic radius behavior of 71% mDEG-PPMA at variable concentration is different from the more hydrophilic 82% mDEG-PPMA and 100% mDEG-PPMA. With the higher hydrophobic composition (dodecyl side chain), the bimodal particle size was observed as 11 and 82 nm indicating the stronger hydrophobic interaction between chains. The size of the micelle grows as the increasing polymer concentration. Smaller concentration interval was tested due to the intriguing finding. Starting from polymer concentration at 1.25 mg/mL, the equilibrium shifted to polymer aggregate side and the size of the aggregate changed from 61 nm at 1.25 mg/mL to 95 nm at 10 mg/mL. Based on the variable concentration DLS results, the cmc of 71% mDEG-PPMA is between 0.62 and 1.25 mg/mL. Amphiphilic comb shaped polymers with similar side chain structures were reported and the cmc decreases with higher hydrophobic composition along the polymer backbone. The 82% mDEG-PPMA and 100% mDEG-PPMA may have higher cmc than the tested range.

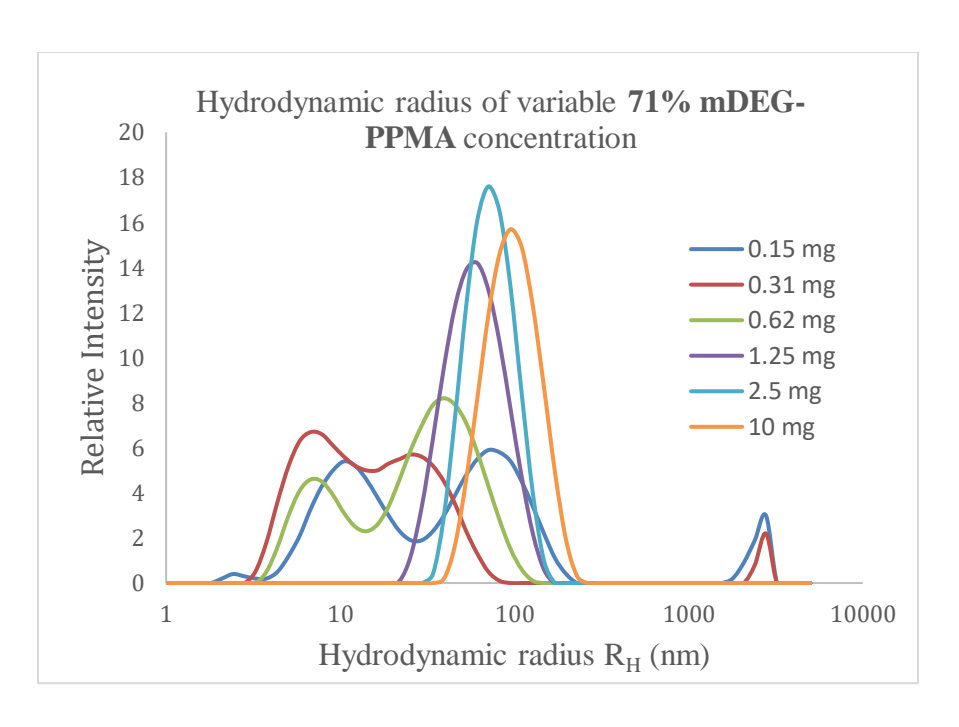


Figure 27. The hydrodynamic radius as a function of **71% mDEG-PPMA** concentration (mg/mL) in MilliQ water.

Lower critical solution temperature

Thermoresponsive polymer materials have coil-globule transition under external temperature changes. These polymers have gained attention for their potential in biomedical applications. 112,113,114 Based on the behavior, the thermo-responsive material can be categorized into two types: material with lower critical solution temperature (LCST) and material with upper critical solution temperature (UCST). 113,115 For the polymer material with LCST, the transition temperature of the polymer solution varies with polymer concentration and polymer molecular weight. The phase diagram is then plotted with the transition temperature versus the polymer volume fraction. The lowest transition temperature on the phase diagram is defined as LCST, shown in Figure 28.

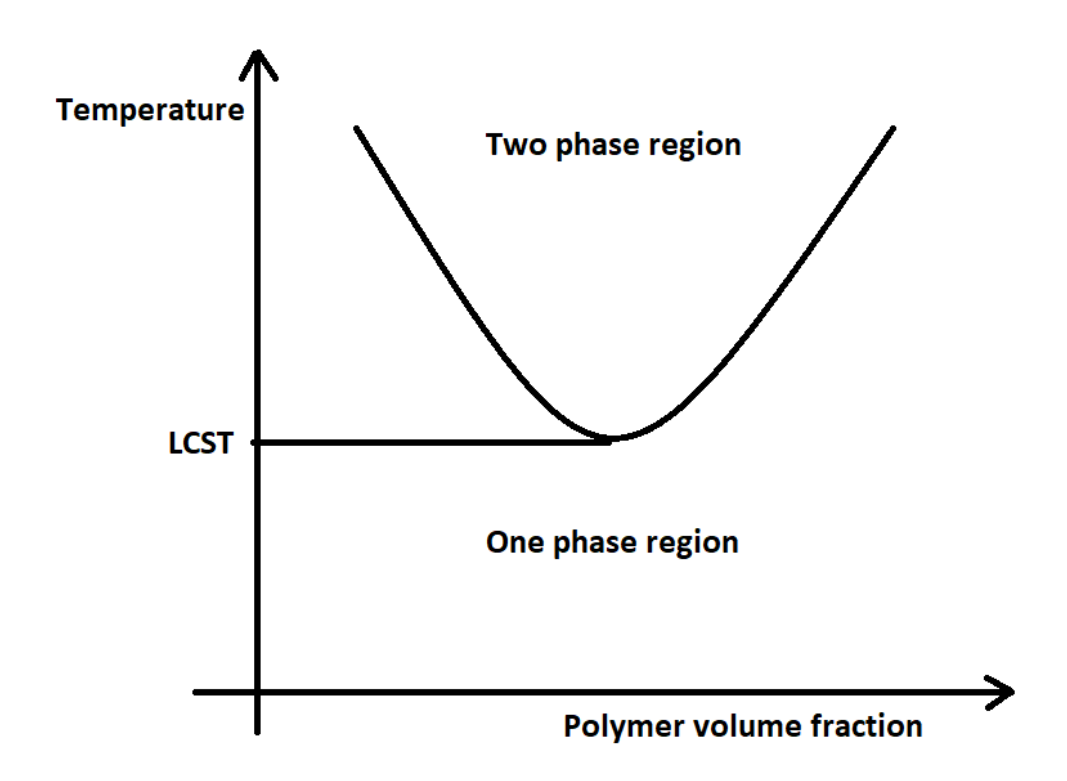


Figure 28. Schematic phase diagram of a polymer with LCST behavior.

The solubility of the polymer with LCST decreases when temperature increases and becomes insoluble above LCST. The solution behavior of Poly(*N*-isopropylacrylamide) (PNIPAM) was first studied by Heskins and Guillet. PNIPAM is the most studied thermo-responsive material for bio applications due to its biocompatibility and the transition temperature (31 °C) that is close to physiological temperature (37 °C). UCST is defined as the highest temperature that the polymer solution can exist as single phase. The solubility of polymer with UCST decreases at lower temperature and becomes insoluble below certain temperature called the upper critical solution temperature (UCST). Polymers that have UCST behavior are poly(acrylic acid) (PAA), polyacrylamide (PAAm), and poly(acrylamide-co-butyl methacrylate).

For a thermodynamically spontaneous process, a negative Gibbs free energy change at the condition is needed. For the polymers with LCST behavior, the polymers

dissolved in aqueous media below LCST. The water molecules interact with the hydrophilic functional groups on the polymer chains and lead to the relatively ordered water molecules around polymer chains than the water molecules in the bulk solution. While increasing the solution temperature, the interactions between water molecules and polymer chains become entropically unfavorable and are not thermodynamically feasible. At the phase transition temperature, polymer chains expel the associated water driven by entropy gain and lead to the precipitation of the polymer and a two-phase solution. One common way to measure the transition temperature or commonly referred as cloud point is to monitor the turbidity using a variable temperature UV-Vis spectroscopy. When the temperature is near the transition temperature, the formation of polymer aggregates blocks the incoming light, and this the transition can be observed by the sharply increasing. The cloud point is assigned to the inflection point on the absorption versus temperature curve. The cloud points of PPMAs (containing different mole% of mDEG chains were determined by plotting the absorbance at 450 nm versus the temperature, shown in Figure 29Figure 29.

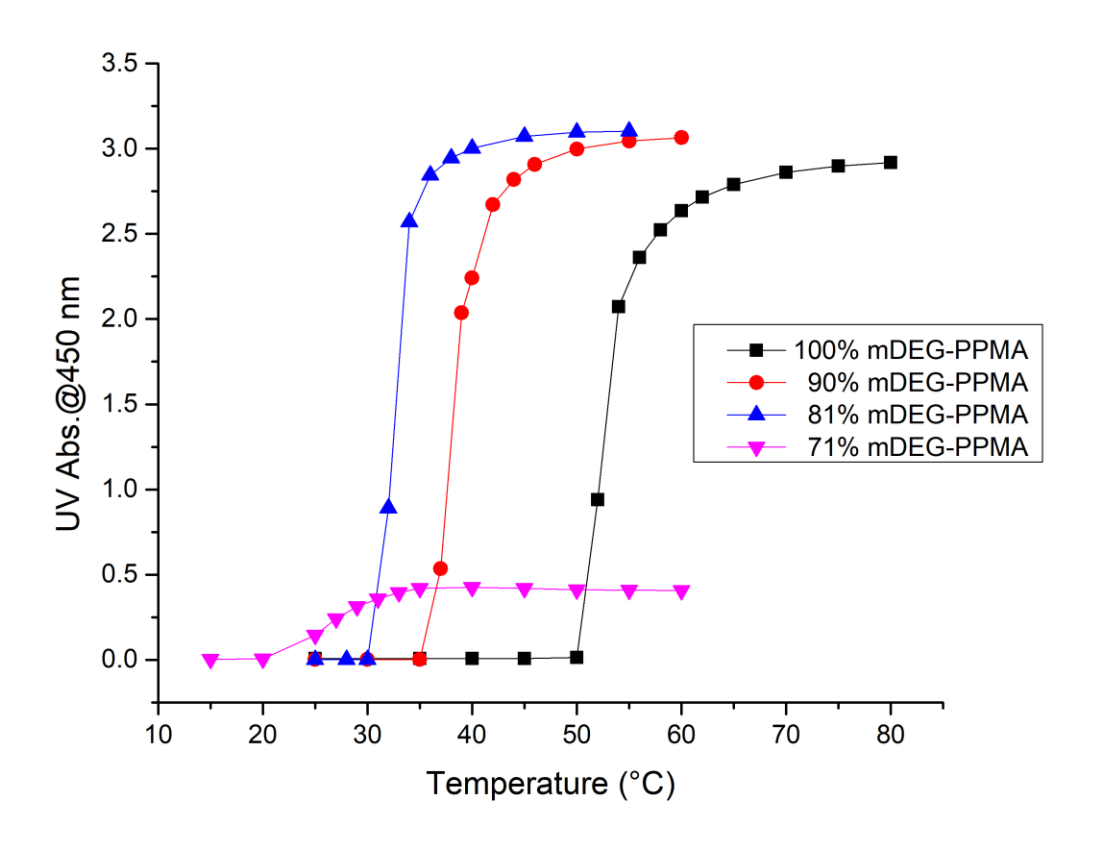


Figure 29. Cloud point determination by variable temperature-UV/Vis spectroscopy. The turbidity was determined by absorbance at 450 nm and all the polymer concentration is 3 mg/mL in MilliQ water. All the polymers have $M_n \sim 90 \text{ kg/mol}$.

The **x% mDEG-PPMAs** were prepared from the same polymer precursor and have the same degree of polymerization (DP = 288). At room temperature, the PPMAs with more than 70% mole fraction of mDEG are soluble in water. Figure 30Figure 30 shows a linear correlation between cloud point of the **x% mDEG-PPMAs** and the mole fraction of hydrophilic mDEG chain along PPMA side chains. This result also indicates the cloud point of **x% mDEG-PPMAs** can be tailored for different applications. CuAAC functionalized poly(glycidyl ether) **PPGE** and **PMGE** were prepared by former group member Dr. Lien using the same hydrophilic (mDEG) and hydrophobic side chains. ¹¹⁷ The

comparison of x% mDEG-PPMA, x% mDEG-PPGE, and x% mDEG-PMGE is shown in Figure 30Figure 30. The cloud points increase for all polymer backbones when enriching the mDEG mole% fraction along the polymer chains. The slope for PPMA backbone is 0.90, slightly greater than the slope for PMGE (0.74), indicating that the PPMA backbone has slightly more influence on the cloud point than the PMGE counterpart. Although the slope of PPGE cannot be obtained due to the poor linearity, PPGE backbone has the widest range of cloud point among the three polymer backbones: from 48 to 96 °C. Another finding is that the hydrophilic PPGE backbone also has higher cloud point than the hydrophobic PPMA backbone at the same side chain structure and similar composition. The cloud point of 80% mDEG-PPGE is 59 °C while the one for 82% mDEG-PPMA is 33 °C.

The cloud point results for PPMA backbone are in good agreement with the previous research on PPGE and PMGE backbones. The results also reveal the impact of the side chain composition and backbone structure on cloud point values. Thermoresponsive material with a specific targeted cloud point can be tailor by choosing proper polymer backbone and manipulating the side chain composition.

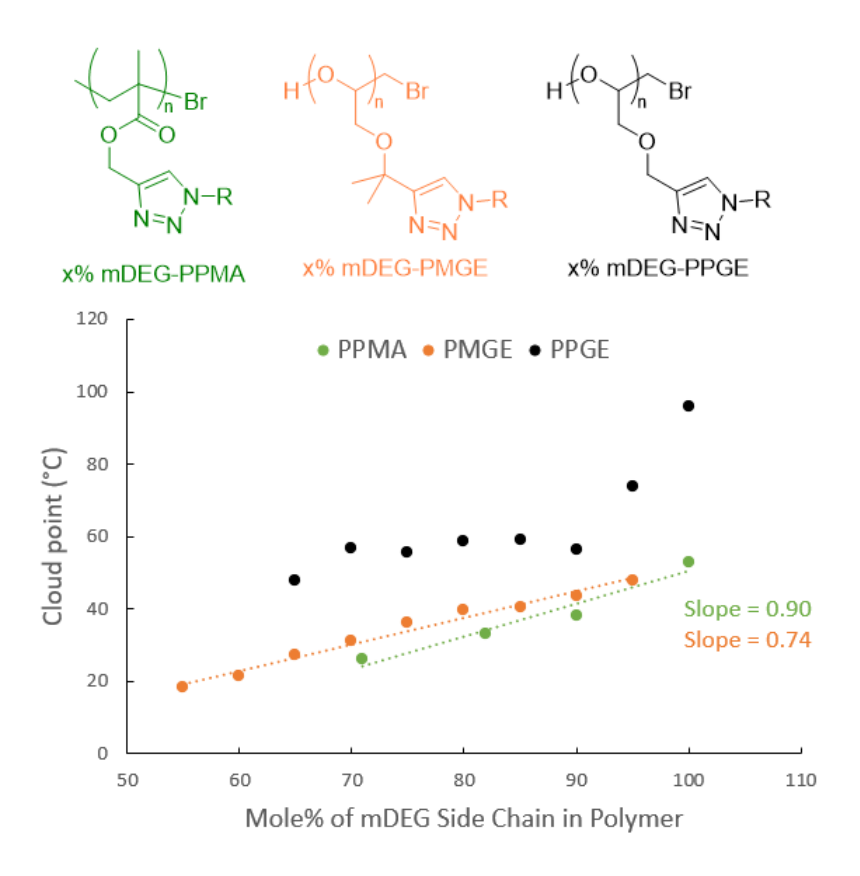


Figure 30. Cloud points versus different mole% of mDEG side chain along different polymer backbones: PPMA (green), PMGE (orange), and PPGE (black). 117

Conclusion

The alkyne-containing polymer backbone PPMAs was observed to have roughly four times slower coupling reaction rate toward benzyl azide than the small molecule counterpart, EMP. Unlike the azide-containing polymer backbone kinetic result from Matyjaszewski group, no anchimeric effect was observed during CuAAC of alkyne-containing polymer PPMA and benzyl azide and the result agreed with the CuAAC mechanism. The slower reaction rate of PPMA may be caused by the less accessibility of alkyne groups on the polymer chains than the alkyne groups on the molecules.

CuAAC can simply modify the PPMA to comb shaped graft copolymers with different ratio of hydrophilic and hydrophobic side chains by simply tuning the ratio of the hydrophilic and hydrophobic azides. The CuAAC functionalized graft copolymers (x% mDEG-PPMA) were found to have cloud points from 26 to 53 °C. The cloud point value of the polymer materials can be adjusted by the mol% of the hydrophilic mDEG chains along PPMA. The backbone structure also affects the cloud point of the thermo-responsive behavior. The more hydrophilic backbone PPGE was found to have higher cloud point than PPMA under the same side chain structure and similar side chain composition. For 82% mDEG-PPMA and 100% mDEG-PPMA, no cmc was observed and the hydrodynamic radius of graft copolymers were similar (5-8 nm) at polymer concentration between 0.15 to 10 mg/mL. The cmc of 71% mDEG-PPMA is between 0.62 and 1.25 mg/mL, which was observed by the shift of the hydrodynamic radius on DLS.

Experimental section

Characterization

The molecular weights of polymers were determined by gel permeation chromatography (GPC) at 35 °C using two PLgel 10μ mixed-B columns in series (manufacturer stated linear molecular weight range of 500-10,000,000 g/mol) with THF as the eluent solvent at a flow rate of 1 mL/min. Optilab rEX (Wyatt Technology Co.) differential refractive index (dRI) detector was used as detector. The columns were calibrated by narrow poly(methyl methacrylate) standards ($M_n = 6$, 12, 30, 60, 127, 350 kg/mol). The GPC samples were prepared by dissolving 1-4 mg of polymer in 1 mL of THF and all GPC samples were filtered through a 0.2 μ m Whatman PTFE syringe filter before injecting into GPC.

Dynamic light scattering (DLS) data were obtained using a Malvern Zetasizer Nano ZS. All samples were filtered through a $0.2~\mu m$ Whatman PTFE syringe filter and then equilibrated in the instrument for 2 minutes at each temperature before taking the data used to calculate the hydrodynamic radius (Rh). The particle size uniformity was determined by a monomodal curve fit, which assumes a single particle size with a gaussian distribution. LCST determination was done by variable temperature UV-vis spectra were recorded with a Shimadzu UV-2600 UV-Vis spectrometer equipped with temperature regulator. The polymer sample was allowed to equilibrate in the instrument for 5 minutes before acquisition.

Synthesis of 1-(2-azidoethoxy)-2-(2-methoxyethoxy)ethane (mDEG-N₃)^{117,118}

TEG azide was synthesized in two steps. Triethylene glycol monomethyl ether (4 g, 24.3 mmol) in THF (12 mL) was added dropwise to a solution of sodium hydroxide (3

g, 75 mmol) in a water/THF mixture (6:4 v/v, 40 mL) at 0 °C. The mixture was stirred at 0 °C for 30 min and then a solution of 4-toluenesulfonyl chloride (6.86 g, 40.0 mmol) of THF (20 mL) was added dropwise. The mixture was stirred at 0 °C for another 30 min and then brought to room temperature for another 6 h. The reaction progress can be monitored by the ¹H NMR signal of the methylene group next to the tosyl group (product) and the signal of the methylene group next to the hydroxyl group (reactant). The crude mixture was poured into 30 mL of ice water. The water layer was extracted with diethyl ether (3×100 mL). The combined organic layers were washed with brine and dried over MgSO₄. Diethyl ether was evaporated, and the tosyl mDEG product was used without further purification (6.57 g, 86% yield).

Tosyl mDEG (6.57 g,) and sodium azide (6.70 g, 103 mmol) were dissolved in a water/acetone mixture (1:3 v/v, 40 mL) and the solution was heated to reflux and stirred overnight. The crude mixture was extracted with diethyl ether (4×50 mL). The combined organic layers were washed with brine and DI water and dried over MgSO₄. Diethyl ether was evaporated under vacuum to obtain mDEG azide (3.54 g, 91.3 % yield) as colorless liquid. ¹H NMR (500 MHz, CDCl₃, 298 K) δ 3.76 – 3.60 (m, 8H), 3.60 – 3.50 (m, 2H), 3.44 – 3.31 (m, 5H). ¹³C{¹H} NMR (125 MHz, CDCl₃, 298 K) δ 71.9, 70.6, 70.6, 70.6, 70.0, 59.0, 50.6.

Synthesis of decyl azide $(C10-N_3)^{118}$

Decyl bromide (6.6 g, 29.8 mmol) was added dropwise to a solution of sodium azide (3 g, 46.1 mmol) in a water/acetone mixture (1:3 v/v, 40 mL) at 0 °C. Then the solution was heated to reflux and stirred overnight. The crude mixture was extracted with petroleum ether (4×50 mL). The combined organic layers were washed with brine and DI

water and dried over MgSO₄. Petroleum ether was evaporated under vacuum to obtain decyl azide (5.067 g, 92.1 % yield) as a colorless liquid. 1 H NMR (500 MHz, CDCl₃, 298 K) δ 3.3 (t, J = 7.0 Hz, 2H), 1.6 (p, J = 7.0 Hz, 2H), 1.4 – 1.2 (m, 14H), 0.9 (t, J = 6.9 Hz, 3H). 13 C{ 1 H} NMR (125 MHz, CDCl₃, 298 K) δ 51.5, 31.9, 29.5, 29.5, 29.3, 29.2, 28.8, 26.7, 22.7, 14.1

Synthesis of 100%mDEG-PPMA¹¹⁷

PPMA (317 mg, 2.55 mmol of alkyne), DMF (7 mL), mDEG-N₃ (1.39 g, 7.34 mmol), and sodium ascorbate (58.3 mg, 0.29 mmol) were added respectively into a Schlenk flask and degassed by three freeze-pump-thaw cycles. After the mixture was thawed, 0.1 M of CuSO₄·5H₂O deoxygenated solution in DMF (1.2 mL, 0.12 mmol) was added and the reaction was stirred at room temperature for 12 h. The crude product was passed through an alumina plug using DCM as eluent to remove sodium ascorbate and copper catalyst. Ion exchange resin beads (Amberlite® IRC-748 ion exchange resin) was stirred with the filtrate for 12 h to further remove residual copper catalyst. The ion exchange resin was filtered out and the excess DCM in the filtrate was remove by rotary evaporator. The residual azides were removed by dialysis (MWCO = 6-8 kDa) in acetone for 24 h and the polymer solution was dried under high vacuum until constant weight. Viscous liquid (682 mg, 86%) was obtained as product. ¹H NMR (500 MHz, CDCl₃) δ 8.04 – 7.85 (m, 1H), 5.08 (br, 2H), 4.61 (br, 2H), 3.92 (br, 2H), 3.68 – 3.50 (m, 8H), 3.36 (s, 3H), 1.94 – 1.58 (m, 2H), 0.87 – 0.46 (m, 3H).

Synthesis of 90%mDEG-PPMA¹¹⁷

PPMA (310 mg, 2.50 mmol of alkyne), DMF (7 mL), mDEG-N $_3$ (1.25 g, 6.60 mmol), C10-N $_3$ (142 mg, 0.77 mmol), and sodium ascorbate (60 mg, 0.30 mmol) were

added respectively into a Schlenk flask and degassed by three freeze-pump-thaw cycles. After the mixture was thawed, 0.1 M of CuSO₄·5H₂O deoxygenated solution in DMF (1.2 mL, 0.12 mmol) was added and the reaction was stirred at room temperature for 12 h. The crude product was passed through an alumina plug using DCM as eluent to remove sodium ascorbate and copper catalyst. Ion exchange resin beads (Amberlite® IRC-748 ion exchange resin) was stirred with the filtrate for 12 h to further remove residual copper catalyst. The ion exchange resin was filtered out and the excess DCM in the filtrate was remove by rotary evaporator. The residual azides were removed by dialysis (MWCO = 6-8 kDa) in acetone for 24 h and the polymer solution was dried under high vacuum until constant weight. Viscous liquid (467 mg, 60%) was obtained as product. ¹H NMR (500 MHz, CDCl₃) δ 8.02 – 7.86 (m, 1H), 5.08 (br, 2H), 4.61 (br, 1.76H, methylene signal on 90 mol% mDEG side chain), 4.41 (br. 0.2H, methylene signal on polymer backbone and 10 mol% C10 side chain), 3.91 (s, 2H), 3.69 – 3.47 (m, 7H), 3.36 (s, 3H), 2.04 – 1.18 (m, 4H, containing methylene signal from C10 side chain), 0.92 – 0.43 (m, 3H, methyl signal on polymer backbone and 10 mol% C10 side chain).

Synthesis of 80%mDEG-PPMA¹¹⁷

PPMA (311 mg, 2.51 mmol of alkyne), DMF (7 mL), mDEG-N₃ (1.10 g, 5.83 mmol), C10-N₃ (267 mg, 1.46 mmol), and sodium ascorbate (59 mg, 0.30 mmol) were added respectively into a Schlenk flask and degassed by three freeze-pump-thaw cycles. After the mixture was thawed, 0.1 M of CuSO₄· 5H₂O deoxygenated solution in DMF (1.2 mL, 0.12 mmol) was added and the reaction was stirred at room temperature for 12 h. The crude product was passed through an alumina plug using DCM as eluent to remove sodium

ascorbate and copper catalyst. Ion exchange resin beads (Amberlite® IRC-748 ion exchange resin) was stirred with the filtrate for 12 h to further remove residual copper catalyst. The ion exchange resin was filtered out and the excess DCM in the filtrate was remove by rotary evaporator. The residual azides were removed by dialysis (MWCO = 6-8 kDa) in acetone for 24 h and the polymer solution was dried under high vacuum until constant weight. Viscous liquid (478 mg, 61%) was obtained as product. ¹H NMR (500 MHz, CDCl₃) δ 8.06 – 7.84 (m, 1H), 5.08 (br, 2H), 4.61 (br, 1.52H, methylene signal on 80 mol% mDEG side chain), 4.42 (br, 0.36H, methylene signal on 20 mol% C10 side chain), 3.92 (br, 1.52H, methylene signal on 80 mol% mDEG side chain), 3.72 – 3.47 (m, 6.38 H, methylene signal on 80 mol% mDEG side chain), 3.36 (s, 2.2H, methyl signal on 80 mol% mDEG side chain), 2.04 – 1.12 (m, 4.86H, methylene signal on polymer backbone and 20 mol% C10 side chain), 0.96 – 0.45 (m, 3.16H, methyl signal on polymer backbone and 20 mol% C10 side chain).

Synthesis of 70%mDEG-PPMA¹¹⁷

PPMA (309 mg, 2.49 mmol of alkyne), DMF (7 mL), mDEG-N₃ (977 mg, 5.16 mmol), C10-N₃ (401 mg, 2.19 mmol), and sodium ascorbate (59 mg, 0.30 mmol) were added respectively into a Schlenk flask and degassed by three freeze-pump-thaw cycles. After the mixture was thawed, 0.1 M of CuSO₄·5H₂O deoxygenated solution in DMF (1.2 mL, 0.12 mmol) was added and the reaction was stirred at room temperature for 12 h. The crude product was passed through an alumina plug using DCM as eluent to remove sodium ascorbate and copper catalyst. Ion exchange resin beads (Amberlite® IRC-748 ion exchange resin) was stirred with the filtrate for 12 h to further remove residual copper

catalyst. The ion exchange resin was filtered out and the excess DCM in the filtrate was remove by rotary evaporator. The residual azides were removed by dialysis (MWCO = 6-8 kDa) in acetone for 24 h and the polymer solution was dried under high vacuum until constant weight. Viscous liquid (516 mg, 66%) was obtained as product. ¹H NMR (500 MHz, CDCl₃) δ 8.09 – 7.79 (m, 1H), 5.08 (br, 2H), 4.61 (br, 1.36H, methylene signal on 70 mol% mDEG side chain), 4.42 (br, 0.59H, methylene signal on 30 mol% C10 side chain), 3.92 (s, 1.35H, methylene signal on 70 mol% mDEG side chain), 3.76 – 3.45 (m, 5.67H, methylene signal on 70 mol% mDEG side chain), 3.36 (s, 2H), 2.01 – 1.14 (m, 6.6H, methylene signal on polymer backbone and 30 mol% C10 side chain).

Synthesis of 60%mDEG-PPMA¹¹⁷

PPMA (214 mg, 1.61 mmol of alkyne), DMF (5 mL), mDEG-N₃ (565 mg, 2.98 mmol), C10-N₃ (358 mg, 1.95 mmol), and sodium ascorbate (39 mg, 0.2 mmol) were added respectively into a Schlenk flask and degassed by three freeze-pump-thaw cycles. After the mixture was thawed, 0.1 M of CuSO₄·5H₂O deoxygenated solution in DMF (0.81 mL, 0.08 mmol) was added and the reaction was stirred at room temperature for 12 h. The crude product was passed through an alumina plug using DCM as eluent to remove sodium ascorbate and copper catalyst. Ion exchange resin beads (Amberlite® IRC-748 ion exchange resin) was stirred with the filtrate for 12 h to further remove residual copper catalyst. The ion exchange resin was filtered out and the excess DCM in the filtrate was remove by rotary evaporator. The residual azides were removed by dialysis (MWCO = 6-8 kDa) in acetone for 24 h and the polymer solution was dried under high vacuum until

constant weight. Viscous liquid (317 mg, 62%) was obtained as product. 1 H NMR (500 MHz, CDCl₃) δ 8.07 – 7.82 (m, 1H), 5.08 (br, 2H), 4.61 (br, 1.13H, methylene signal on 60 mol% mDEG side chain), 4.42 (s, 0.74H, methylene signal on 40 mol% C10 side chain), 3.92 (s, 1.18H, methylene signal on 60 mol% mDEG side chain), 3.70 – 3.49 (m, 4.78H, methylene signal on 60 mol% mDEG side chain), 3.36 (s, 1.67H, methyl signal on 60 mol% mDEG side chain), 2.02 – 1.14 (m, 7H, methylene signal on polymer backbone and 30 mol% C10 side chain), 0.96 – 0.53 (m, 3.74H, methyl signal on polymer backbone and 30 mol% C10 side chain).

Synthesis of ethynyl 2-methylpropanoate (EMP)¹¹⁹

A solution of propargyl alcohol (20 mL, 0.29 mol) and triethylamine (20 mL, 0.36 mol) in dry DCM (100mL) was cooled to 0 °C and a solution of isobutyryl chloride (30 mL, 0.29 mol) in dry DCM (100 mL) was added dropwise over 1 h. The mixture was then stirred at room temperature overnight. The triethylammonium chloride was filtered out from the crude product. Ammonium chloride was further removed by precipitation by the addition of diethyl ether and filtration. The filtrate was washed with 1M HCl solution and brine. The organic layer was dried over sodium sulfate and concentrated using rotary evaporator. The product was then passed through a silica plug using HEX/ether = 25: 1 as eluent. The excess solvents were removed by rotary evaporator. The product is a volatile liquid that easily evaporates by rotary evaporator. A pale-yellow oil was obtained (15.49 g, 42.4 %). 1 H NMR (500 MHz, CDCl₃, 298 K) δ 4.67 (d, J = 2.5 Hz, 2H), 2.59 (p, J = 7.0 Hz, 1H), 2.46 (t, J = 2.5 Hz, 1H), 1.18 (d, J = 7.0 Hz, 6H).

General Procedure for deprotecting PTMSPMA99

The deprotection of the trimethylsilyl protecting group was carried out by the procedure reported by Yhaya and co-workers.⁹⁹ The trimethylsilyl protected polymer and acetic acid (2.0 equiv vs the alkyne trimethylsilyl groups) were dissolved in THF (10 mL). Nitrogen was purged through the solution over 20 min, before cooling it to 0 °C. A 1 M solution of tetrabutylammonium fluoride trihydrate (TBAF-3H₂O) in THF (2.0 equiv vs the alkyne trimethylsilyl groups) was added slowly via syringe over 2–3 min. The resulting turbid mixture was stirred at 0 °C for 30 min and then brought to room temperature. The deprotection was monitored by ¹H NMR. The disappearance of the silane signal at 0.2 ppm and the appearance of the alkyne proton signal at 2.5 ppm indicate the completion of deprotection, and the excess volatile liquid was removed by rotary evaporation. The resulting viscous solution was then precipitated in methanol several times to remove excess TBAF and the residual silane. Following precipitation, the excess methanol was decanted out and the amorphous polymer solid was dried overnight under vacuum. ¹H NMR (500 MHz, CDCl₃, 298 K) δ 4.71 – 4.51 (m, 2H), 2.52 (s, 1H), 2.14 – 1.57 (m, 2H), 1.34 – 0.78 (m, 3H).

Synthesis of PMMA-co-PPMA (10: 1 mol ratio)

Preparation of 0.043 M EBPA in MMA/TMSPMA mixture (10: 1 mol ratio)

EBPA (93 μL, 0.53 mmol) was mixed with a monomer mixture containing MMA (10.2 mL, 96 mmol) and TMSPMA (2 mL, 9.6 mmol) to make the stock solution.

Copolymerization of MMA and TMSPMA by ARGET ATRP

In a 10 mL Schlenk flask equipped with a magnetic stir bar, anisole (12.2 mL), 0.076 M Cu^{II}Br₂ in DMF (2.1 mL, 0.159 mmol), dNbpy (135 mg), DMF (2.1 mL), and 0.043 M EBPA in MMA/TMSPMA (12.2 mL) were added respectively. The solution was

degassed by three freeze-pump-thaw cycles. A copper wire (length = 120 mm, diameter = 0.25 mm) was coiled around a glass pipette and added to the mixture under a nitrogen flow. The reaction mixture was kept frozen and applied three evacuation and backfill cycles to remove the oxygen. The reaction was thawed, stirred at 35 °C, and monitored by 1 H NMR. The viscous crude product was diluted with DCM and passed through a basic alumina plug to remove the catalyst. The excess solvent was removed by rotary evaporator and the polymer product was added dropwise into methanol while stirring. The MeOH supernatants were decanted and the solid was dried under high vacuum overnight. The product is a white fine powder (7.20 g, 63% yield). The mole fraction of the MMA/TMSPMA = 9.9: 1 was determined by 1 H NMR and the molecular weight M_{n} : 31,500, PDI: 1.17 was determined by GPC.

Synthesis of PMMA-co-PPMA (deprotection procedure)⁹⁹

The poly(methyl methacrylate)-*co*-poly(trimethylsilylpropargyl methacrylate) (PMMA-co-PTMSPMA) (7 g, containing 5.90 mmol of TMSPMA group) and glacial acetic acid (0.8 mL, 14 mmol, 2.4 equivalents with respect to the trimethylsilyl alkyne groups) were dissolved in THF (50 mL). Nitrogen was purged through the solution over 20 min and then cooled to 0 °C. A 1 M solution of tetrabutylammonium fluoride (TBAF·3H₂O) in THF (12 mL, 12 mmol, 2.0 equiv) was added slowly via syringe over 2-3 min. The mixture was stirred at 0 °C for 30 min and warmed to room temperature. The deprotection was monitored by ¹H NMR. The disappearance of the silane signal at 0.2 ppm and the appearance of the alkyne proton signal at 2.5 ppm indicate the completion of deprotection, and the excess volatile liquid was removed by rotary evaporation. The resulting viscous solution was then precipitated by methanol several times to remove excess TBAF and the residual silane. The MeOH supernatants were decanted and the amorphous polymer gel-like solid was dried overnight under vacuum. The product is a white solid (6 g, 91% yield). After deprotection a smaller molecular weight was observed by GPC, $M_n = 29,100$, PDI = 1.20. The mole fraction of PMMA and PPMA is 9.8 to 1, determined by ¹H NMR. ¹H NMR (500 MHz, CDCl₃) δ 4.61 (s, 2H), 3.59 (s, 30H), 2.47 (s, 1H), 2.02 - 1.71 (m, 20H), 1.50 - 0.62 (m, 34H).

Chapter 4. Polymeric Micelles as Enzyme Stabilizers in Organic Solvents

Introduction

A former group member, Dr. Yu-Ling Lien, prepared functionalized poly(glycidyl ether) bearing dodecyl, poly(ethylene glycol), and ionic side chains. The amphiphilic polymers was found to decelerate the aggregation rate of the model enzyme (*Subtilisin Carlsberg*) in aqueous buffer solution. The polymer micelles prepared by CuAAC from poly(propargyl methacrylate) were proposed to form reverse micelle in the organic media and may stabilize enzymes in organic solvents. The local hydrophilic core of the micelle may enhance the enzymatic activity in an array of chemical environments. The side chain ratios of hydrophilic and hydrophobic side chains and enzyme activities relationship is further studied. The side chain structure of poly(propargyl methacrylate) could potentially be tailored to specific enzymes to optimize their activities.

Enzymatic activity of *Subtilisin Carlsberg* using 4-nitophenolate as chromophore (4-NP assay)

To study the performance of polymeric micelles in stabilizing enzymes in anhydrous organic media, a serine protease, *Subtilisin Carlsberg (SC)*, was chosen as the hydrophilic guest biomacromolecule. *Subtilisin Carlsberg* is a well-characterized industrially important protease from *Bacillus licheniformis*, a microorganism, and catalyzes hydrolysis of proteins and peptide amides.¹²⁰

To understand the activity of *SC* entrapped by polymeric micelles, the enzymatic activity is determined by enzymatic assays, using substrates that can bind and react with the active site of the *SC*. One of the common enzymatic assays is colorimetric enzymatic

assays, where the enzymatic reaction that converts a substrate into colored product(s) easily detected by a spectrometric method like UV/Vis spectroscopy. The first colorimetric substrate we chose is z-Ala-ONp, which was reported by Reimann and colleagues to determine the activity of SC adsorbed on silica particles in hexane. 121 The substrate has low solubility in hexane, we choose toluene as the reaction media due to the better substrate solubility and immiscibility with water, which is important for extracting the product 4nitrophenol out of the reaction media. The experimental design is shown in Scheme 20. First, the SC samples were lyophilized both with, and without, mDEG-PPMA polymers. In the former case, the mole ratio of the mDEG-PPMA to SC was 2:1. After lyophilization, three different biocatalysts—SC, SC entrapped in 100% mDEG-PPMA (SC@100%) mDEG-PPMA), and SC entrapped in 80%mDEG-PPMA (SC@80% mDEG-PPMA) were obtained and the colorimetric assay I, using z-Ala-ONp as the substrate was used to determine the activity of each composition. The SC or SC@mDEG-PPMA catalyzed the transesterification of z-Ala-ONp and n-butanol, which breaks the ester bond (red bond shown in Scheme 20) to generate 4-nitrophenol as the product. The procedure involved adding *n*-butanol (458 µL) and 0.01 M toluene solution of (z-Ala-ONp) to a vial containing the lyophilized biocatalysts, and the mixture was mixed by a benchtop orbital shaker set at 300 rpm. The aliquots were taken periodically from the reaction media. After extracting the aliquots from the reaction mixture with 0.1 N NaOH solution, the 4-nitrophenol was converted into 4-nitrophenolate, which has a strong yellow color under the basic condition. The extinction coefficient was determined by UV-Vis spectrum with variable concentration of 4-nitrophenolate in 0.1 N NaOH solution, shown in Figure 31 and Figure 32. The extinction coefficient is 17893 L·mol⁻¹cm⁻¹ in 0.1 N NaOH_(aq), which is slightly smaller than the literature value (18800 $L \cdot mol^{-1}cm^{-1}$).¹²¹ Since the UV-Vis will be measured in 0.1 N NaOH(aq), ϵ =17893 $L \cdot mol^{-1}cm^{-1}$ was used for determining the 4-nitrophenolate concentrations for the assay.

Scheme 20. Colorimetric enzymatic assay using z-Ala-ONp as a substrate in toluene. [substrate] = 0.01 M, [n-BuOH] = 1 M, [SC] = 0.2 mg/mL, [SC]: [mDEG-PPMA] = 1: 2. Aliquots (50 μ L) were taken periodically, mixed with 500 μ L of 0.1 N NaOH_(aq), and vortexed for 30 s before measuring the UV-Vis of the aqueous layer.

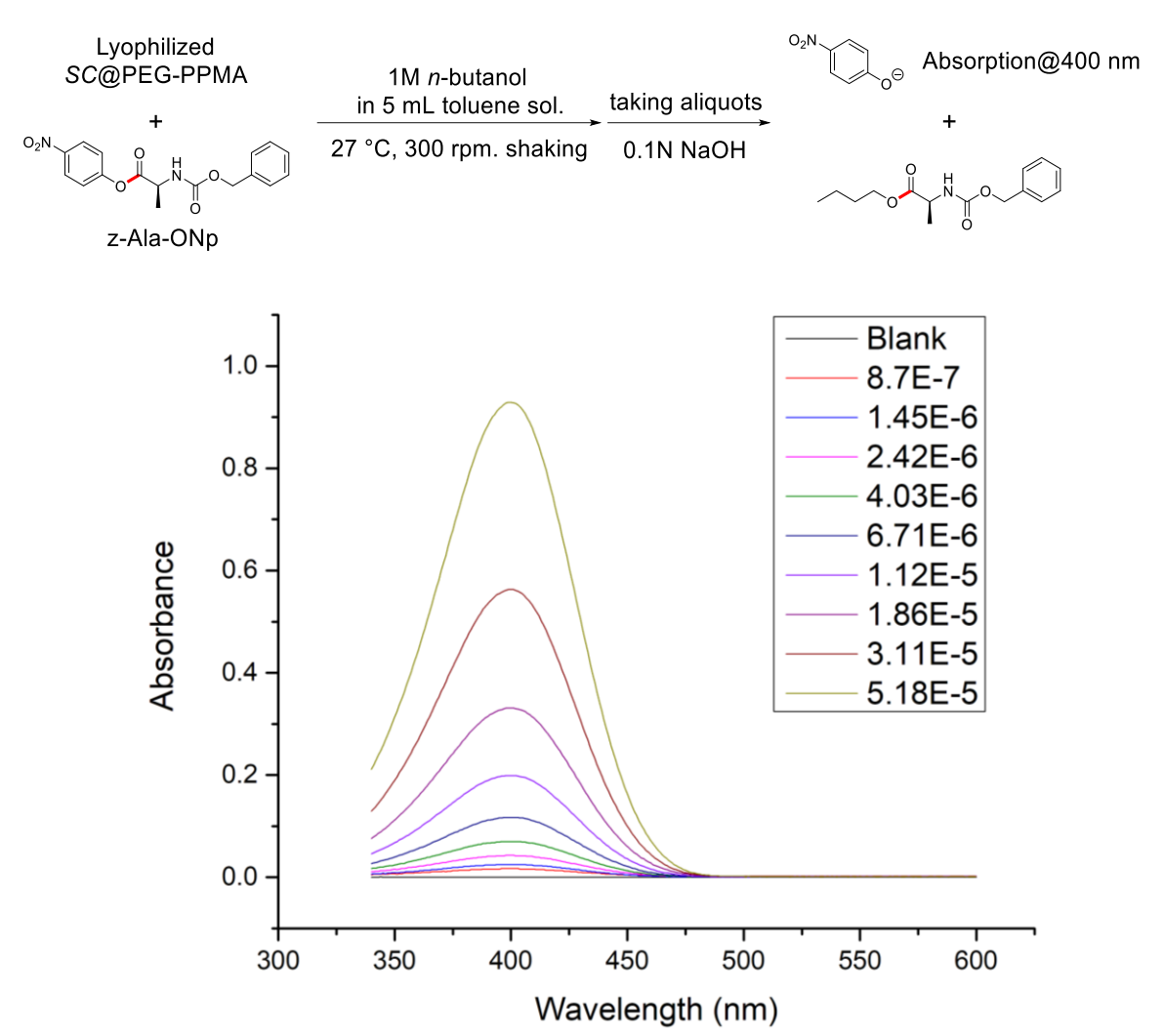


Figure 31. Overlapped UV-Vis spectra of variable 4-nitrophenolate concentration in 0.1 N NaOH_(aq). The wavelength of maximum absorbance is at 400 nm.

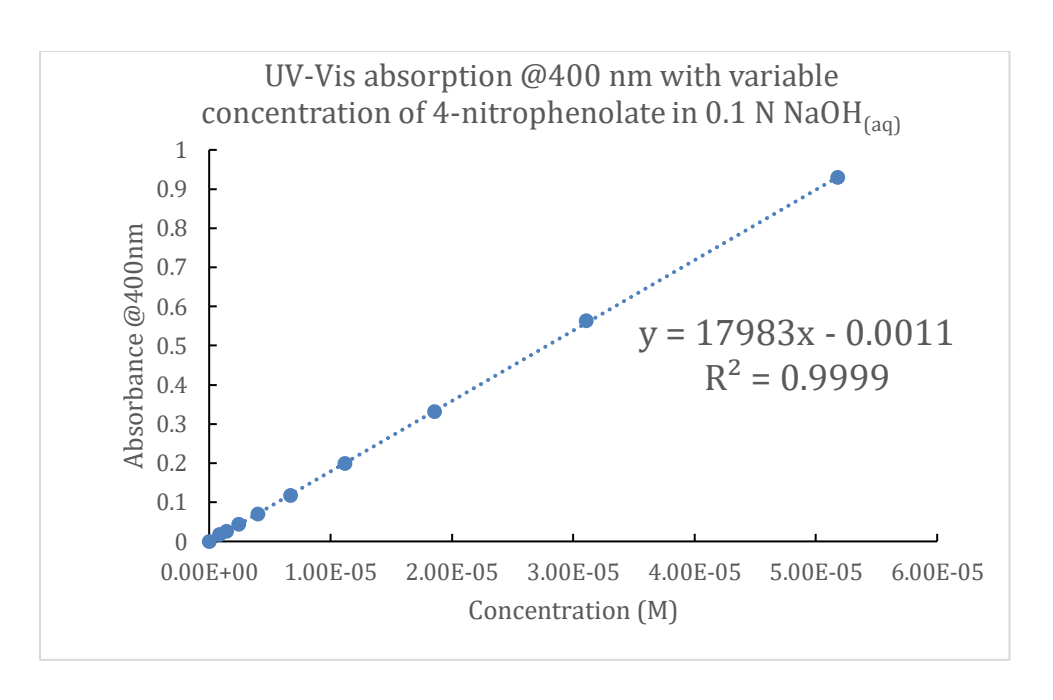


Figure 32. Determination of extinction coefficient of 4-nitrophenolate in 0.1 N NaOH_(aq) by UV-Vis spectroscopy.

The amounts of enzymatic product (4-nitrophenolate) versus reaction time in the presence of various biocatalysts were plotted in Figure 33. In the lyophilized *SC* experiment, very little 4-nitrophenolate (< 5% conversion) was produced over the 40 minutes and the amount of the product generated was close to the control experiment, which only contained the substrate without biocatalyst, indicating low to no activity of the lyophilized *SC*. In the *SC*@100%mDEG-PPMA experiment, the biocatalyst was more active than lyophilized *SC* and the conversion of the enzymatic assay reached 30% conversion over 40 min reaction period. The *SC*@82%mDEG-PPMA was found to be the most active biocatalyst and the enzymatic assay passed 60% conversion within 40 minutes. The enzymatic activity follows this order: *SC*@82%mDEG-PPMA > *SC*@100%mDEG-PPMA > *SC*. The enzymatic assay of *SC*@82%mDEG-PPMA and *SC* was repeated three times and yielded a consistent result, shown in Figure 34 and Figure 35. Polymeric micelles may serve two functions to keep *SC* active in organic media. First, the polymeric micelles

may act as lyoprotectants to keep a layer of protein-bound water on the enzyme surface, which is vital to the enzyme structure and activity. The other is that the polymeric micelles may form reverse micelle in the organic media, generating a hydrophilic microenvironment within the micelles, and shield the enzyme from the bulk organic media. The 80% mDEG-PPMA can form more stable micelle in toluene than 100% mDEG-PPMA due to the 20% hydrophobic dodecyl side chains. The more stable micelle can keep the protein-bound water from leaking into organic solvent and enhance the enzymatic activity.

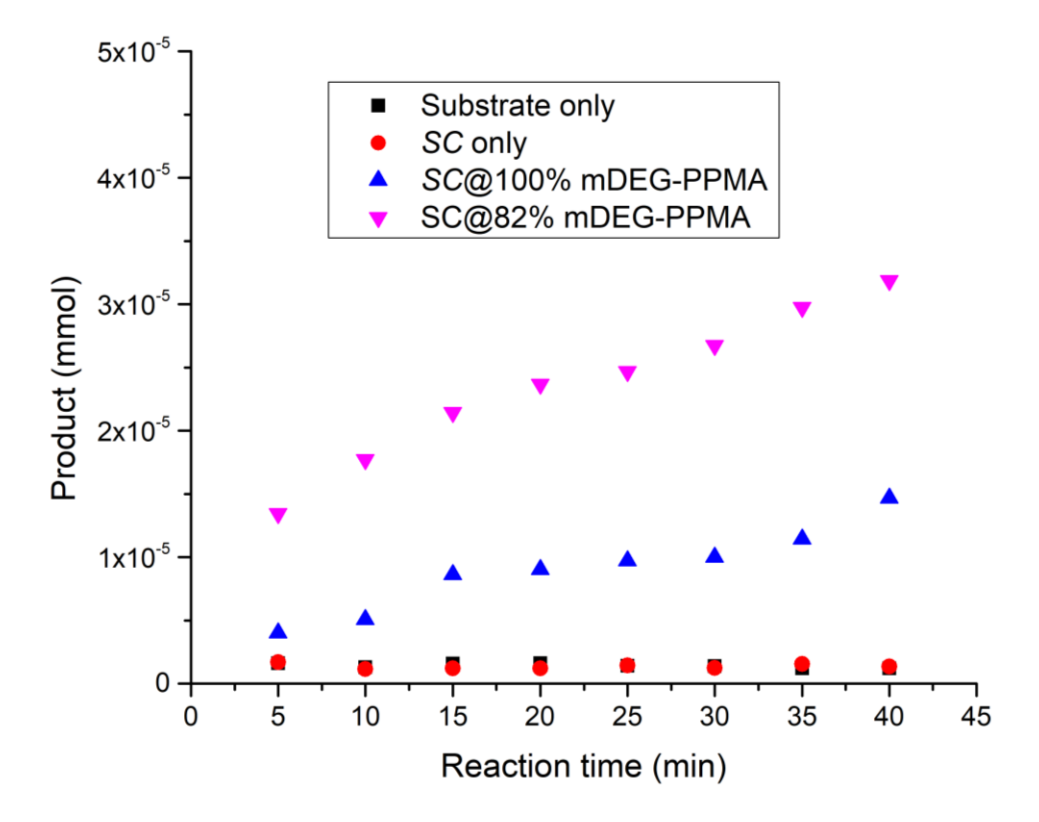


Figure 33. Mole of enzymatic assay product (4-nitrophenolate) versus reaction time plot of different biocatalysts: SC@82%mDEG-PPMA (magenta diamond), SC@100%mDEG-PPMA (blue triangle), SC (red dot), control (substrate only, black square). Assay was used z-Ala-ONp as substrate in toluene. [substrate] = 0.01 M, [n-BuOH] = 1 M, [SC] = 0.2 mg/mL, [SC]: [xx%mDEG-PPMA] = 1: 2 (mol ratio). Aliquots (50 μ L) were taken periodically, mixed with 500 μ L of 0.1 N NaOH_(aq), and vortexed for 30 s before determining the aqueous layer by UV-Vis spectroscopy.

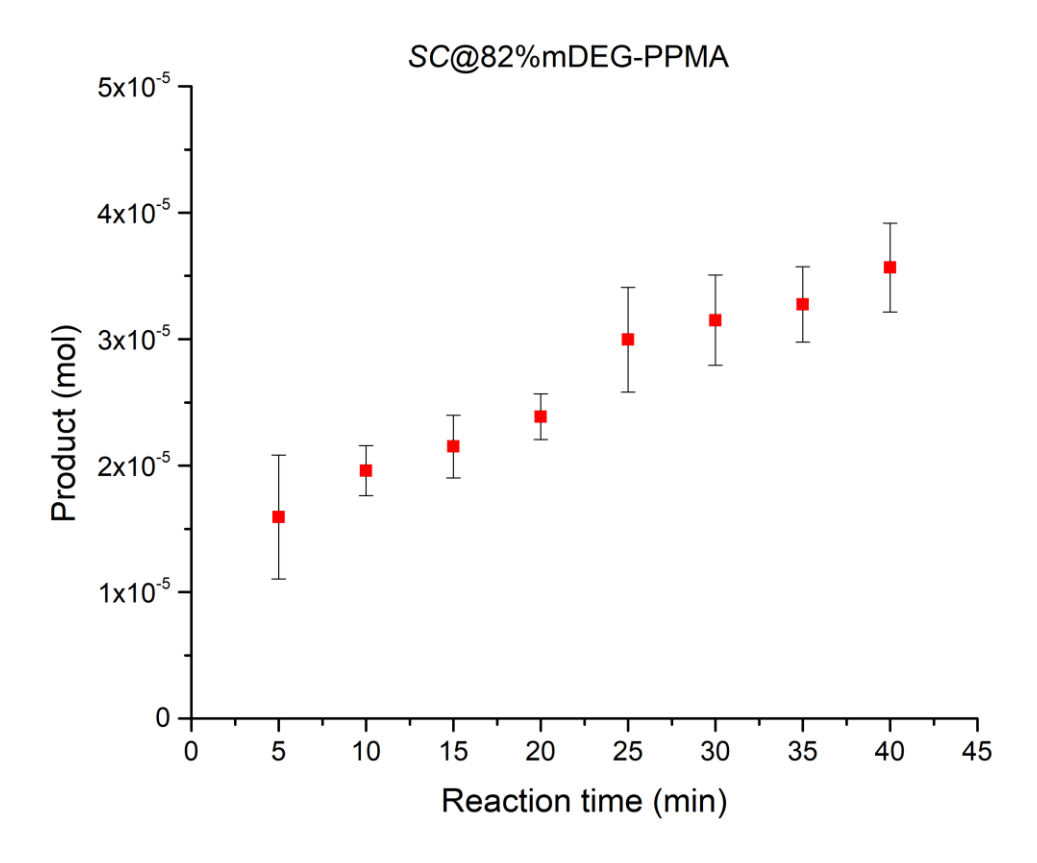


Figure 34. Triplicate of enzymatic assay of SC@82%mDEG-PPMA using z-Ala-ONp as substrate in toluene. [substrate] = 0.01 M, [n-BuOH] = 1 M, [SC] = 0.2 mg/mL, [SC]: [mDEG-PPMA] = 1: 2 (mol ratio). Aliquots (50 μ L) were taken periodically, mixed with 500 μ L of 0.1 N NaOH_(aq), and vortexed for 30 s before determining the aqueous layer by UV-Vis spectroscopy.

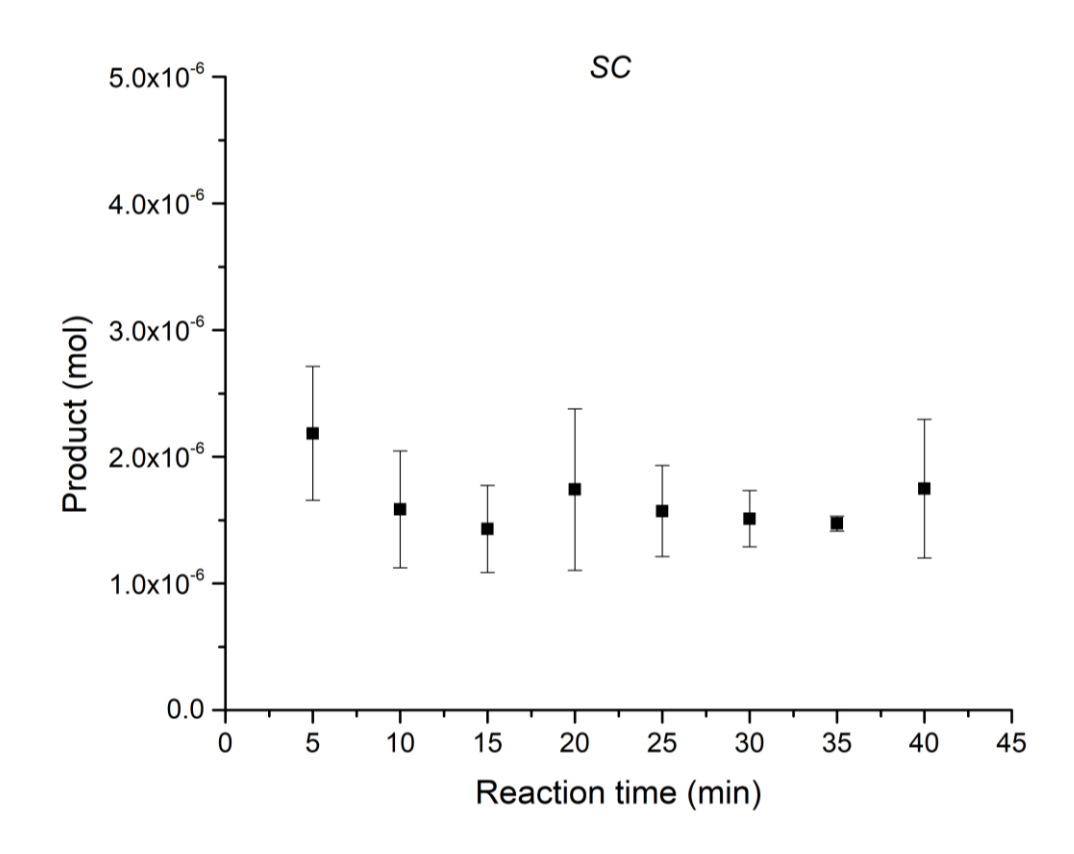


Figure 35. Triplicate of enzymatic assay of SC using z-Ala-ONp as substrate in toluene. [substrate] = 0.01 M, [n-BuOH] = 1 M, [SC] = 0.2 mg/mL, [SC]: [mDEG-PPMA] = 1: 2 (mol ratio). Aliquots (50 μ L) were taken periodically, mixed with 500 μ L of 0.1 N NaOH_(aq), and vortexed for 30 s before determining the aqueous layer by UV-Vis spectroscopy.

Alcohols are common deactivators for enzymes and *n*-butanol was one of the reagents used in the enzymatic assay. We exchanged the order of reagent addition — *n*-butanol and substrate solution (z-Ala-ONp)— to study the impact of sequence of addition to the enzymatic activity. The experiments following the standard procedure (adding 458 µL of *n*-butanol first) and the control procedure (adding 0.01 M substrate solution in toluene first) were conducted side by side and the enzymatic assay results were shown in Figure 36. The enzymatic assays following different order of addition had similar reaction rate and reached ~70% conversion at 40 minutes, indicating the order of reagent addition did not alter the enzymatic activity.

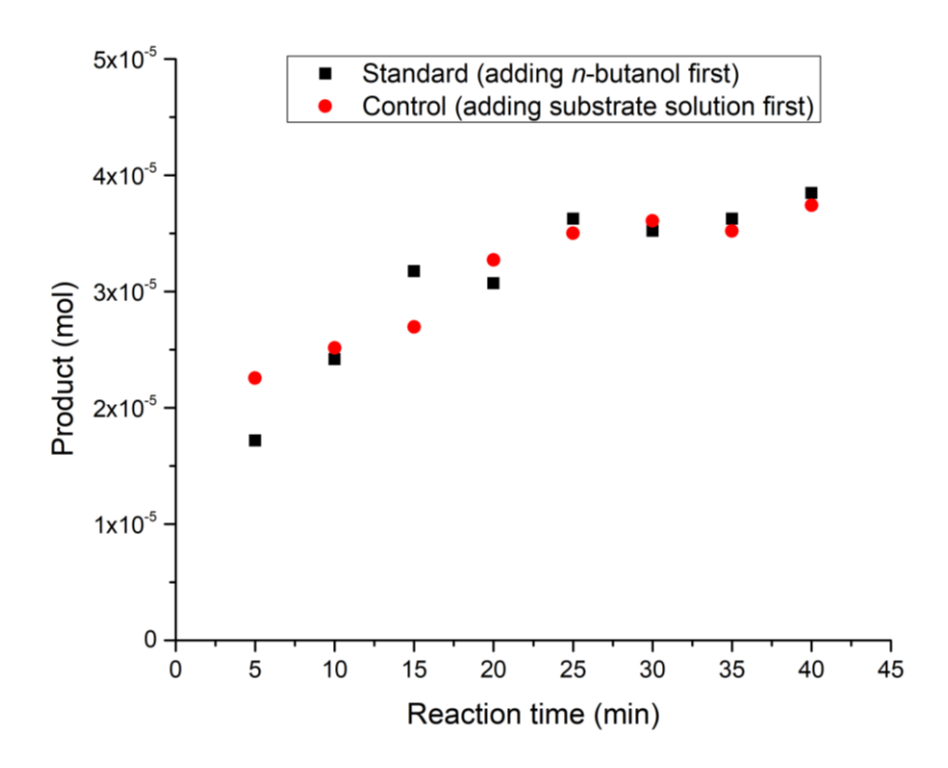


Figure 36. The enzymatic assay results of different order of reagent addition. Standard procedure: in a vial containing biocatalyst *SC*@82%mDEG-PPMA, adding *n*-butanol and substrate solution, respectively (black square). Control procedure: in a vial containing biocatalyst *SC*@82%mDEG-PPMA, adding substrate solution and *n*-butanol, respectively (red dot).

We had a hypothesis that if the SC@82%mDEG-PPMA are soluble in toluene, the enzymatic activity will be detected in the upper clear toluene solution. To test our hypothesis, the freshly lyophilized SC@82%mDEG-PPMA was incubated and shaken in toluene for 5 or 25 minutes at 300 rpm. After shaking, the top clear solutions were carefully transferred to different vials and charged with substrate and n-butanol respectively, and the enzymatic activity was assayed with the same procedure. The results are shown in Figure 37. We did find the enzymatic activity on the top clear solution. The SC@82%mDEG-PPMA was still observed to be the most active biocatalyst, followed by the SC@82%mDEG-PPMA with 25 min incubation time in toluene, then SC@82%mDEG-PPMA with 5 min incubation time, and the inactive SC. The activities of the dissolved

biocatalysts increase with the longer incubation time. Based on the results, we concluded only part of the biocatalysts was dissolved, and the dissolving process is a slow process. Majority of the enzymatic activity was from the heterogenous biocatalyst.

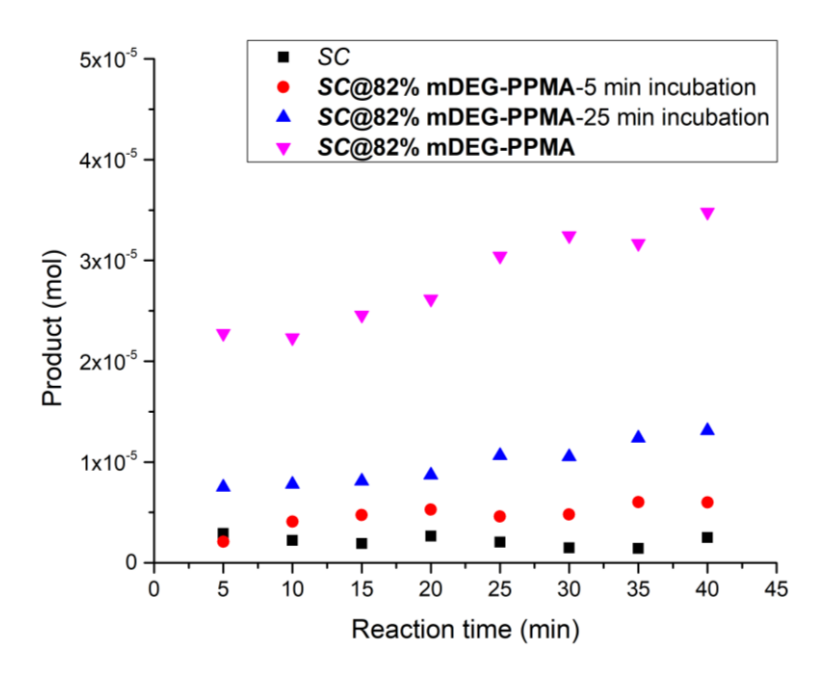


Figure 37. Mole of enzymatic assay product (4-nitrophenolate) versus reaction time plot of different biocatalysts: SC@82%mDEG-PPMA (magenta diamond), SC@82%mDEG-PPMA-25 min incubation time (blue triangle), SC@82%mDEG-PPMA-5 min incubation time (red dot), SC (black square).

Enzymatic activity of *Subtilisin Carlsberg* using 4-thiopyridone as chromophore (4-TP assay)

In the previous section, the enzymatic assay using 4-nitrophenolate as chromophore was used to determine the activity of the biocatalysts. Another colorimetric assay (4-thiopyridone as chromophore) was used to verify biocatalyst activity trend. Egwim and colleagues 122 reported that 4,4′-dithiodipyridine (DTDP) can spectroscopically measure organic thiols in the organic media with better sensitivity due to the higher reactivity of DTDP toward thiols than Ellman's reagent, 5,5′-dithio-bis(2-nitroben-zoic acid). The mechanism of DTDP reacting with a thiol is illustrated in Scheme 21. The thiol–disulfide exchange reaction between the thiol and DTDP releases one equivalent of 4-mercaptopyridine and then tautomerizes into the chromophore, 4-thiopyridone, under

acidic condition. The thiol–disulfide exchange is a fast process when catalyzed by 0.12% (v/v) triethylamine in DMSO, which only requires 3 minutes of incubation and then can be quenched with acetic acid to drive the equilibrium to 4-thiopyridone side. To verify the effectiveness of DTDP reacting with thiols, we prepared various concentrations of thiophenol following the procedure from Egwim and colleagues. The overlapped UV-Vis spectra of variable thiophenol concentration are shown in Figure 38. The linear correlation of UV-Vis absorption@352 nm versus the concentration of thiophenol was observed and shown in Figure 39, validating that Egwim's procedure can be used to characterize thiophenol in DMSO solution.

Scheme 21. Mechanism of 4,4′-dithiodipyridine (DTDP) reacting with a thiol to release a 4-mercaptopyridine and then tautomerizing into 4-thiopyridone chromophore.

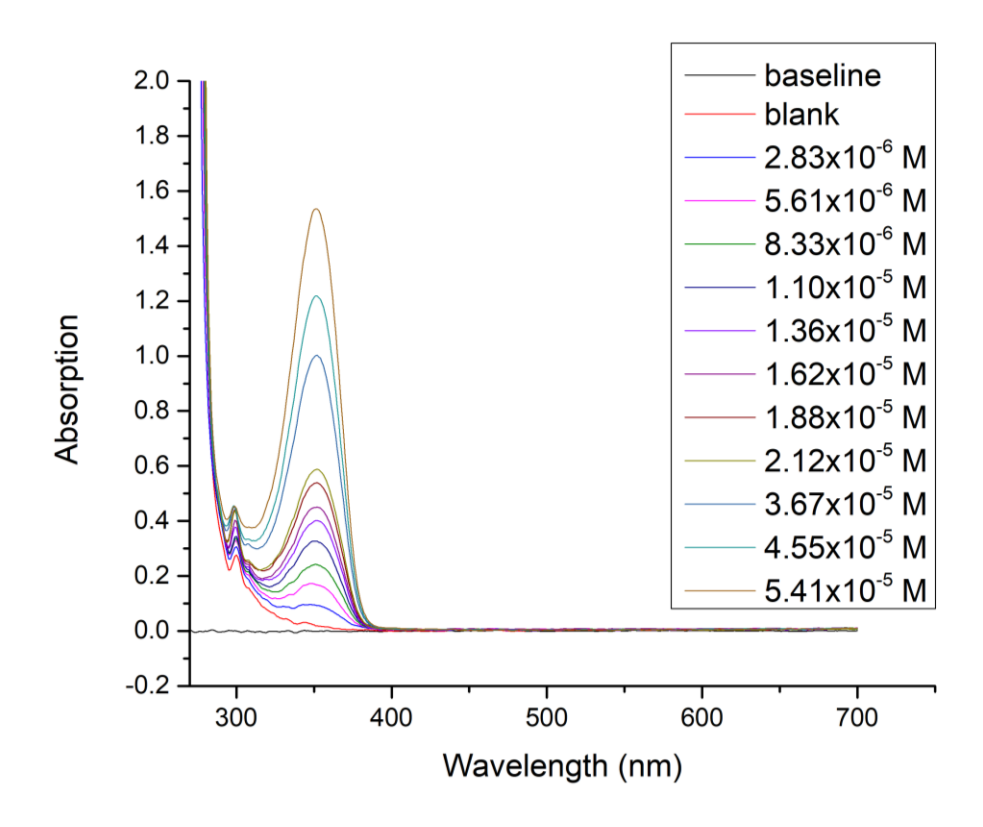


Figure 38. Calibration curve of variable concentration of thiophenol reacting with DTDP. [DTDP] = 1×10^{-4} M in DMSO solution containing 0.12% (v/v) triethylamine.

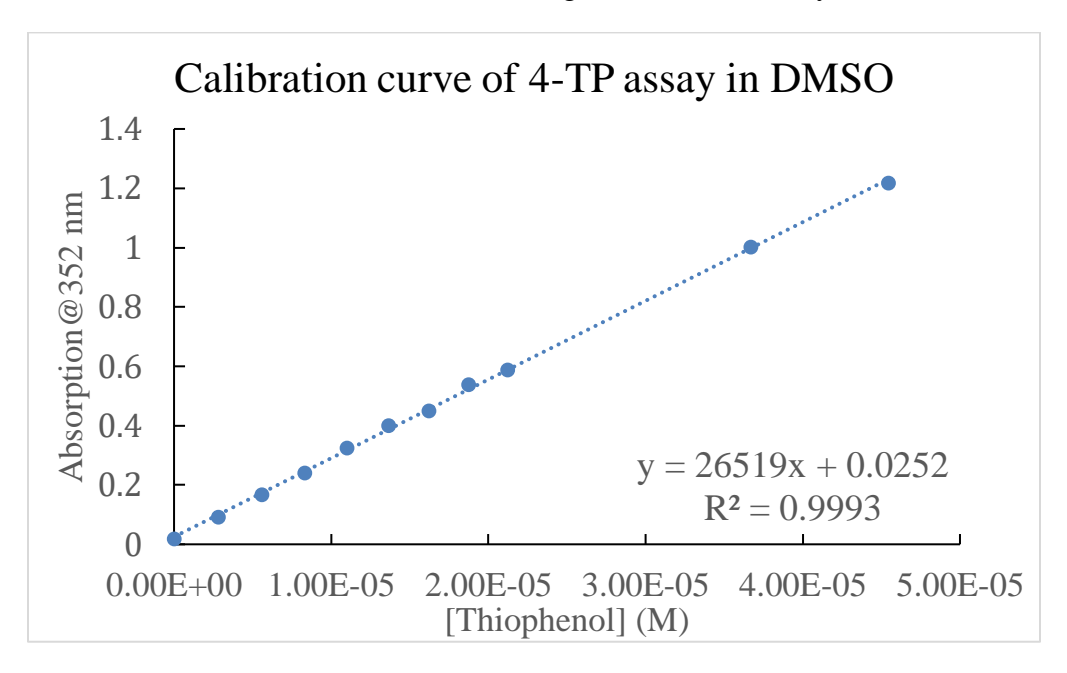


Figure 39. Calibration curve of UV-Vis absorption@352 nm versus variable thiophenol concentration. [DTDP] = 1×10^{-4} M in DMSO solution containing 0.12% (v/v) triethylamine.

Cummings and colleague 123 determined the activity of chymotrypsin-poly(2-(dimethylamino)ethyl methacrylate) conjugates in acetonitrile by a colorimetric assay utilizing the thiol-disulfide exchange idea. The design of colorimetric enzymatic assay is shown in Scheme 22Scheme 22. The thioester bond in the substrate (N-acetyl Lphenylalanine thiophenylester (APTE)) is cleaved by the enzyme, releasing an equivalent of thiophenol, whose triethylamine-catalyzed reaction with DTDP generates the 4thiopyridone chromophore. The enzymatic activities of SC@82%mDEG-PPMA and SC were determined by the amount of 4-thiopyridone (4-TP) generated, shown in Figure 40. There are several observations from this result. First, the enzymatic activity of SC@82%mDEG-PPMA is higher than SC, which follows the trend observed from the enzymatic assay using 4-nitrophenolate as chromophore (4-NP assay). The initial rate of SC@82%mDEG-PPMA is 13-fold faster than SC, shown in Figure 41. Second, the SC@82%mDEG-PPMA was active between 600 min (27.9% conversion at 10 h) and 1860 min (44.3% conversion at 31 h). While the conversion of SC was 3.0% at 600 min and 6.0% at 1860 min. The results indicate the 80% mDEG-PPMA not only keeps the SC active but also enhances the long-term durability of SC in toluene.

Scheme 22. The design of enzymatic assay using 4-thiopyridone as chromophore

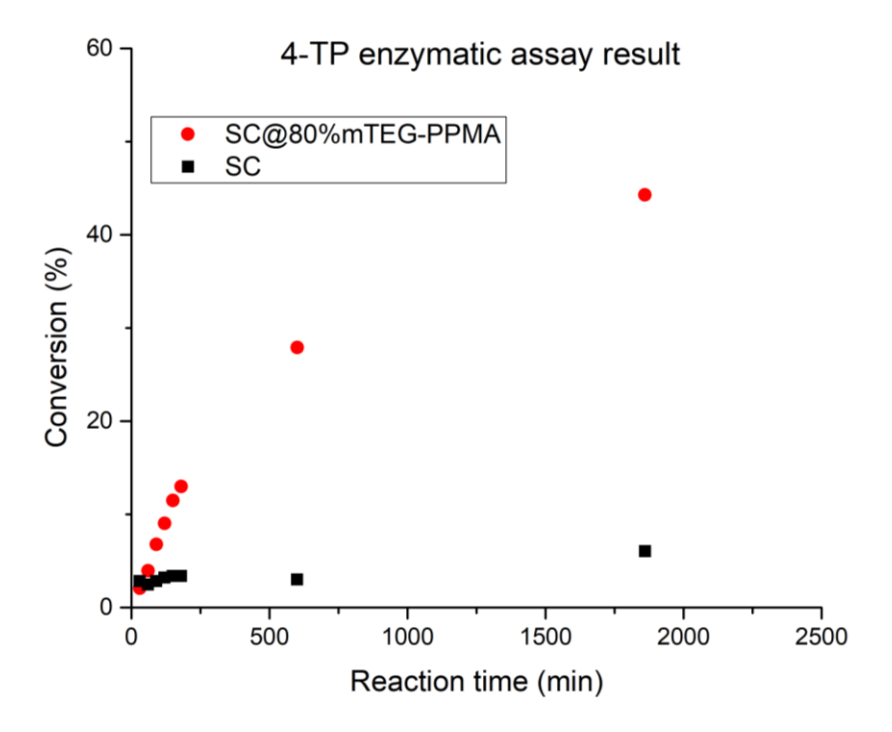


Figure 40. Enzymatic assay result using 4-thiopyridone (4-TP) as chromophore. SC@82%mDEG-PPMA (red dot) and SC (black square) were tested using APTE as substrate in toluene. [APTE] = 1 mM, [n-butanol] = 0.1 M.

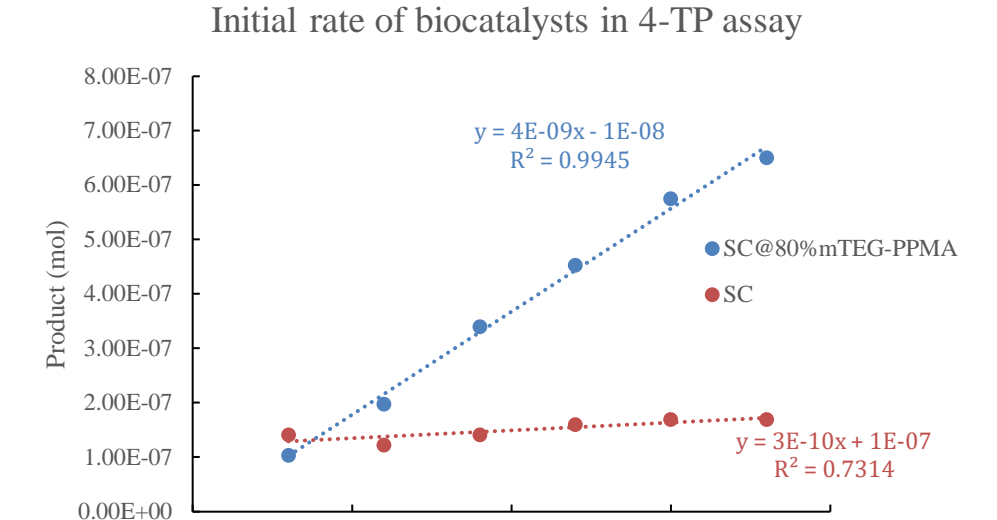


Figure 41. Initial rate of biocatalysts in 4-TP assay. *SC*@82%mDEG-PPMA (blue) and *SC* (red).

100

Reaction time (min)

50

200

150

Conclusion

The micelles prepared by post-polymerization modification were used as enzyme stabilizers in toluene. The residual activity of *Subtilisin Carlsberg* was determined by two different enzymatic assays (4-nitrophenoate and 4-thiopyridone). In 4-nitrophenoate assay, SC@82%mDEG-PPMA was found to be the most active biocatalyst followed by SC@100%mDEG-PPMA. The SC without polymer micelles showed remarkably lower activity. The 4-thiopyridone, the SC@82%mDEG-PPMA was ten times more active than the SC without polymer. Although the reaction rates were different in these assays, the SC@82%mDEG-PPMA were both more active than the SC only, indicating the effectiveness of 82%mDEG-PPMA as enzyme stabilizer in toluene.

Experimental Section

Materials

Subtilisin Carlsberg (SC) was purchased form Sigma-Aldrich as Protease from Bacillus licheniformis (Type VIII, lyophilized powder, 7-15 units/mg solid) and was kept in the freezer. Anhydrous toluene was kept with activated 4Å molecular sieves. Triethylamine was kept with potassium hydroxide pallets. All the other chemicals were used as received without further purification.

Lyophilization procedure

The enzyme stock solution (1 mg/mL) was prepared by dissolving *Subtilisin Carlsberg* (*SC*) (5 mg) by phosphate-buffered saline (PBS buffer) (5 mL, pH 7.4, RNasefree). The polymer stock solutions (6 mg/mL) were made by dissolving specific graft polymer **x% mDEG-PPMA** in corresponded volume of phosphate-buffered saline. The *SC* entrapped by graft polymer sample (*SC@x%* mDEG-PPMA) was prepared by transferring the enzyme stock solution (1 mL) and the polymer stock solution (1 mL) into a 20 mL scintillation vials, and loosely tighten the cap. The solution mixture was briefly swirled and freeze by keeping the vial in a liquid nitrogen bath. After the solution was frozen, the vial was kept under vacuum for 12 h to remove the water. For the *SC* only sample, the enzyme stock solution (1 mL) was mixed with PBS buffer (1 mL) in a 20 mL scintillation vials and followed the rest of the lyophilization process. For the polymer only sample, the polymer stock solution (1 mL) was mixed with PBS buffer (1 mL) in a 20 mL scintillation vials and followed the rest of the lyophilization process. After the lyophilization, the enzymatic activity must be determined immediately.

Enzymatic assay (4-nitrophenolate as chromophore)¹²¹

The 0.01 M substrate stock solution was prepared by dissolving substrate z-Ala-ONp (86 mg, 0.25 mmol) in anhydrous toluene (25 mL). The scintillation vial containing the lyophilized samples was then charged with 0.01 M substrate stock solution (5 mL, 0.05 mmol) and 1-butanol (458 μL, 5 mmol). The reaction was started after adding 1-butanol and the mixture was shaken at 300 rpm. Aliquots (50 μL) was taken periodically from the reaction mixture to monitor the reaction progression. The aliquots (50 μL) were mixed with 1M Na₂CO_{3(aq)} by vortexing the mixture for 30 seconds. The product concentration (4-nitrophenolate) was then determined by UV/Vis spectrometer.

Synthesis of N-acetyl L-phenylalanine thiophenylester (APTE)¹²³

A Schlenk flask, charged with N-acetyl-L-phenylalanine (2.00 g, 9.7 mmol, 1 equiv), anhydrous DCM (100 mL), triethylamine (1.5 mL, 10.7 mmol, 1.1 equiv), and a magnetic stir bar, was purged with nitrogen briefly. Under an ice bath, isobutyl chloroformate (1.3 mL, 10.3 mmol, 1.06 equiv) was slowly added to the reaction solution and stirred under room temperature for 30 minutes. A solution of thiophenol (1.0 mL, 9.7 mmol, 1 equiv) in dry DCM (10 mL) was then added to the reaction mixture and stirred at room temperature. After stirring for 30 minutes, the mixture was washed with 0.1 N HCl aq. (50 mL × 2), saturated NaHCO₃ aq. (50 mL × 2) and saturated brine (50 mL × 2). The organic layers were dried over anhydrous MgSO₄, and the excess solvents were evaporated using rotary evaporator. The product was further recrystallized by EtOH and water mixture (2:1 volume ratio). 2.1 g (72%) of product was obtained. ¹H NMR (500 MHz, CDCl₃) δ 7.14 – 7.46 (m,

10 H, phenyl), 5.82 (br, 1 H, J = 8.6 Hz), 5.12 (td, 1 H, J = 6.6, 8.6 Hz), 3.18 (d, 2 H, J = 6.6 Hz), 2.01 (s, 3 H) ppm.

Enzymatic assay (4-thiopyridone)^{122,123}

The 0.01 M substrate stock solution was prepared by dissolving substrate APTE (74.8 mg, 0.25 mmol) in anhydrous toluene (25 mL). The scintillation vial containing the lyophilized samples was then charged with 0.01 M substrate stock solution (5 mL, 0.05 mmol) and 1-butanol (458 µL, 5 mmol). The reaction was started after adding 1-butanol and the mixture was shaken at 300 rpm. Aliquots (50 µL) were taken periodically from the reaction mixture and mixed with 0.01 M 4,4'-dithiodipyridine (DTDP) (1 mL) solution in DMSO and vortexed for 30 seconds before taking UV/Vis spectra. Noteworthily, the reaction between thiophenol and DTDP is much faster in DMSO than in toluene. The product concentration (4-thiopyridone) was then determined by UV/Vis spectrometer.

Chapter 5. Amino acids solution as CO₂ capturing absorbents and NMR study of the CO₂ adducts

Introduction

Cultivating microalgae for post-combustion capture

The Liao group at MSU has reported utilizing a culture of selected freshwater microalgae (chlorophyte alga as dominating domain) in a pilot-scale photobioreactor for post-combustion capture at MSU's T.B. Simon power plant, which is a natural gas fired power plant. The photobioreactor is a PHYCO2 APB unit, shown in Figure 42. CO₂ in the flue gas from the natural gas power plant and ammonium nitrate were used as the carbon source and nitrogen source respectively for the microalgae culture during a 12-month continuous operation. The biomass productivity reached 0.43 \pm 0.14 g L⁻¹ d⁻¹, and the biomass was comprised of proteins (58.60 \pm 2.41%), carbohydrates (19.5 \pm 2.44%), ash (12.20 \pm 1.52%), and lipids (9.70 \pm 1.68%). In the Liao-Smith collaboration, peptides and amino acids from the digested biomass were proposed to be use as CO₂ absorbents or as building blocks for value-adding polymer materials, which can fix CO₂ in longer term than turning biomass into fuel.

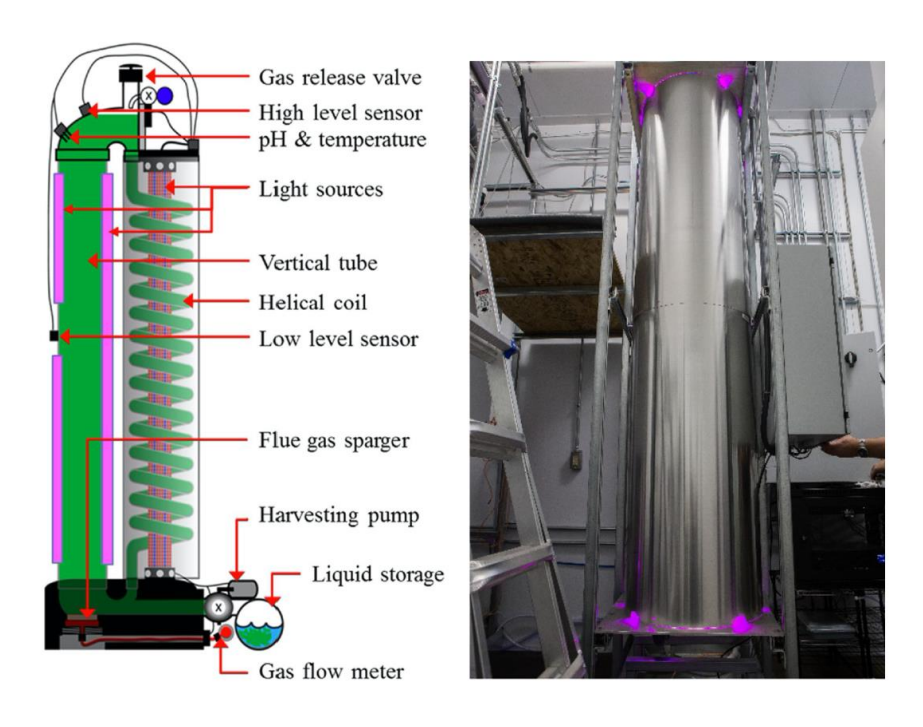


Figure 42. Microalgae photobioreactor, PHYCO2 APB unit. Diagram of the photobioreactor (left) and the photobioreactor at the MSU. T.B. Simon power plant (right). 124,125

Amino acid salts as CO₂ absorbents for post-combustion capture

Characterization of the CO₂ capturing intermediates by ¹³C{¹H} NMR

Glycine, alanine, proline, and lysine were chosen as the model amino acids to mimic the mixture from the algal biomass and tested the CO_2 capturing performance. Amino acids are amphoteric molecules due to the presence of the acidic carboxylic acid group and the basic amino group. Amino acids have three ionization state in different pH environments. When pH < p K_{a1} , both the amino and acid groups are protonated. When p K_{a1} < pH < p K_{a2} , the amino acid exists in a zwitterionic form, which contains a deprotonated carboxylic acid group and a protonated amino group. When pH > p K_{a2} , both acid and amino groups are deprotonated.

Scheme 23. Ionization states of amino acid in different pH value.

To enhance the affinity of the amino group toward CO₂, one equivalent of potassium hydroxide versus amino acid was added to deprotonate the ammonium group on the zwitterion form. The pH values of the amino acid salt solutions are higher than p K_{a2} to ensure the complete deprotonation of the ammonium group. The CO₂ absorption experiment was done by my colleagues, Dr. Uludag-Demirer and Adam Smerigan, and the setup was shown in the Figure 43. The gas entering the absorption reactor contains 10 vol% CO₂ and 90 vol% air to mimic the flue gas from the power plant with a flow rate maintained between 0.5 to 0.7 L/min and is monitored by a digital flow meter. The absorption reactor is a 250 mL gas washing bottle with 100 mL of the desired concentration of amino acid salt solution as an absorbent. The CO₂ concentration in the exhaust gas was monitored by GC (SRI 310 C) and plotted versus reaction time, shown in Figure 44. The absorption traces (blue circles and orange triangles trace in Figure 44) showed fast CO₂ capture kinetic and nearly 100% CO₂ capture was observed for 20 minutes. The CO₂ capture capability decreased after 20-minute reaction time and the CO₂ concentration in exhaust gas started increasing and reached a plateau around 80 minutes and the absorption experiment was stopped.

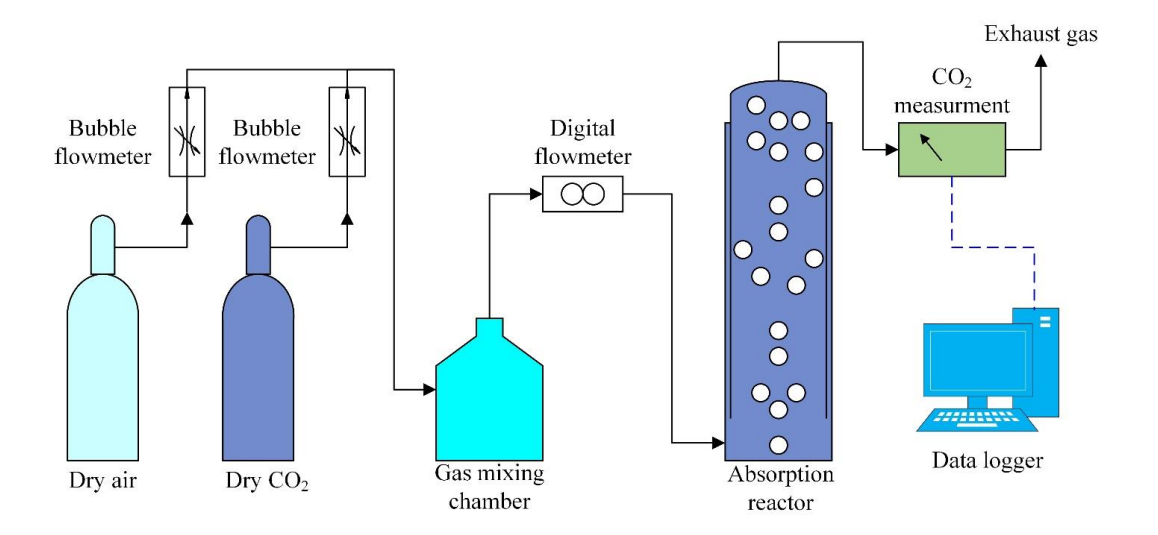


Figure 43. The CO₂ absorption experimental setup. From reference

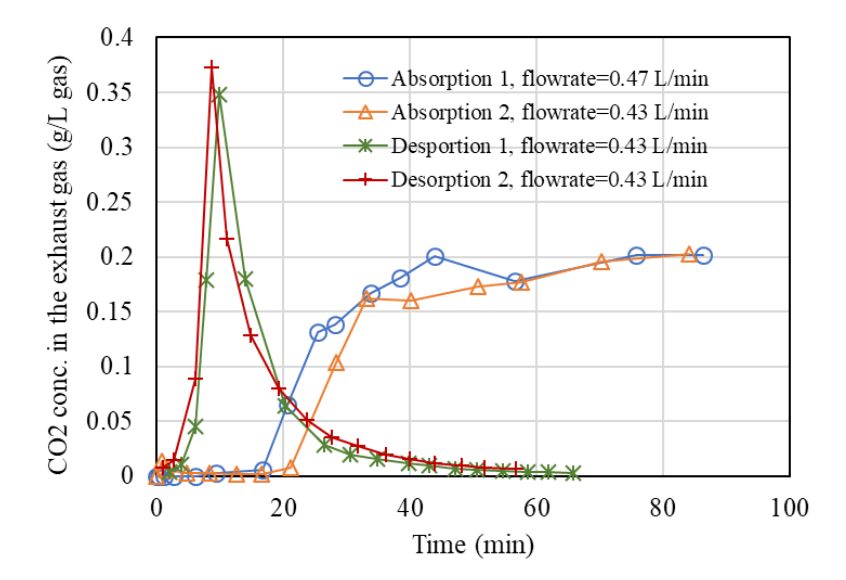


Figure 44. The CO₂ absorption (blue circle and orange triangle) and desorption (green star and red cross) progression plot using potassium glycinate solution as absorbent.

During CO₂ absorption, the amino acid form carbamate and bicarbonate as products. For the primary and secondary amine interacting with CO₂, the zwitterion mechanism proposed by Caplow¹²⁶ and Danckwerts¹²⁷ is the most accepted carbamate formation mechanism, shown in Scheme 24. The zwitterion mechanism is also supported by kinetic studies of aqueous monoethanolamine (MEA) solutions reacting with CO₂.¹²⁸ Kinetic

studies^{129,130,131} have concluded that the total reaction order is 2 and the partial order for MEA is 1. The rate law of the CO₂ absorption into MEA solution is shown in Eq 12.

$$Rate = k[MEA][CO_2]$$
 Eq 12

The kinetic data also indicates that the deprotonation is a fast process, and the formation of carbamate zwitterion is the rate-determining step. A parallel reaction during CO₂ absorption is the formation of bicarbonate ion by the reaction between hydroxide ion (under basic reaction media) with dissolved CO₂, shown in Scheme 25. However, at the early stage of the CO₂ capture process, the carbamate formation is faster than the bicarbonate formation due to the higher nucleophilicity of amino group of the MEA than hydroxide ion.^{132,133} Another bicarbonate ions formation route is by the decomposition of the carbamate, shown in Scheme 26.

Scheme 24. MEA carbamate formation via zwitterion mechanism.

Scheme 25. Formation of bicarbonate ion by reaction between hydroxide ion with dissolved CO_2 (aq).

Scheme 26. Formation of bicarbonate ion by carbamate decomposition.

$$\stackrel{\bigcirc}{\bigcirc}$$
 $\stackrel{\mathsf{H}}{\bigcirc}$ $\stackrel{\mathsf{OOC}}{-\mathsf{R}-\mathsf{N}-\mathsf{COO}}$ + $\stackrel{\mathsf{H}_2\mathsf{O}}{\bigcirc}$ + $\stackrel{\mathsf{O}}{\bigcirc}$ + $\stackrel{\mathsf{OOC}}{\bigcirc}$ + $\stackrel{\mathsf{OOC}}{\bigcirc}$ + $\stackrel{\mathsf{OOC}}{\bigcirc}$ Carbamate Bicarbonate

Several studies have proposed the formation of amino acid carbamate following the same zwitterion mechanism as the MEA carbamate formation. ^{134,135,136} The carbamate formation starts with the amino group on the amino acid react with CO₂ molecule to form a carbamate zwitterion intermediate and another amino acid molecule acts as base to abstract the acidic ammonium proton to generate carbamate and amino acid zwitterion, shown in Scheme 27.

Scheme 27. Formation of amino acid carbamate and amino acid zwitterion.

The formation of amino acid carbamate is much faster than the formation of bicarbonate ion by hydroxide ion reacting with dissolved CO₂, shown in Scheme 25, and is supported by the study from Li and colleagues. ¹³⁷ Quantitative ¹³C{¹H} NMR spectroscopy was used to monitor the mole fraction of carbamate and bicarbonate during the CO₂ absorption into 3 M potassium glycinate solution. In the low CO₂ loading (higher pH of the solution), the glycine carbamate concentration is increasing faster comparing to the bicarbonate and carbonate concentration. The mole fractions of each species are replotted versus the CO₂ loading in Figure 45. The potassium glycinate carbamate (KG-CO₂) is formed at low CO₂ loading and kept increasing until CO₂ loading = 0.56 (mol

 CO_2 /mol amine). While the mole fraction of bicarbonate and carbonate ions (HCO_3 -/ CO_3 ²⁻) is low at the early stage of the CO_2 absorption process because the lower hydrophilicity of the hydroxide ion than the amino group on the potassium glycinate so majority of CO_2 is consumed by forming carbamate at this stage. ¹³³¹³³ The mole fraction of bicarbonate and carbonate increases sharply after CO_2 loading = 0.56 (mol CO_2 /mol amine) due to the decomposition of carbamate in relatively acidic condition (pH drop from 10.02 to 8.40 at CO_2 loading = 0.56 and 0.76, respectively), which is also supported the proposed carbamate mechanism (Scheme 26).

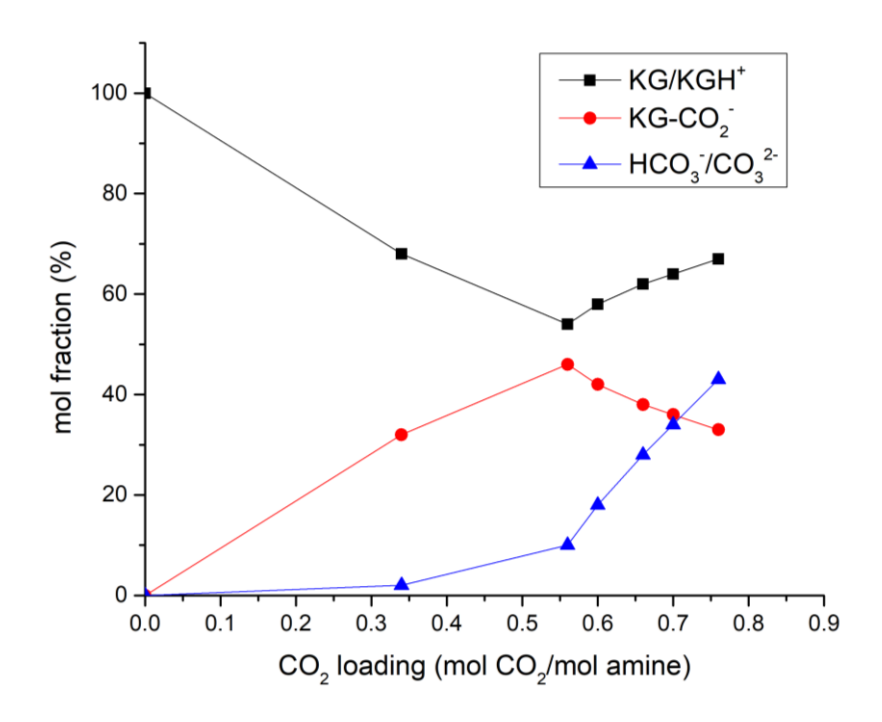


Figure 45. The mole fraction of potassium glycine and its protonated form (KG/KGH⁺, black square), potassium glycine carbamate (KG-CO₂⁻, red dot), and bicarbonate and carbonate ions (HCO₃⁻/CO₃²-, blue triangle) versus the CO₂ loading, characterized by quantitative ¹³C{¹H} NMR. CO₂ loading is calculated by dividing the sum of potassium glycine carbamate and bicarbonate with the initial potassium glycinate concentration. The data are from reference 137.

In the Liao-Smith collaboration, the goal is to use mixture of amino acid solutions as CO₂ absorbents and to analyze the products quantitatively and qualitatively after absorption experiment by ¹³C{¹H} NMR for studying the structure–property relationship. ¹³C{¹H} NMR is powerful tool to quantify the CO₂ adducts in MEA solutions or in amino acid solutions due to the ability to characterize bicarbonate and carbonate concentration and less signal overlapping than ¹H NMR. However, the low natural abundance of the NMR active ¹³C nuclei leads to lower sensitivity of the ¹³C{¹H} NMR and required longer experiment time. ¹³⁸

Quantitative ¹³C{¹H} NMR study with different relaxation delays (d1)

To obtain quantitative NMR result, two factors are critical: (1) the relaxation delay time must be sufficient to avoid saturating the resonances (rule of thumb is four to five times of the longest T_1 carbon nuclei); (2) using a decoupling pulse sequence that avoids contributions to the signal from nuclear Overhauser (NOE) effects. Due to the low signal-to-noise ratio causing by the relatively dilute sample (1 M), the T_1 determination of carbon can take several days. Ciftja and colleagues reported 13 C relaxation times of a mixture of 2 M glycine and 2 M MEA in aqueous solution. 139 The species with the longest d1 is bicarbonate and carbonate ion: 16.3 s. The standard 13 C{ 1 H} NMR experiment parameters are relaxation delay (d1) = 60 s, number of scan (NS) = 1000-2000 (higher number of scan is needed for the sample containing low concentration CO_2 adducts), decoupled–NOE mode. To verify that the d1 (60 s) in the standard method is long enough, a control experiment was performed with the same sample (mixture of proline, alanine, and lysine after CO_2 absorption, abbreviated as PAL absorption sample) and the same parameters (using NS = 1000 and decoupled–NOE mode), except the d1 = 120 s. The integration value

of CO₂ adducts in experiments with different relaxation delays (d1) are compared, with the proline integration value set to 1.00, are shown in Table 8. The results from the two different d1 experiments are similar and indicates the 60 s relaxation delay is adequate in our purpose.

Table 8. Integration value of CO₂ adducts in a mixture of proline, alanine, and lysine solution after CO₂ absorption obtained by ¹³C{¹H} NMR experiments with different relaxation delay (d1). The integration value of proline was set as 1.00.

CO ₂ adducts	Integration value $d1 = 60 \text{ s}$	Integration value $d1 = 120 \text{ s}$
A	1.08	1.01
A-CO ₂	0.16	0.15
P	1.00	1.00
P-CO ₂	0.27	0.26
L	0.53	0.49
$L-CO_2(\alpha)$	0.31	0.31
$L-CO_2(\epsilon)$	0.08	0.09
HCO_3/CO_3^{2-}	1.23	1.14

Assigning ¹³C{¹H} NMR signals of the amino acid sample after CO₂ absorption

Ciftja and co-workers reported a quantitative CO₂ adduct study of using monoethanolamine (MEA) mixed with different amino acids as absorbents including glycine, L-alanine, taurine, sarcosine, L-serine, L-proline by ¹³C{¹H} NMR. ¹⁴⁰ This paper provides a valuable starting point to identify the CO₂ adduct in our amino acid samples. The ¹³C{¹H} NMR signals of alanine solution after CO₂ absorption are assigned based on Ciftja's report (Figure 46). The set of signals (182, 164, 56, and 20 ppm) appeared next to the alanine signals (173, 48, and 17 ppm) are assigned to alanine carbamate and the chemical structure is shown in Figure 46. All the integration values from the carbamate signals are similar (either 0.24 or 0.25), indicating the NMR experiment was quantitative. The peak at 162 ppm is assigned to bicarbonate and carbonate ion. Due to the fast proton

exchange, bicarbonate and carbonate are indistinguishable by NMR. The bicarbonate ions $(HCO3^-)$ should be the major species in the solution after CO_2 absorption (pH = 9.12) based on the pK_a value of the carbonic acid (6.4 and $10.3)^{141}$. The glycine and proline absorption samples are assigned in a similar way and the spectra are shown in the experimental section.

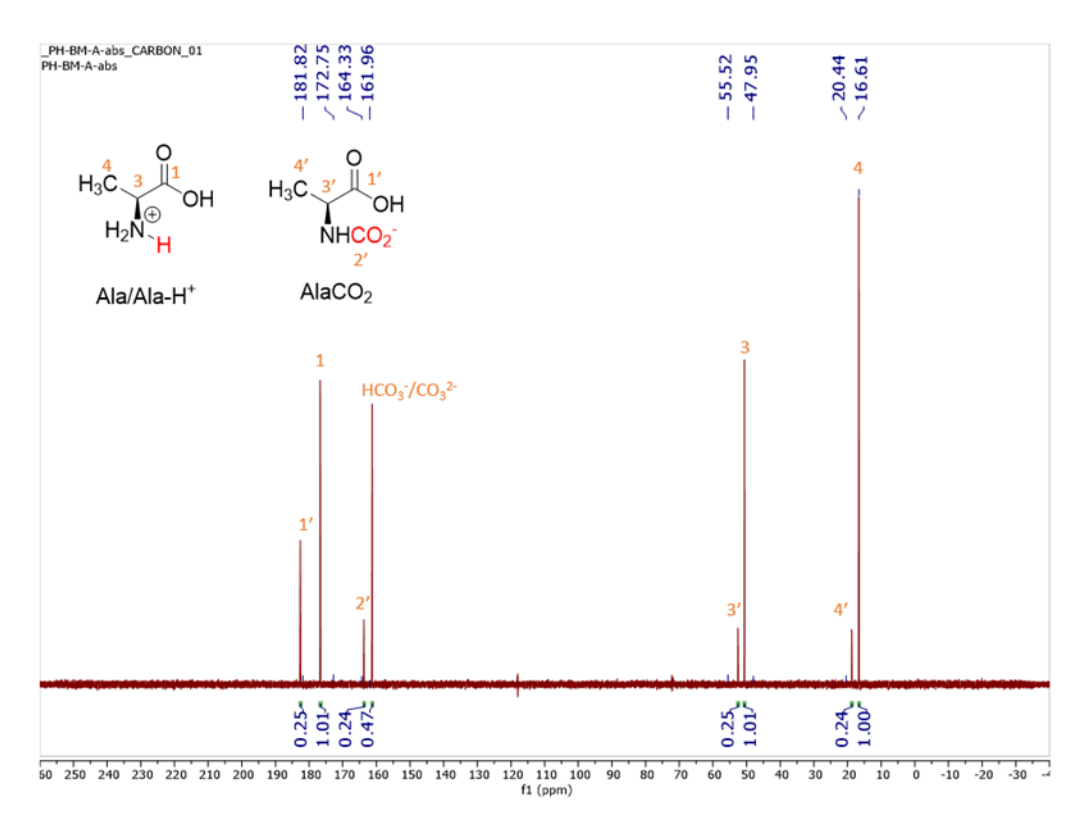


Figure 46. ¹³C{¹H} NMR spectrum of alanine absorption sample in H₂O: D₂O = 5: 1 (v/v).

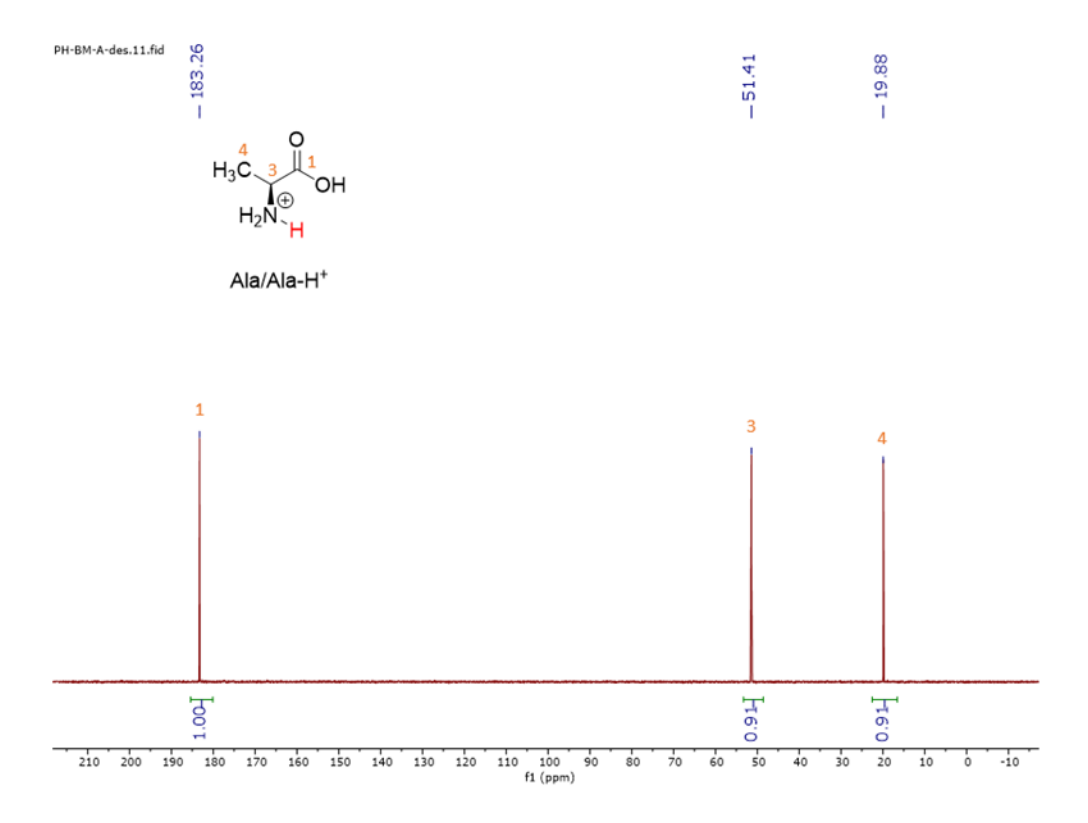


Figure 47. $^{13}C\{^{1}H\}$ NMR spectrum of alanine desorption sample in $H_2O: D_2O = 5: 1 (v/v)$.

The CO₂ desorption process was done by heating the alanine solution to boiling. The pH of the alanine solution increased from 9.12 to 11.08 during the desorption process. The disappearance of the carbamate, carbonate, and bicarbonate ¹³C{¹H} NMR signals indicates that the complete CO₂ desorption from the alanine solution. The carbonyl signal of alanine shifted 10 ppm downfield due to the changing pH environment. The pH value of the amino acid solutions before CO₂ absorption, after CO₂ absorption, and after CO₂ desorption are summarized in Table 9. The pH value of the proline solution after desorption (11.77) is significantly lower than the pH before CO₂ absorption (12.32). The lower pH can be explained by the incomplete desorption observed by ¹³C{¹H} NMR, shown in Figure 48. The desorption mechanism was proposed to be reverse to the absorption process, which the bicarbonate and carbonate ions are decomposed during desorption process so a higher

carbamate concentration compared to bicarbonate and carbonate concentration was observed. Incomplete desorption was also found in glycine sample after desorption with only trace amount of carbamate detected (Figure 49). CO₂ was completely desorbed in lysine and alanine solution.

Table 9. Average pH values of the amino acid salt solution at 298 K before CO₂ absorption, after CO₂ absorption, and after CO₂ desorption. The synthetic gas used in CO₂ absorption process contains 10% CO₂ and 90% air. The pH value was measured by pH meter.

Amino acid	pH value of the solution			
Allillo acid	Before CO ₂ absorption	After CO ₂ absorption	After CO ₂ desorption	
Glycine (G)	11.24±0.028	8.78±0.064	11.10±0.049	
Alanine (A)	11.43±0.021	9.12±0.078	11.08±0.014	
Proline (P)	12.32±0.057	8.91±0.064	11.77±0.035	
Lysine (L)	10.52±0.028	8.36±0.078	10.57±0.085	

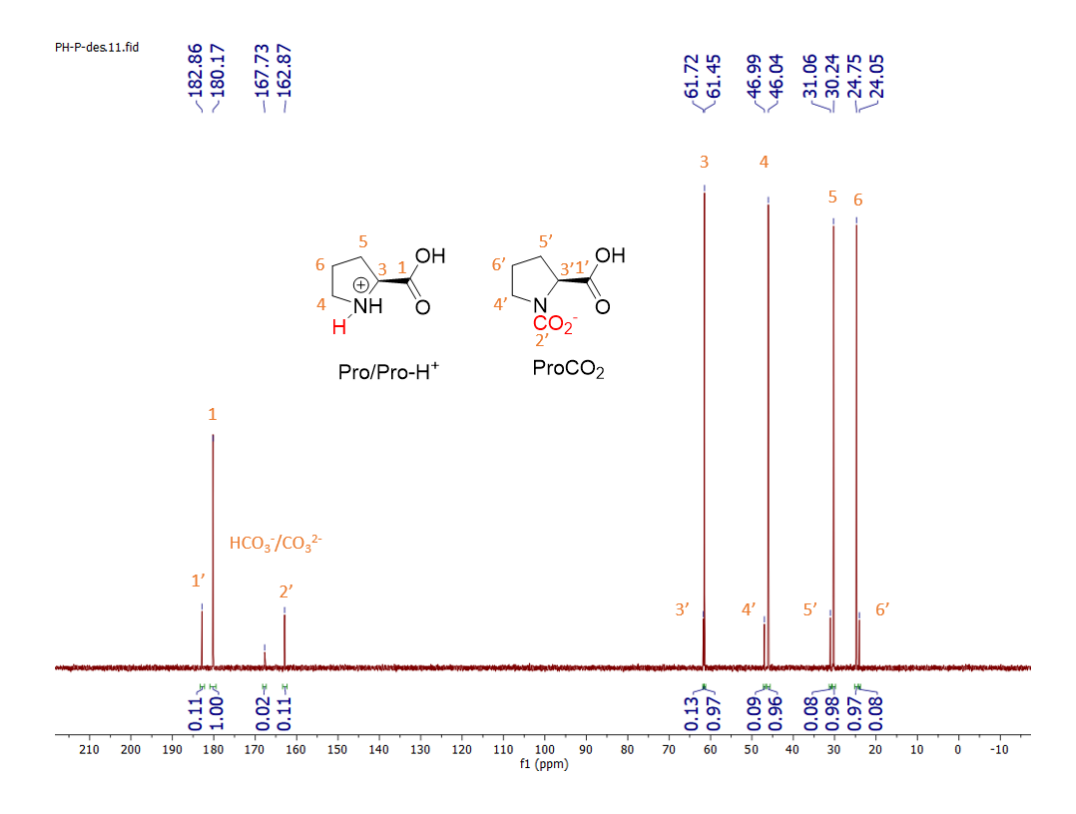


Figure 48. $^{13}C\{^{1}H\}$ NMR spectrum of proline desorption sample in H_2O : $D_2O=5$: 1 (v/v).

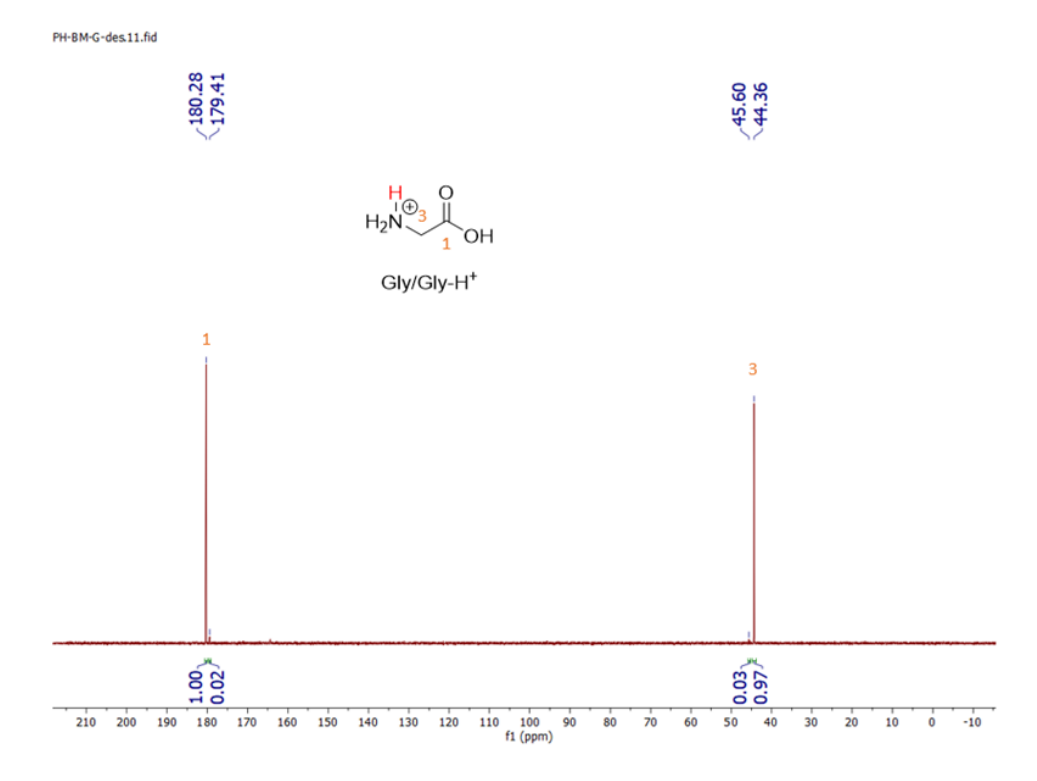


Figure 49. ¹³C{¹H} NMR spectrum of glycine desorption sample in H₂O: $D_2O = 5:1$ (v/v).

Assigning ¹³C{¹H} NMR signals of the lysine sample after absorption

Peak assignments of lysine carbamates were reported by Al-Terkawi and coworkers. 142 The 13 C{ 1 H} NMR spectrum of lysine after absorption has three carbonyl signals (181.43, 175.55, and 175.41 ppm), shown in Figure 50. Based on the observation from other samples, the signal at 175.55 ppm was assigned to lysine (structure A in Scheme 28) due to the bigger integration value than other two signals. Based on the integration value, two sets of carbamate signals were observed. One set of signals contains peaks at 181.43 and 163.76 ppm . Another set of signals are at 175.40 and 164.73 ppm. 2D NMR experiment, Heteronuclear Multiple Bond Correlation (HMBC), was used to assign the carbonyl signals to the α -carbamate (structure B in Scheme 28) and ϵ -carbamate (structure C in Scheme 28). The proton next to the carboxylic acid on the α -carbamate (proton B2 in Figure 51) was shifted downfield due to the proximity to the carbamate. The proton next

to the carboxylic acid on the ε -carbamate was not affected by the carbamate formation since the carbamate is five bonds away. Therefore, the cross-peak between the 1H signal at 3.7 ppm (proton B2) and ^{13}C signal at 181.43 ppm (carbon B1), shown in Figure 51 (blue line), is assigned to α -carbamate (structure B in Scheme 28). The another set of signals (175.40 and 164.73 ppm) is assigned to ε -carbamate (structure C in Scheme 28). The peak assignment of lysine absorption sample is shown in Figure 52 and Figure 53. After assigning peaks on the $^{13}C\{^1H\}$ NMR spectrum, quantitative analysis of the CO₂ adducts will be discussed in the following sections.

Scheme 28. Chemical structures of lysine CO₂ adducts after absorption.

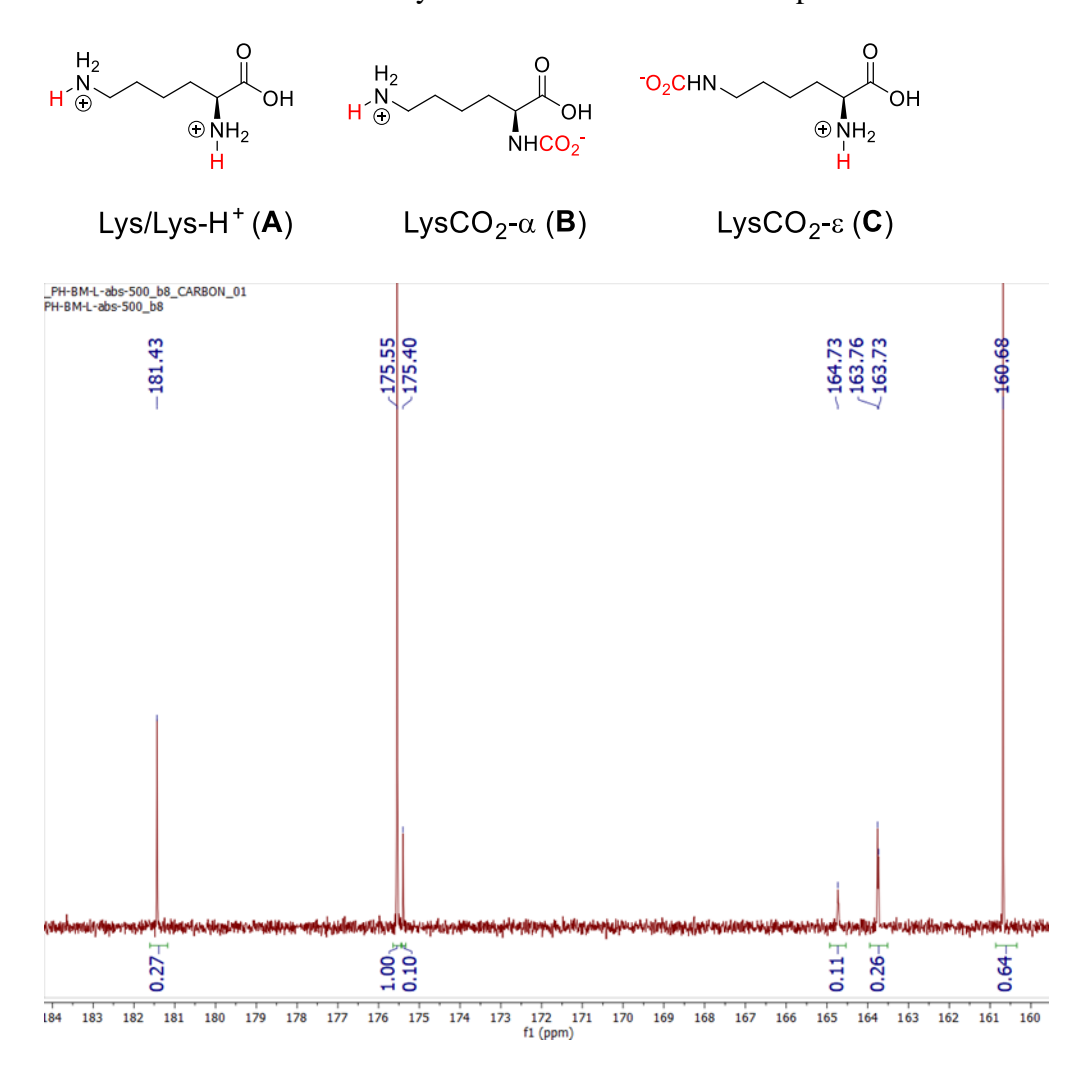


Figure 50. $^{13}C\{^{1}H\}$ NMR of lysine sample after absorption (carbonyl region only) in H_2O : $D_2O=5:1$ (v/v).

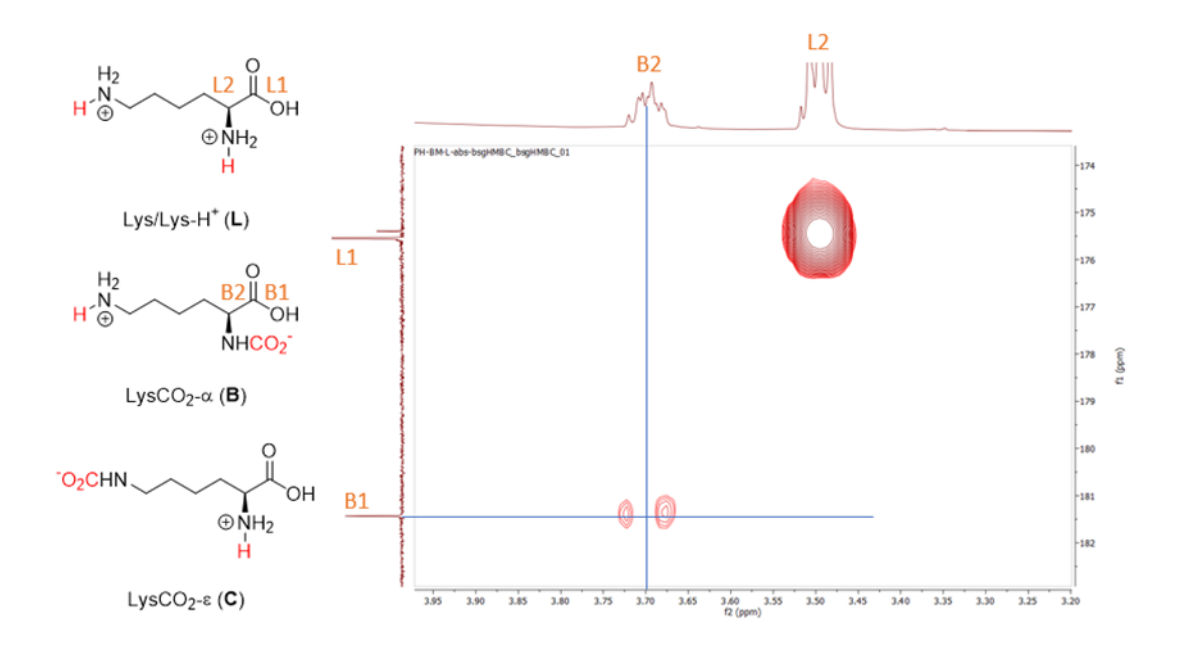


Figure 51. HMBC spectrum of lysine sample after absorption in $H_2O:D_2O = 5:1$ (v/v).

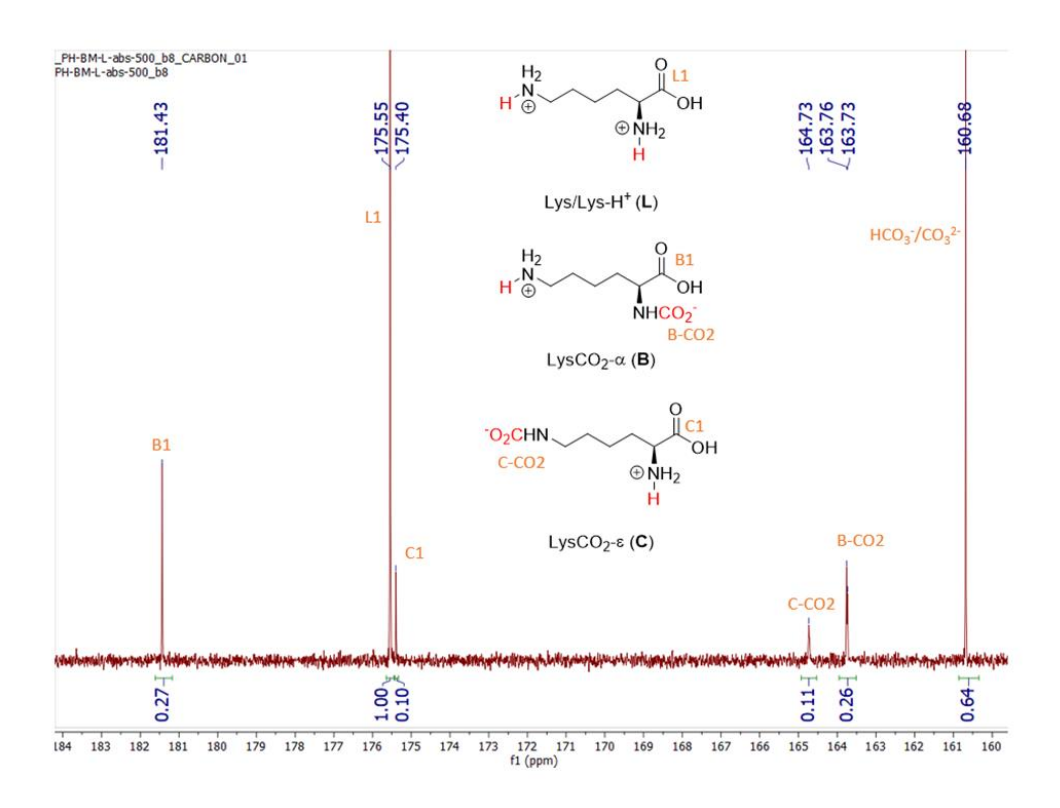


Figure 52. $^{13}C\{^{1}H\}$ NMR spectrum of lysine sample after absorption in D_2O (carbonyl region only).

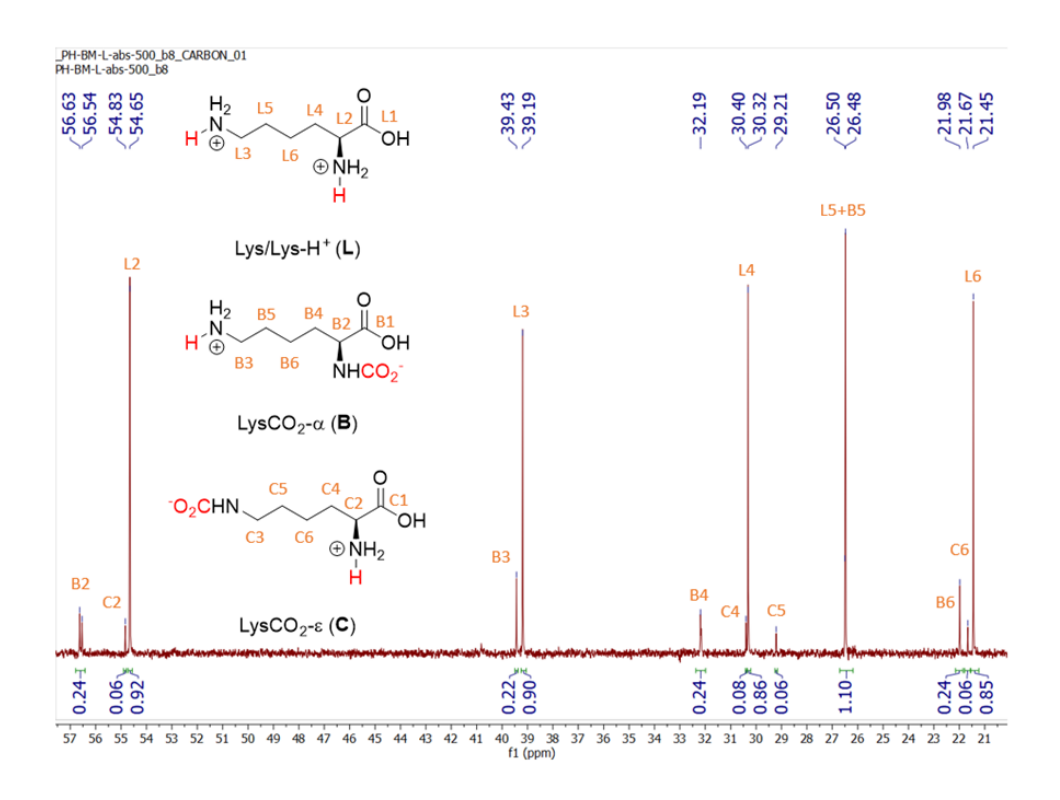


Figure 53. $^{13}C\{^{1}H\}$ NMR spectrum of lysine sample after absorption in D_2O (aliphatic region only).

Determination of initial concentration of amino acid solutions

The total concentration of amino acid containing species (zwitterion amino acid and amino acid carbamate) was assumed to remain constant during CO₂ absorption due to the low volatility of amino acid. If all the initial amino acid converts into zwitterion form and carbamate, the [zwitterion amino acid] and [carbamate] can be calculated by the initial concentration and the product integration ratio. Therefore, the accurate determination of initial concentrations of amino acid solutions (before CO₂ absorption) is critical. The initial concentration was determined by ¹H NMR with water suppression pulse to obtain a flat baseline. The experiment setup is shown in Figure 54. The known concentration of disodium maleate (2 M) was used as the NMR external standard, which was located in the NMR inner tube (red area in Figure 54). The calibration curve was prepared by known

concentration of glycine (0.05 to 1.0 M), located at the outer tube (green area in the Figure 54). The volume normalized integration ratios under different [glycine] were calculated by Eq 13Eq 13 and the results are summarized in Table 10. A linear correlation can be observed if [glycine] was plotted versus volume normalized integration ratios, shown in Figure 55. The calibration curve was then used to determine the initial concentration of all amino acid samples and the results are shown in Table 11.

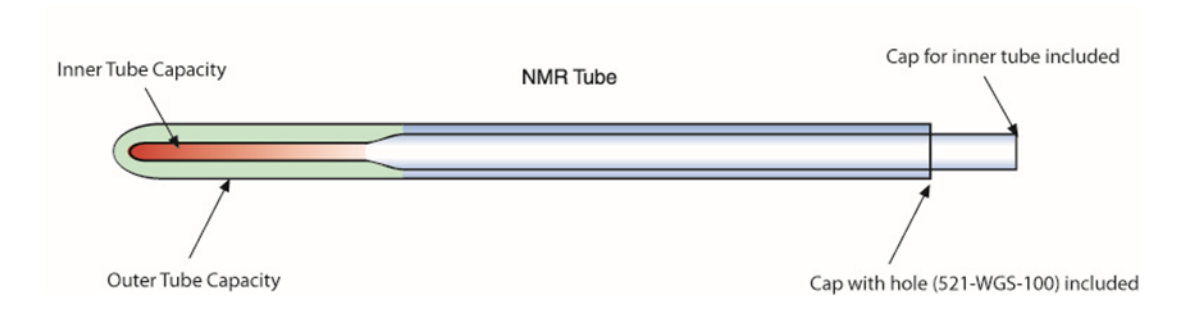


Figure 54. The NMR setup with stem coaxial insert NMR tube. Samples is in the outer tube (green) and the external standard is in the inner tube (red). 143

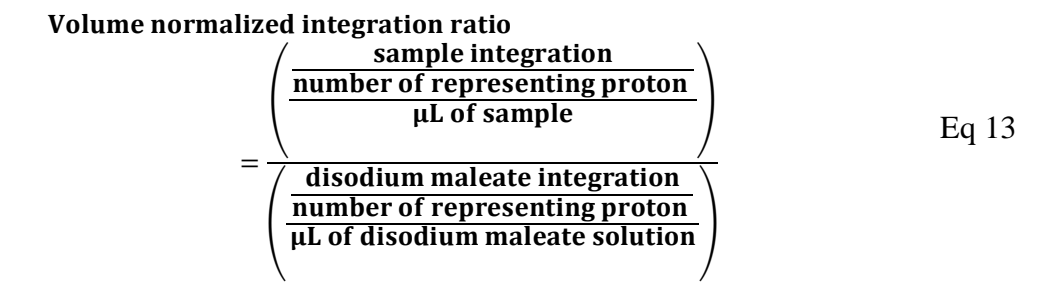


Table 10. Volume normalized integration ratio over different glycine concentration determined by 1H NMR. Known concentration of glycine (600 μ L in outer tube) and 2 M of disodium maleate (60 μ L in inner tube) in $H_2O: D_2O = 5: 1$ (v/v).

Volume Normalized Integration Ratio	[Glycine] (M)	
0.0220	0.051	
0.0888	0.202	
0.1765	0.404	
0.2695	0.606	
0.4407	1.010	

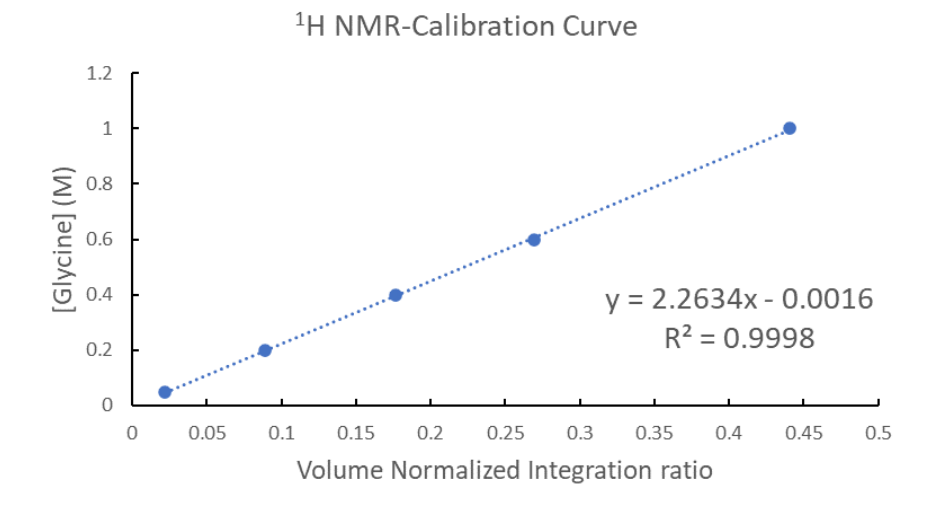


Figure 55. The 1H NMR calibration curve using external standard (60 μL of 2 M disodium maleate solution).

Table 11. Initial concentration of amino acid samples before absorption. (G: glycine, A: alanine, P: proline, and L: lysine)

Sample	Initial	Sample	Initial
	concentration (M)		concentration (M)
G	0.893	GL	0.755
A	0.888	PL	0.779
P	0.856	GAP	0.887
L	0.679	GPL	0.820
AP	0.890	PAL	0.778
GA	0.875	GAL	0.838
GP	0.926	GAPL	0.793
AL	0.772		

Determination of CO₂ adduct by ¹³C{¹H} NMR integral ratio (primary method)

With the accurate determination of initial concentration, the zwitterionic amino acid concentration and carbamate concentration can be calculated by the integration values of the zwitterion amino acid and the carbamate. Based on the assumption, the total concentration of zwitterion glycine and glycine carbamate in the sample after absorption equals to the initial concentration of glycine from the previous section (0.893 M). The normalized integration value is calculated by dividing initial concentration after dilution (0.744 M, diluting with D_2O for NMR sample preparation) with the total integration value of zwitterion glycine (100.00, signal G1 in Figure 56) and glycine carbamate (33.01, signal G1 $^{\prime}$ in Figure 56), shown in Eq 14Eq 14. The normalized integration value was then used to determine the concentration of the CO_2 adducts by multiplying the corresponding integral vales and the dilution factor (1.2). The concentration of each species is: [glycine zwitterion] = 0.674 M, [carbamate] = 0.222 M, [HCO₃ $^{\prime}$ /CO₃ $^{\prime}$ -] = 0.282 M. The result will then be verified by the external standard method using the same sample. More details will be discussed in the next section.

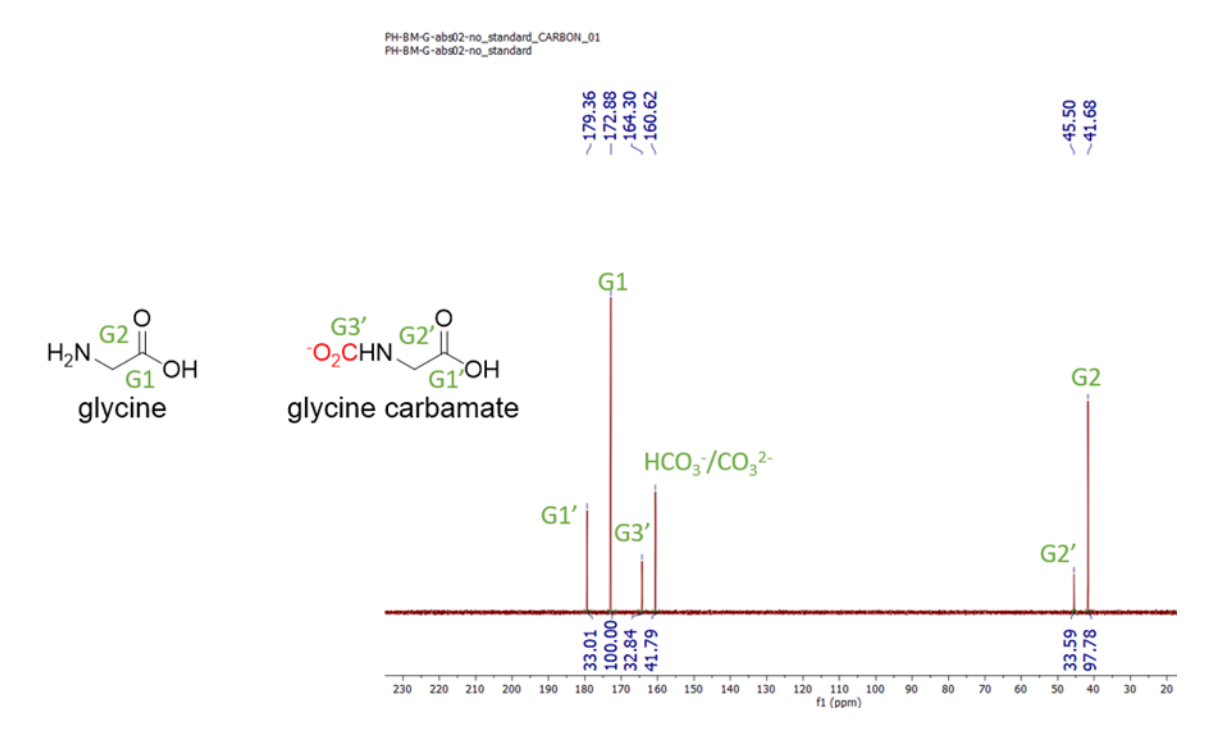


Figure 56. ¹³C{¹H} NMR spectrum of glycine sample after absorption.

Normalized integral value (glycine)
$$= \frac{initial\ concentration\ (M)}{integral\ value\ of\ amino\ acid\ containing\ products}$$

$$= \frac{0.744}{100.00 + 33.01} = 0.0056\ (M/integral\ value)$$
Eq 14

Verifying the primary method by ¹³C{¹H} NMR experiment with external standard

Obtaining the absolute concentration by NMR using coaxial insert tube with external standards was reported by Koichi, ¹⁴⁴ Fulton, ¹⁴⁵ and Henderson. ¹⁴⁶ An external standard with known concentration is used to verify the glycine concentration obtained from the primary method shown in the previous section. Disodium maleate was chosen as external standard due to its low volatility, good solubility in D₂O, and containing minimum interfering signals to the desired peaks. The ¹³C NMR samples were taken in the NMR coaxial insert tube and the setup is like the one used for determining initial concentration. The volume normalized integration ratio is calculated by Eq 15Eq 15.

$$Volume \ normalized \ integration \ ratio: \ \frac{\left(\frac{glycine \ integration}{\mu L \ of \ glycine}\right)}{\left(\frac{disodium \ maleate \ integration}{\mu L \ of \ disodium \ maleate}\right)} \ Eq \ 15$$

The calibration curve was plotted by glycine concentration versus volume normalized integration ratio, shown in Figure 57. The same glycine sample after absorption from the previous section was ran with the external standard, and the spectrum is shown in Figure 58. The amount of CO₂ adducts was determined by the ¹³C NMR calibration curve.

The results are compared with the primary method from the previous section and summarized in Table 12. The CO₂ adduct concentration from both methods are similar, which suggest that the concentration determined by primary method is accurate and can be used to determine rest of the samples after absorption or desorption.

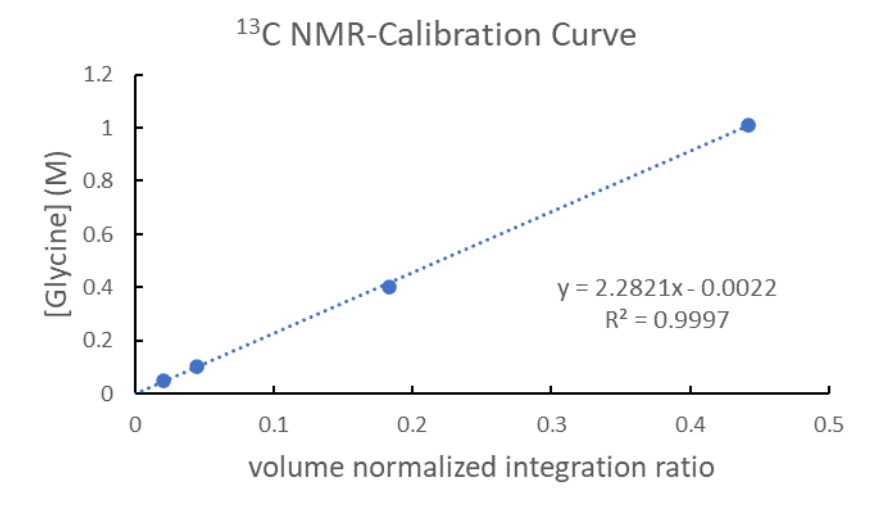


Figure 57. ¹³C{¹H} NMR calibration curve using external standard (2 M disodium maleate solution).

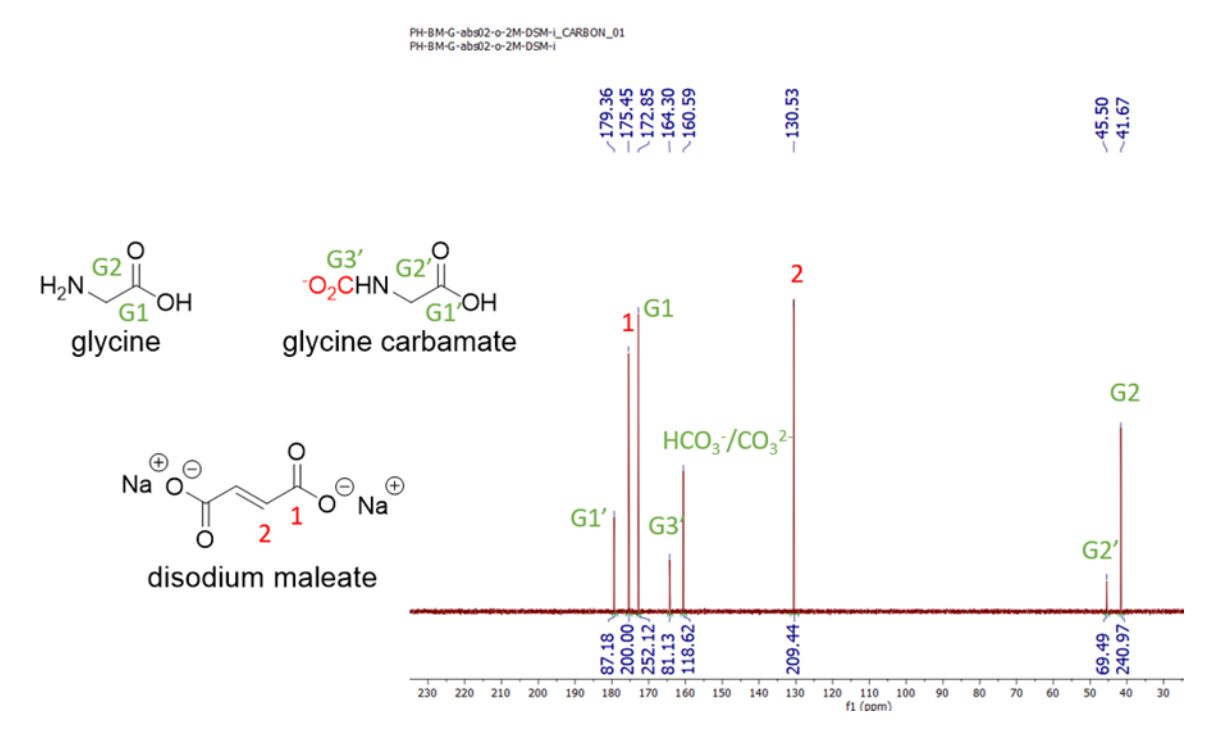


Figure 58. $^{13}C\{^{1}H\}$ NMR spectrum of glycine sample after absorption (600 μ L) with 2 M disodium maleate (60 μ L) as external standard.

Table 12. Glycine sample after absorption characterized by different methods (primary method versus external standard method).

Glycine after absorption	Glycine	Carbamate	HCO ₃ ⁻ /CO ₃ ² -
Primary method (Initial conc. = 0.893 M)	0.674 M	0.222 M	0.282 M
External standard method	0.688 M	0.237 M	0.323 M

Comparing different amino acid solutions as CO₂ absorbents

Different amino acid solutions were utilized as CO₂ absorbents and the CO₂ adducts were characterized by ¹³C{¹H} NMR using primary method mentioned above. The results are summarized in Table 13. The absorption experiments were ended when the CO₂ concentration became constant from CO₂ scrubber outlet. At this point, we considered the absorbent solutions reached an equilibrium with CO₂. Glycine sample has the highest

carbamate concentration due to the stable carbamate structure formed by less hindered amino group. The methyl group on the alanine leads to a less stable carbamate structure due to the steric repulsion between oxygen and methyl group as, shown in Scheme 29. Carbamate formation is an inefficient CO₂ capture route since it consumes two equivalents of amine to react with one equivalent of CO₂ (Scheme 27). The formation of bicarbonate is more favorable and can maximize the CO₂ capture efficiency. Sartorl and Savage studied the carbamate stability of hindered and conventional amino alcohols by ¹³C{¹H} NMR.¹⁴⁷ They found that the carbamate stability constants decrease with the increase steric repulsion around the amino group: monoethanolamine (MEA) (12.5 at 40 °C), diethanolamine (DEA) (2.0 at 40 °C), and aminomethyl propanol (AMP) (< 0.1 at 40 °C). The less stable carbamate from steric hindered amine decomposes to bicarbonate ion via hydrolysis (Scheme 26) and releases the free amine for another CO₂ capture process. Hook also reported the steric hindered amines, like AMP, potassium alaninate, potassium methyl alaninate, have enhanced absorption capacities.¹⁴⁸ This explanation is consistent with our alanine result. Alanine absorbs 0.574 mol of CO₂ per mol of amino acid, which is 3% higher than the glycine counterpart. Proline has less steric hinderance around the amino group than alanine due to the protruding amino group. It has carbamate and [HCO₃⁻/CO₃²-] concentration between glycine and alanine. Lysine has the highest absorption capacity probably due to the presence of two amino groups. The absorption capacity follows the order: lysine > proline > alanine > glycine.

The steric hindrance also deactivates the amino group and decrease the CO₂ absorption rate at lower CO₂ loading (0–0.3 mol CO₂/mol amine). Therefore, mixture of amines containing different structures is a common strategy to obtain absorbents with fast

reaction kinetic and high capture capacity. Mixtures of amino acids as CO_2 absorbents will be discussed in the next section.

Table 13. Summary of CO₂ adducts of single amino acid solutions. AA is amino acid and AA-CO₂ is amino acid carbamate.

	Glycine	Alanine	Proline	Lysine
Species	Concentration (M)	Concentration (M)	Concentration (M)	Concentration (M)
AA	0.645	0.715	0.651	0.498
AA-CO ₂	0.252	0.177	0.208	0.134 (α -carbamate)
				0.050 (ε-carbamate)
HCO ₃ ⁻ /CO ₃ ² -	0.245	0.333	0.293	0.318
Initial conc. (M)	0.893	0.888	0.856	0.679
Absorption capacity* (mol CO ₂ /mol AA)	0.557	0.574	0.585	0.740

^{*} Absorption capacity is divided the sum of carbamate and HCO₃⁻/CO₃²⁻ concentration with initial concentration.

Scheme 29. The steric effect to the amino acid-CO₂ intermediate stability.

Mixture solutions containing two amino acids as CO₂ absorbents

The mixture solutions containing two amino acids were used as CO₂ absorbents and their CO₂ adducts were characterized by ¹³C{¹H} NMR, shown in Table 14. All the mixture solutions have higher absorption capacity (0.586–0.665 mol CO₂/mol AA) than

the glycine, alanine, and proline single amino acid solution (0.557–0.585 mol CO₂/mol AA). The expected absorption capacity is calculated by Eq 16Eq 16. The sum of each amino acid concentration in the mixture times the corresponded absorption capacity was divided by the initial concentration of the mixture solution. To determine the enhancing absorption capacity of the mixture amino acid solutions, the %difference between experimental and expected absorption capacity is calculated by Eq 17Eq 17. Following the % difference, the AP has the highest %difference (9.8%) than other amino acid mixture solutions. All the mixture AA solutions with positive %difference have relatively high HCO₃-/CO₃²⁻ concentration, indicating that the CO₂ capture through bicarbonate formation is critical. It is also supported by the steric hindered alanine is presented in 3 out of 4 sample with positive %difference.

The two amino acid mixtures can also be seen as competition experiments for two absorbent species reacting with CO₂. In GA and GP samples, the glycine form more stable carbamate with CO₂ and has the higher carbamate concentration than alanine and proline. In AP sample, alanine has lower carbamate concentration than proline, which indicate the proline carbamate may be more stable than the alanine carbamate.

Expected absorption capacity

$$= \frac{\text{(each AA concentration)(single AA absorption capacity)}}{\text{initial concentration}}$$
Eq 16

% Difference

$$= \frac{\text{(experimental absorption capacity } - \text{ expected absorption capacity)}}{\text{expected absorption capacity}} \times 100$$

Table 14. CO₂ adducts of solutions containing two amino acids. (G: glycine, A: alanine, P: proline, and L: lysine)

Species	PL Conc. (M)	GL Conc. (M)	AL Conc. (M)	GA Conc. (M)	GP Conc. (M)	AP Conc. (M)
A			0.388	0.395		0.360
$A-CO_2$			0.055	0.043		0.074
G		0.309		0.279	0.323	
$G-CO_2$		0.111		0.163	0.161	
P	0.362				0.396	0.353
P-CO ₂	0.080				0.050	0.106
L	0.217	0.235	0.203			
$L-CO_2(\alpha)$	0.094	0.074	0.092			
$L-CO_2(\epsilon)$	0.029	0.028	0.037			
HCO_3 - $/CO_3$ ² -	0.253	0.269	0.328	0.317	0.350	0.389
Initial conc. (M)	0.779	0.755	0.772	0.875	0.926	0.890
Experimental absorption capacity (mol CO ₂ /mol AA)*	0.586	0.639	0.665	0.597	0.606	0.639
Expected absorption capacity (mol CO ₂ /mol AA) [#]	0.655	0.640	0.648	0.569	0.573	0.582
%Difference@	-10.5	-0.2	2.6	4.9	5.8	9.8

A is alanine; G is glycine; P is proline; L is lysine. *Experimental absorption capacity is divided the sum of carbamate and HCO_3 -/ CO_3 -concentration with initial concentration. # Expected absorption capacity is defined by Eq 16Eq 16. [@] % difference is defined by Eq 17Eq 17.

Mixture solutions containing three and four amino acids as CO₂ absorbents

CO₂ capture by the mixture solutions containing three or four amino acids were tested and analyzed by the same method as the two amino acid mixtures. The absorption capacities of GAL (0.674 mol CO₂/mol AA) and GPL (0.723 mol CO₂/mol AA) samples are higher than the two amino acid mixtures. These two samples also have much higher HCO₃-/CO₃²- concentration (0.370 and 0.373 M, respectively) than the rest of the three or four mixture samples.

The four amino acid mixture GAPL have higher absorption capacity than expected capacity but the HCO_3^{-}/CO_3^{2-} concentration is significantly lower than GAL and GPL samples. In GAPL sample, the mole fraction of each amino acid carbamate still follows the order: glycine > lysine > proline > alanine.

Table 15. CO₂ adducts of solutions containing three or four amino acids. (G: glycine, A: alanine, P: proline, and L: lysine)

Species	PAL Conc. (M)	GAP Conc. (M)	GAL Conc. (M)	GPL Conc. (M)	GAPL Conc. (M)
A	0.246	0.234	0.282		0.185
$A-CO_2$	0.036	0.043	0.028		0.022
G		0.157	0.217	0.196	0.133
$G-CO_2$		0.125	0.090	0.105	0.07
P	0.228	0.266		0.260	0.187
P-CO ₂	0.061	0.066		0.032	0.031
L	0.121		0.147	0.147	0.107
$L-CO_2(\alpha)$	0.071		0.056	0.064	0.046
$L-CO_2(\epsilon)$	0.018		0.020	0.019	0.015
HCO ₃ ⁻ /CO ₃ ² -	0.280	0.276	0.370	0.373	0.325
Initial conc. (M)	0.778	0.887	0.838	0.820	0.793
Experimental absorption capacity (mol CO ₂ /mol AA)*	0.600	0.575	0.674	0.723	0.643
Expected absorption capacity (mol CO ₂ /mol AA) [#]	0.625	0.575	0.613	0.620	0.610
% Difference [@] A is alanine: G is glyc	-4.0%	0%	10.0%	16.6%	5.4%

A is alanine; G is glycine; P is proline; L is lysine. *Experimental absorption capacity is divided the sum of carbamate and HCO_3^-/CO_3^{-2-} concentration with initial concentration. # Expected absorption capacity is defined by Eq 16Eq 16. [@] % difference is defined by Eq 17Eq 17.

Conclusion

Different amino acids were tested as post combustion capture absorbents. The CO₂ adducts such as carbamate and HCO₃-/CO₃²⁻, were quantitatively analyzed by ¹³C{¹H}

NMR. The amino acid structures affect the stabilities of the corresponded amino acid carbamates. The amino group with less steric hinderance like glycine stabilizes the carbamate and inhibits the formation of HCO_3^-/CO_3^{-2} . The bulky substituent around amino group destabilizes the carbamate structure and further decomposes to HCO_3^- and CO_3^{-2} ions, which enhances the absorption capacity. The absorption capacity of single amino acid solution follows this order: lysine > proline > alanine > glycine. Most of the amino acid mixture solutions have higher absorption capacity than the single amino acid solutions. We found GPL and GAL are the mixture solutions with the highest absorption capacity (0.723 and 0.674 mol CO_2/mol AA, respectively), which is 16.6% and 10.0% higher than the expected absorption capacity, respectively. The results prove that the proper formulation can enhance the CO_2 absorption capacity and pave the way to use amino acid mixtures from biomass as absorbents.

Experimental section

The NMR spectra were collected either on a Bruker Avance III HD 500 MHz NMR spectrometer equipped with 5mm iProbe (X-nucleus optimized double resonance broad band probe) or on a Varian Inova 500 MHz NMR spectrometer equipped with 5mm PFG broad band switchable probe. Both spectrometers operate at a frequency of 125 MHz for ¹³C and 500 MHz for ¹H. All the NMR experiments were run at 25 °C. The NMR samples were prepared by diluting 0.5 mL of the aqueous amino acid solutions after absorption or desorption with 0.1 mL of deuterium oxide (D₂O) for the signal lock.

Quantitative ¹H NMR parameters

The original amino acid concentrations were determined by 1H NMR using Agilent DirectDrive2 500 spectrometer at 25 °C. The spectra were run with water suppression pulse, (H)wet1D experiment, and used the following parameters: number of scans, NS = 8; acquisition time, AT = 4; relaxation delay, $D_1 = 60$ s (relaxation time of nuclei $D_1 \ge 5T_1$, T_1 : the longest carbon nuclei relaxation time constant). The $^{13}C\{^1H\}$ NMR spectra were phase corrected automatically, baseline corrected (Whittaker Smoother), and integrated using MestReNova software v.14.2.0.

Quantitative ¹³C{¹H} NMR parameters

Quantitative 13 C{ 1 H} NMR spectra were collected on either of the spectrometers (Bruker HDIII 500 MHz NMR and Varian Inova 500 MHz NMR). The samples ran with Bruker used the following parameters: pulse duration $p_1 = 5 \mu s$ for 45° pulse, NS = 800-1600 (a larger number of scans were used for the three and four amino acid mixtures to get better signal-to-noise ratio), AT = 1.10 s, and D₁ = 60 s. The samples ran on the Varian

were with the following parameters: pulse duration $p_1 = 5.25~\mu s$ for 45° pulse, NS = 800-1600, AT = 1.04 s, and $D_1 = 60~s$ (relaxation time of nuclei $D_1 \ge 5T_1$, T_1 : the longest carbon nuclei relaxation time constant). The $^{13}C\{^1H\}$ NMR spectra were phase corrected automatically, baseline corrected (Whittaker Smoother), and integrated using MestReNova software v.14.2.0.

Chapter 6. Amino acid derived polyurea materials

Introduction

In Smith-Liao collaboration, algal biomass is produced by the CO₂ capture process with algae culture solution and Table 16 lists top 7 abundant amino acids in the algal biomass. The goal is to turn the amino acids from the biomass into value-adding polymeric materials and can fix CO₂ for long term. Polyurea is commonly used in elastic fibers like Spandex[®], surface coating for protecting surface from weathering or salt corrosion. Polyurethane and polyurea coating are commonly used for roof and floor coating due to its chemical resistance and durability. Several considerations for the retrosynthesis of amino acid derived polyurea are: (1) the polyurea polymerization is a catalyst free but moisture sensitive process; (2) to synthesize diamine from the amino acids, protecting amino groups is needed to prevent dimerization. The 4,4′-methylenediphenyl diisocyanate (4,4′-MDI) is one of the commonly used aromatic diisocyanates if the product is not exposed to sunlight. The aliphatic diisocyanates like 1,6-hexamethylene diisocyanate have better light stability and are used for the outdoor application.

Table 16. Amino acid profile of the algal biomass (g per 100 g crude protein). Only the top 7 abundant amino acids are included.

Amino acids	Content (g/100 g crude protein)		
Alanine	13.35		
Glycine	11.04		
Glutamic acid	10.51		
Lysine	10.32		
Leucine	8.52		
Valine	7.96		
Aspartic acid	5.79		

Figure 59. Retrosynthesis of polyurea from aromatic diisocyanate and diamine from amino acids.

Synthesis of symmetric diamine monomers from amino acids

L-Phenylalanine, L-leucine, and L-alanine, which will be referred as phenylalanine, leucine, and alanine, respectively, are introduced to the monomer structures to study the

structure–property relationship of the resulted polyurea materials. Different spacer lengths (C2 and C12) were studied to understand its effect on polymer properties. The synthetic routes to monomers bearing different amino acid and spacer length are shown in Scheme 30. Amino groups on the amino acids were protected by tert-butyloxycarbonyl (Boc) group first and the carboxylic groups were then activated by coupling with Nhydroxysuccinimide (NHS). The amidation is done by reacting Boc protected amino acid NHS esters with diamines with different lengths (ethylenediamine or 1,12diaminododecane) to form Boc-protected diamines. The deprotection process can be easily done by either HCl in methanol or trifluoroacetic acid in DCM. The solubility of the symmetric diamine monomers is greatly affected by the amino acid structure and spacer length. The monomers containing leucine and phenylalanine have higher solubility in the organic solvents like DCM, diethyl ether, and ethyl acetate due to their hydrophobic side chains. However, after neutralizing with NaOH solution, the highly water-soluble NH₂-Ala-C2-Ala-NH₂ cannot be extracted into the organic layers. The longer spacer length counterpart (NH₂-Ala-C12-Ala-NH₂) was easily isolated with better yield (92%).

Scheme 30. Synthesis of symmetric diamine monomers from different amino acids (phenylalanine, leucine, and alanine) and two different spacer lengths (C2 and C12).

The polymerizations of symmetric diamines and 4,4'-MDI were conducted in anhydrous DMF at 50 °C, shown in Scheme 31. The polymerization rate is fast and polymer solutions became viscous within 10 minutes, but the prolonged reaction time was given to ensure the polymerization was complete. The isocyanate end groups on the polyurea were quenched during work-up by stirring with methanol for 1 hour and the solid products were filtered out and dried under vacuum until constant weight. The nomenclature is based on the diamine monomer structure so the polyurea prepared from NH₂-Phe-C12-Phe-NH₂ is named as PU-NH-Phe-C12-Phe-NH. The IR spectra of polyureas and 4,4'-MDI were overlapped and the distinctive NCO stretching band from 4,4'-MDI was not observed in all the IR spectra of polyurea series, shown in Figure 60. All the isocyanate was consumed during polymerization or quenched during the workup.

Scheme 31. Polymerization of symmetrical diamine monomers with 4,4′-MDI.

Figure 60. Overlapped FT-IR spectrum of 4,4'-MDI (green), PU-NH-Leu-C12-Leu-NH (black), PU-NH-Phe-C12-Phe-NH (red), and PU-NH-Ala-C12-Ala-NH (blue).

Assigning ¹H NMR signals of the polyureas

¹H NMR signals of the polyureas were assigned based on gradient-selected Correlation spectroscopy (gCOSY) spectra. The ¹H NMR spectrum of PU-NH-Phe-C2-

Phe-NH was shown in Figure 61 as an example of peak assignment and the proton signals of the rest polyurea samples were assigned in a similar fashion. The protons 5 (in Figure 61) is a distinctive signal from the methine from the phenylalanine moiety and was used it as a starting point to assign other signals by gCOSY. The highlighted cross-peaks with protons 5 were shown in Figure 62 and the protons 6 were identified as the urea protons next to protons 5 based on the chemical shift. Another two cross-peaks (protons 1 and 2) are assigned to the methylene group neighboring to the protons 5. The relatively downfield protons 4 were found to have a cross-peak with protons 7 and this match with the methylene group from the 4,4'-MDI (Figure 63). Now the methylene groups on the C2 spacer were the only aliphatic protons left and were assigned to protons 3. The protons 10 were then assigned to the amide protons because of the cross-peak between protons 3 and protons 10 (Figure 64). The most downfield protons 11 did not have a cross-peak on gCOSY and was assigned to another urea protons next to the 4,4'-MDI moiety. All the proton signals of PU-NH-Phe-C2-Phe-NH were assigned and shown in Figure 65.

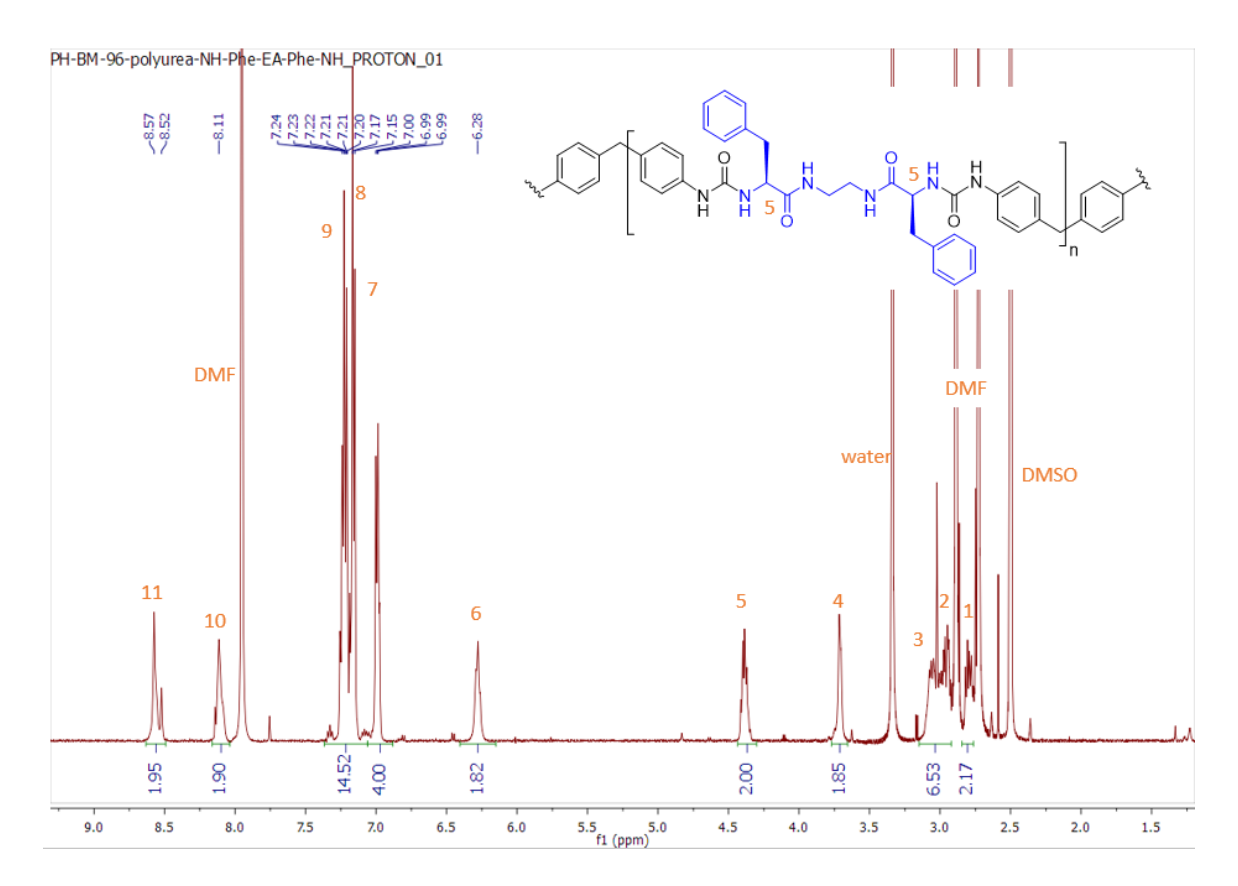


Figure 61. ¹H NMR of PU-NH-Phe-C2-Phe-NH in DMSO-*d*₆.

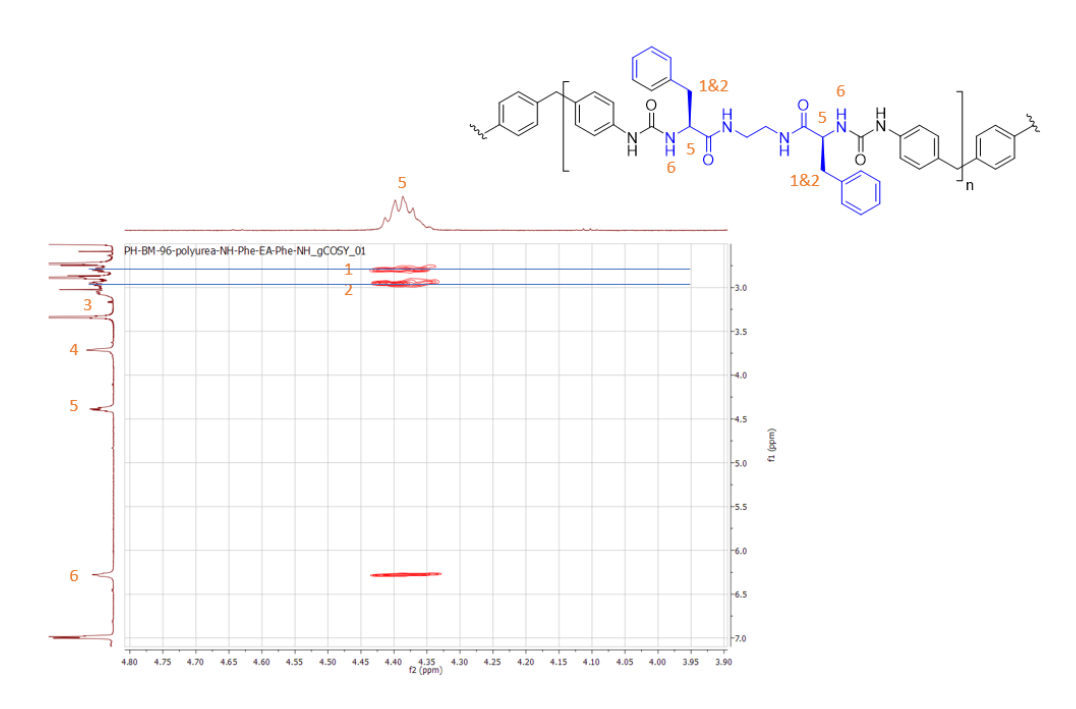


Figure 62. gCOSY of PU-NH-Phe-C2-Phe-NH in DMSO- d_6 highlighting the cross-peaks with protons 5.

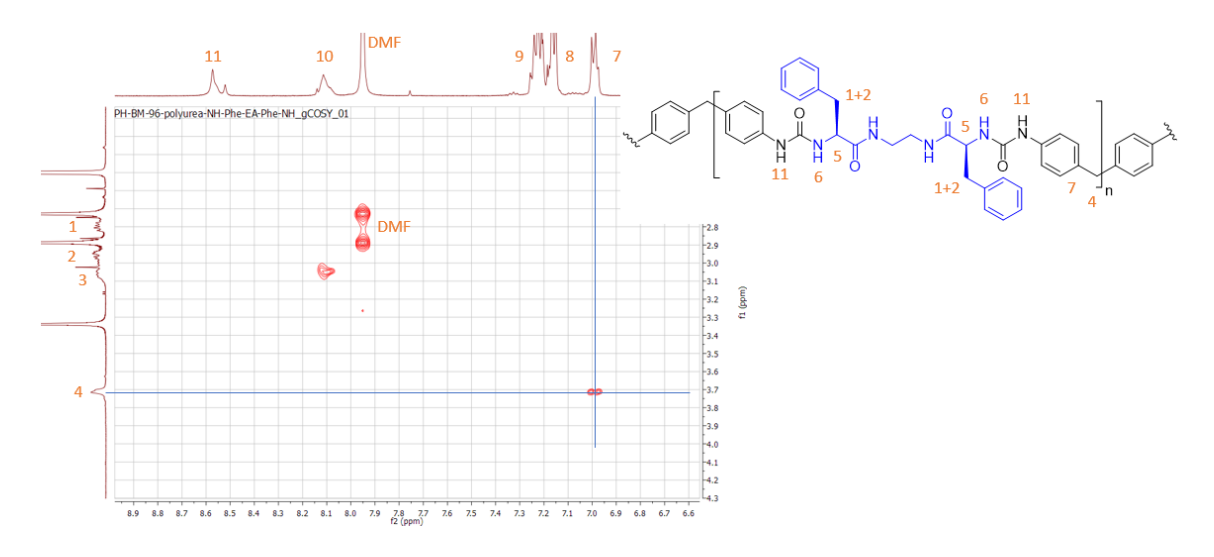


Figure 63. gCOSY of PU-NH-Phe-C2-Phe-NH in DMSO- d_6 highlighting the cross-peaks between protons 4 and protons 7.

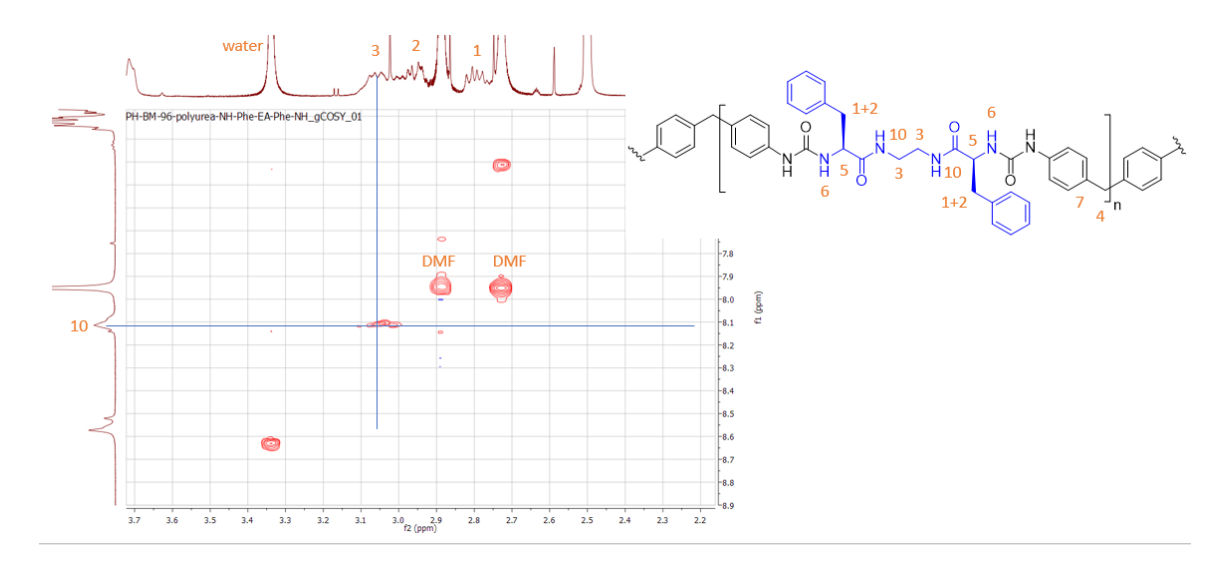


Figure 64. gCOSY of PU-NH-Phe-C2-Phe-NH in DMSO- d_6 highlighting the cross-peaks between protons 3 and protons 10.

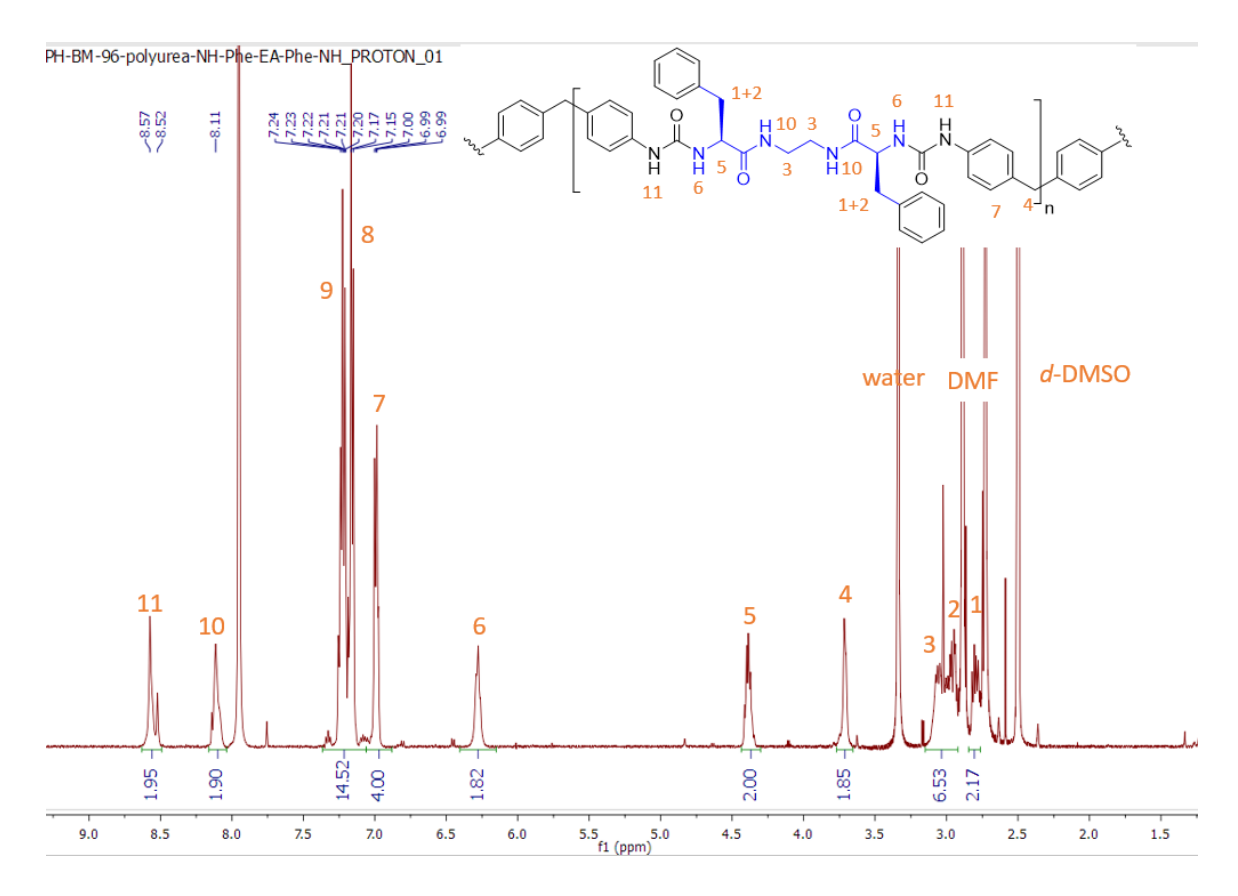


Figure 65. ¹H NMR of PU-NH-Phe-C2-Phe-NH in DMSO- d_6 with all the signals assigned on the polymer chemical structure.

The overlaid proton spectra of polyureas are shown in Figure 66. Similar proton signal patterns were observed over polyurea series and were assigned by the method mentioned above.

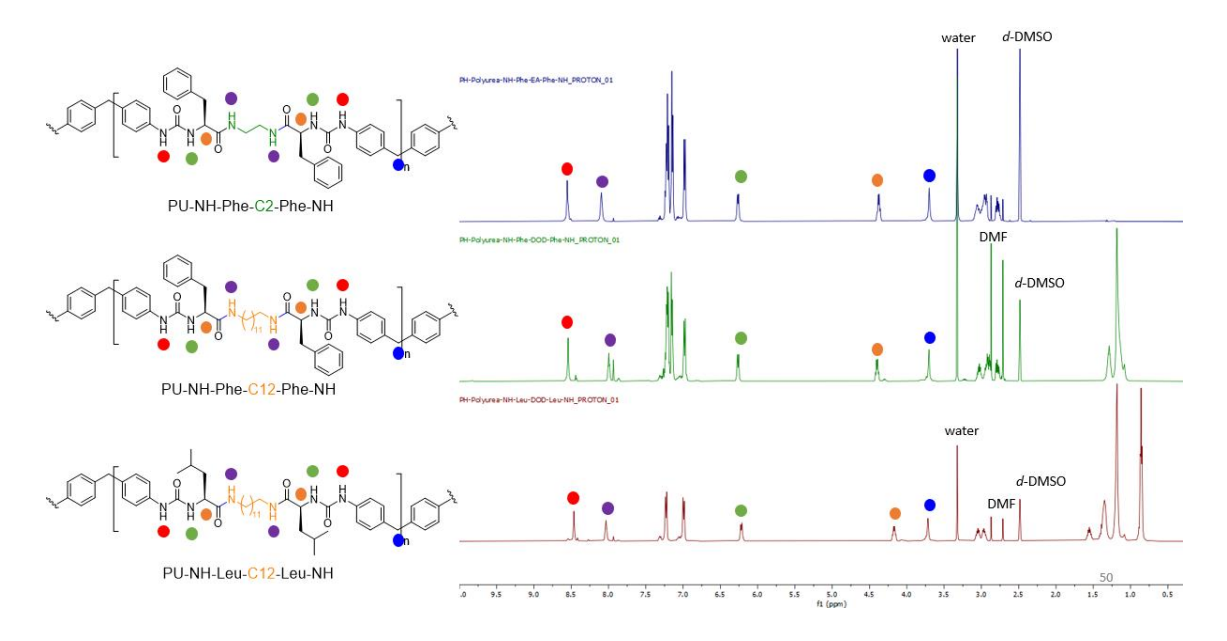


Figure 66. Overlapped ¹H NMR of PU-NH-Phe-C2-Phe-NH (top), PU-NH-Phe-C12-Phe-NH (middle), and PU-NH-Leu-C12-Leu-NH (bottom).

Thermal analysis of polyureas

Thermal analysis studies the property variation of the sample over a temperature range under careful temperature control. Thermal analysis plays an important role for understanding the performance and limitation of the polymer materials. Differential Scanning Calorimetry (DSC), Thermogravimetric Analysis (TGA), Thermomechanical Analysis (TMA), and Dynamic Mechanical Analysis (DMA) are the four common thermal analysis techniques. DSC and TGA are used to characterize the glass transition temperature and onset temperature of polyureas bearing amino acids.

Glass transition temperature (T_g) is a reversible transition from a hard and brittle glassy state to viscous rubbery state and results in a considerable drop of the polymer mechanical strength. T_g provides the polymer properties under a specific working temperature and is a critical thermal property for selecting a proper material for the desire application.

Study the effect of spacer length

The Differential scanning calorimetry (DSC) data for PU-NH-Phe-C2-Phe-NH is shown in Figure 67 and the middle point of the transition was taken as glass transition temperature (T_g) , analyzed by TA instruments Universal Analysis 2000 software. The DSC data of phenylalanine-bearing polyureas with different spacer length was replotted and overlapped by Origin and the $T_{\rm g}$ of all polyureas were analyzed and determined by TA instruments Universal Analysis 2000 software in the same way, shown in Figure 68. The T_g increases from 49 °C to 55 °C when the spacer length increases from two carbons to twelve carbons. The rubber to glass transition corresponds to the freezing of long-range polymer backbone rearrangement. The higher T_g of PU-NH-Phe-C12-Phe-NH may be explained by the molecular weight difference. Under the same polymerization condition, if the degree of polymerization is similar, the polyurea with longer spacer length would have a higher molecular weight. However, proper molecular weight characterization is needed to reach definitive conclusion on the cause of higher $T_{\rm g}$. The dependence of the $T_{\rm g}$ to the macromolecular weight can be explained by the free-volume concept. 149 The free volume is defined as the volume of void in the polymer material that is not occupied by the polymer chains, shown in Figure 69. 150 The lower end group concentration on the higher molecular weight polymers decreases free volume at end group region, hindering the longrange backbone rearrangement, and increases the $T_{\rm g}$.

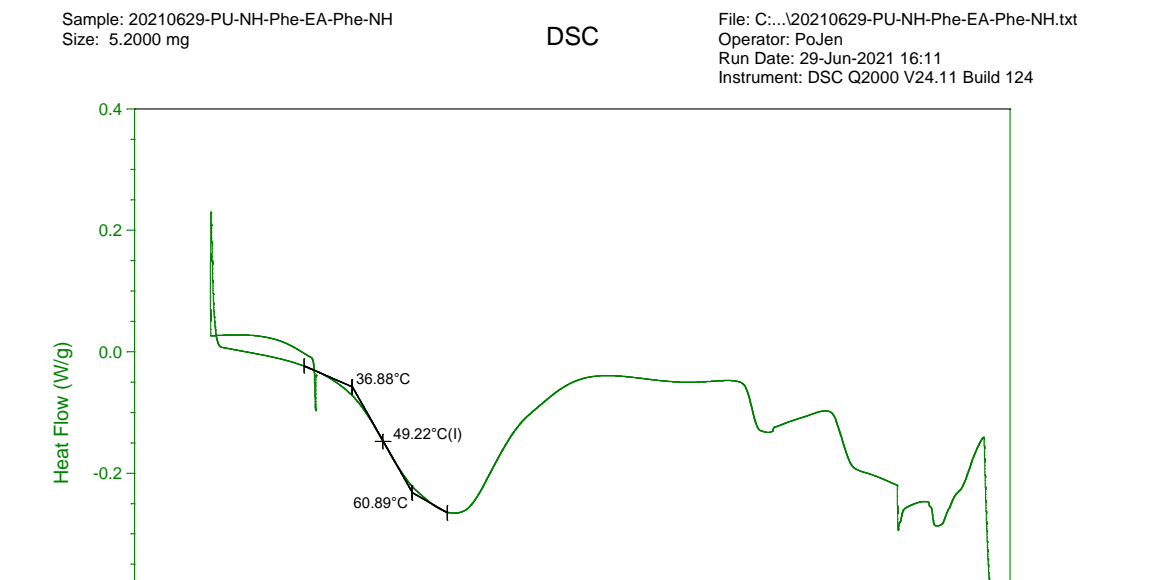


Figure 67. Differential scanning calorimetry (DSC) data for PU-NH-Phe-C2-Phe-NH and the $T_{\rm g}$ was analyzed by TA instruments Universal Analysis 2000 software. The sample was equilibrated at -20 °C and ramp 10 °C/min up to 300 °C.

Temperature (°C)

200

250

Universal V4.5A TA Instruments

-0.4

-0.6

Exo Up

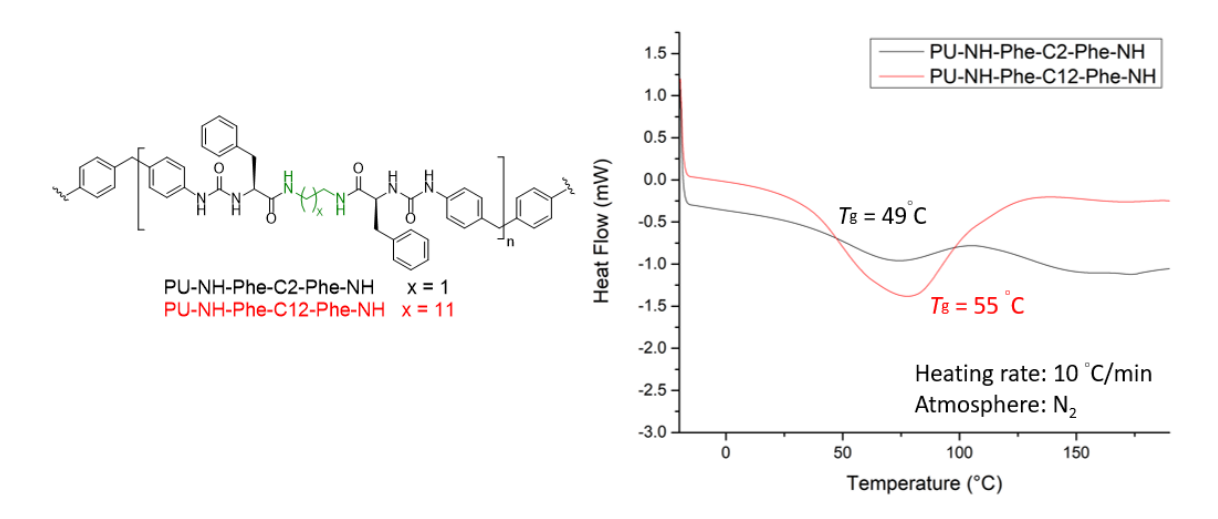


Figure 68. Overlapped differential scanning calorimetry (DSC) data for PU-NH-Phe-C2-Phe-NH (black) and PU-NH-Phe-C12-Phe-NH (red) and the $T_{\rm g}$ was analyzed by TA instruments Universal Analysis 2000 software. Heating rate is 10 °C/min under nitrogen atmosphere.

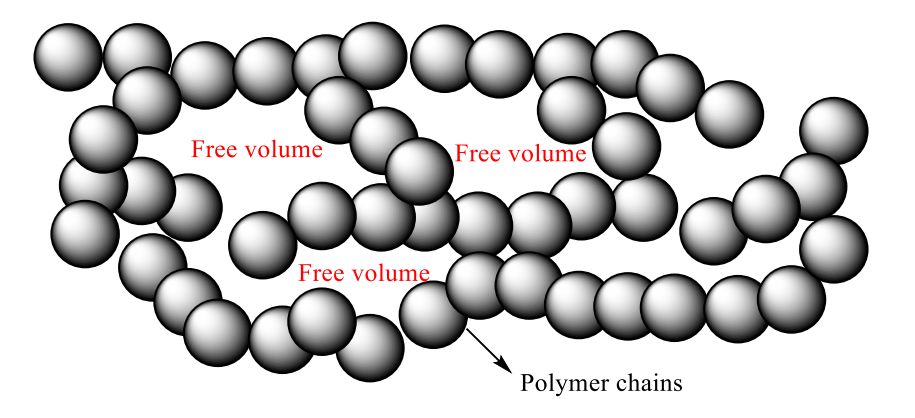


Figure 69. Schematic representation of the free volume in a polymer.

The thermal stability of polyureas with different spacer length and their onset temperatures were determined by Thermogravimetric Analysis (TGA) and analyzed by TA instruments Universal Analysis 2000 software. The weight loss curve and first derivative weight loss curve of PU-NH-Phe-C2-Phe-NH are shown in Figure 70. The overlapped TGA data were replotted by Origin. The onset temperature of PU-NH-Phe-C12-Phe-NH is

9 °C higher than the PU-NH-Phe-C2-Phe-NH, indicating that the longer spacer enhances the thermal stability of the resulted polyurea, shown in Figure 71.

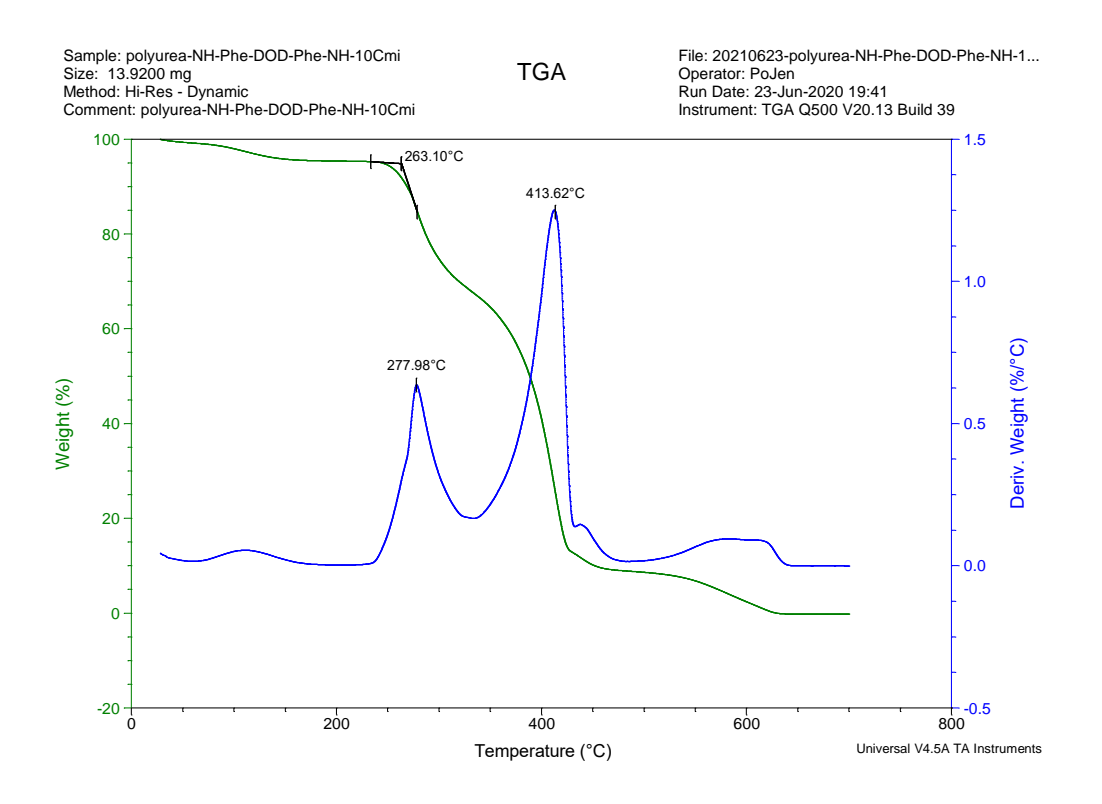


Figure 70. The thermogravimetric curve (green) and first derivative weight loss curve (blue) of PU-NH-Phe-C2-Phe-NH. Data are plotted and processed by TA instruments Universal Analysis 2000 software. Heating rate is 10 °C/min under nitrogen atmosphere.

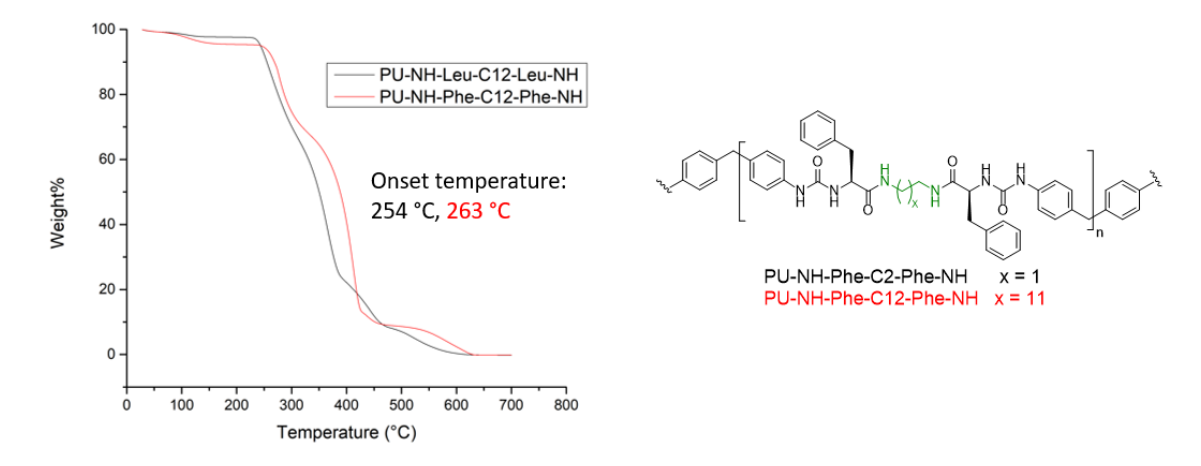


Figure 71. The thermogravimetric curve of PU-NH-Phe-C2-Phe-NH (black) and PU-NH-Phe-C12-Phe-NH (red) and the onset temperatures were analyzed by TA instruments Universal Analysis 2000 software. Heating rate is 10 °C/min under nitrogen atmosphere.

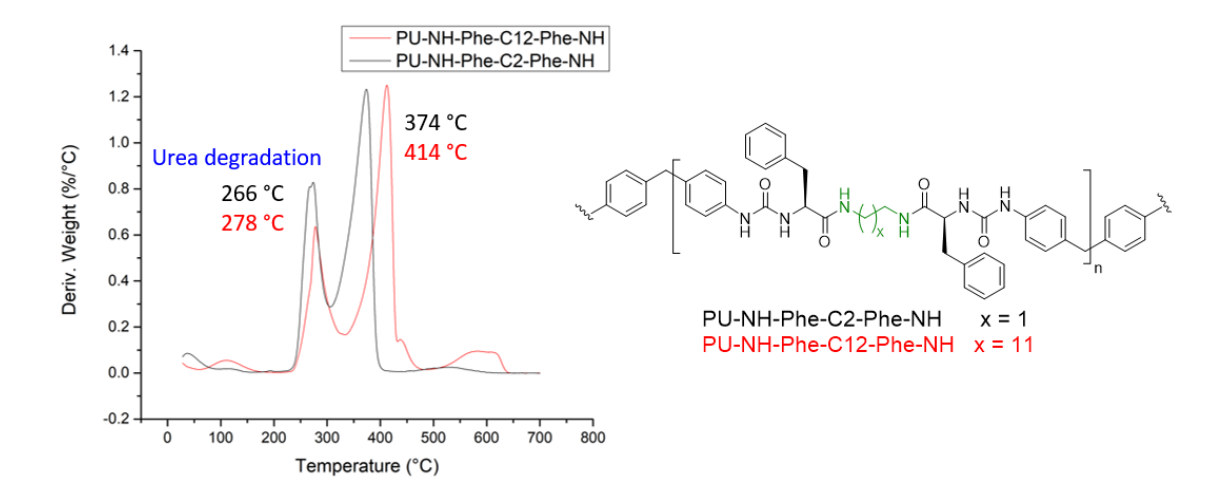


Figure 72. First derivative of the thermogravimetric curve of PU-NH-Phe-C2-Phe-NH (black) and PU-NH-Phe-C12-Phe-NH (red).

The overlapped first derivative of the weight loss curve of two polyureas is shown in Figure 72. The first major weight loss happened at 266 and 278 °C for the PU-NH-Phe-C2-Phe-NH and PU-NH-Phe-C12-Phe-NH respectively, which corresponded to the reverse polymerization process reported by pyrolysis of polyureas and characterized by mass spectroscopy. The second major weight loss occurred at 374 and 414 °C and the polyurea with longer spacer has 40 °C higher second major weight loss than the shorter spacer counterpart. The longer spacer length increases the onset temperature and T_g of the polyurea.

Study the effect of side chain structure

The $T_{\rm g}$ of polyureas bearing different side chain structures (different amino acid structures) are analyzed by DSC and the overlapped data are shown in Figure 73. The $T_{\rm g}$ of PU-NH-Phe-C12-Phe-NH is the highest among three samples, followed by PU-NH-Leu-C12-Leu-NH, and PU-NH-Ala-C12-Ala-NH. The $T_{\rm g}$ trend follows the bulkiness of

the side chain (phenyl > isobutyl > methyl) and the larger side chain impede the polymer backbone rearrangement and increase the $T_{\rm g}$. ¹⁴⁹

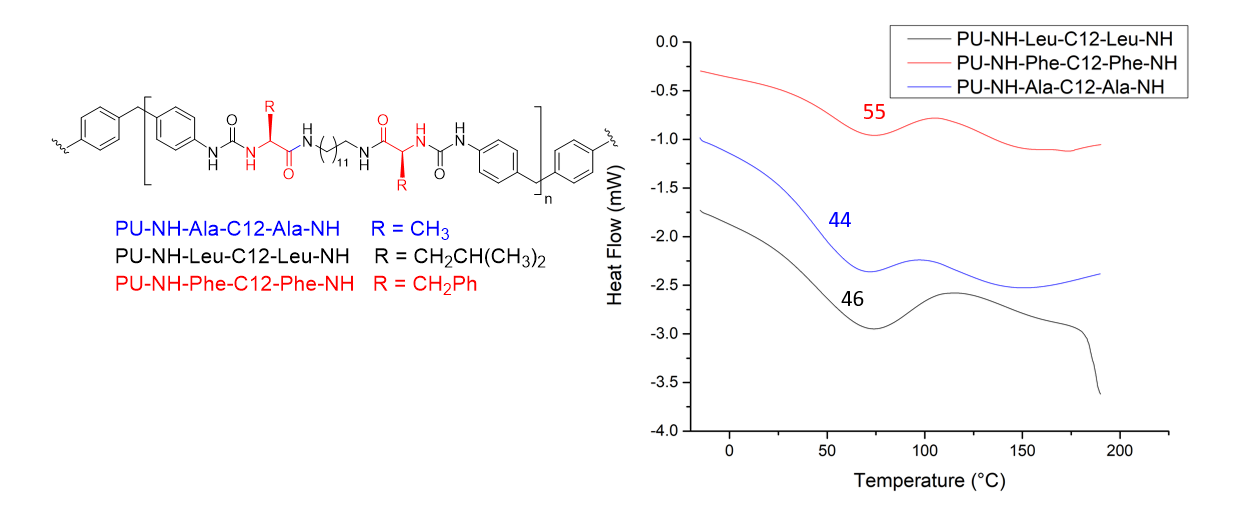


Figure 73. The overlapped DSC data of PU-NH-Phe-C12-Phe-NH (red), PU-NH-Ala-C12-Ala-NH (blue), and PU-NH-Leu-C12-Leu-NH (black). The numbers in the Figure are the $T_{\rm g}$ of the corresponded sample. The PU-NH-Ala-C12-Ala-NH data was shifted along the y-axis for clarity. Heating rate is 10 °C/min under nitrogen atmosphere.

The PU-NH-Phe-C12-Phe-NH has the highest onset temperature (263 °C) and the best thermal stability among three polyureas. Noteworthily, the onset temperature and Tg follow different order between PU-NH-Leu-C12-Leu-NH (onset temperature: 240 °C; T_g : 46 °C) and PU-NH-Ala-C12-Ala-NH (onset temperature: 259 °C; T_g : 44 °C). The molecular weight information of the PU-NH-Leu-C12-Leu-NH and PU-NH-Ala-C12-Ala-NH would guide us to better answer. The overlapped first derivative of the weight loss curve of three polyureas is shown in Figure 75. The first major weight loss for the polyurea bearing C12 spacer and different amino acids occurred between 257 to 278 °C, which is close to the polyurea with C2 spacer. The first major weight loss is less sensitive to the polyurea structure than the second major weight loss and is corresponded to the decomposition of the urea linkages (the reverse polymerization process). 149 The second

major weight loss peak of PU-NH-Leu-C12-Leu-NH (263 °C) is 50 °C higher than the PU-NH-Leu-C12-Leu-NH (364 °C). However, no literature example about the mechanism of the second major weight loss process can be found.

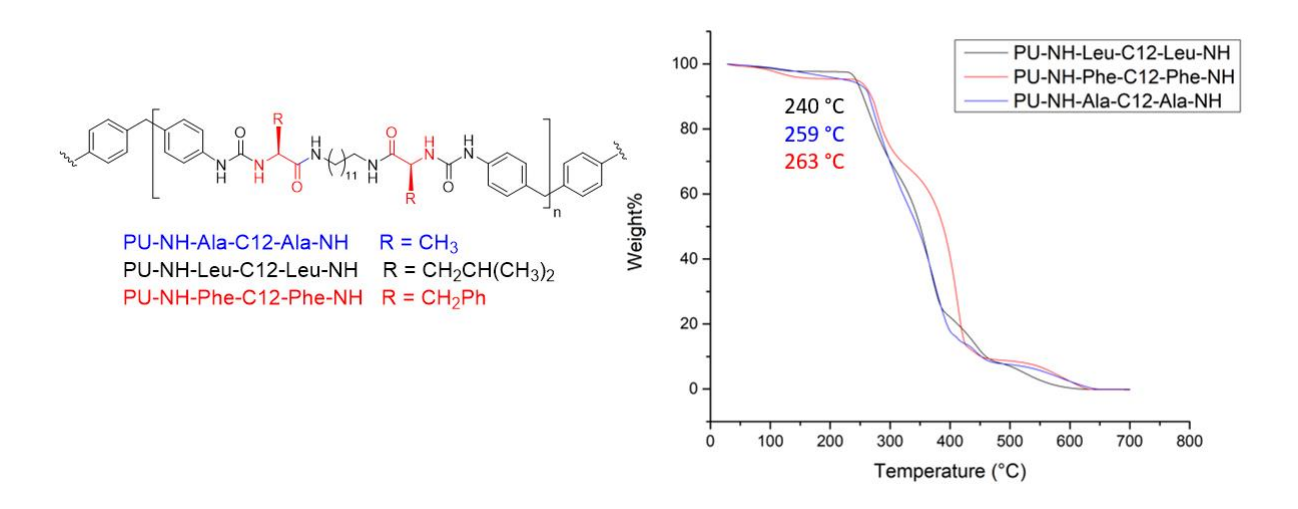


Figure 74. The thermogravimetric curve of PU-NH-Ala-C12-Phe-NH (blue), PU-NH-Leu-C12-Leu-NH (black), and PU-NH-Phe-C12-Phe-NH (red). The onset temperatures were analyzed by TA instruments Universal Analysis 2000 software and shown on the figure. Heating rate is 10 °C/min under nitrogen atmosphere.

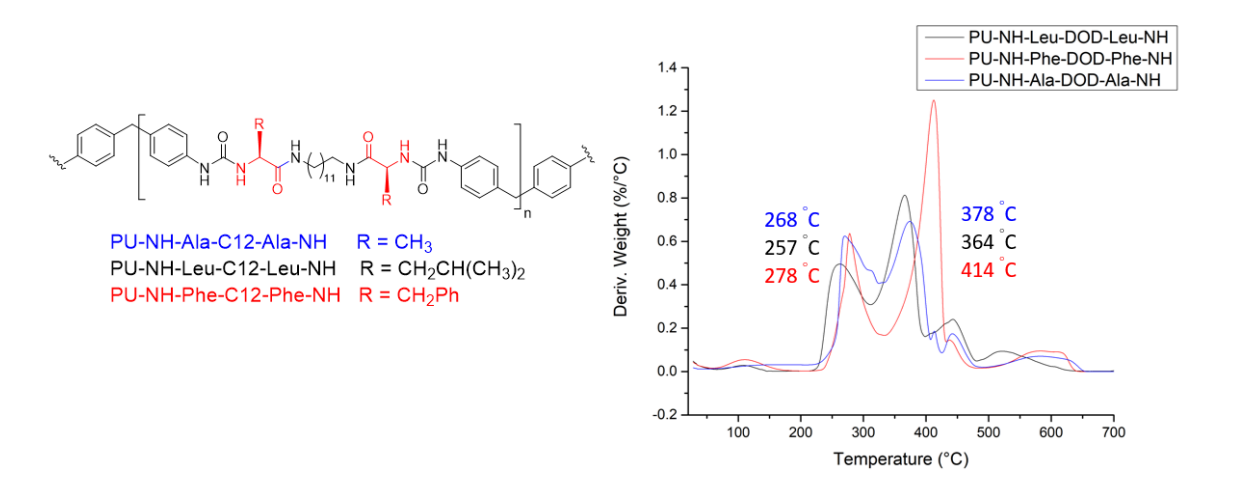


Figure 75. First derivative of the thermogravimetric curve of PU-NH-Ala-C12-Phe-NH (blue), PU-NH-Leu-C12-Leu-NH (black), and PU-NH-Phe-C12-Phe-NH (red).

Table 17. The summary of thermal analysis results of polyurea containing different spacer lengths and side chain structures.

Polyurea sample	T _g (°C)	Onset temperature (°C)	First derivative thermogravimetric peaks (°C)
PU-NH-Phe-C2-Phe-NH	49	254	266, 374
PU-NH-Ala-C12-Ala-NH	44	259	268, 378
PU-NH-Leu-C12-Leu-NH	46	240	257, 364
PU-NH-Phe-C12-Phe-NH	55	263	278, 414

The thermal analysis results of polyurea materials are summarized in Table 17. Two observations were made: (1) The longer spacer length and bulkier side chain group leads to higher T_g and onset temperature; (2) The first major weight loss is the decomposition of urea linkages and are less sensitive to the polymer structures than the second major weight loss.

Conclusion

We designed and synthesized the polyurea from amino acid-derived diamines with different spacer lengths. The polyurea materials were characterized by FT-IR and NMR with the molar ratio of diamine and diisocyanate segments determined as 1 to 1 mole ratio. The onset temperature and the glass transition temperature increase with the longer spacer length and the bulkier phenyl side chain structure of the polyureas. The polyurea with longer spacer length might have bigger molecular weight and has lower end group concentration and impeded the backbone rearrangement and increases the $T_{\rm g}$. The bulkier side groups also inhibit the backbone rearrangement and increase the $T_{\rm g}$. The peak around 260–270 °C on the first derivative TGA plot is the decomposition of urea linkages and is observed in all the polyurea samples.

Experimental Section

Materials

All the Boc-protected amino acids were purchased from Chem-Impex. All the chemicals were used as received.

Characterization

Differential Scanning Calorimetry (DSC) analysis of the polymers were obtained using a TA DSC Q2000. Samples were run under a nitrogen atmosphere at a heating rate of 10 °C/min. Thermogravimetric analysis (TGA) of polymers was obtained using a TA TGA Q500. Samples were run under a nitrogen atmosphere at a heating rate of 10 °C/min. All the DSC and TGA data was processed and analyzed by TA instruments Universal Analysis 2000 software and replotted and overlapped by Origin 9.0.

General procedure for preparing N-hydroxysuccinimide (NHS) ester of amino acids

At 0 °C, 1-ethyl-3-(3-dimethylaminopropyl)carbodiimide·HCl (EDC-HCl, 1 equiv) was added in several portions into a solution of Boc-protected amino acid (1 equiv), NHS (1 equiv), and DMAP (0.1 equiv) in dry DCM. The mixture was then allowed to react overnight at room temperature. The crude product was extracted with 0.5 M HCl solution, saturated Na₂CO₃ solution, and brine. The organic layer was collected and dried over sodium sulfate and concentrated using rotary evaporator. The solid product was further purified by stirred with IPA for 2 h and collected by vacuum filtration.

Boc-protected L-phenylalanine NHS ester (Boc-Phe-OSu)¹⁵²

Boc-Phe-OSu was prepared according to the general procedure. White solid was obtained as product (25.5 g, 92%). 1 H NMR (500 MHz, CDCl₃) δ 7.52 – 7.10 (m, 5H), 5.06 – 4.57 (m, 2H), 3.40 – 3.09 (m, 2H), 2.85 (s, 4H), 1.41 (s, 9H).

Boc-protected L-leucine NHS ester (Boc-Leu-OSu)¹⁵³

Boc-Leu-OSu was prepared according to the general procedure. White solid was obtained as product (15.2 g, 72.4%). 1 H NMR (500 MHz, CDCl₃) δ 5.15 – 4.30 (m, 2H), 2.82 (br, 4H), 1.86 – 1.73 (m, 1H), 1.73 – 1.57 (m, 1H), 1.45 (d, 9H, rotamer), 0.97 (m, 6H).

Boc-protected L-alanine NHS ester (Boc-Ala-OSu)

Boc-Ala-OSu was prepared according to the general procedure. White solid was obtained as product (22.4 g, 77.1%). 1 H NMR (500 MHz, CDCl₃) δ 5.11 – 4.39 (m, 1H), 2.82 (br, 4H), 1.56 (d, J = 7.3 Hz, 3H), 1.45 (s, 9H).

Boc-Phe-C2-Phe-Boc

Ethylenediamine (2.1 mL, 31.8 mmol) was dropwise added to a solution of Boc-Phe-OSu (25.47 g, 71.0 mmol), dry triethylamine (11 mL, 79.7 mmol), and DMF (45 mL). The white suspensions were formed while adding the ethylenediamine and the mixture was

allowed to stir at room temperature for 12 h. The reaction was stopped by adding an excess amount of DI water and the product was precipitated out from the reaction mixture. The product was filtered and washed with DI water. A white solid (17.44 g, 99 %) was obtained as the product. 1 H NMR (500 MHz, CDCl₃) δ 7.35 – 7.28 (m, 6H), 7.18 (m, 4H), 5.67 (br, 2H), 5.10 (br, 2H), 4.13 (br, 2H), 3.23 – 3.12 (m, 2H), 2.98 (m, 6H), 1.42 (s, 18H).

Boc-Leu-C2-Leu-Boc

In a round bottom flask, ethylenediamine (1.4 mL, 21.0 mmol) was dissolved in DMF (10 mL) and added to a solution of Boc-Leu-OSu (15.2 g, 328.4 mmol) and anhydrous triethylamine (9 mL, 64.6 mmol) in DMF (50 mL). The reaction mixture formed white suspensions instantly and DCM (5 mL) was added to dissolve the suspension but failed. The reaction was stirred at room temperature for 12 h. The white suspension was filtered out and recrystallized by DCM. The residual NHS was observed by NMR at 2.6 ppm using DMSO- d_6 as solvent. The NHS is removed by triturating the product with water. The product is a white powder (5.77 g, 57%). ¹H NMR (500 MHz, CDCl₃) δ 7.03 (br, 2H), 5.08 (br, 2H), 4.04 (br, 2H), 3.53 (br, 2H), 3.16 (br, 2H), 1.65 (m, 4H), 1.44 (s, 18H), 0.95 (m, 12H).

Boc-Phe-C12-Phe-Boc

Boc-Phe-OSu (5.29 g, 14.6 mmol), dry triethylamine (5 mL, 35.9 mmol), and DCM (50 mL) are mixed. 1,12-Diaminododecane (1.3 g, 6.5 mmol) was added in several portions into the reaction mixture and was allowed to stir at room temperature for 12 h. The crude solution was purified by extracting with brine and collected the organic layers. The organic layer was dried over sodium sulfate, and the excess solvent was removed using rotary evaporator. A white solid (4.5 g, 89 %) was obtained as the product. ¹H NMR (500 MHz, CDCl₃) δ 7.31 – 7.17 (m, 10H), 6.03 (br, 2H), 5.28 (br, 2H), 4.29 (br, 2H), 3.23 – 2.88 (m, 8H), 1.55 – 1.01 (m, 38H).

Boc-Ala-C12-Ala-Boc

Boc-Ala-OSu (4.85 g, 16.9 mmol), dry triethylamine (6 mL, 43.1 mmol), and DCM (50 mL) are mixed. 1,12-Diaminododecane (1.5 g, 7.5 mmol) was added in several portions into the reaction mixture and was allowed to stir at room temperature for 12 h. The crude solution was purified by extracting with brine and collected the organic layers. The organic layer was dried over sodium sulfate, and the excess solvent was removed using rotary evaporator. A white solid (4.0 g, 99 %) was obtained as the product. 1H NMR (500 MHz, CDCl₃) δ 6.38 (br, 2H), 5.17 (br, 2H), 4.14 (br, 2H), 3.20 (m, 4H), 1.42 (s, 20H), 1.32 (m, 6H), 1.29 – 1.18 (m, 18H).

Boc-Leu-C12-Leu-Boc

Boc-Leu-OSu (6.87 g, 20.9 mmol), dry triethylamine (7 mL, 50.2 mmol), and DCM (50 mL) are mixed. 1,12-Diaminododecane (1.9 g, 9.5 mmol) was added in several portions into the reaction mixture and was allowed to stir at room temperature for 12 h. The crude solution was purified by extracting with brine and collected the organic layers. The organic layer was dried over sodium sulfate, and the excess solvent was removed using rotary evaporator. A white solid (6.3 g, 99 %) was obtained as the product. 1 H NMR (500 MHz, CDCl₃) δ 6.67 (br, 2H), 5.32 – 4.61 (m, 2H), 4.20 – 3.88 (m, 2H), 3.31 – 3.04 (m, 4H), 1.76 – 1.11 (m, 44H), 0.88 (m, 12H).

General Boc-deprotection procedure using TFA

The Boc-protected diamine monomer (1 equiv) was suspended in dry DCM at 0 °C. The trifluoroacetic acid (20 equiv) was dropwise added to the reaction mixture. The white suspensions were dissolved after adding trifluoroacetic acid and the reaction was allowed to stir at room temperature for 2 h. After removing the volatile by a rotary evaporator, the diamine-TFA salt was dissolved with minimum amount of DI water and adjusted the pH to 14 by adding NaOH pellets. Then the solution was extracted with DCM three times and organic layers were collected. The organic layers were further washed with brine and dried over sodium sulfate, and the excess DCM was removed using rotary evaporator.

General Boc-deprotection procedure using 3M HCl in MeOH

At 0 °C, the Boc-protected diamine monomer (1 equiv) was slowly mixed with 3M HCl in MeOH (20 equiv). The reaction was allowed to stir at room temperature for 2 h. After removing the volatile by a stream of nitrogen gas, the diamine-HCl salt was dissolved with minimum amount of DI water and adjusted the pH to 14 by adding NaOH pellets. Then the solution was extracted with DCM three times and organic layers were collected.

The organic layers were further washed with brine and dried over sodium sulfate, and the excess DCM was removed using rotary evaporator.

NH-Phe-C2-Phe-NH¹⁵⁴

Boc-Phe-C2-Phe-Boc was deprotected by 3M HCl in MeOH procedure. NH-Phe-C2-Phe-NH (5.6 g, 60%) was obtained as product. 1 H NMR (500 MHz, CDCl₃) δ 7.56 (s, 2H), 7.38 – 7.14 (m, 10H), 3.58 (s, 2H), 3.46 – 3.31 (m, 4H), 3.24 (m, 2H), 2.68 (dd, J = 13.6, 9.2 Hz, 2H), 1.58 – 1.33 (m, 4H). 13 C{ 1 H} NMR (125 MHz, CDCl₃) δ 175.16, 137.87, 129.31, 128.71, 126.83, 56.52, 41.12, 39.44.

NH-Leu-C2-Leu-NH HCl salt¹⁵⁵

Boc-Leu-C2-Leu-Boc was deprotected by 3M HCl in MeOH procedure. NH-Phe-C2-Phe-NH (0.63 g, 60%) was obtained as product. The NMR reported here is from the HCl salt. 1 H NMR (500 MHz, D₂O) δ 3.81 (t, J = 7.3 Hz, 2H), 3.36 – 3.25 (m, 2H), 3.24 – 3.12 (m, 4H), 1.61 – 1.43 (m, 6H), 0.80 (dd, J = 6.3 Hz, 12H). 13 C{ 1 H} NMR (125 MHz, D₂O) δ 170.59, 51.85, 48.76, 39.82, 38.52, 23.80, 21.71, 20.86.

NH-Ala-C12-Ala-NH

Boc-Ala-C12-Ala-Boc was deprotected by TFA procedure. NH-Ala-C12-Ala-NH (2.0 g, 81%) was obtained as product. 1 H NMR (500 MHz, CDCl₃) δ 7.41 – 7.13 (br, 2H), 3.46 (m, 2H), 3.21 (m, 4H), 1.56 – 1.19 (m, 30H). 13 C{ 1 H} NMR (125 MHz, CDCl₃) δ 175.49, 50.77, 38.99, 29.61, 29.49, 29.48, 29.26, 26.90, 21.87.

NH-Phe-C12-Phe-NH

$$H_2N$$
 H_2N
 H_2N

Boc-Phe-C12-Phe-Boc was deprotected by TFA procedure. NH-Phe-C12-Phe-NH (4.57 g, 82%) was obtained as product. 1 H NMR (500 MHz, CDCl₃) δ 7.41 – 7.14 (m, 10H), 3.64 – 3.52 (m, 2H), 3.40 – 3.13 (m, 6H), 2.68 (m, 2H), 1.47 (br, 4H), 1.26 (br, 22H).

NH-Leu-C12-Leu-NH

Boc-Leu-C12-Leu-Boc was deprotected by TFA procedure. NH-Phe-C12-Phe-NH (3.69 g, 85%) was obtained as product. 1 H NMR (500 MHz, CDCl₃) δ 7.27 (s, 2H), 3.38 (m, 2H), 3.24 (m, 4H), 1.79 – 1.66 (m, 4H), 1.50 (m, 4H), 1.44 – 1.18 (m, 22H), 0.96 (m, 12H). 13 C{ 1 H} NMR (125 MHz, CDCl₃) δ 175.41, 53.57, 44.19, 39.02, 29.65, 29.52, 29.28, 26.93, 24.91, 23.47, 21.36.

General polyurea synthesis procedure

In a round bottom flask equipped with a magnetic stir bar, amino acid diamine (1 equiv) and 4,4'-MDI (1.1 equiv) were added and the air in the system was evacuated and backfilled with nitrogen for three cycles. The dry DMF (12 mL) was added, and the

reaction mixture was heated to 50 °C. A viscous clear solution was obtained after all the solids dissolved. The mixture was stirred at 50 °C for 17 h to ensure the reaction reach completion. The polymer was precipitated by methanol and the was stirred in methanol for 2 h. The polymer solid was collected by vacuum filtration and dried using rotary evaporator until constant weight was observed. Due to the limited solubility, the NMR samples were prepared by dissolving polyurea in hot DMSO- d_6 and only partially dissolved.

Polyurea-NH-Phe-C2-Phe-NH

¹H NMR (500 MHz, DMSO- d_6) δ 8.65 – 8.44 (br, 2H), 8.10 (br, 2H), 7.32 – 7.08 (m, 14H), 6.98 (dd, J = 7.8, 5.3 Hz, 4H), 6.27 (s, 2H), 4.38 (m, 2H), 3.70 (br, 2H), 3.12 – 2.91 (m, 4H), 2.82 – 2.76 (m, 2H).

Polyurea-NH-Leu-C2-Leu-NH

¹H NMR (500 MHz, DMSO- d_6) δ 8.48 (s, 2H), 8.09 (s, 2H), 7.23 (td, J = 6.7, 3.2 Hz, 4H), 7.10 – 6.94 (m, 4H), 6.23 (d, J = 8.2 Hz, 2H), 4.19 – 4.10 (m, 2H), 3.72 (s, 2H), 3.09 (s, 4H), 1.61 – 1.50 (m, 2H), 1.46 – 1.29 (m, 2H), 0.85 (dt, J = 6.2, 3.1 Hz, 12H).

Polyurea-NH-Phe-C12-Phe-NH

¹H NMR (500 MHz, DMSO- d_6) δ 8.54 (s, 2H), 8.00 (t, J = 5.7 Hz, 2H), 7.35 – 7.07 (m, 14H), 6.98 (d, J = 8.4 Hz, 4H), 6.26 (d, J = 8.3 Hz, 2H), 4.40 (q, J = 7.2 Hz, 2H), 3.70 (s, 2H), 3.10 – 2.99 (m, 2H), 2.99 – 2.88 (m, 2H), 2.83 – 2.74 (m, 2H), 1.29 (t, J = 7.2 Hz, 4H), 1.24 – 1.06 (m, 18H).

Polyurea-NH-Leu-C12-Leu-NH

$$\begin{array}{c|c} & & & & \\ & &$$

¹H NMR (500 MHz, DMSO- d_6) δ 8.46 (s, 2H), 8.03 (t, J = 5.7 Hz, 2H), 7.23 (d, J = 8.2 Hz, 4H), 6.99 (d, J = 8.2 Hz, 4H), 6.22 (d, J = 8.5 Hz, 2H), 4.27 – 4.10 (m, 2H), 3.73 (d, J = 14.2 Hz, 2H), 3.11 – 2.92 (m, 4H), 1.55 (dq, J = 13.4, 6.7 Hz, 2H), 1.46 – 1.06 (m, 24H), 0.86 (t, J = 6.1 Hz, 12H).

Polyurea-NH-Ala-C12-Ala-NH

 1 H NMR (500 MHz, DMSO- d_{6}) δ 8.74 – 8.28 (m, 2H), 7.93 (s, 2H), 7.44 – 6.81 (m, 8H), 6.28 (d, J = 13.5 Hz, 2H), 4.25 – 3.97 (m, 2H), 3.73 (s, 2H), 1.56 – 0.94 (m, 22H). Four proton peaks are overlapped with residual DMF (polymerization solvent) and NMR solvent peaks.

APPENDIX

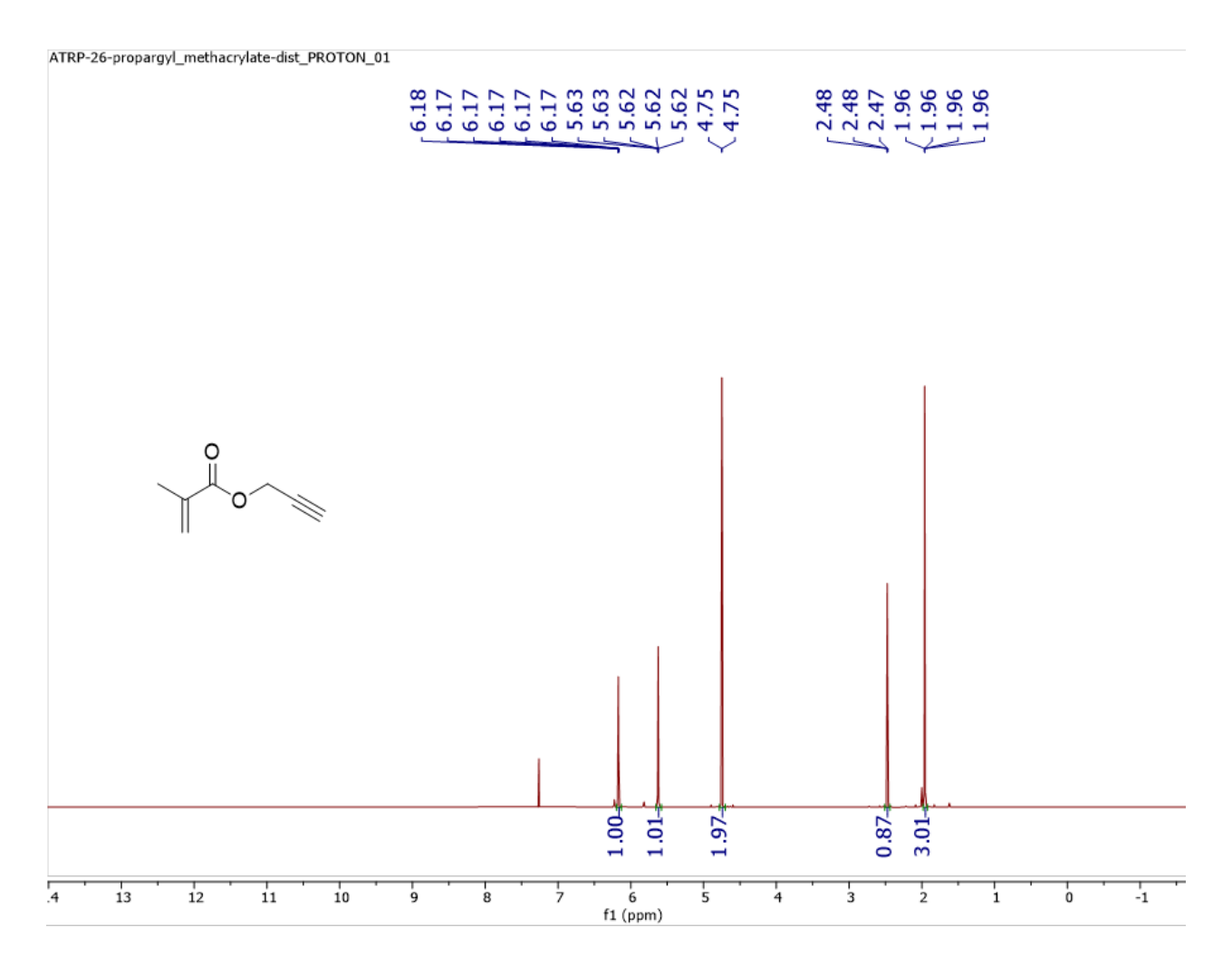


Figure A1. ¹H NMR spectrum of PMA in CDCl₃.

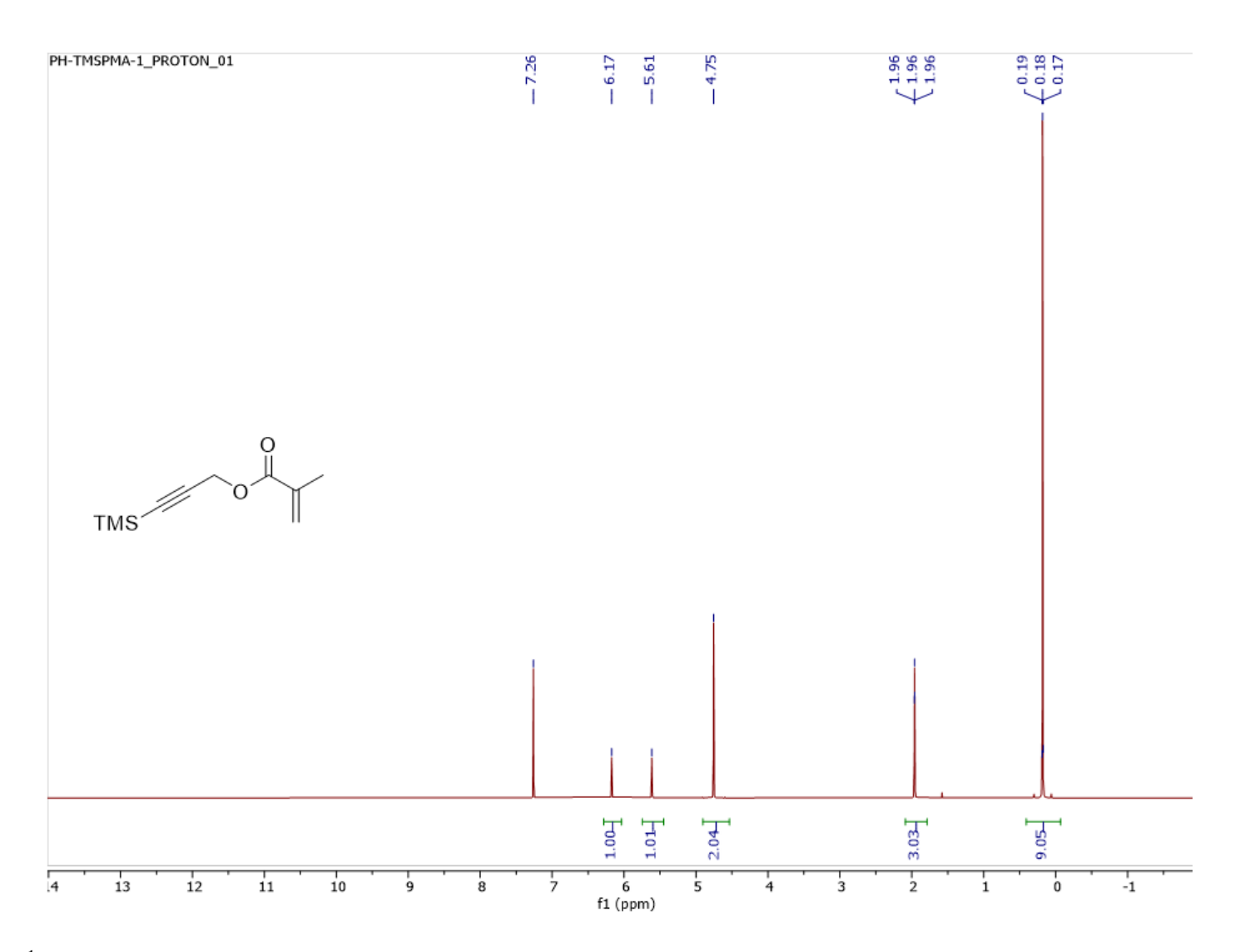


Figure A2. ¹H NMR spectrum of TMSPMA in CDCl₃.

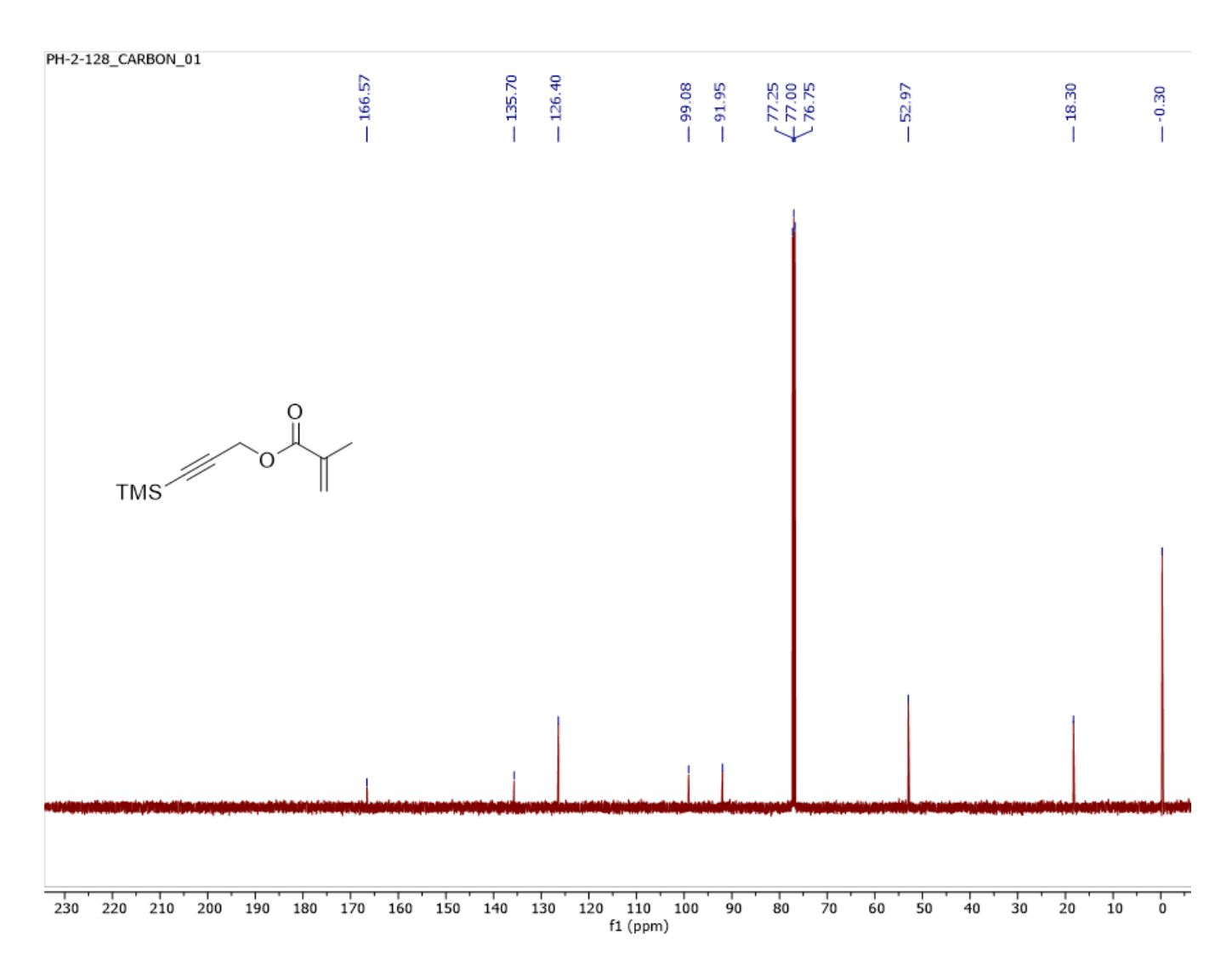


Figure A3. ¹³C{¹H} NMR spectrum of TMSPMA in CDCl3.

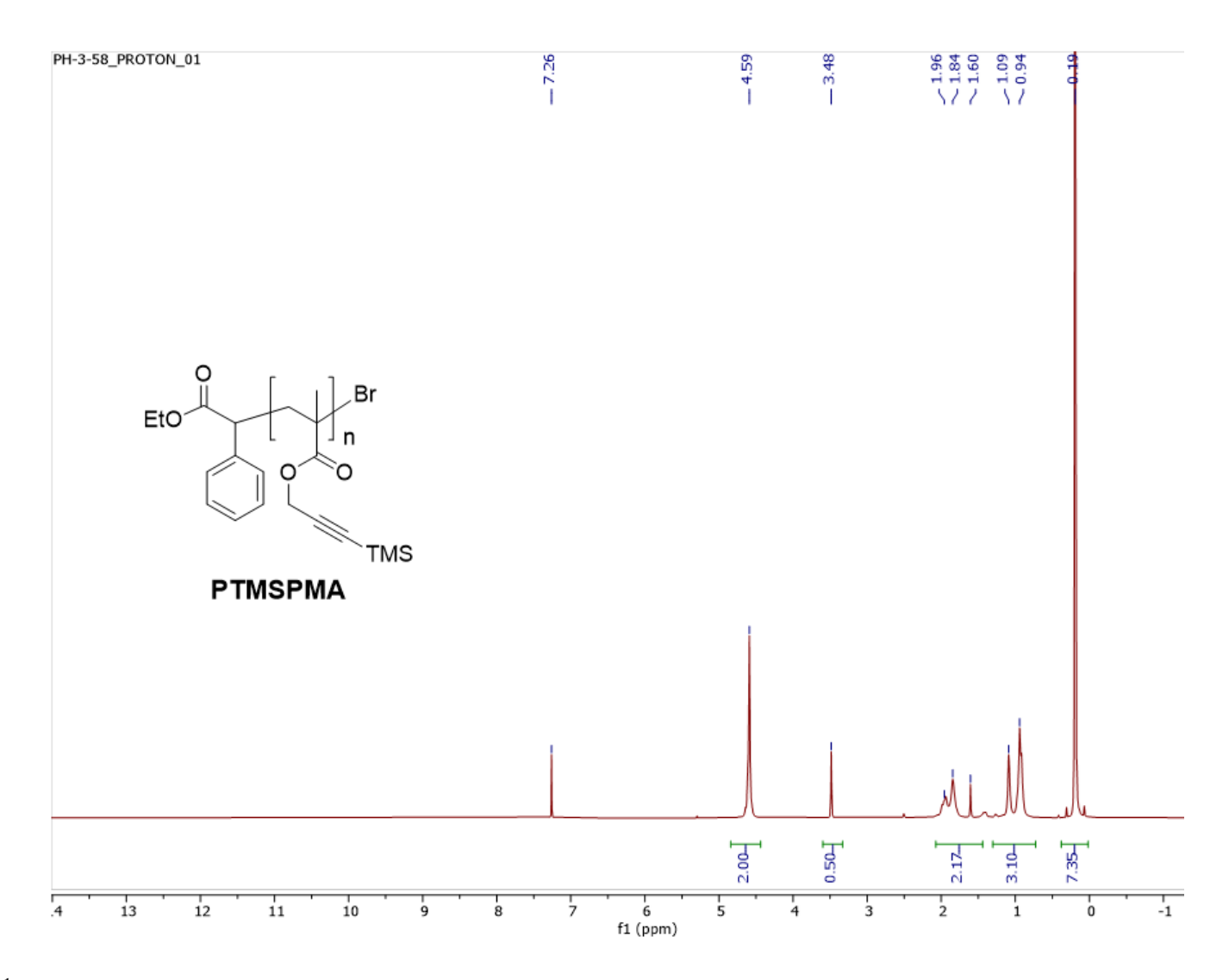


Figure A4. ¹H NMR spectrum of PTMSPMA in CDCl₃.

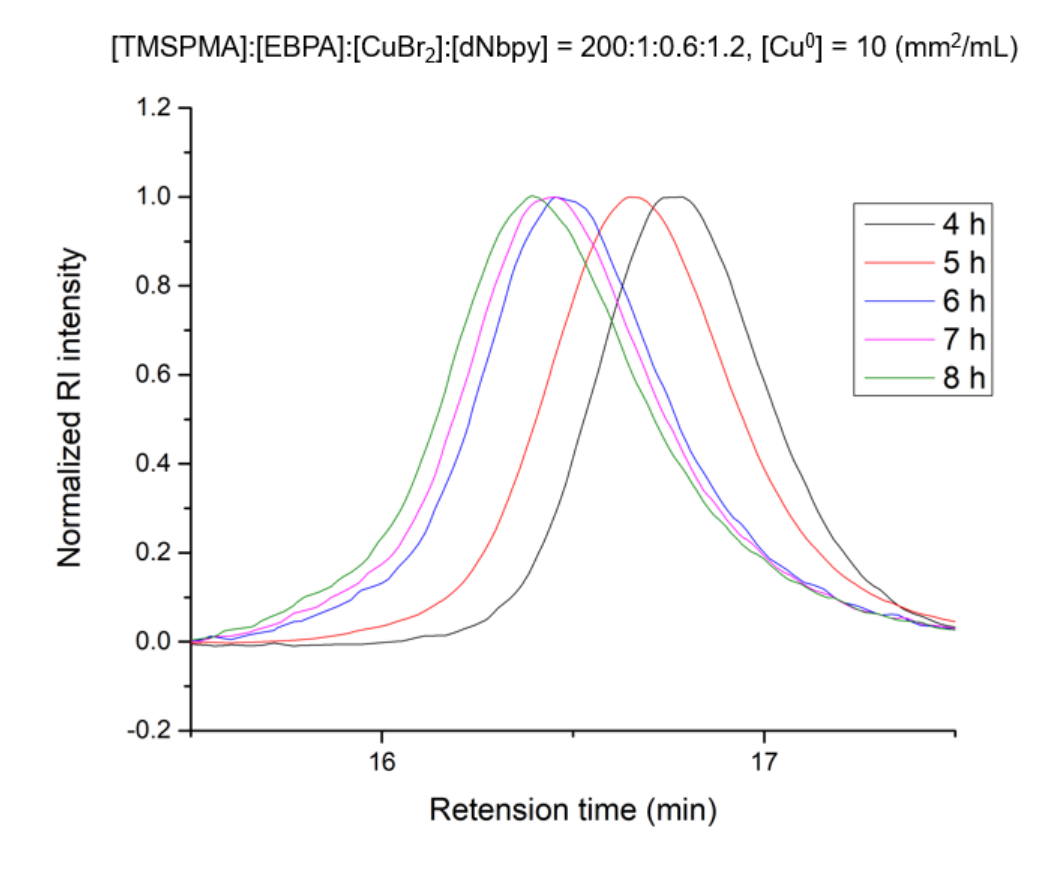


Figure A5. Overlapped GPC traces during ATRP polymerization kinetic reaction. [TMSPMA]:[EBPA]:[Cu^{II}Br₂]:[dNbpy] = 200:1:0.6:1.2, [Cu⁰] = 10 (mm^2).

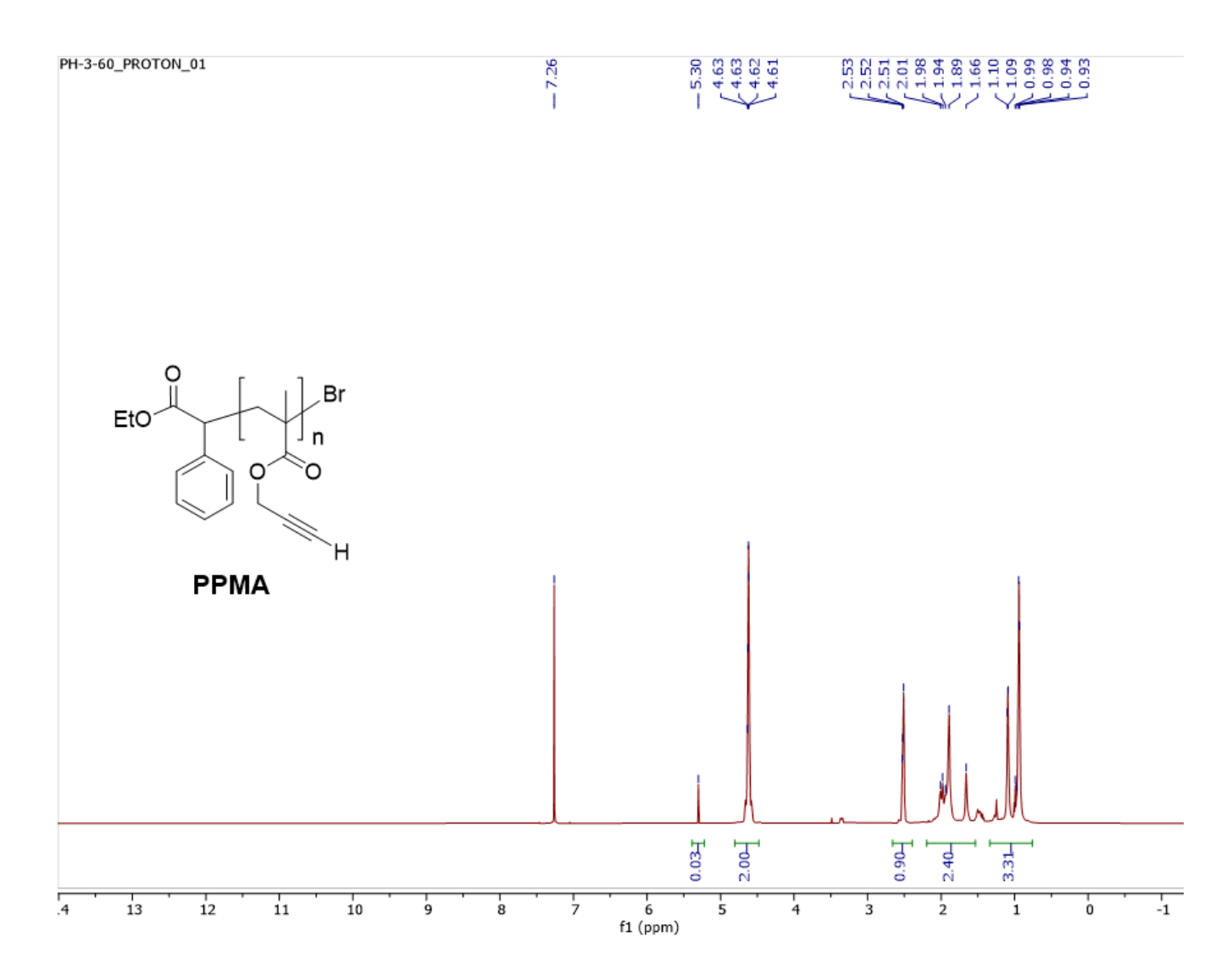


Figure A6. ¹H NMR spectrum of PPMA in CDCl₃.

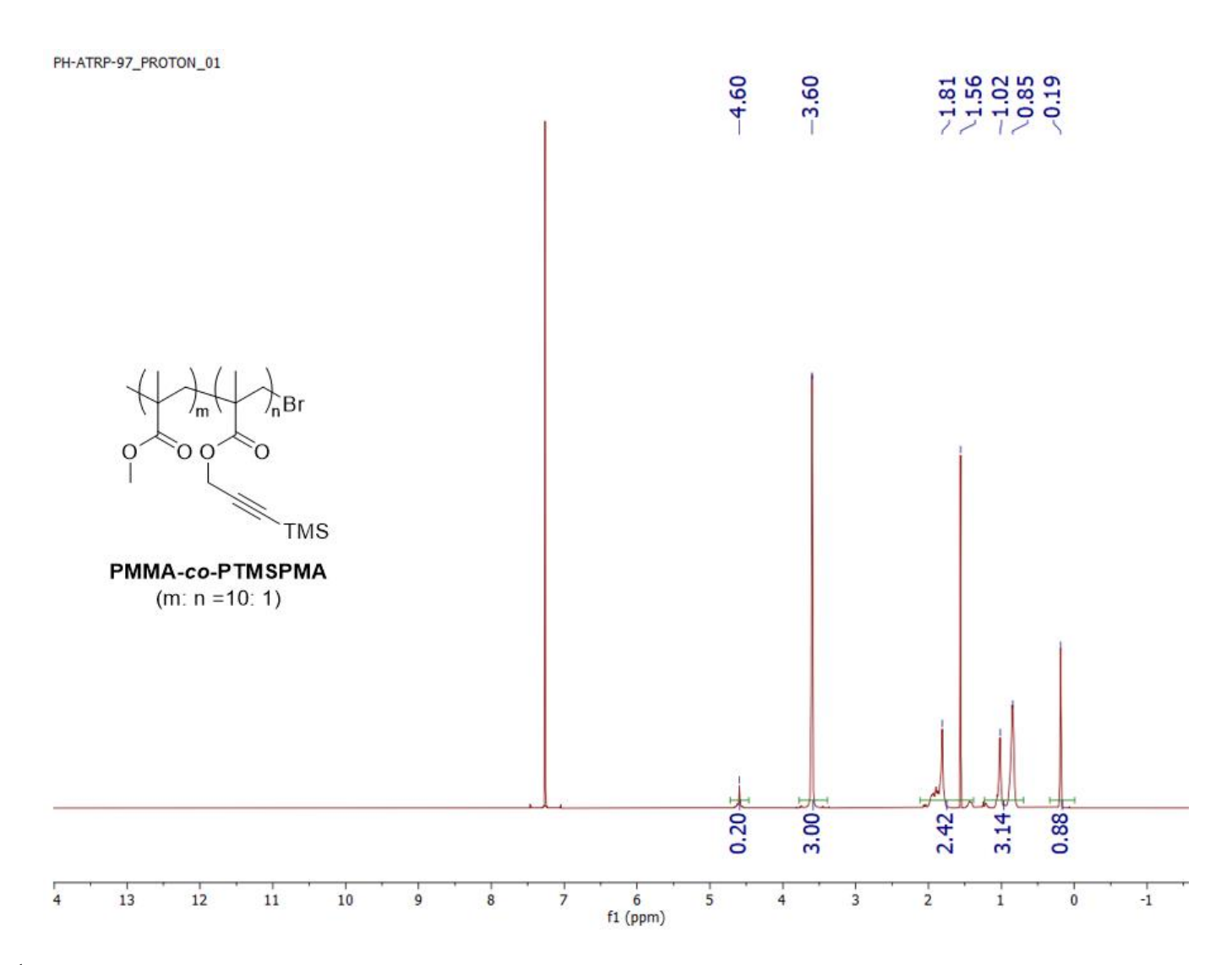


Figure A7. ¹H NMR spectrum of PMMA-co-PTMSPMA (mol ratio = 10 : 1) in CDCl₃.

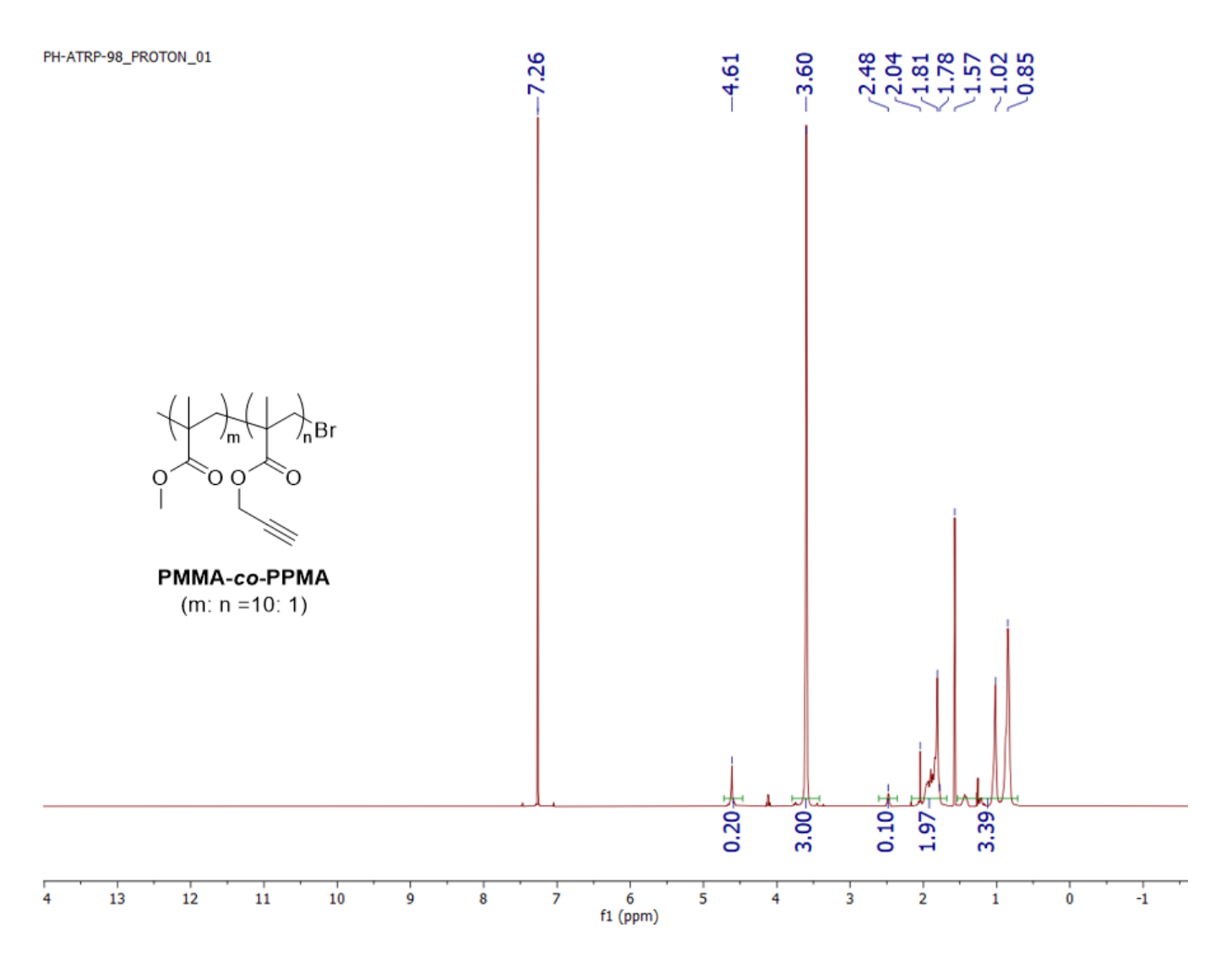


Figure A8. 1 H NMR spectrum of PMMA-co-PPMA (mol ratio = 10:1) in CDCl₃.

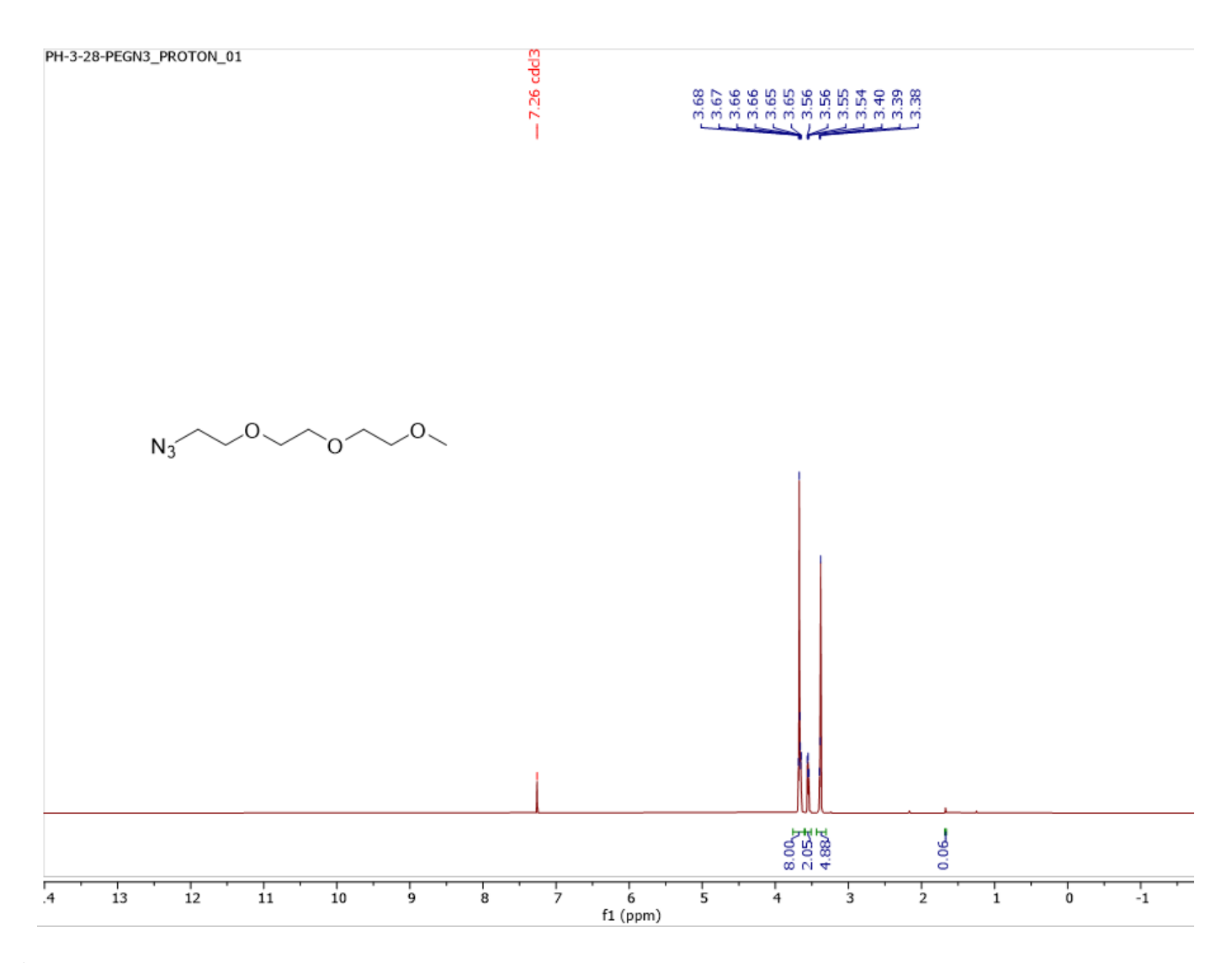


Figure A9. ¹H NMR spectrum of mDEG-azide in CDCl₃.

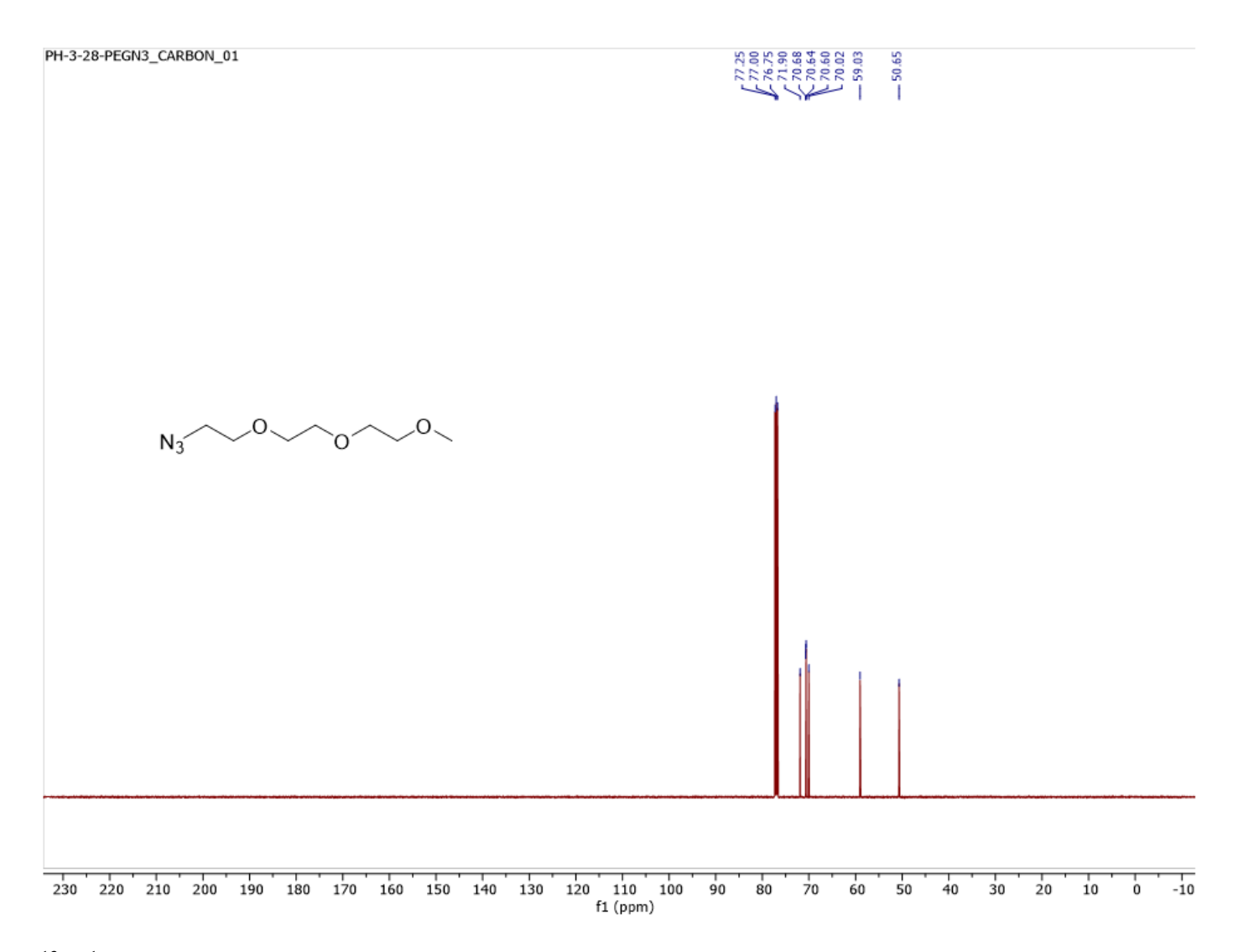


Figure A10. ¹³C{¹H} NMR spectrum of mDEG-azide in CDCl₃.

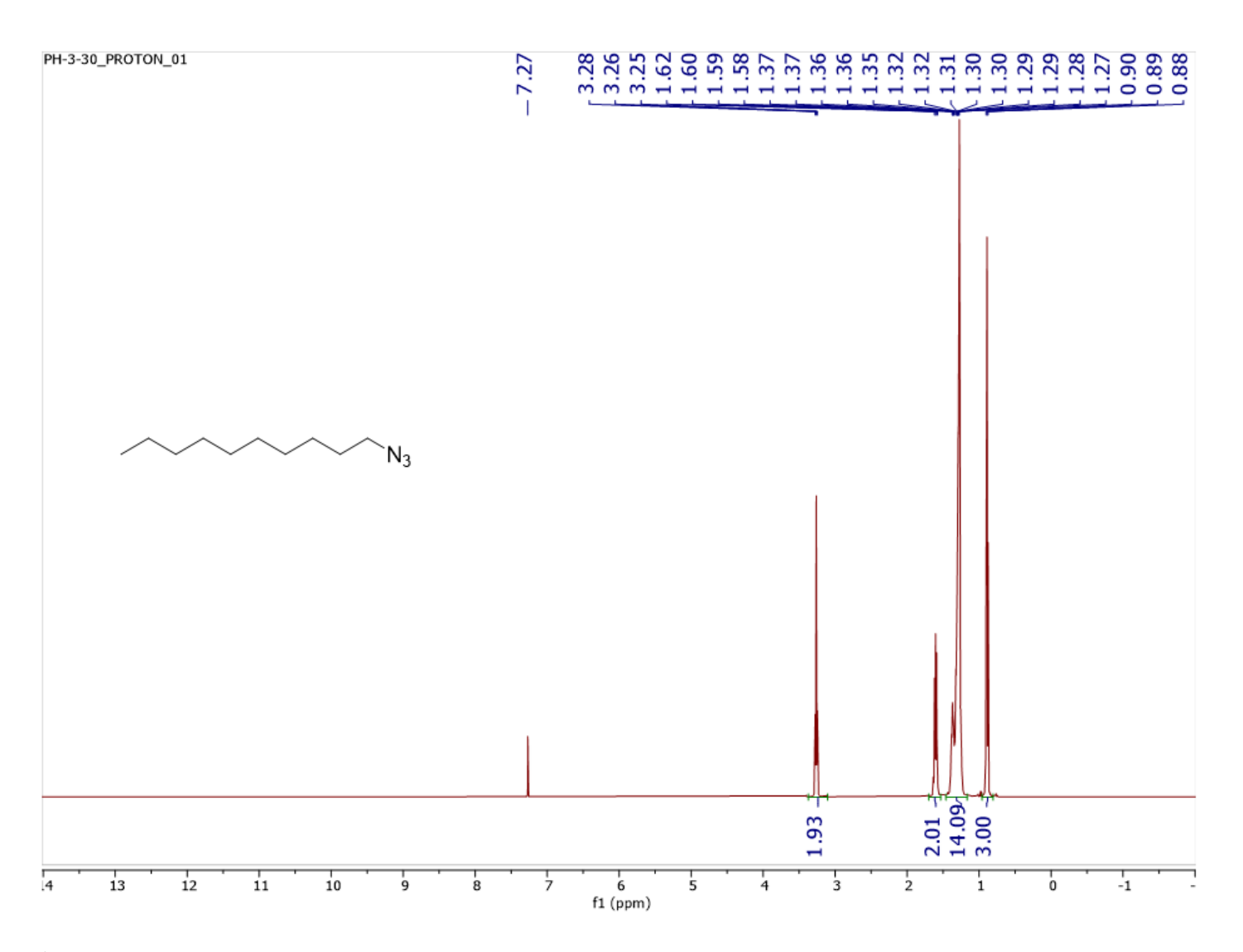


Figure A11. ¹H NMR spectrum of dodecyl azide in CDCl₃.

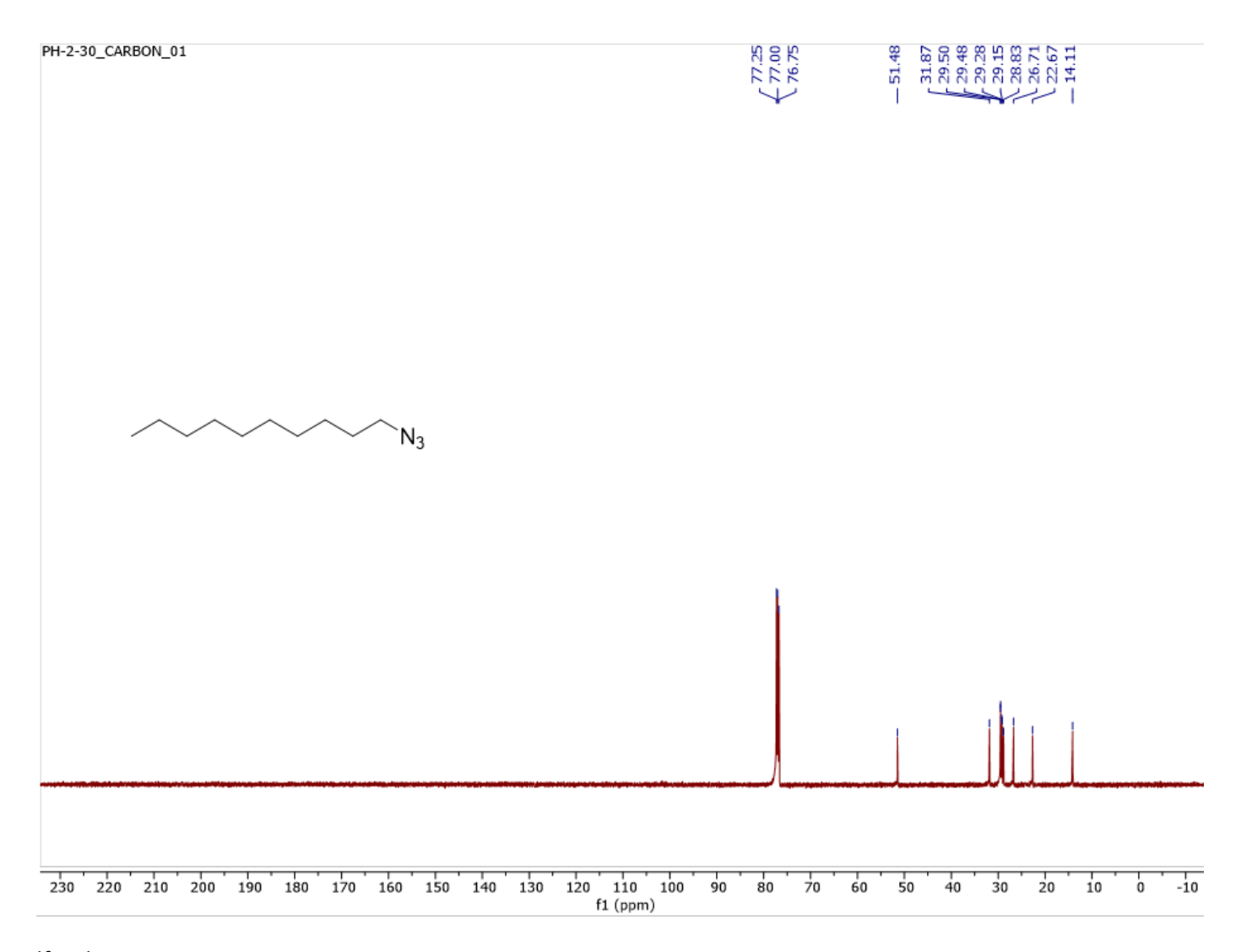


Figure A12. ¹³C{¹H} NMR spectrum of dodecyl azide in CDCl₃.

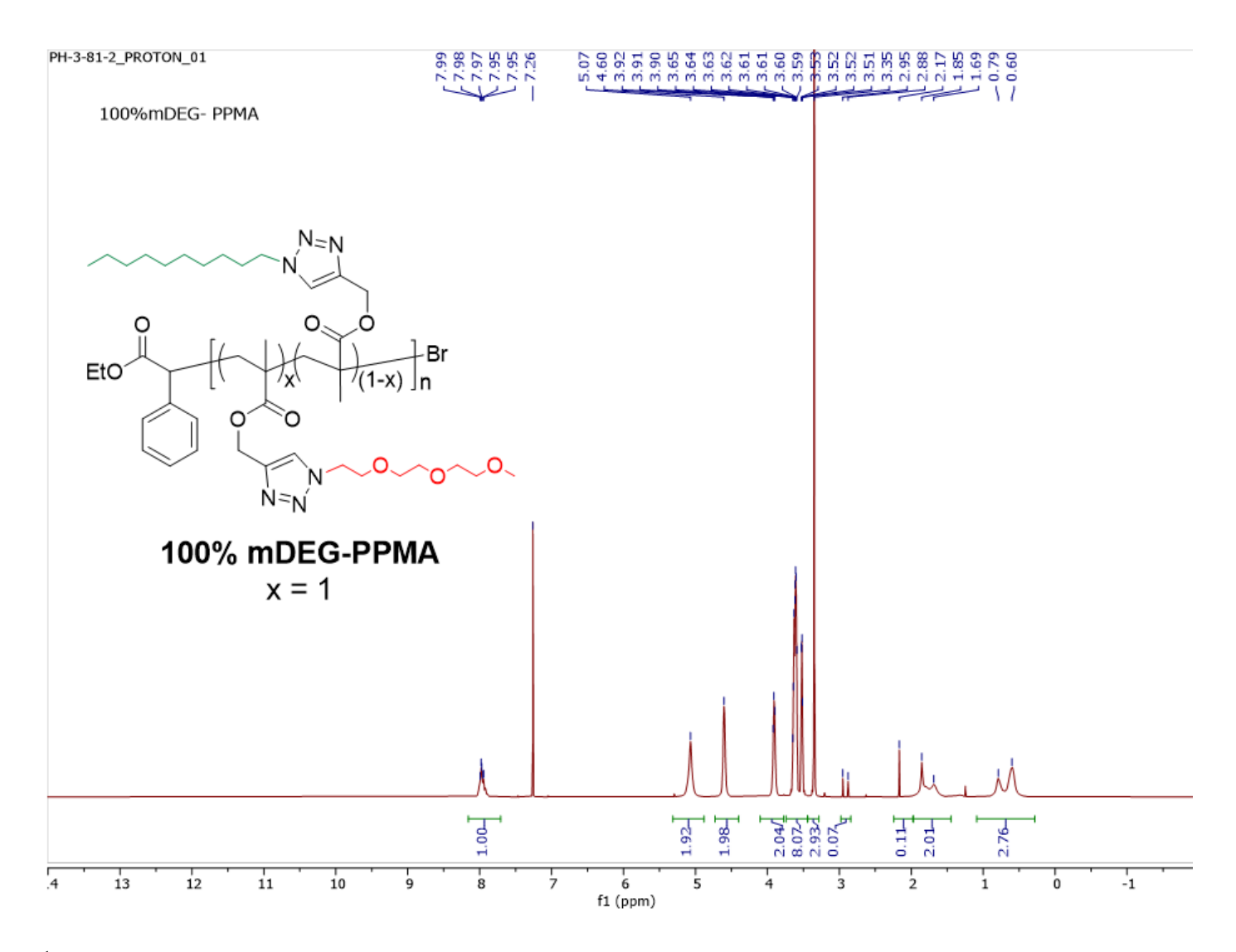


Figure A13. ¹H NMR spectrum of 100% mDEG-PPMA in CDCl₃.

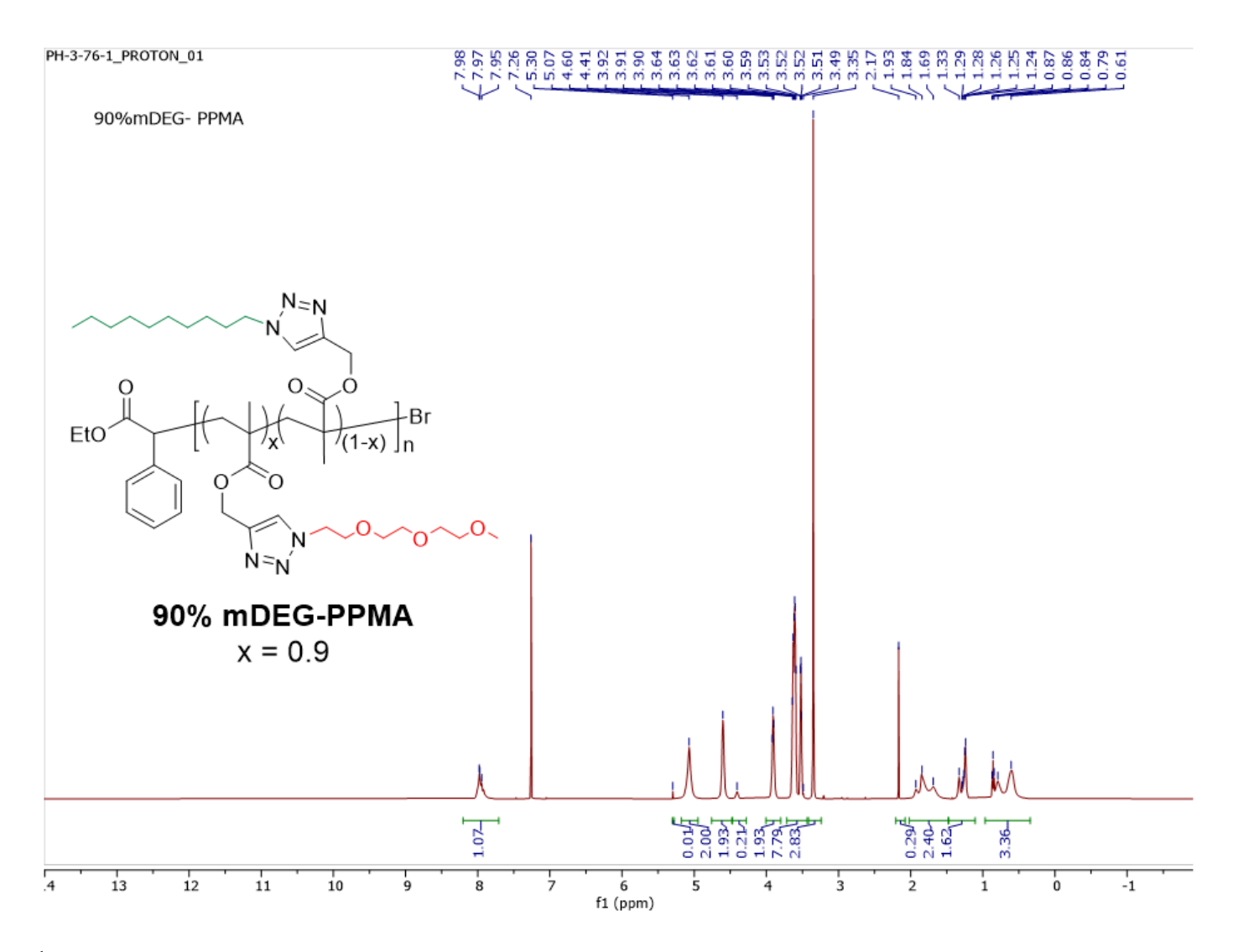


Figure A14. ¹H NMR spectrum of 90% mDEG-PPMA in CDCl₃.

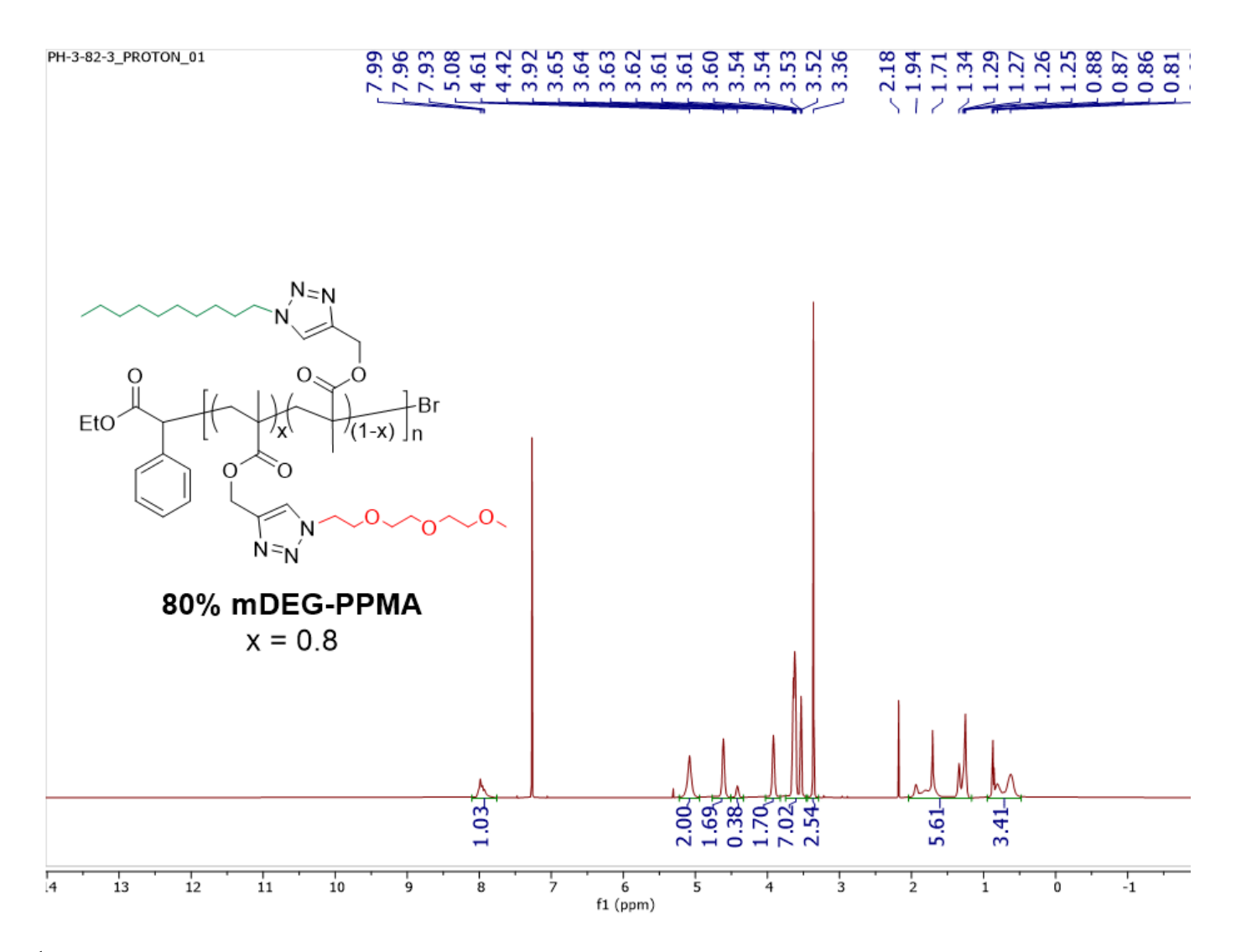


Figure A15. ¹H NMR spectrum of 80% mDEG-PPMA in CDCl₃.

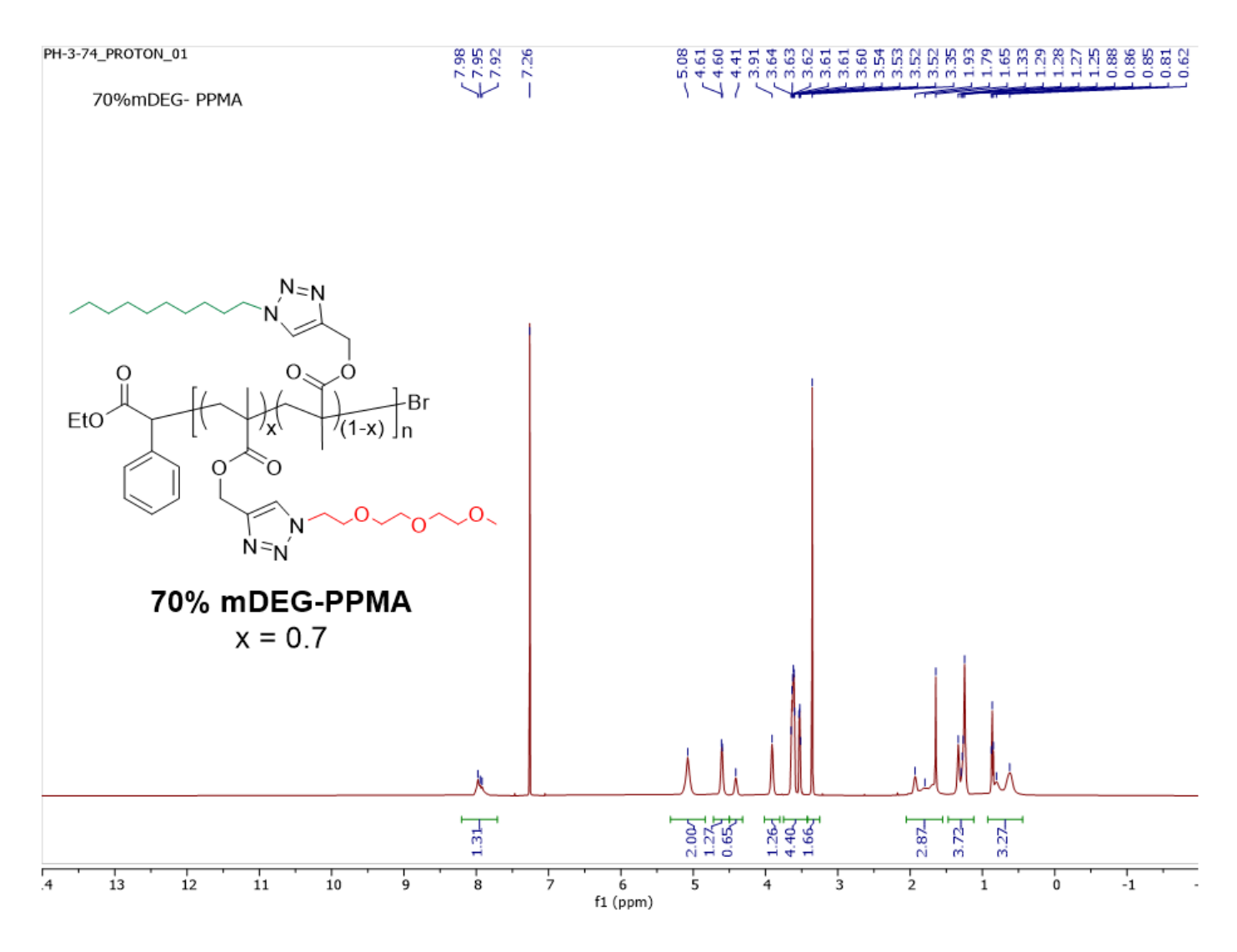


Figure A16. ¹H NMR spectrum of 70% mDEG-PPMA in CDCl₃.

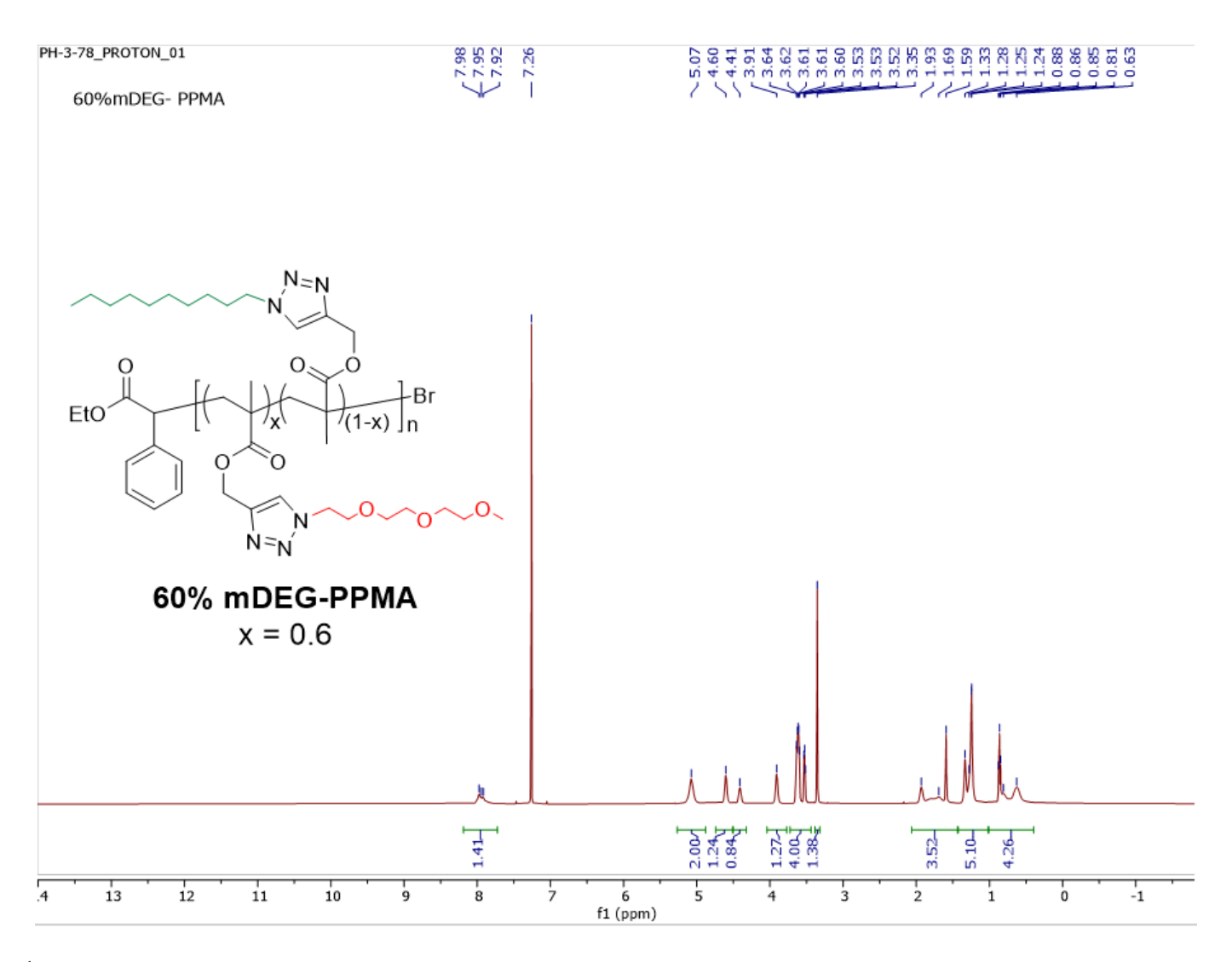


Figure A17. ¹H NMR spectrum of 60% mDEG-PPMA in CDCl₃.

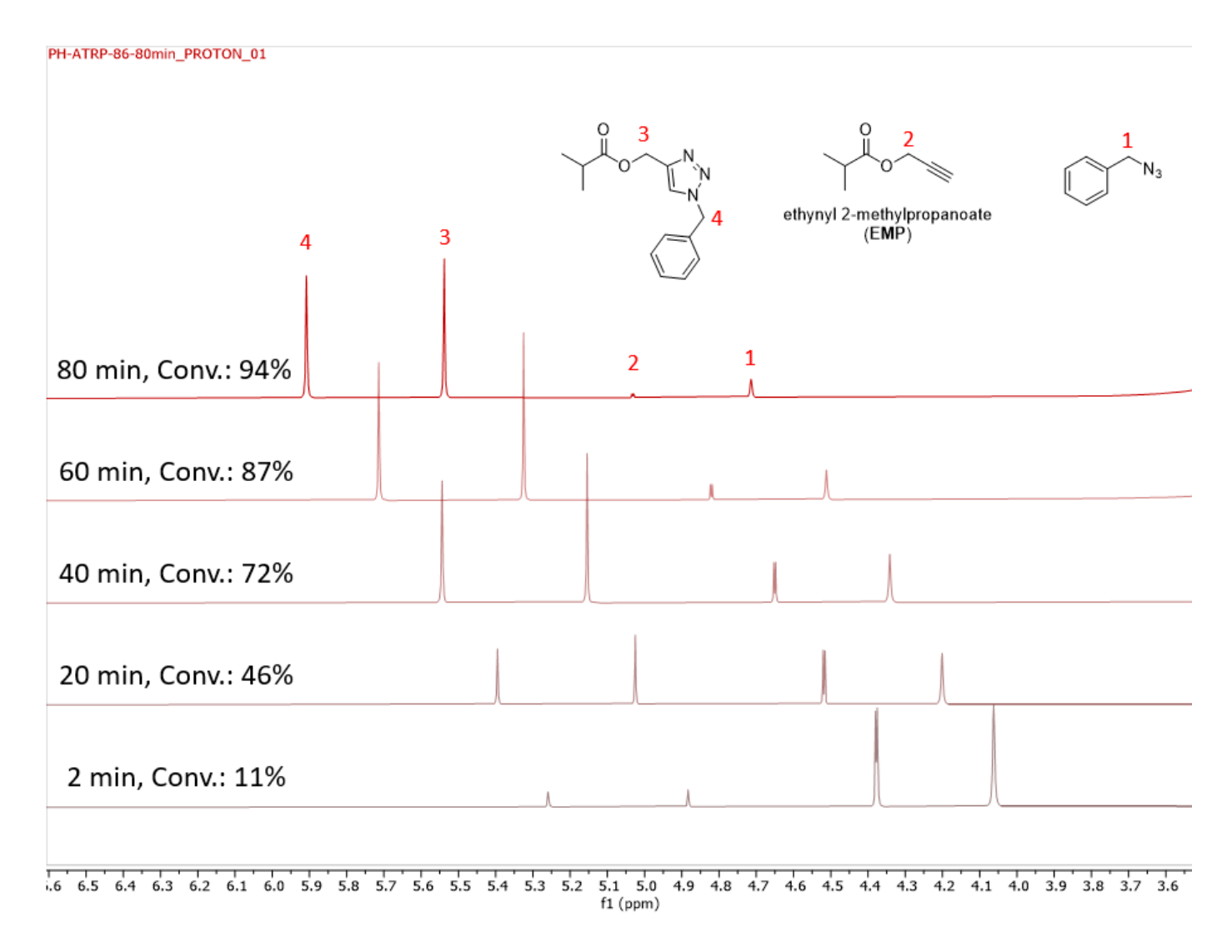


Figure A18. Overlapped ¹H NMR spectrum of CuAAC kinetic result between EMP and benzyl azide.

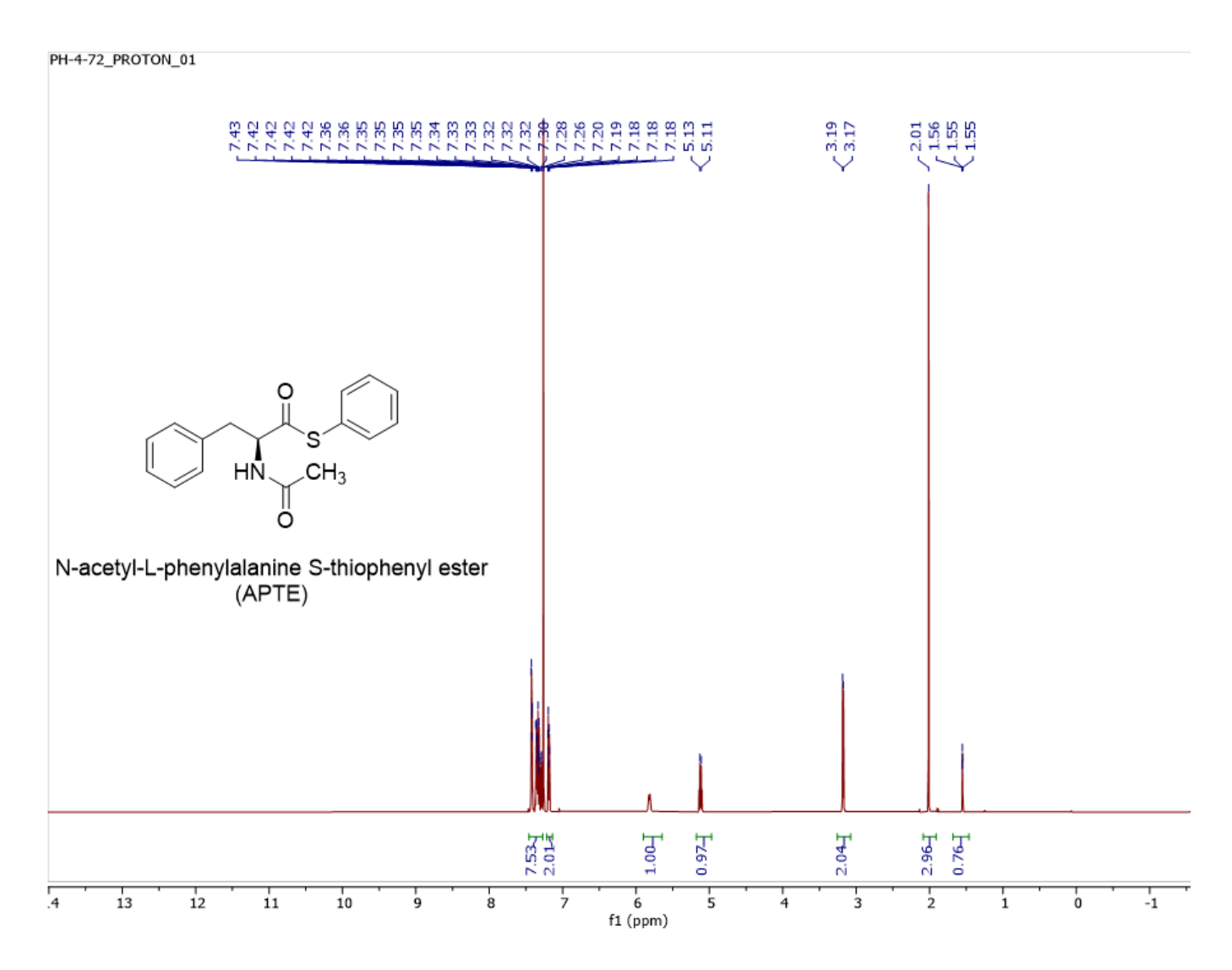


Figure A19. ¹H NMR spectrum of N-acetyl-L-phenylalanine S-thiophenyl ester (APTE) in CDCl₃.

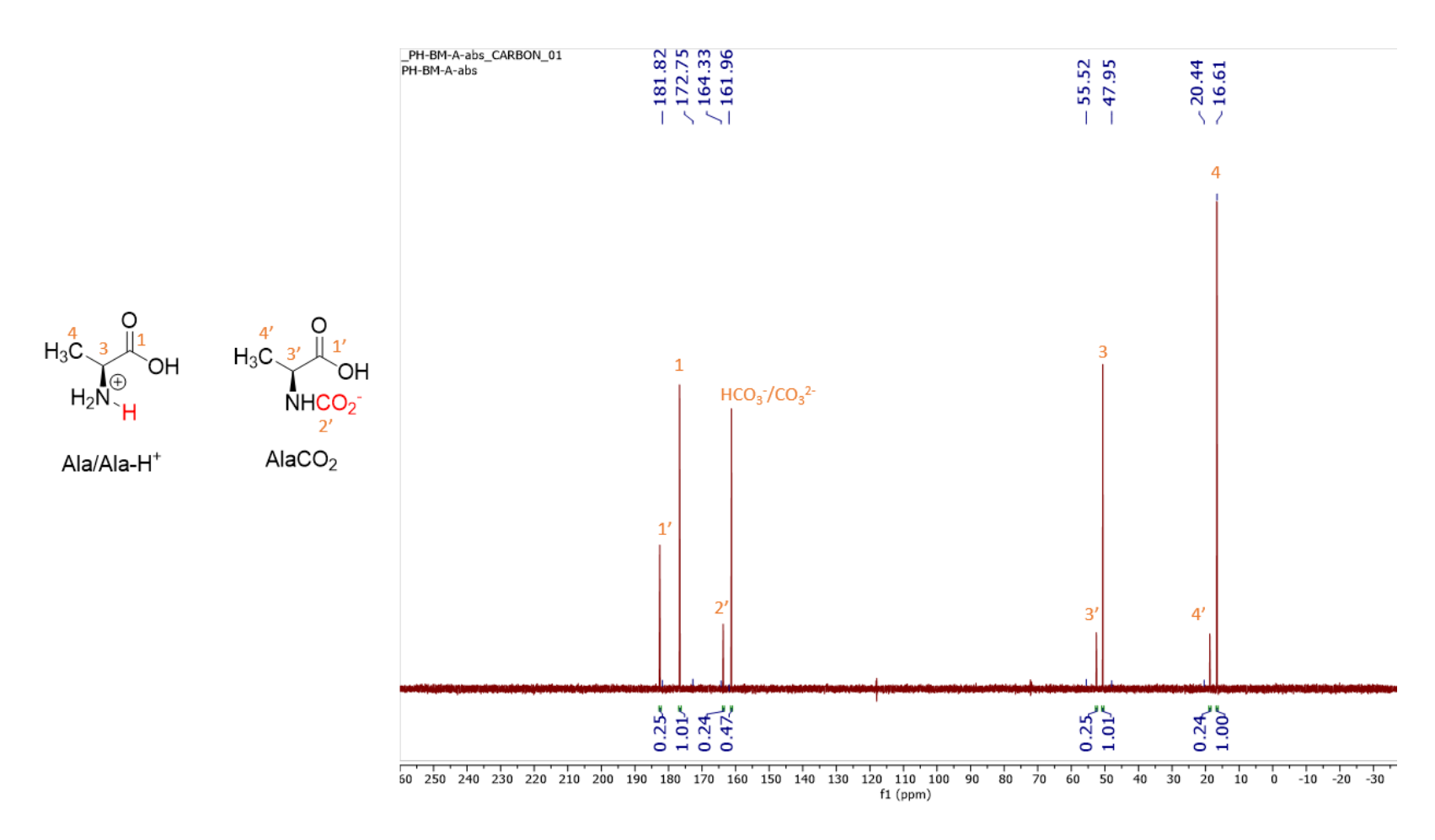


Figure A20. ¹³C{¹H} NMR spectrum of alanine sample after CO₂ absorption in D₂O.

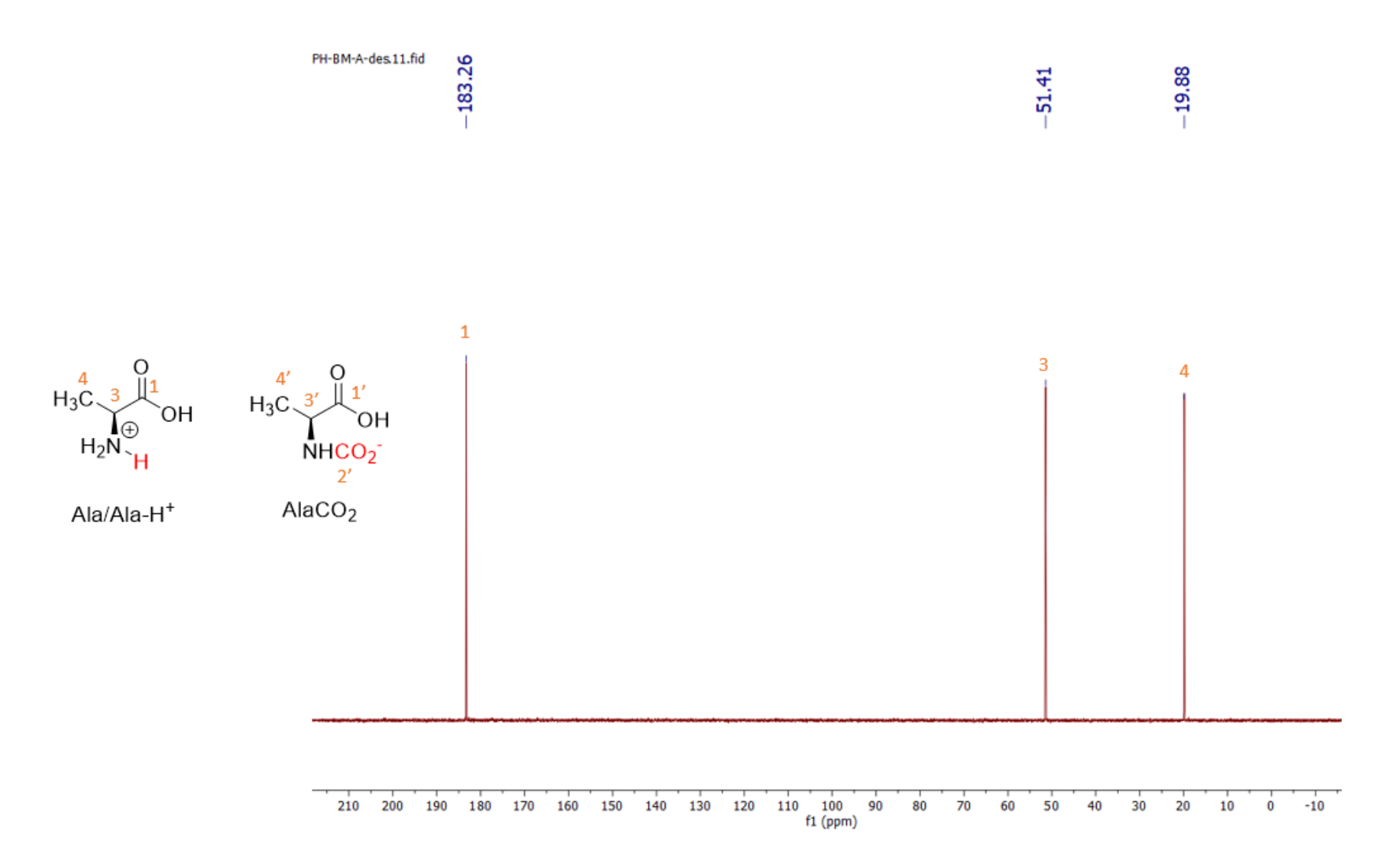


Figure A21. ¹³C{¹H} NMR spectrum of alanine sample after CO₂ desorption in D₂O.

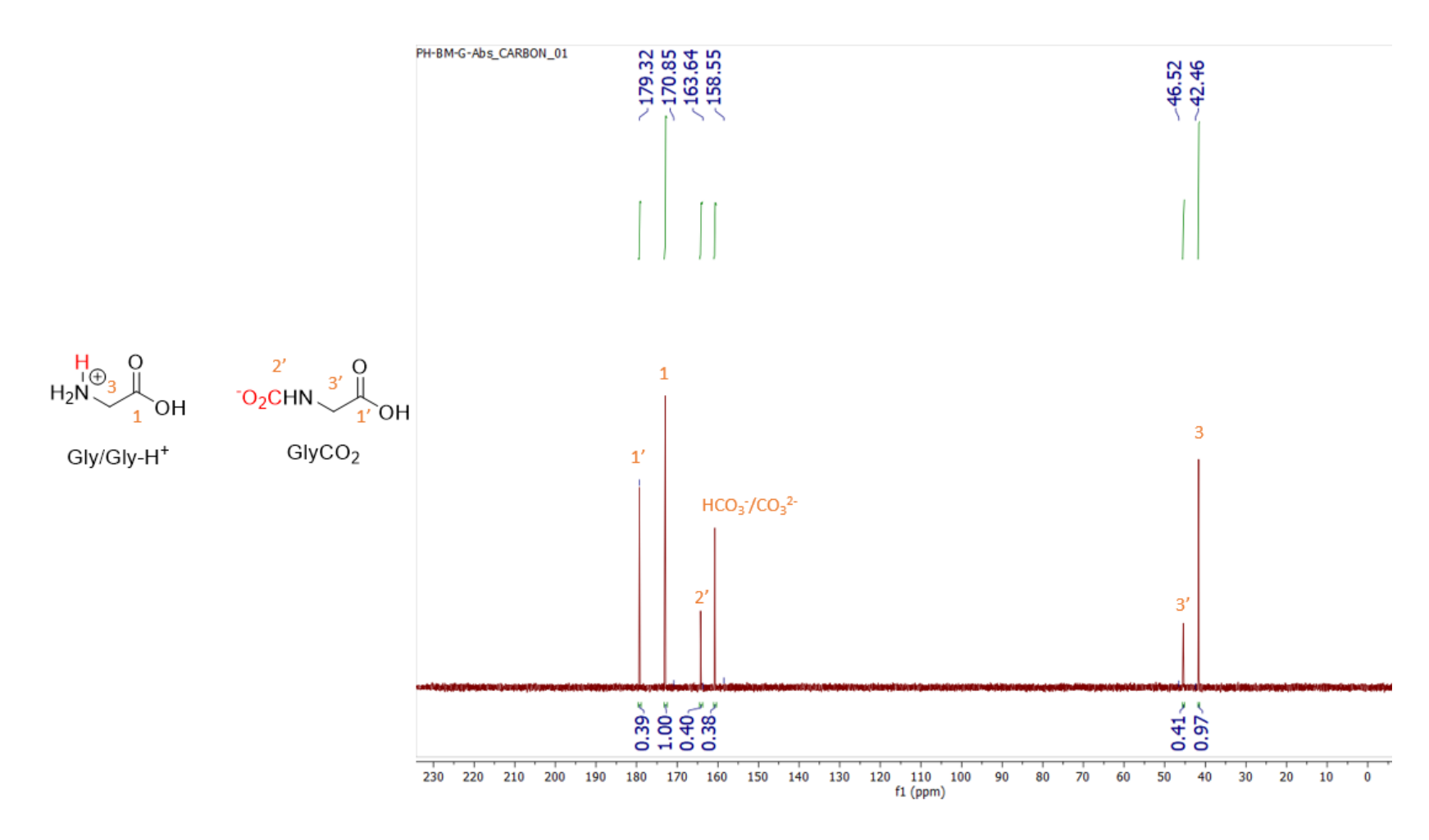


Figure A22. ¹³C{¹H} NMR spectrum of glycine sample after CO₂ absorption in D₂O.

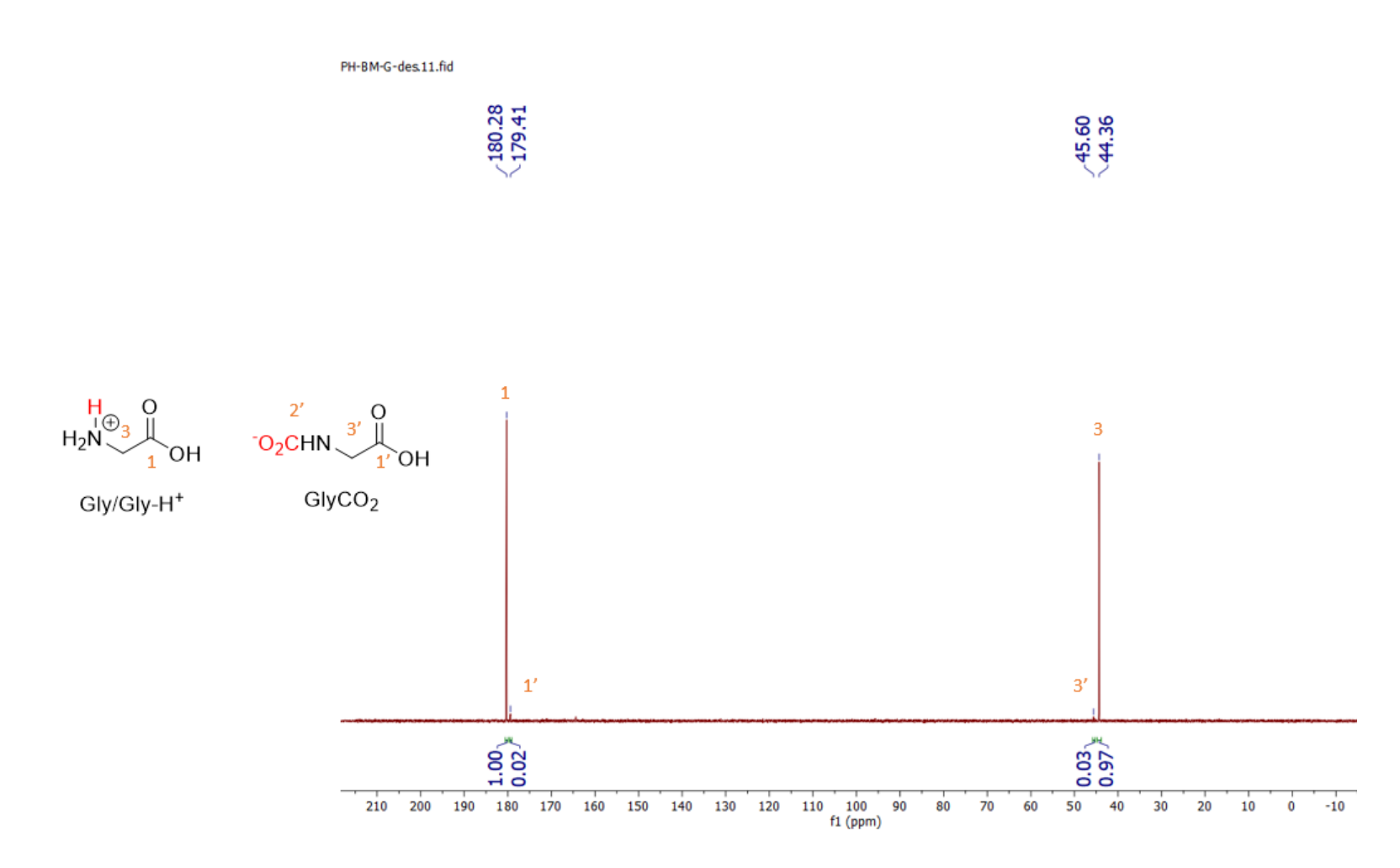


Figure A23. ¹³C{¹H} NMR spectrum of glycine sample after CO₂ desorption in D₂O.

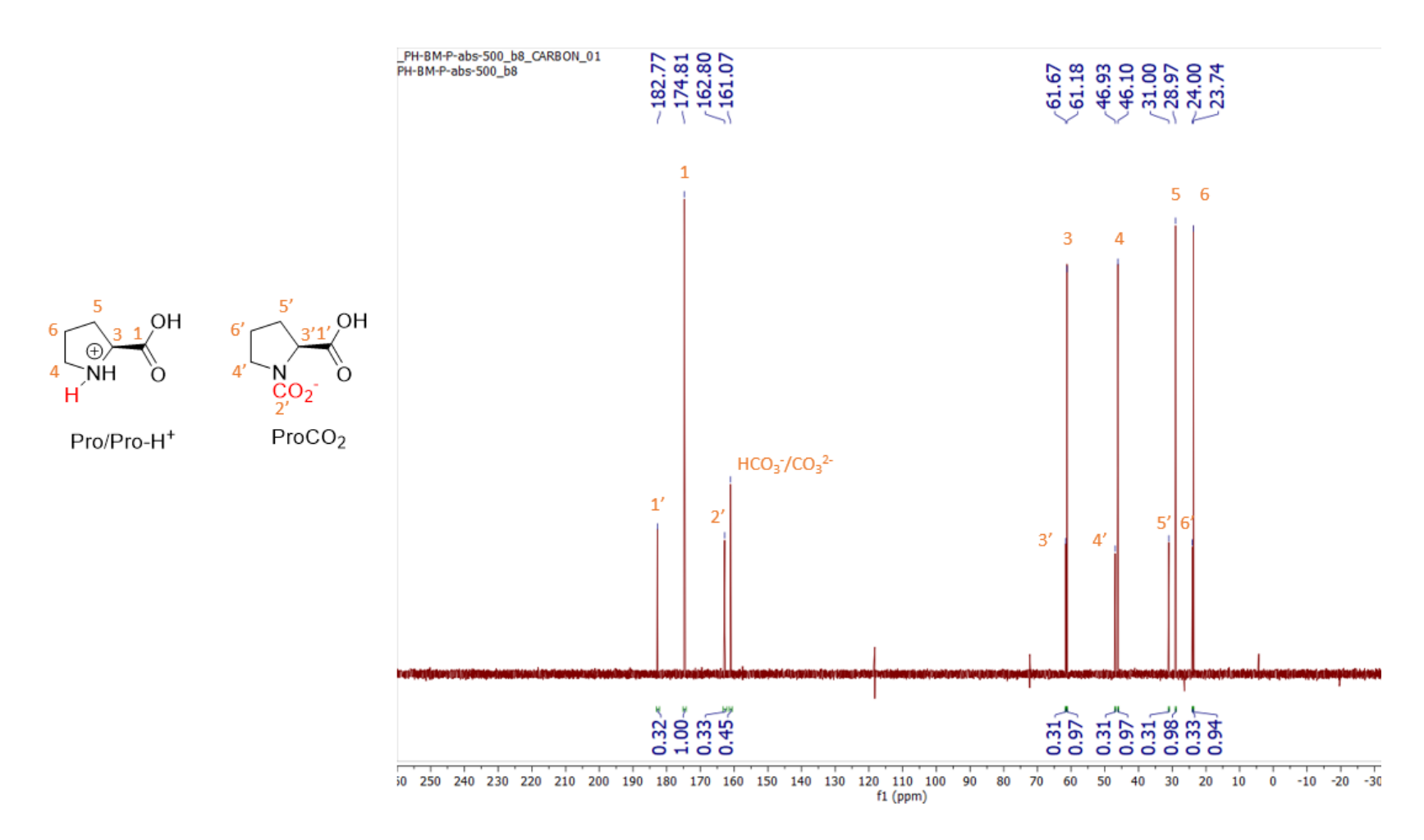


Figure A24. $^{13}C\{^{1}H\}$ NMR spectrum of proline sample after CO₂ absorption in D₂O.

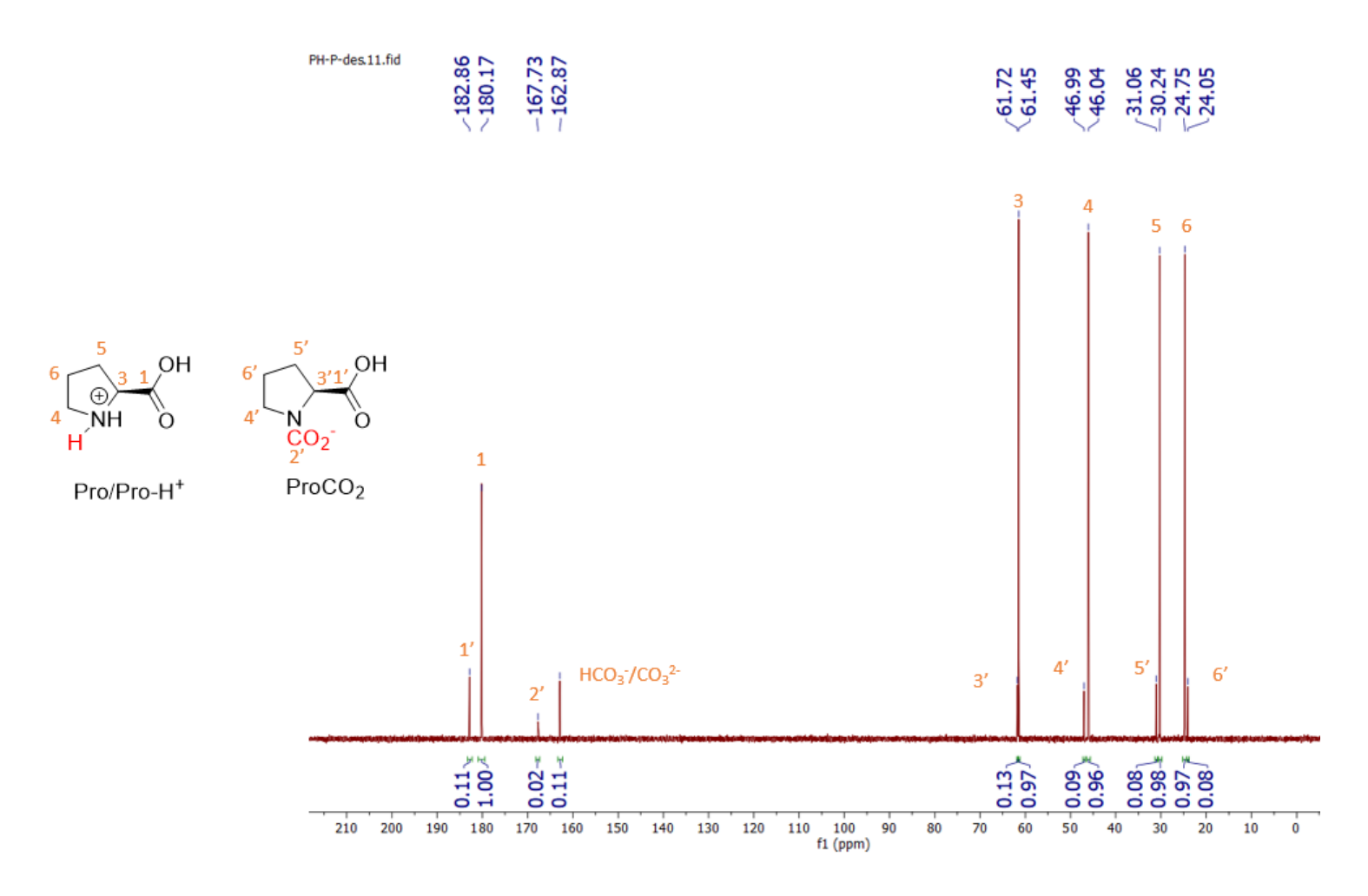


Figure A25. ¹³C{¹H} NMR spectrum of proline sample after CO₂ desorption in D₂O.

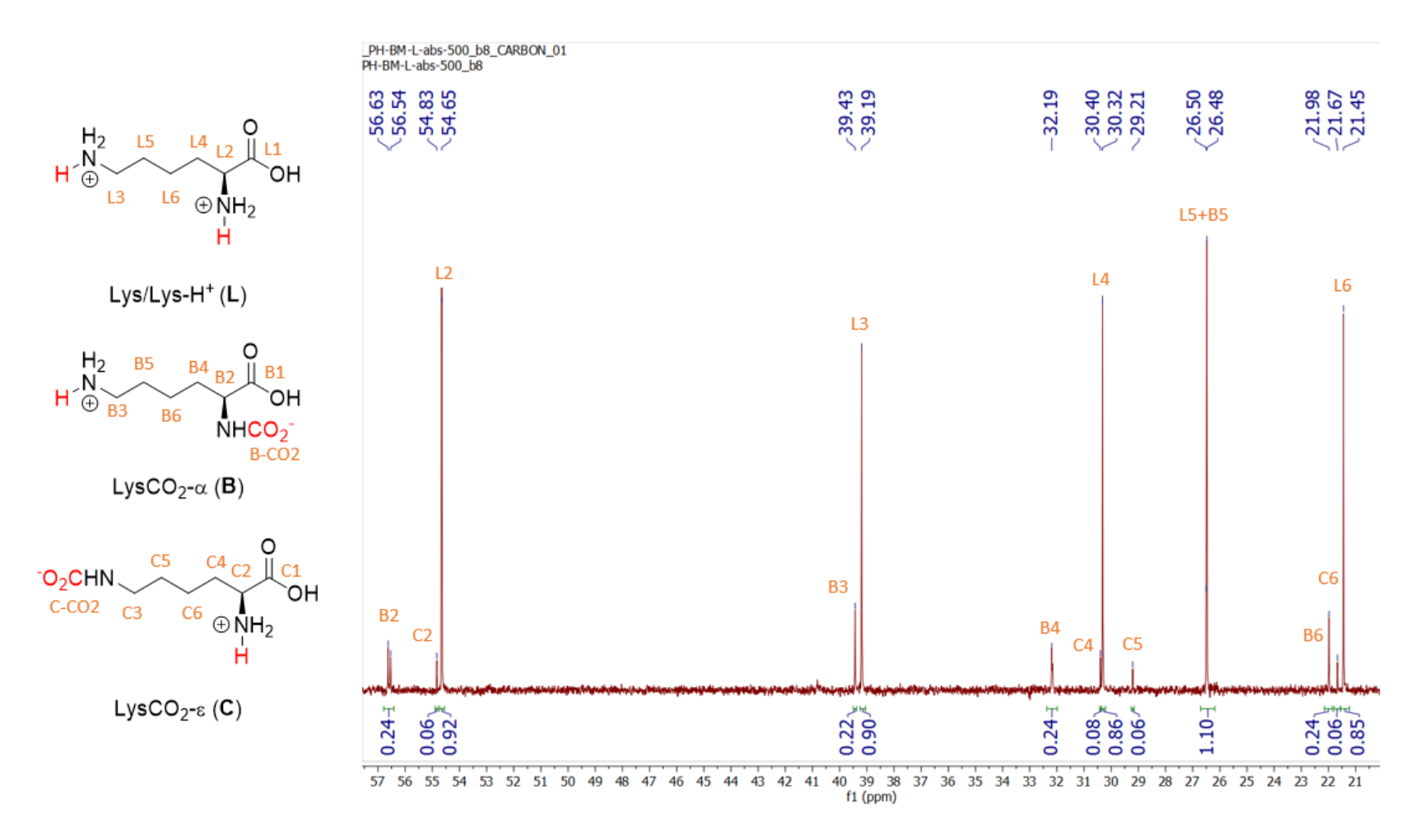


Figure A26. ¹³C{¹H} NMR spectrum of lysine sample after CO₂ absorption in D₂O (aliphatic region only).

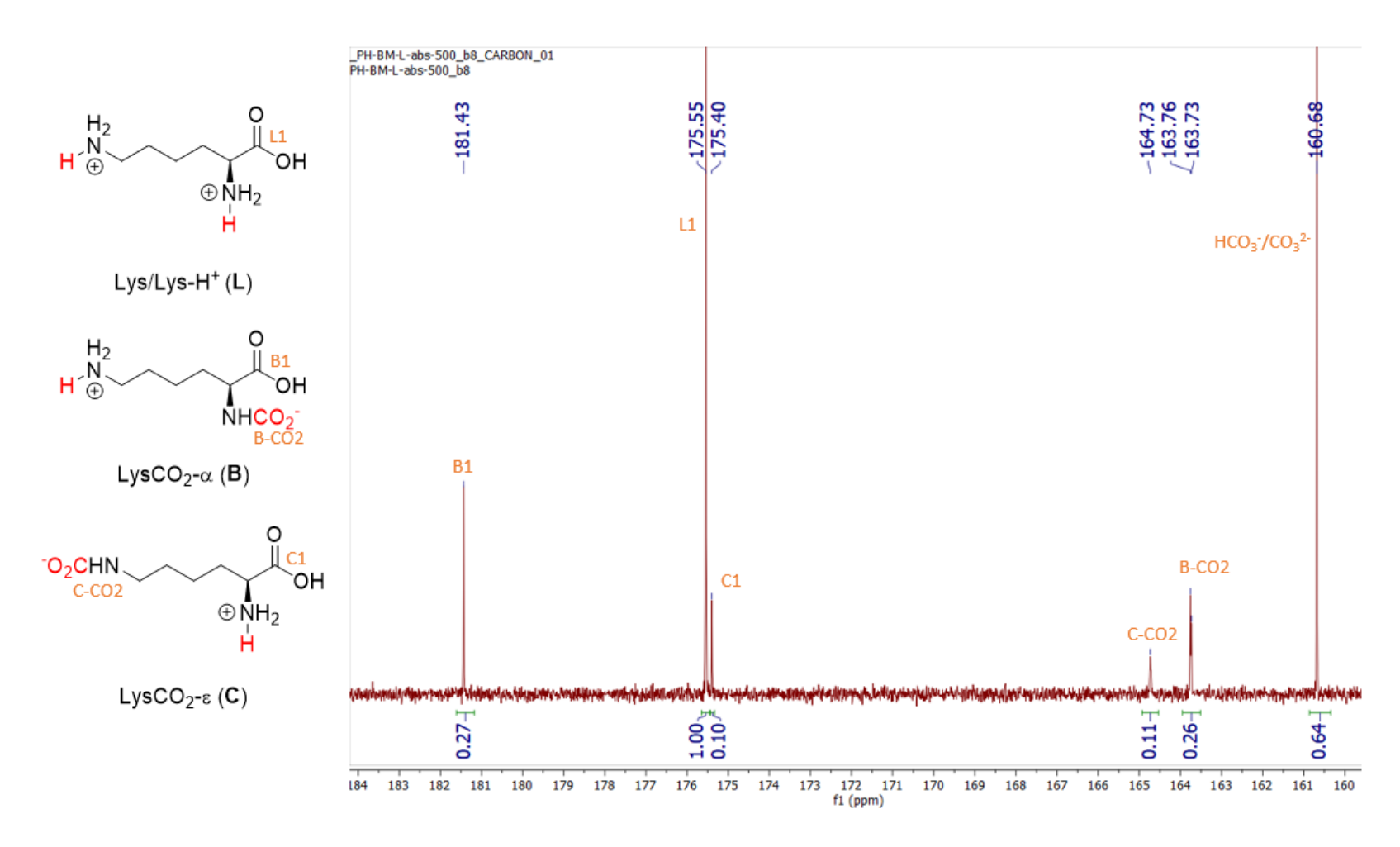


Figure A27. ¹³C{¹H} NMR spectrum of lysine sample after CO₂ absorption in D₂O (carbonyl region only).

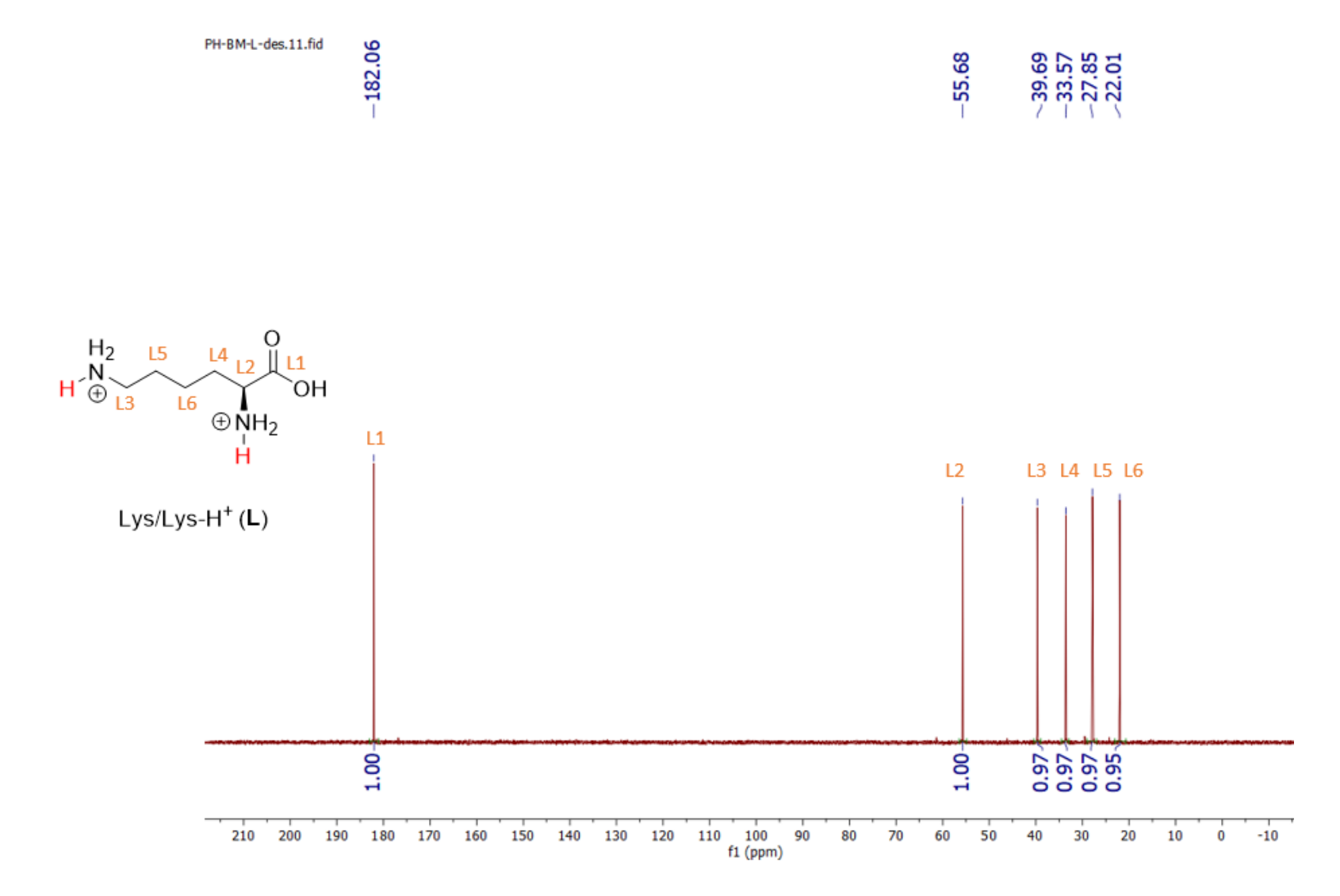


Figure A28. ¹³C{¹H} NMR spectrum of lysine sample after CO₂ desorption in D₂O.

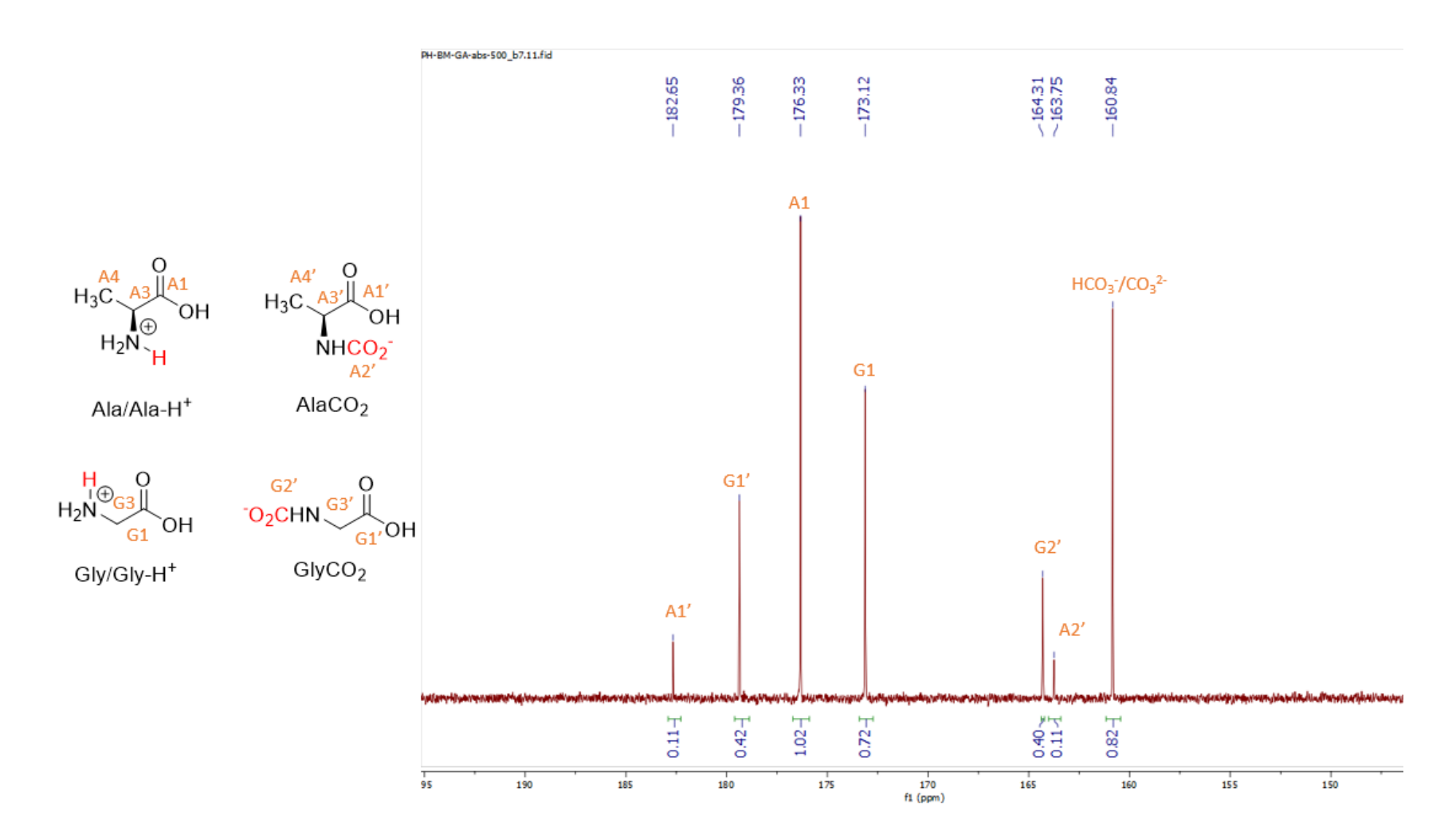


Figure A29. ¹³C{¹H} NMR spectrum of GA sample after CO₂ absorption in D₂O (carbonyl region only).

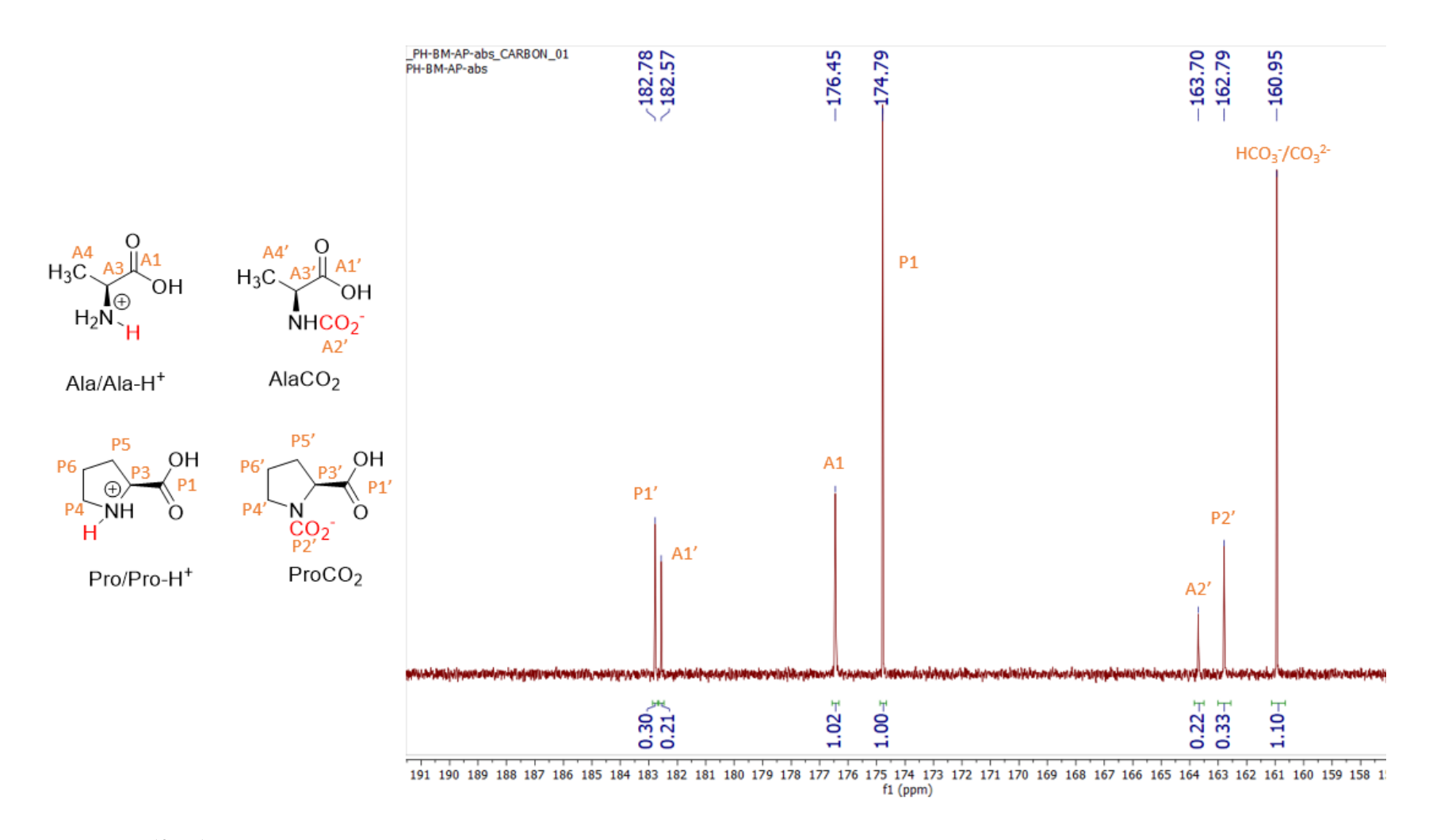


Figure A30. $^{13}C\{^{1}H\}$ NMR spectrum of AP sample after CO_2 absorption in D_2O (carbonyl region only).

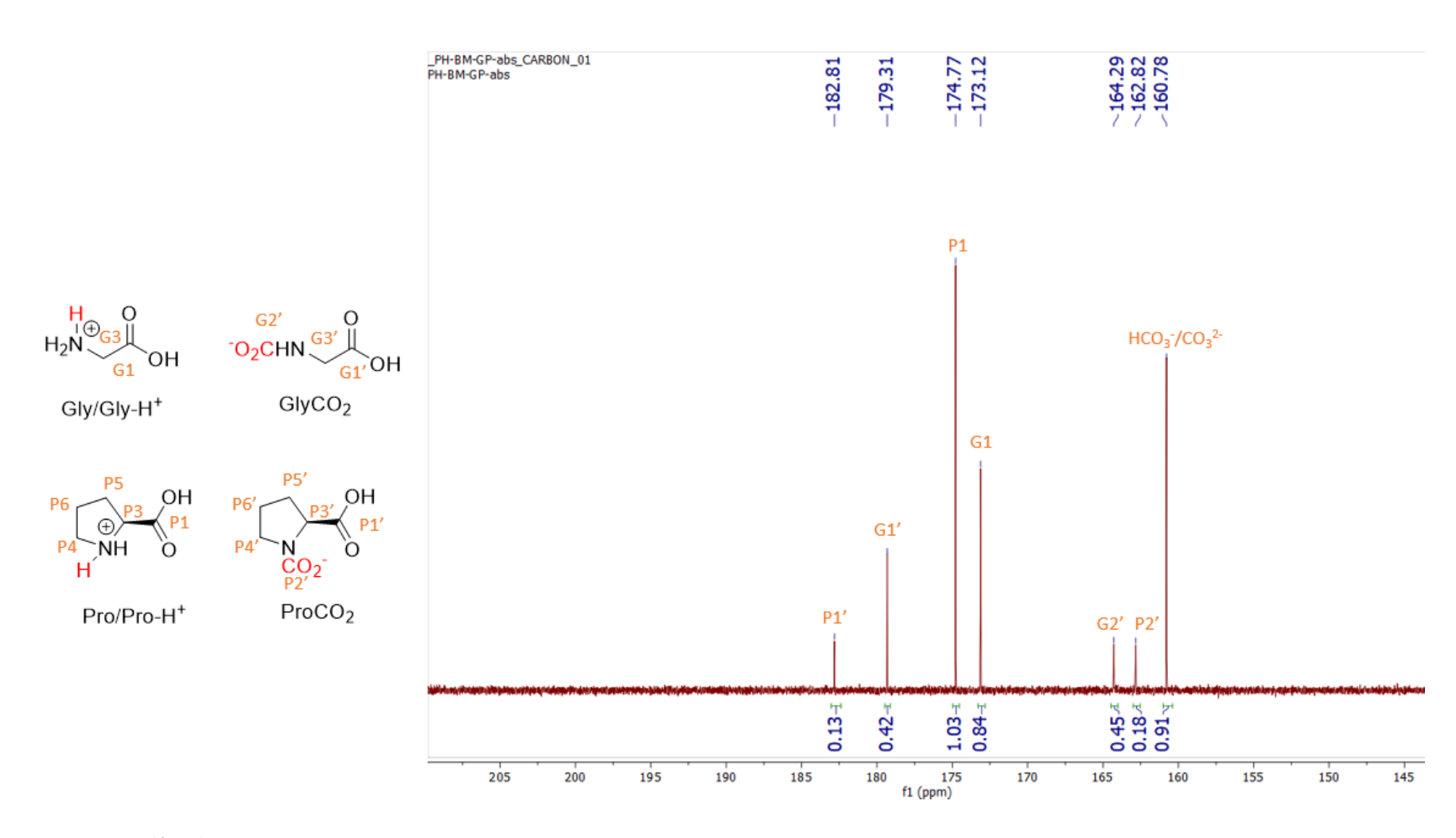


Figure A31. ¹³C{¹H} NMR spectrum of GP sample after CO₂ absorption in D₂O (carbonyl region only).

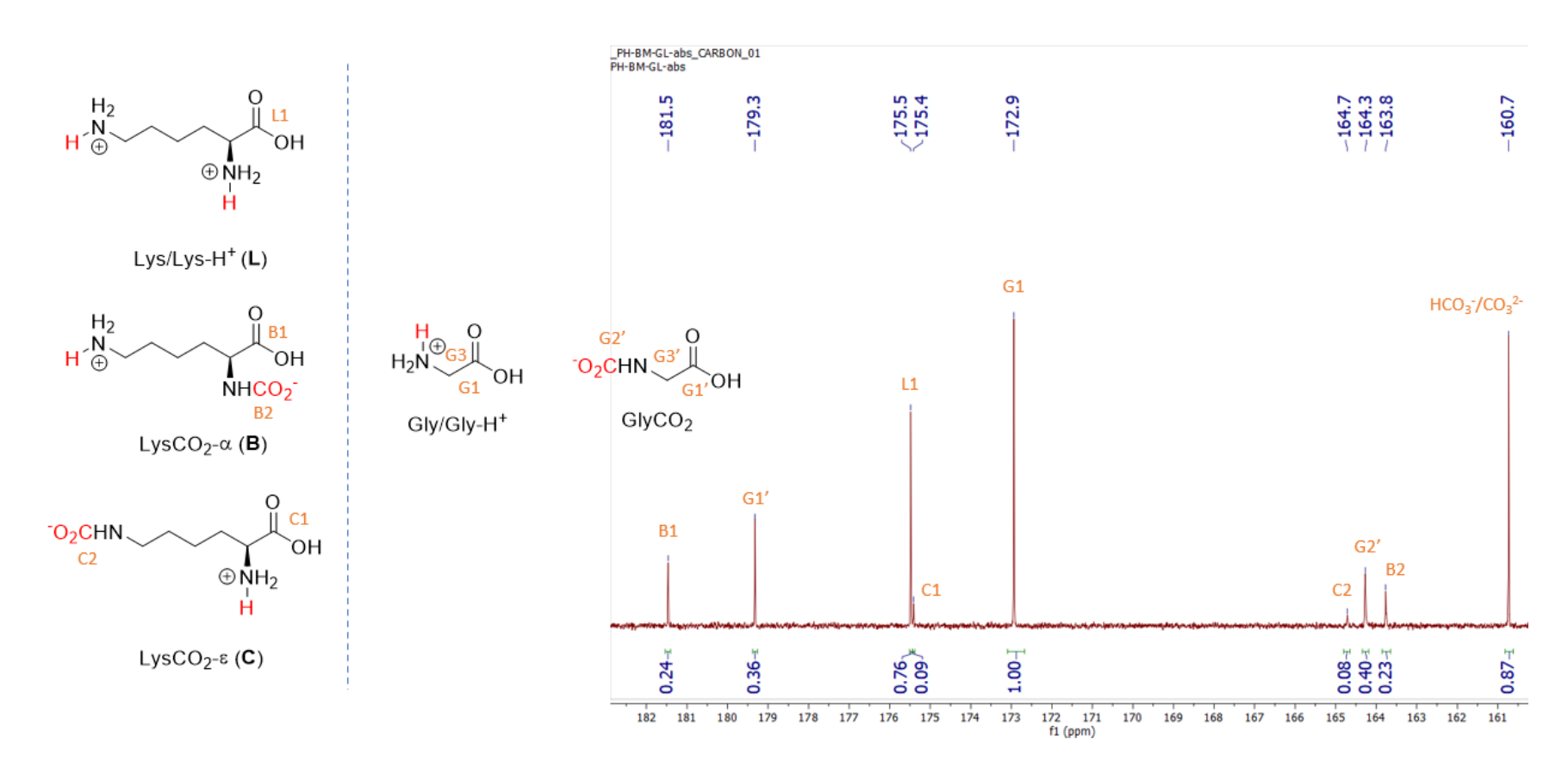


Figure A32. ¹³C{¹H} NMR spectrum of GL sample after CO₂ absorption in D₂O (carbonyl region only).

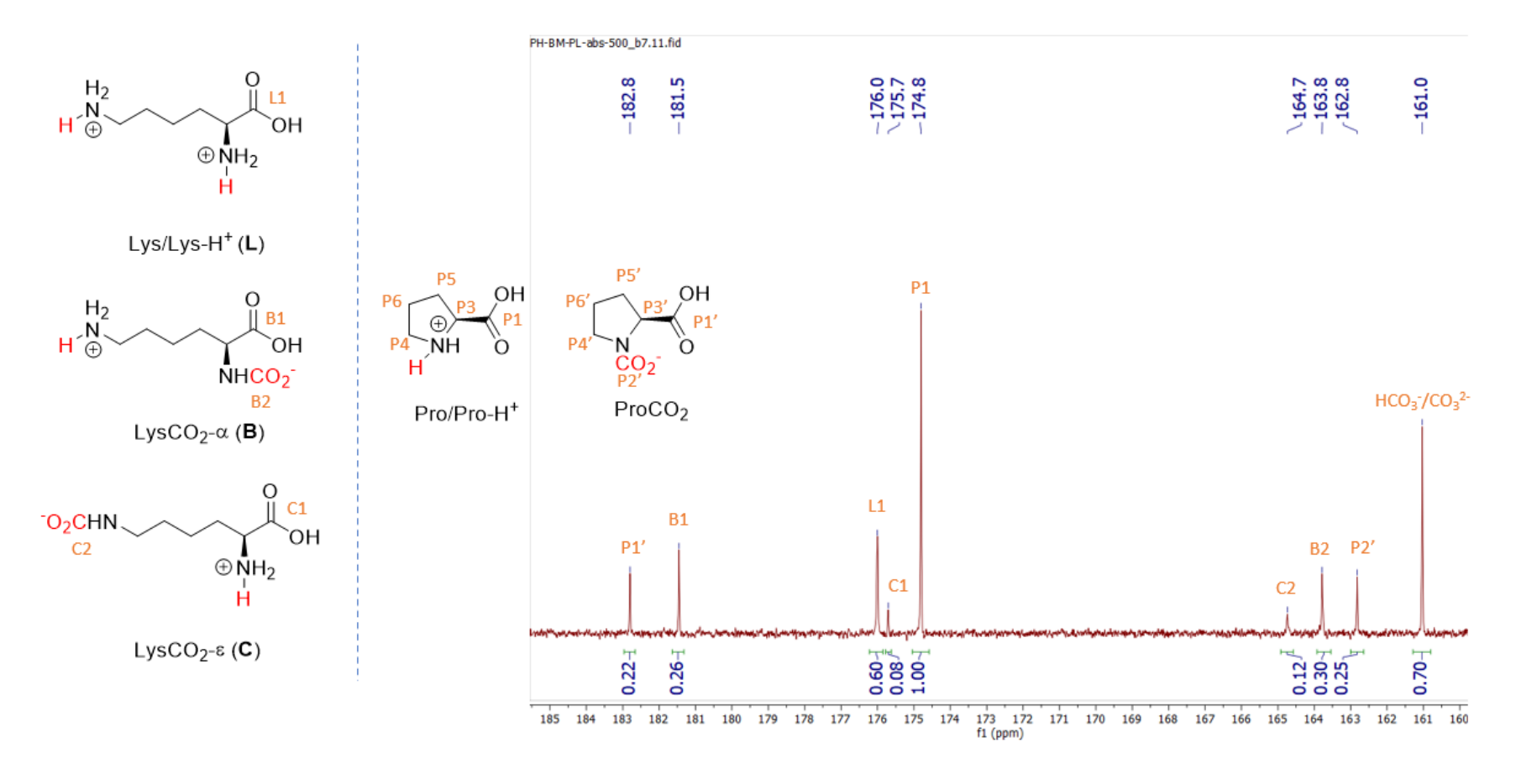


Figure A33. ¹³C{¹H} NMR spectrum of GL sample after CO₂ absorption in D₂O (carbonyl region only).

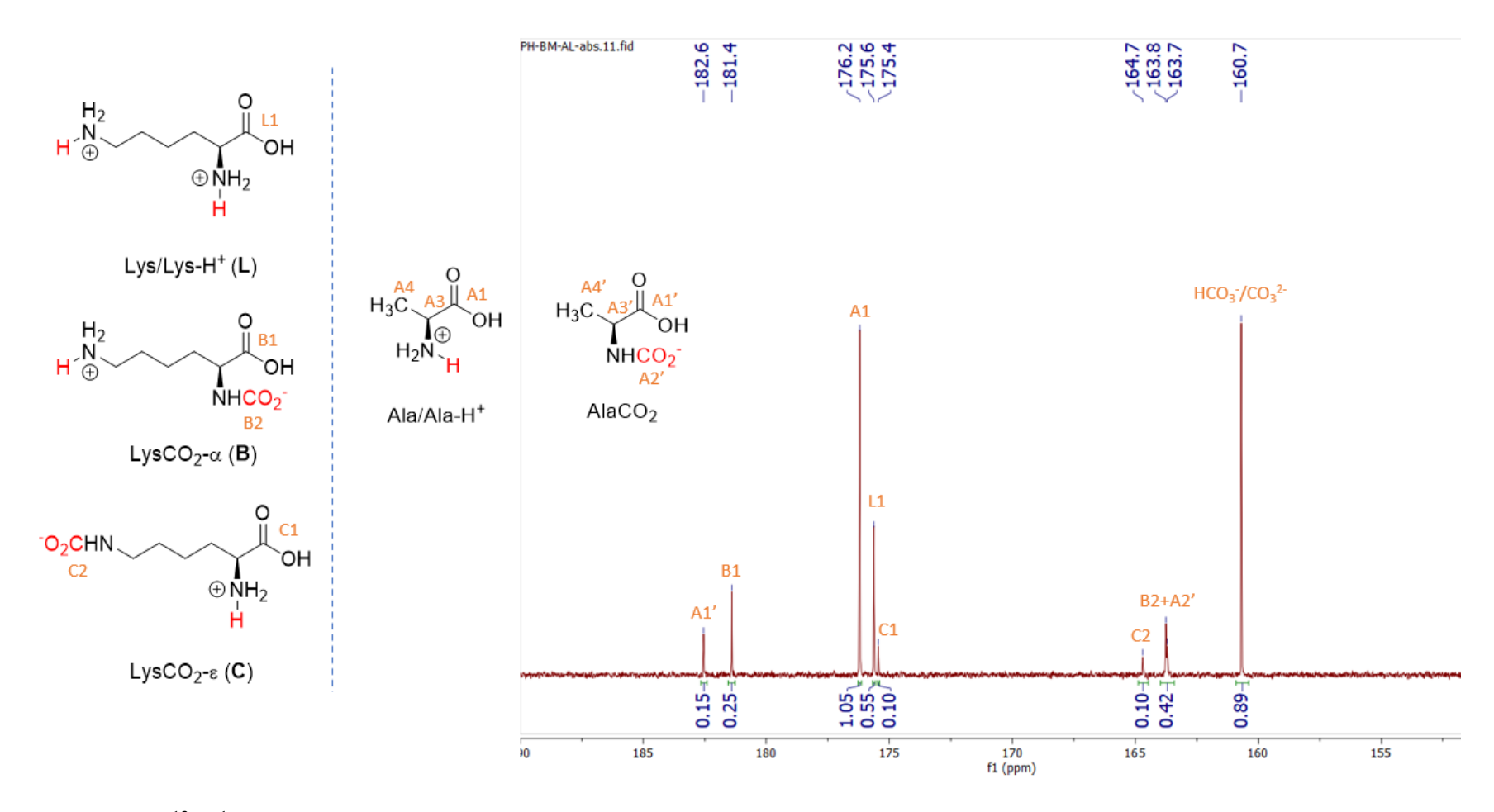


Figure A34. ¹³C{ ¹H} NMR spectrum of AL sample after CO₂ absorption in D₂O (carbonyl region only).

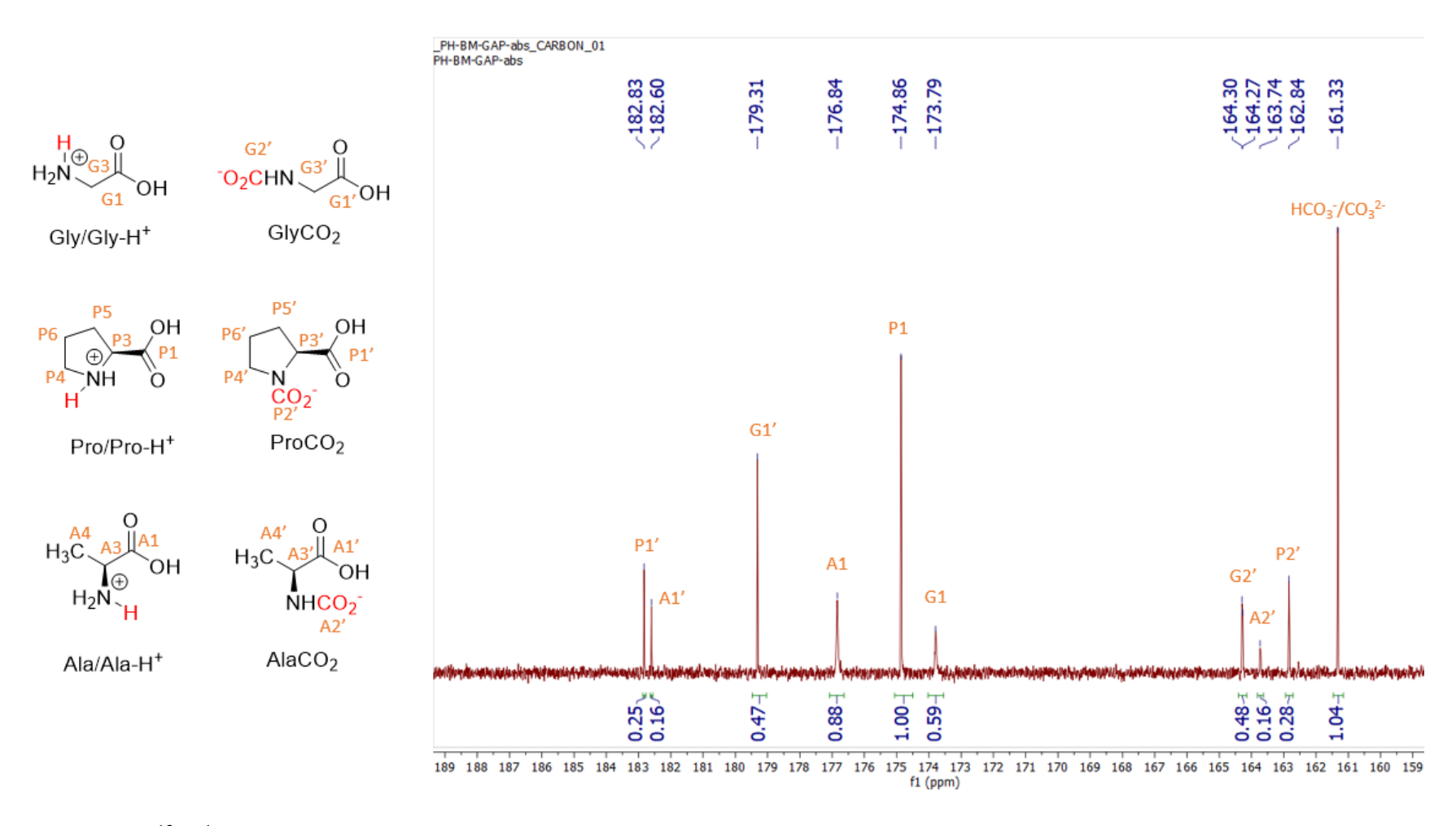


Figure A35. ¹³C{¹H} NMR spectrum of GAP sample after CO₂ absorption in D₂O (carbonyl region only).

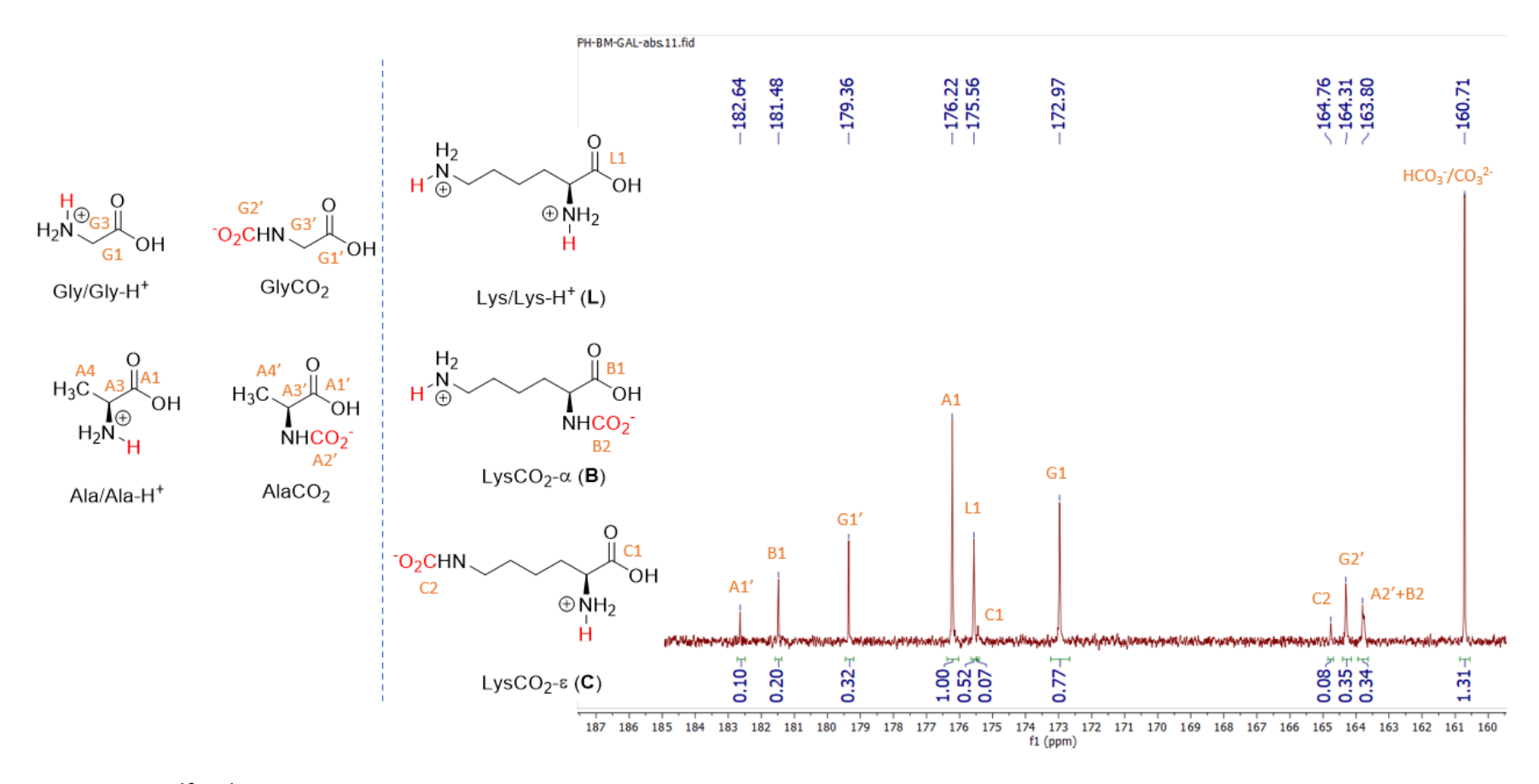


Figure A36. ¹³C{¹H} NMR spectrum of GAL sample after CO₂ absorption in D₂O (carbonyl region only).

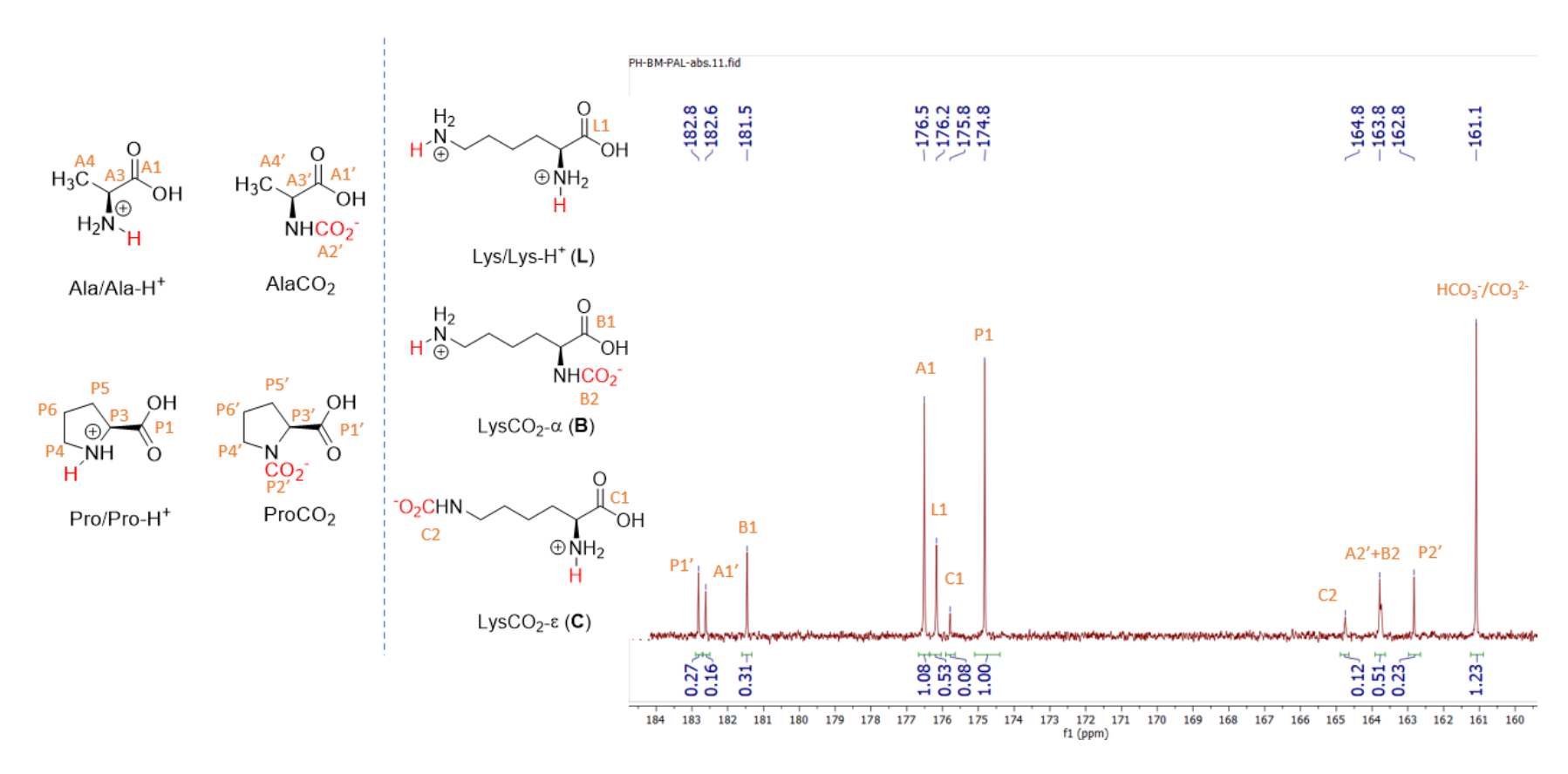


Figure A37. ¹³C{¹H} NMR spectrum of PAL sample after CO₂ absorption in D₂O (carbonyl region only).

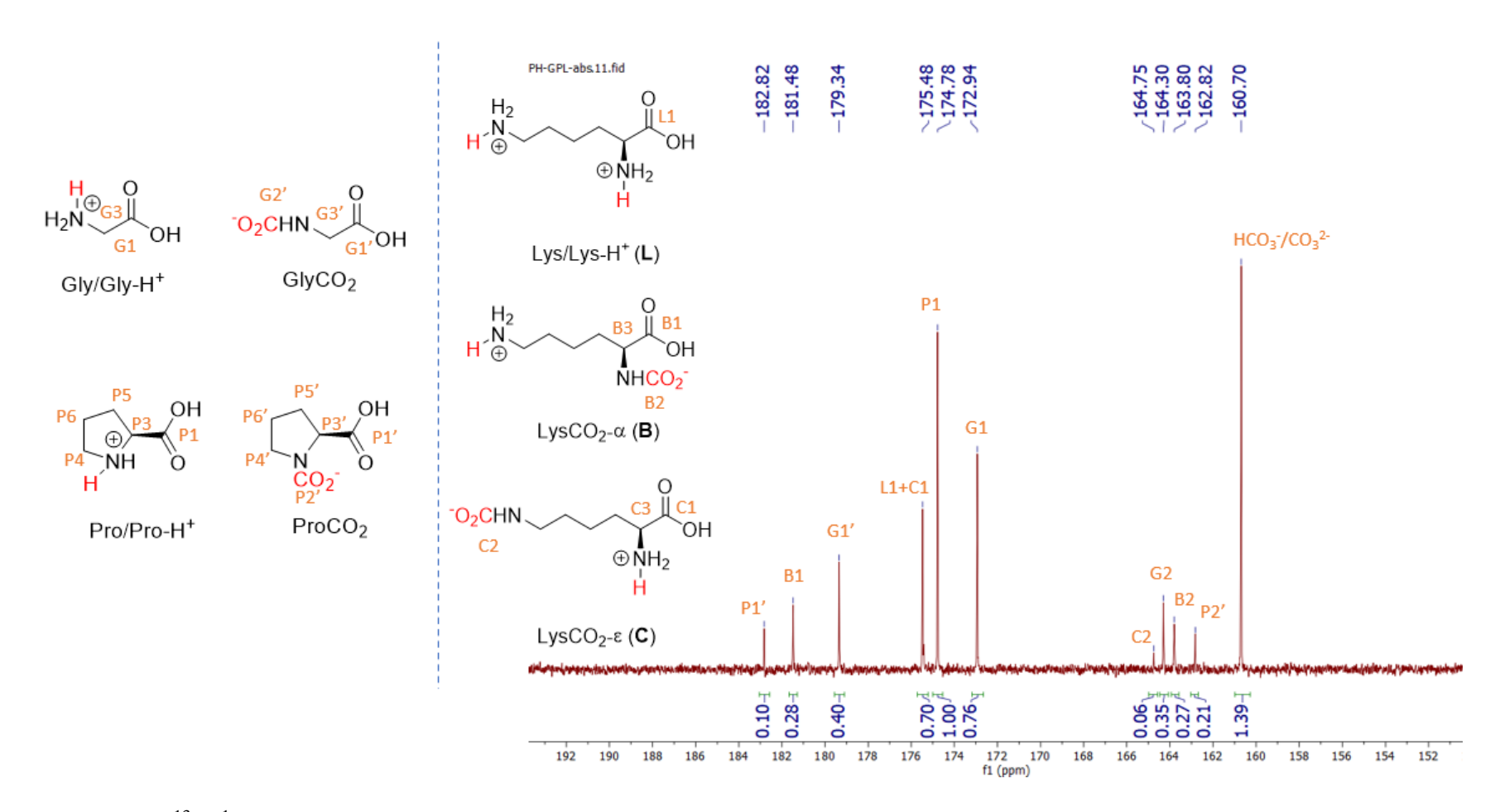


Figure A38. ¹³C{¹H} NMR spectrum of GPL sample after CO₂ absorption in D₂O (carbonyl region only).

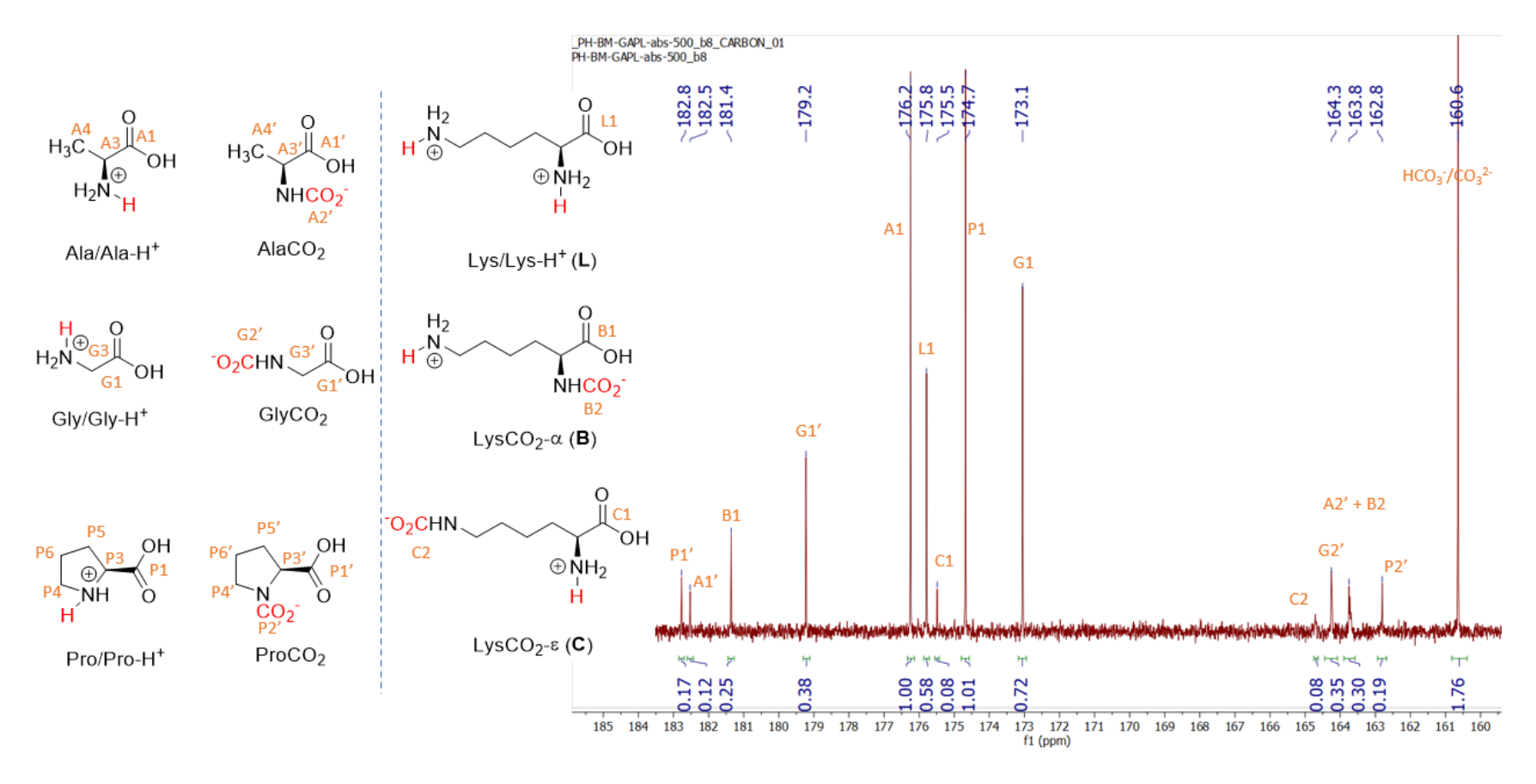


Figure A39. ¹³C{¹H} NMR spectrum of GAPL sample after CO₂ absorption in D₂O (carbonyl region only).

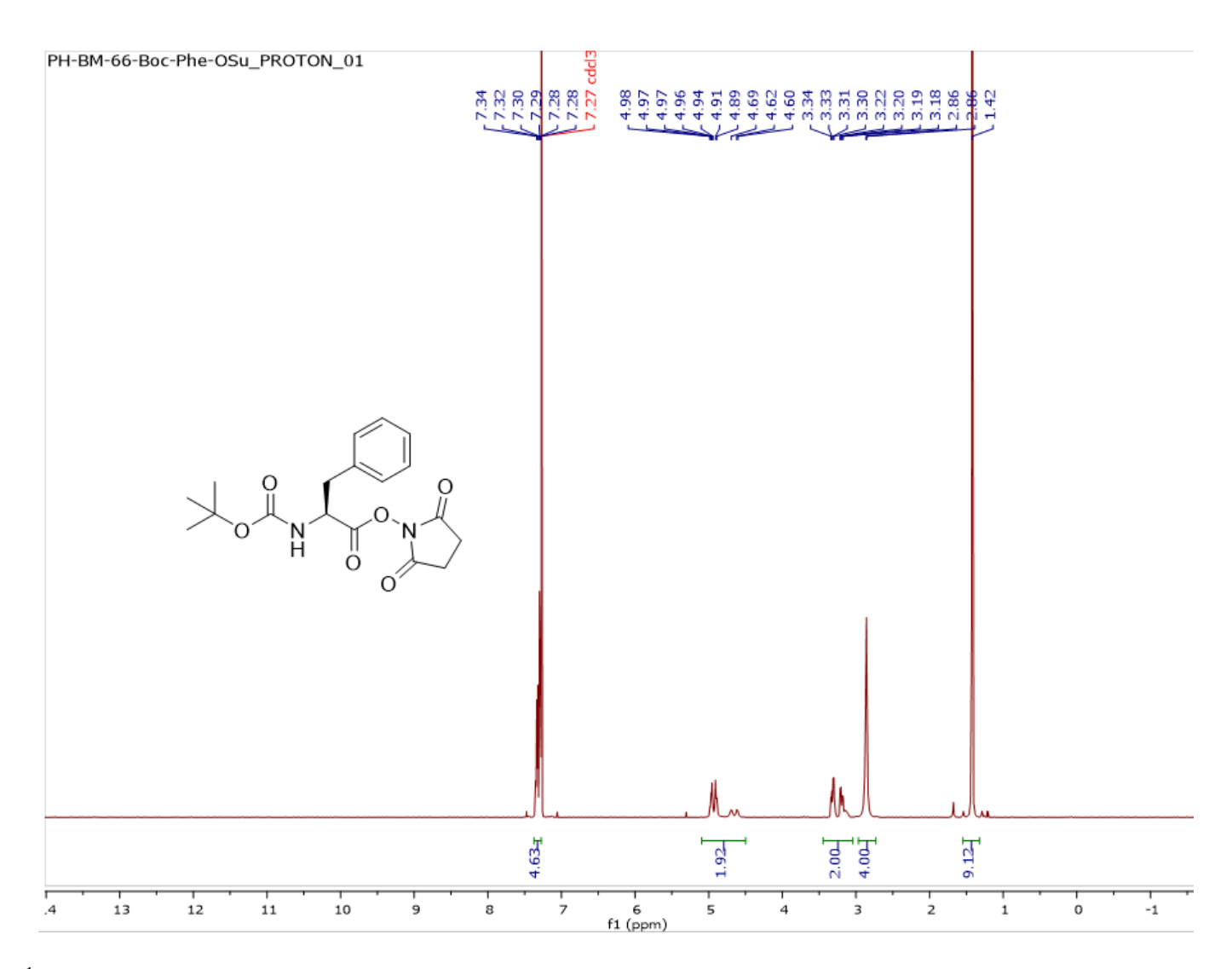


Figure A40. ¹H NMR spectrum of Boc-Phe-OSu in CDCl₃.

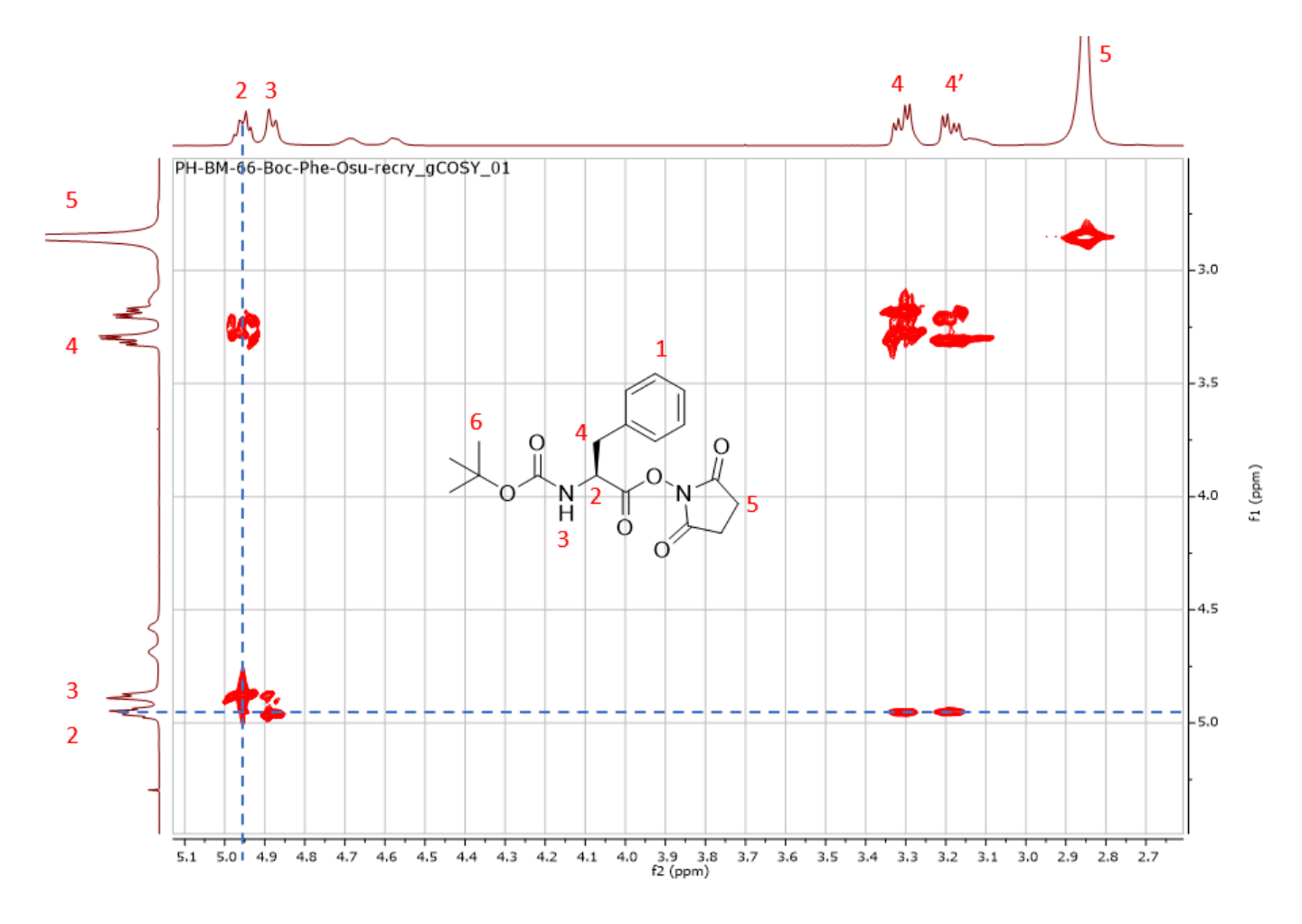


Figure A41. gCOSY of Boc-Phe-OSu in CDCl₃.

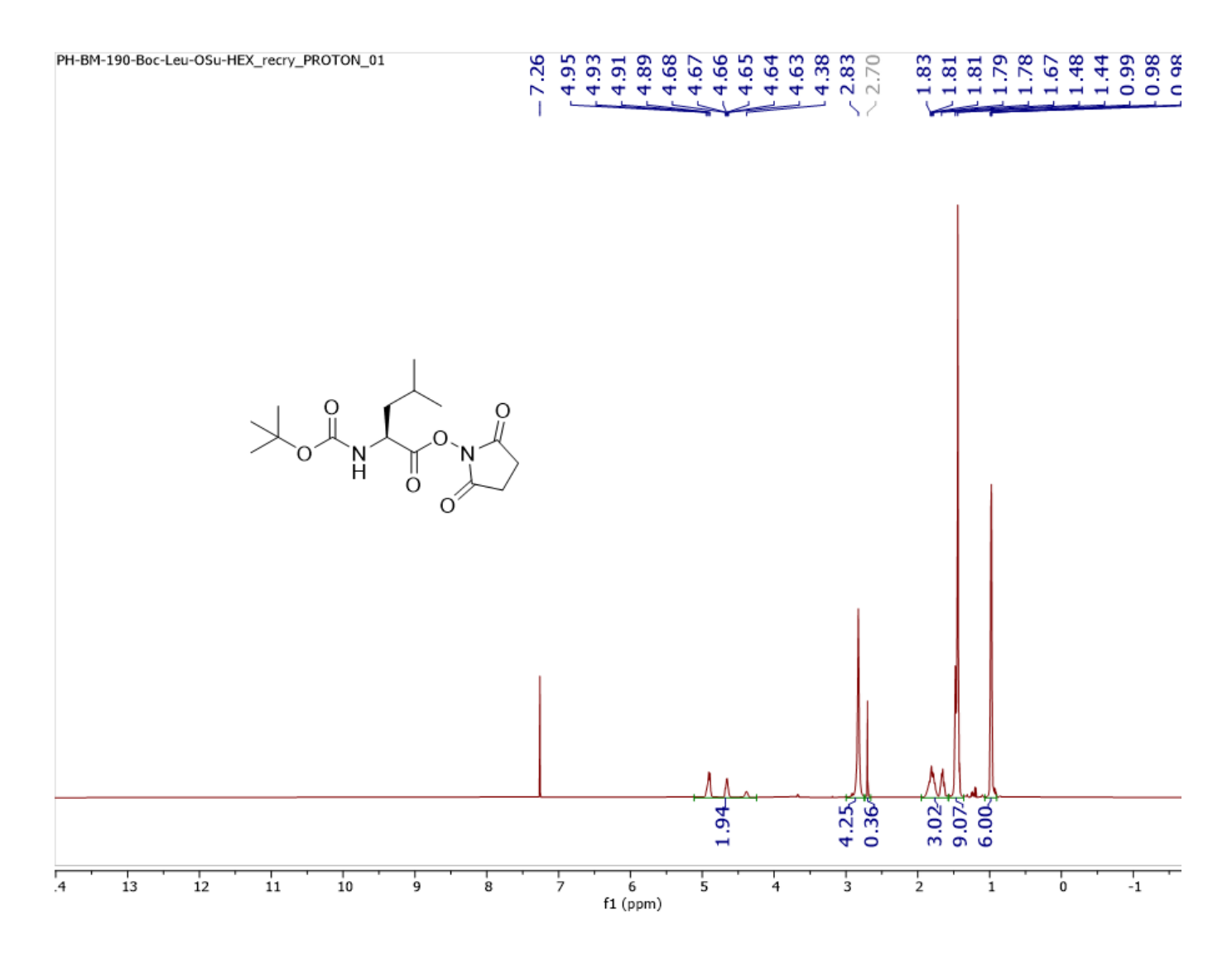


Figure A42. ^1H NMR spectrum of Boc-Leu-OSu in CDCl $_3$.

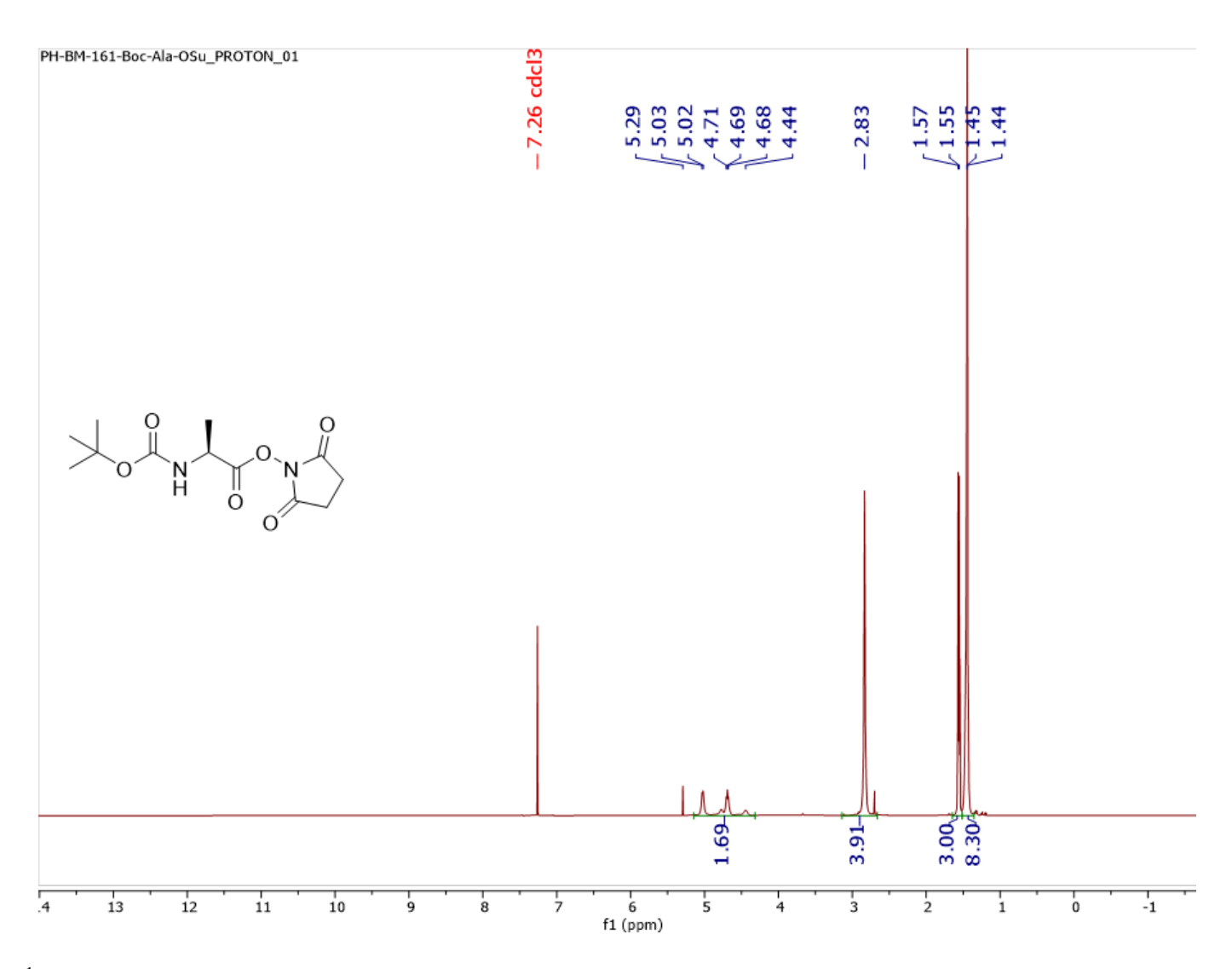


Figure A43. ¹H NMR spectrum of Boc-Ala-OSu in CDCl₃.

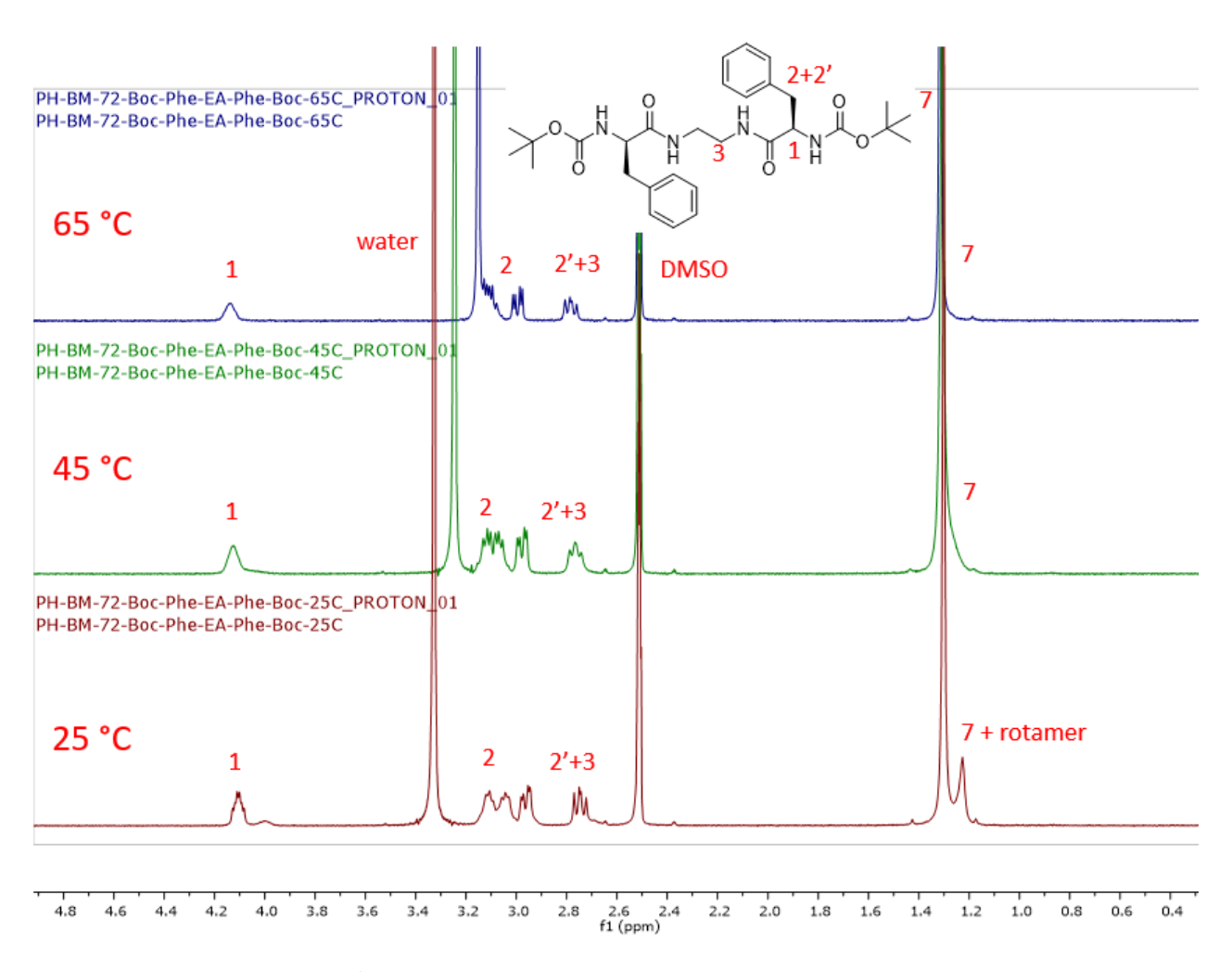


Figure A44. Overlapped variable temperature ¹H NMR spectrum of Boc-Phe-C2-Phe-Boc in CDCl₃ at 25 °C (bottom), at 45 °C (middle), and 65 °C (top).

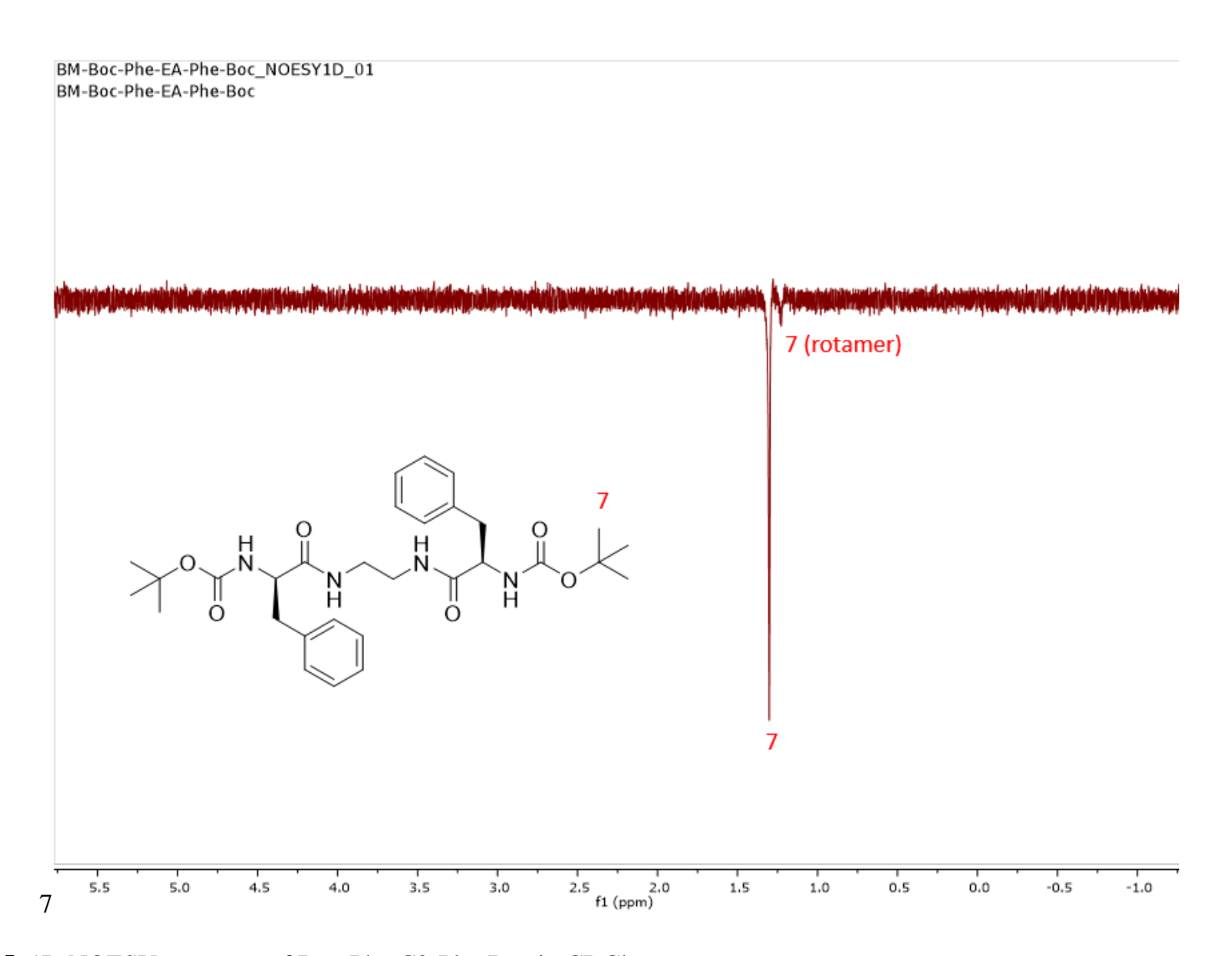


Figure A45. 1D NOESY spectrum of Boc-Phe-C2-Phe-Boc in CDCl₃.

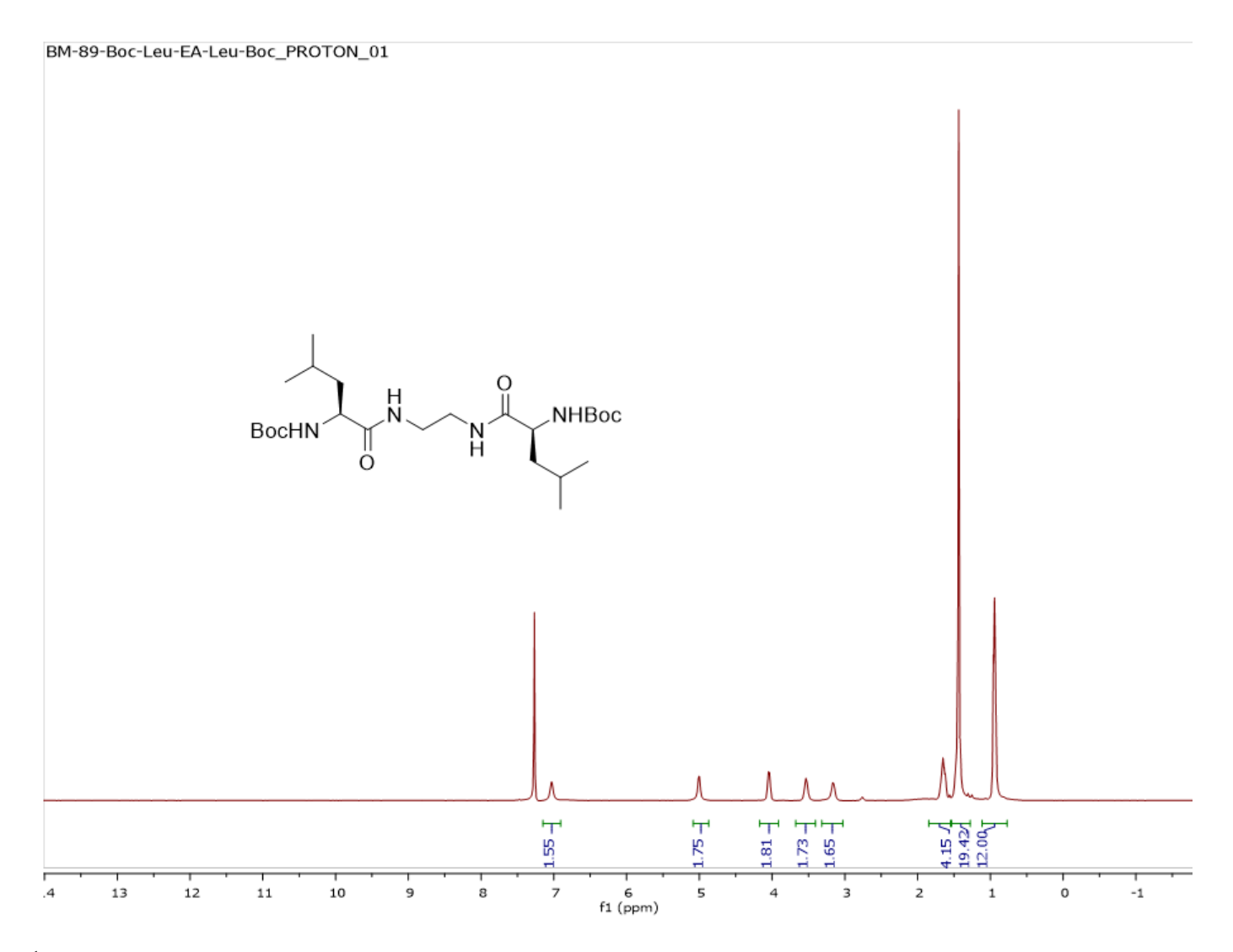


Figure A46. ¹H NMR spectrum of Boc-Leu-C2-Leu-Boc in CDCl₃.

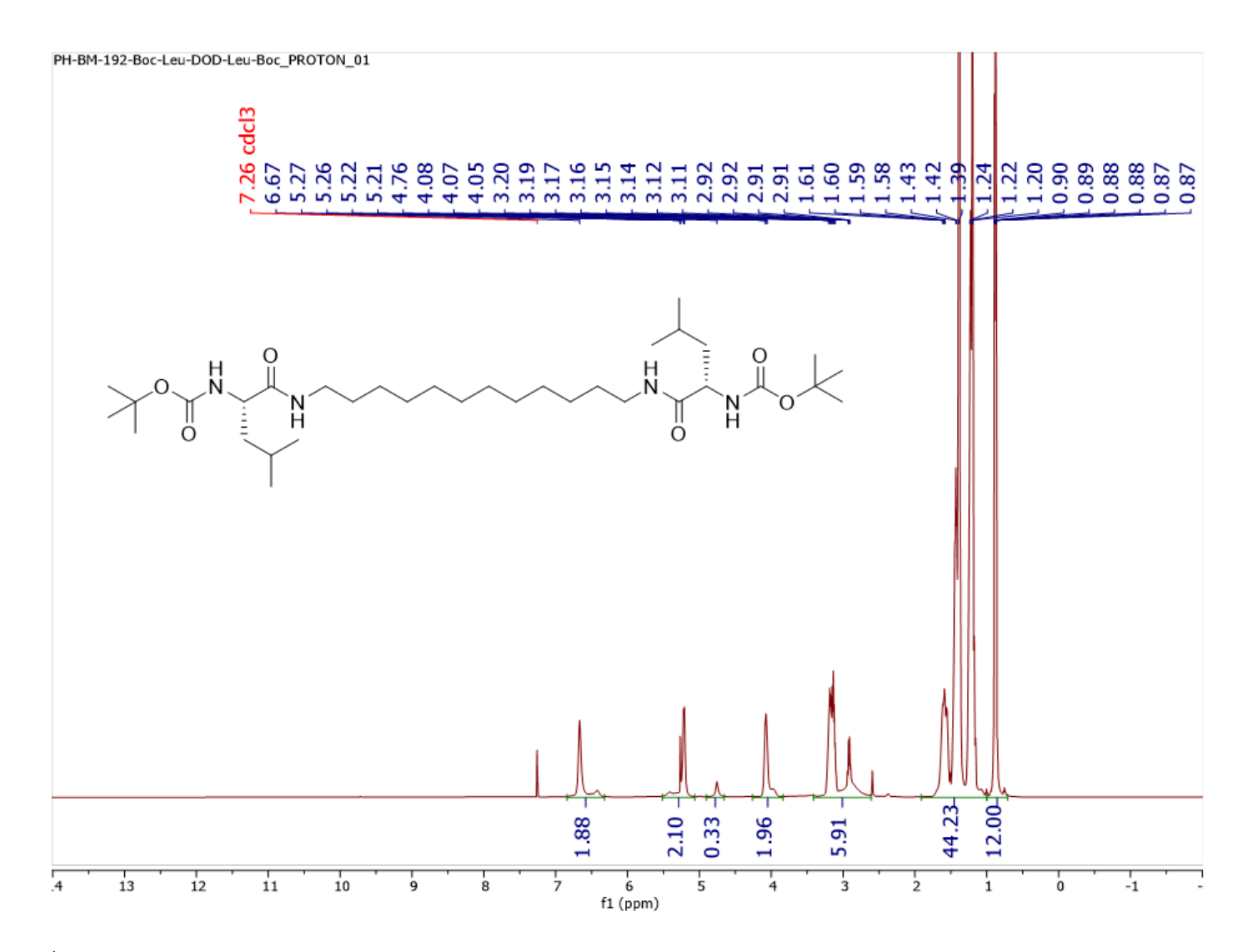


Figure A47. ¹H NMR spectrum of Boc-Leu-C12-Leu-Boc in CDCl₃.

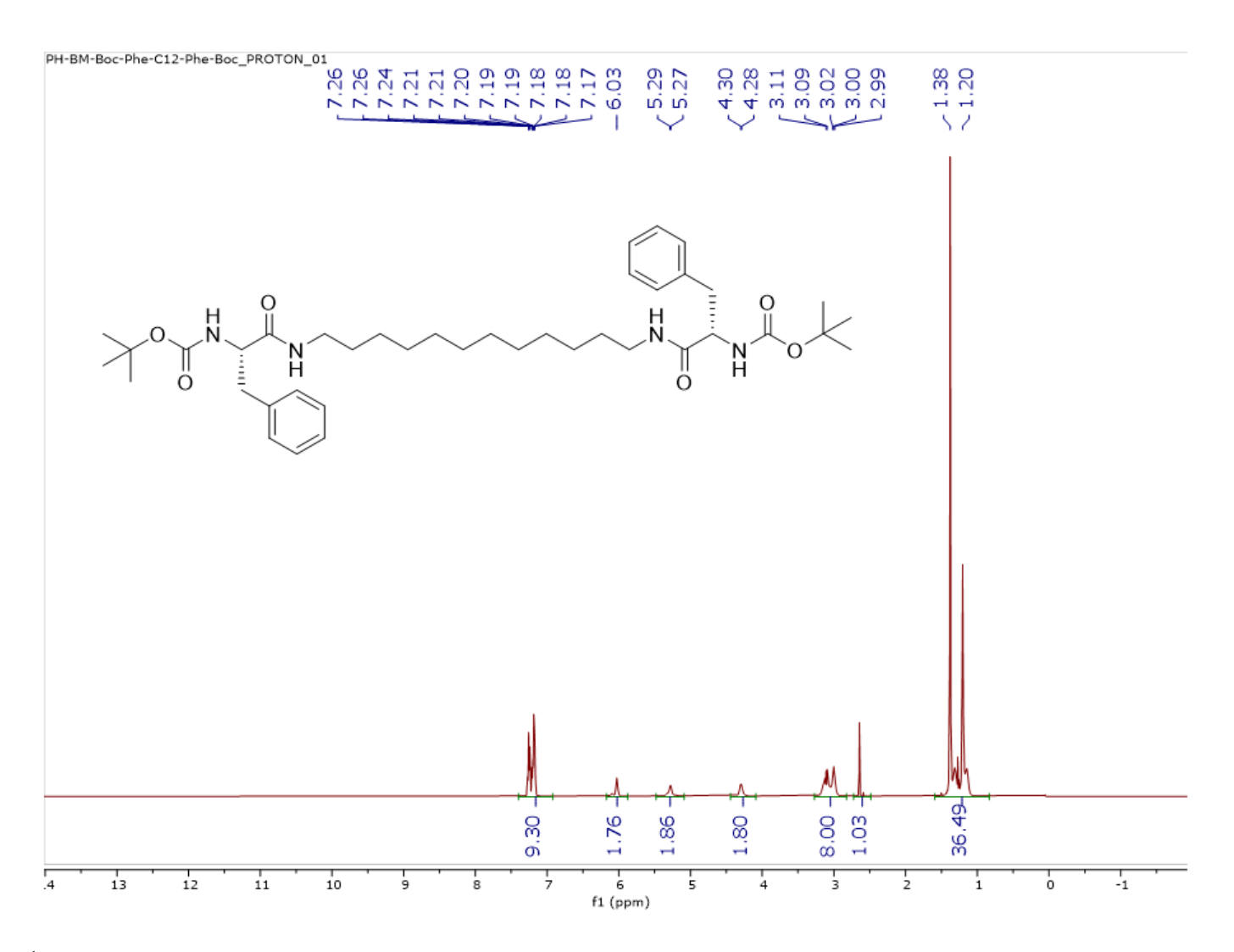


Figure A48. ¹H NMR spectrum of Boc-Phe-C12-Phe-Boc in CDCl₃.

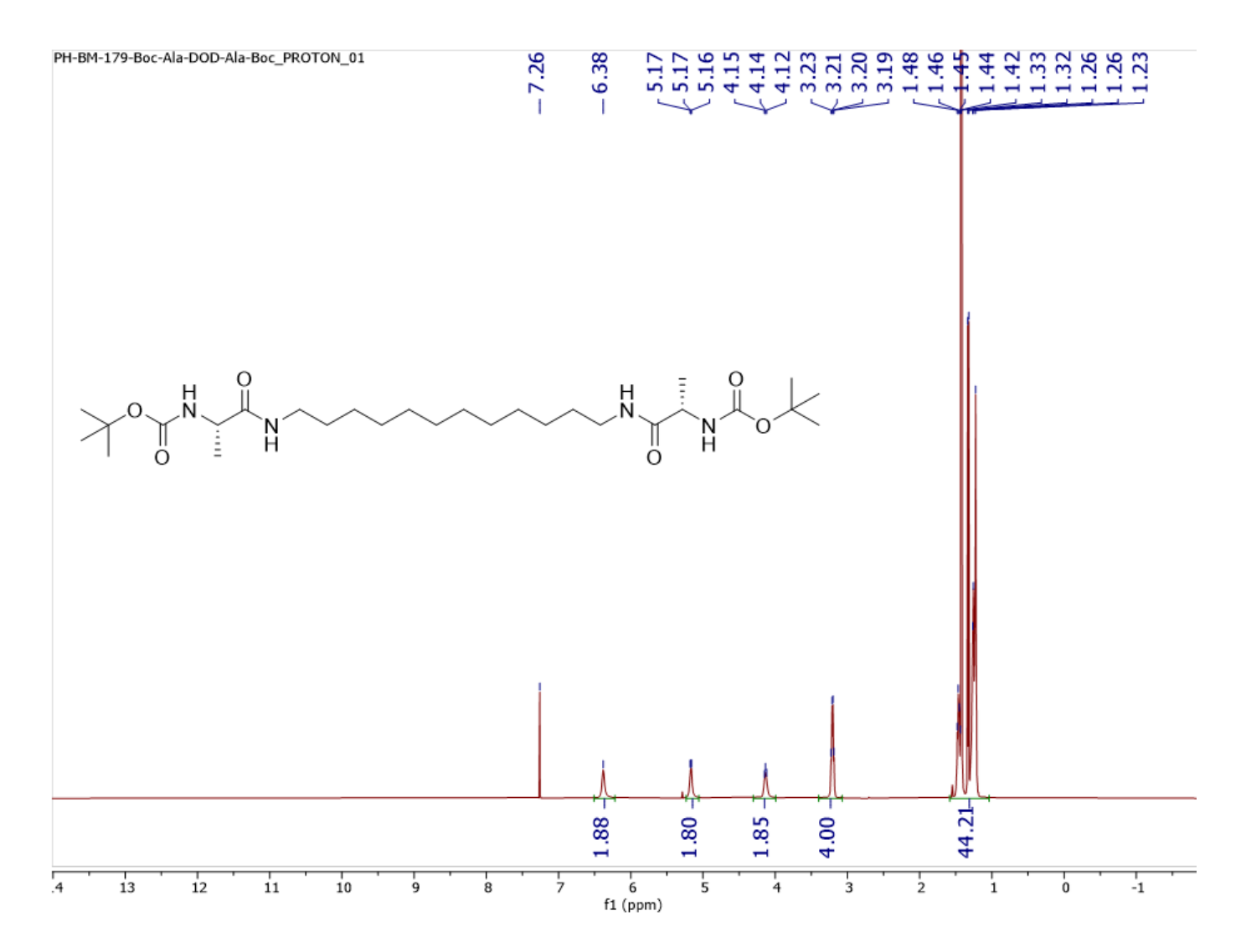


Figure A49. ¹H NMR spectrum of Boc-Ala-C12-Ala-Boc in CDCl₃.

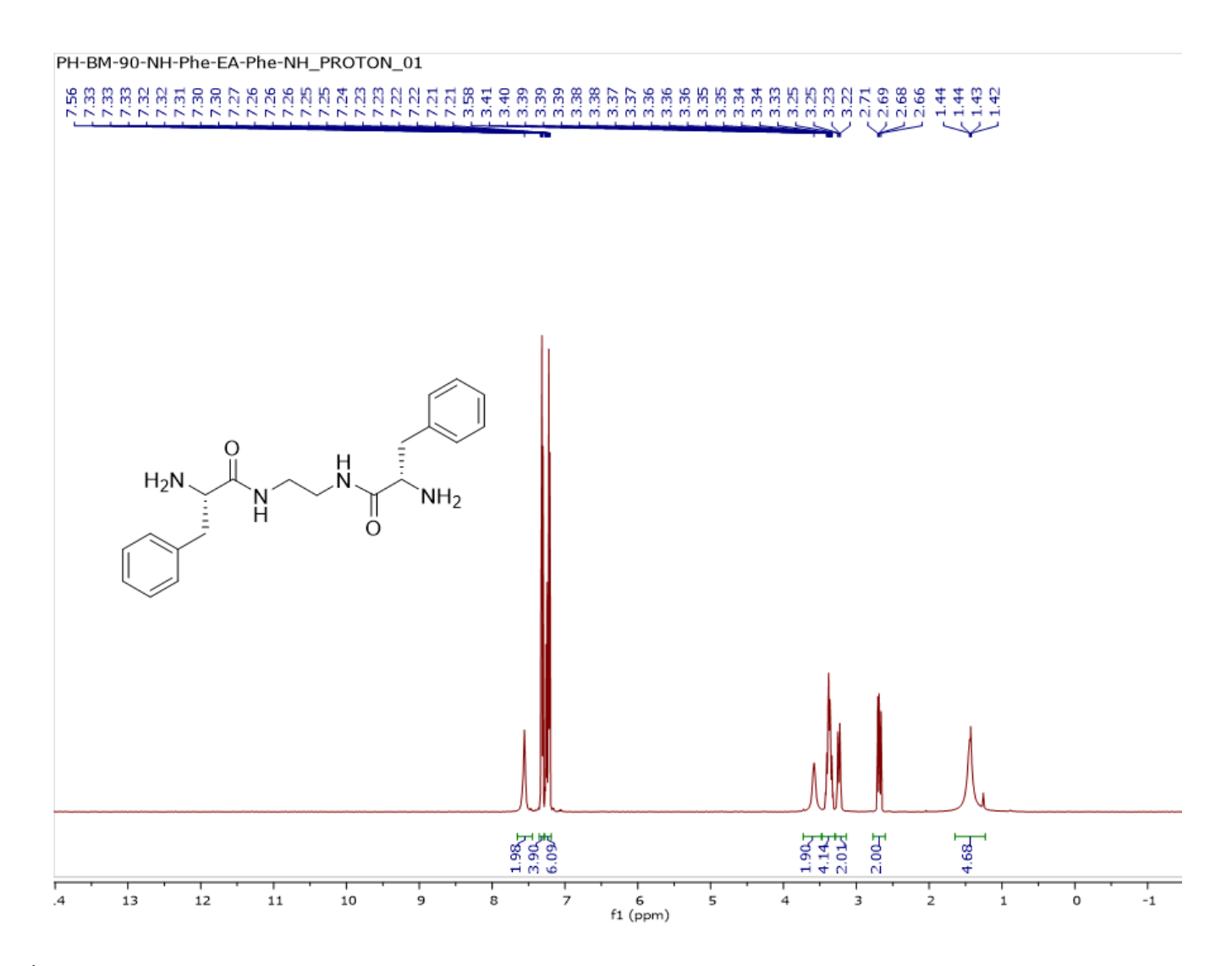


Figure A50. ¹H NMR spectrum of NH-Phe-C2-Phe-NH in CDCl₃.

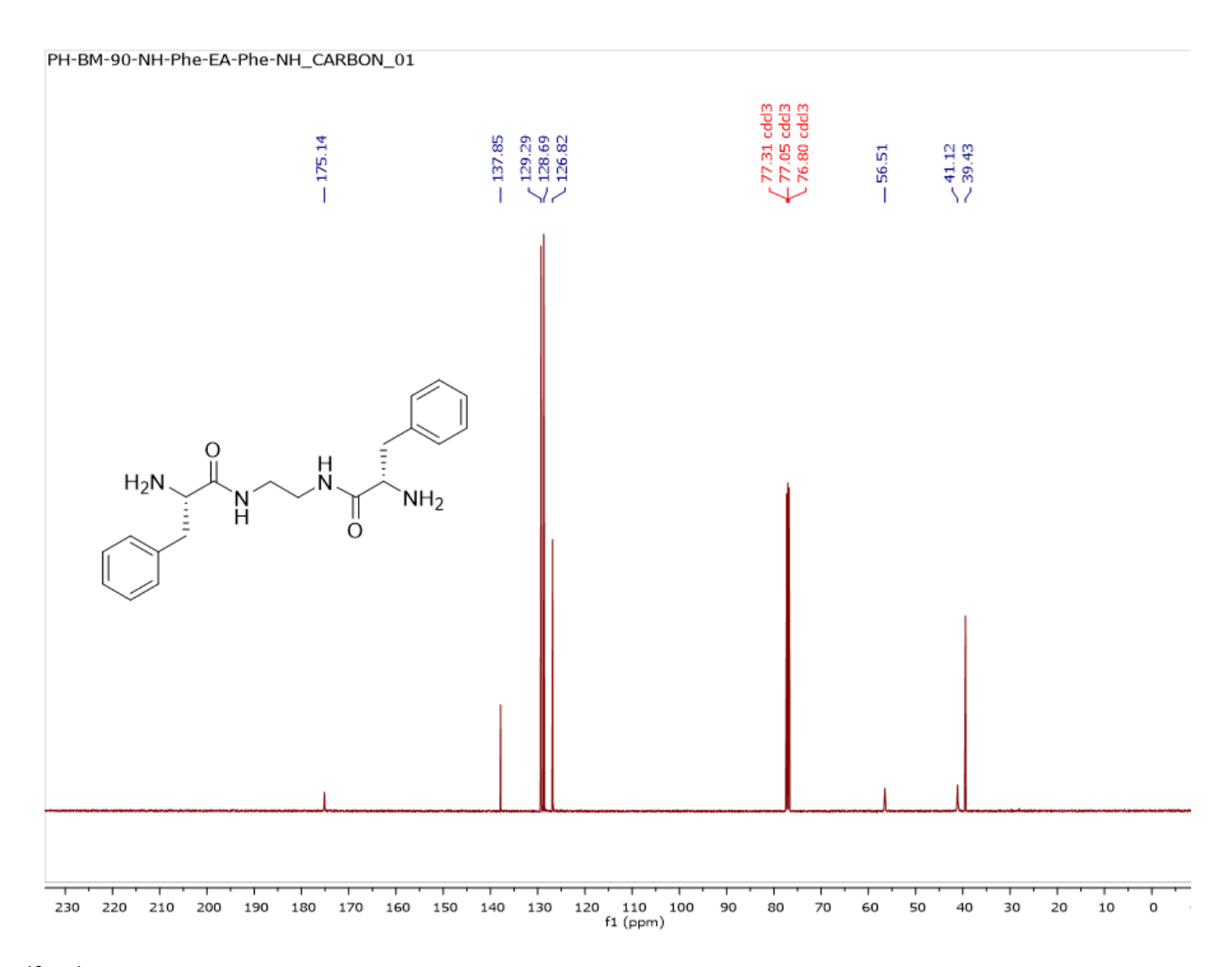


Figure A51. $^{13}C\{^{1}H\}$ NMR spectrum of NH-Phe-C2-Phe-NH in CDCl₃.

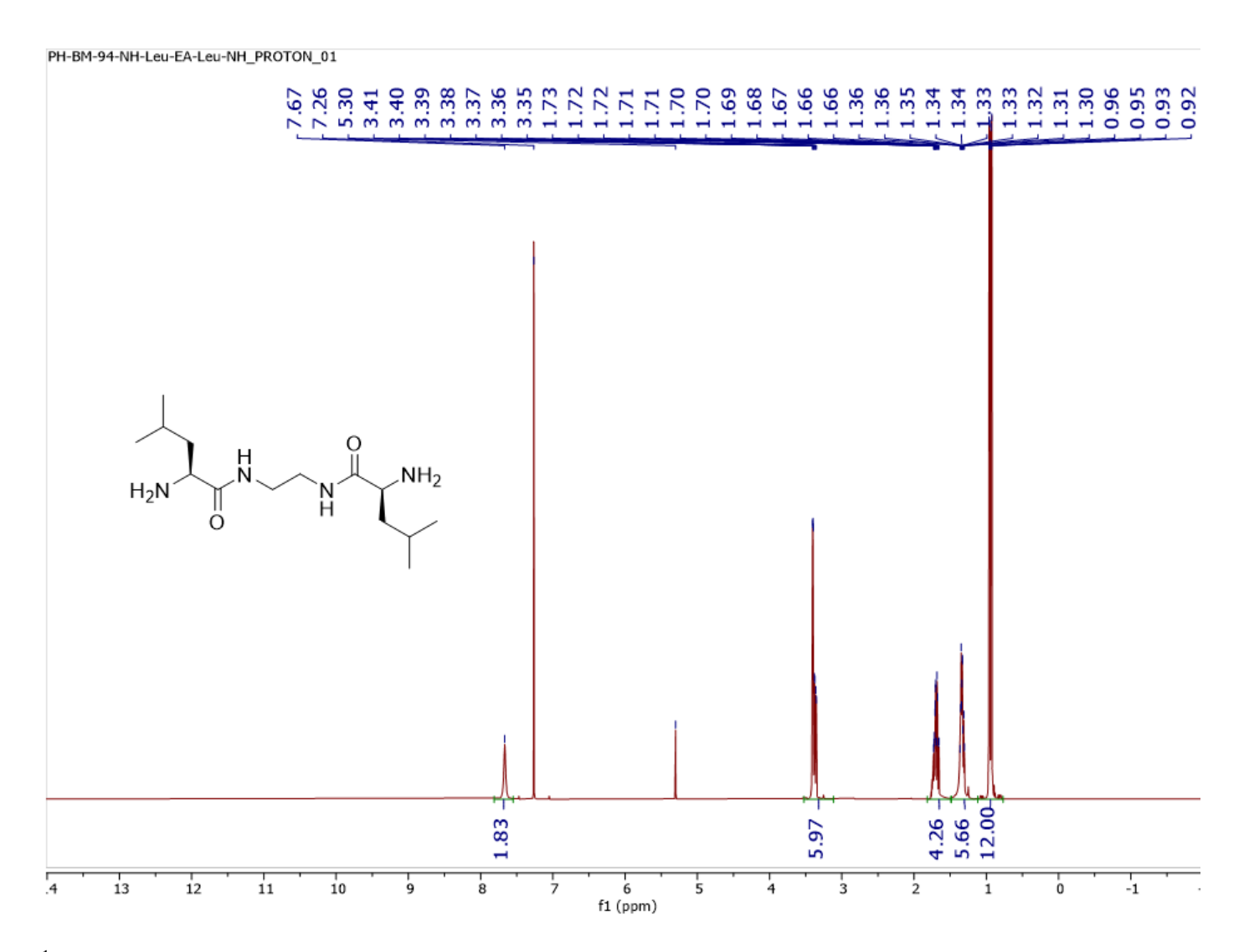


Figure A52. ¹H NMR spectrum of NH-Leu-C2-Leu-NH in CDCl₃.

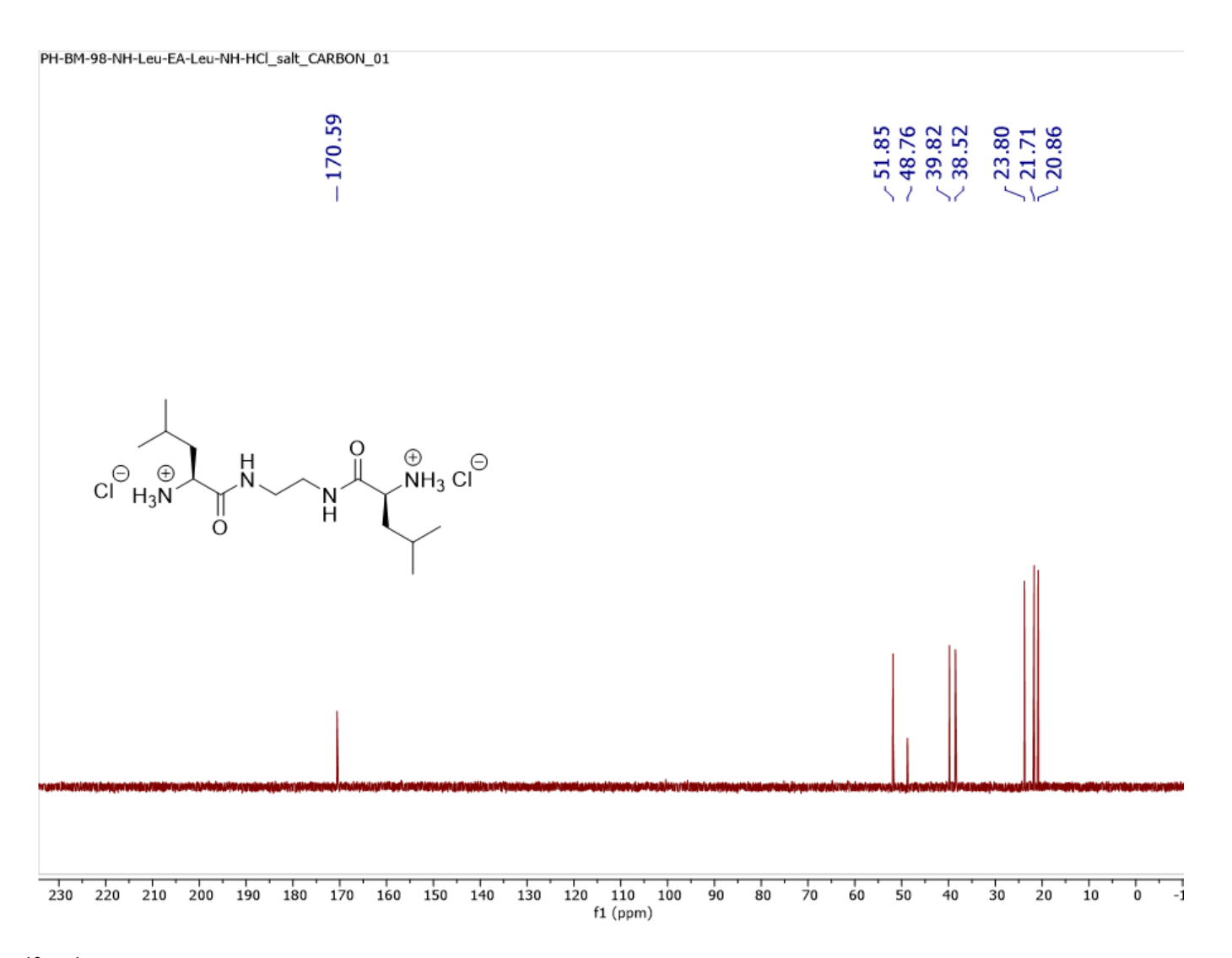


Figure A53. ¹³C{¹H} NMR spectrum of NH-Leu-C2-Leu-NH HCl salt in D₂O.

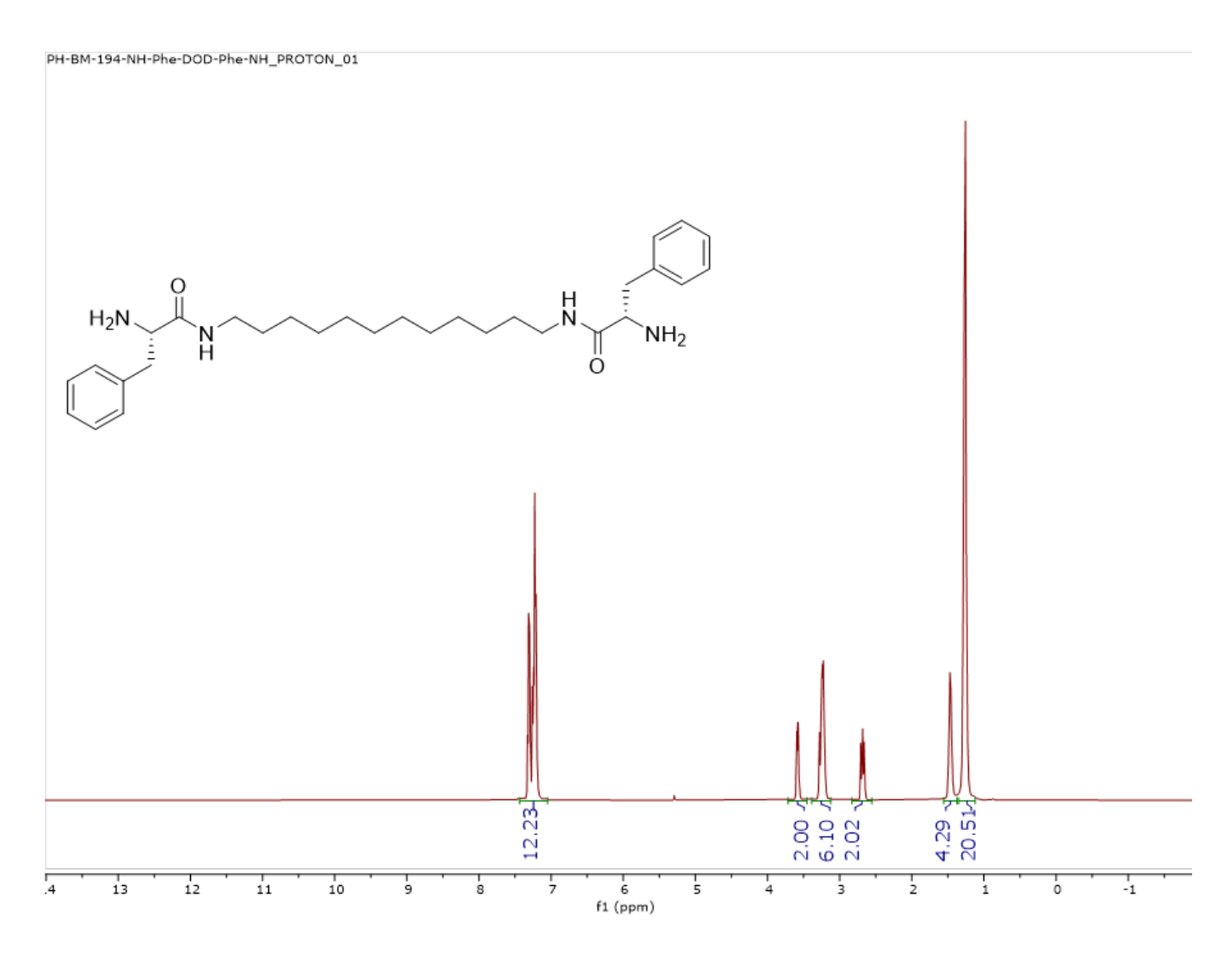


Figure A54. ¹H NMR spectrum of NH-Phe-C12-Phe-NH in CDCl₃.

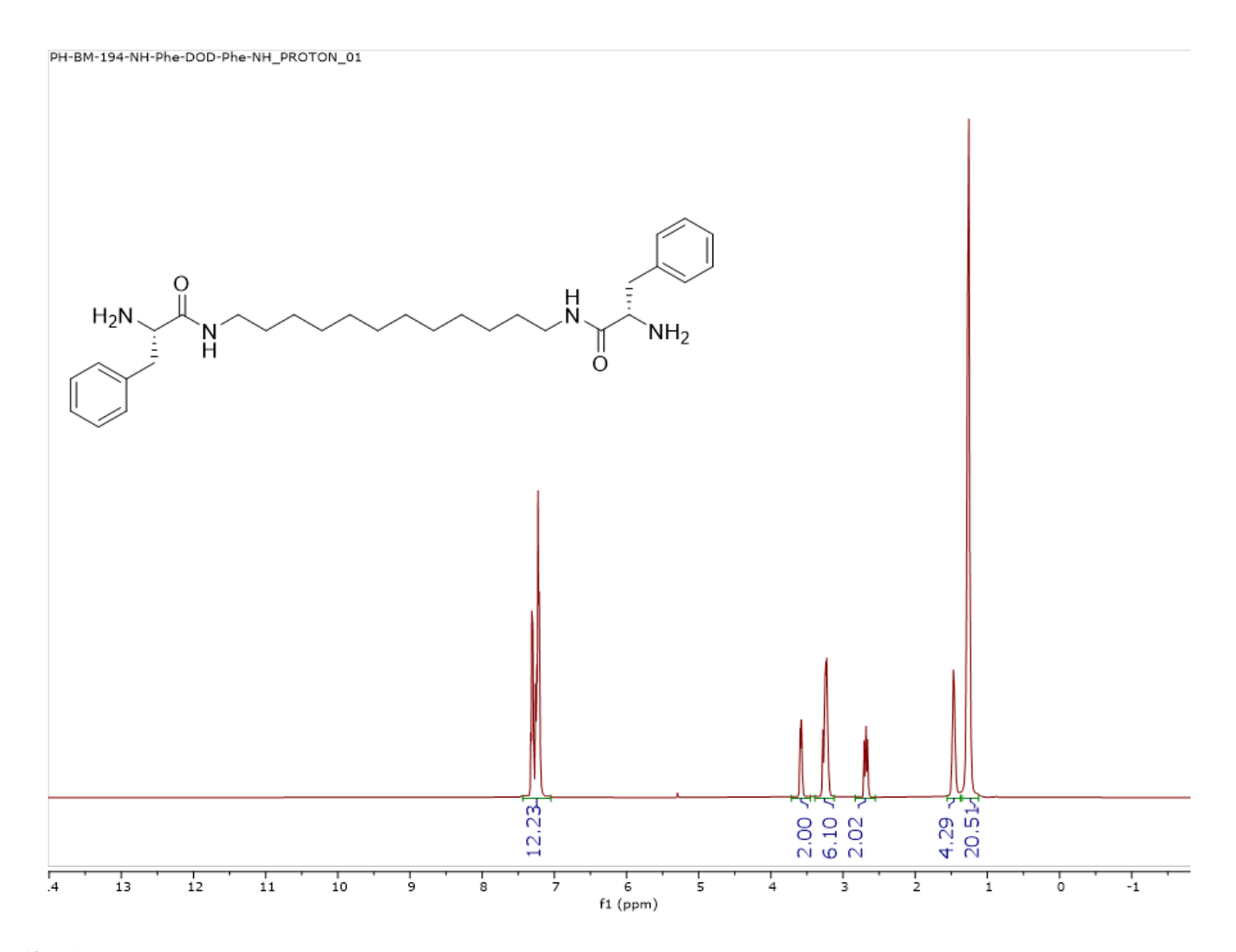


Figure A55. $^{13}C\{^{1}H\}$ NMR spectrum of NH-Phe-C12-Phe-NH in CDCl₃.

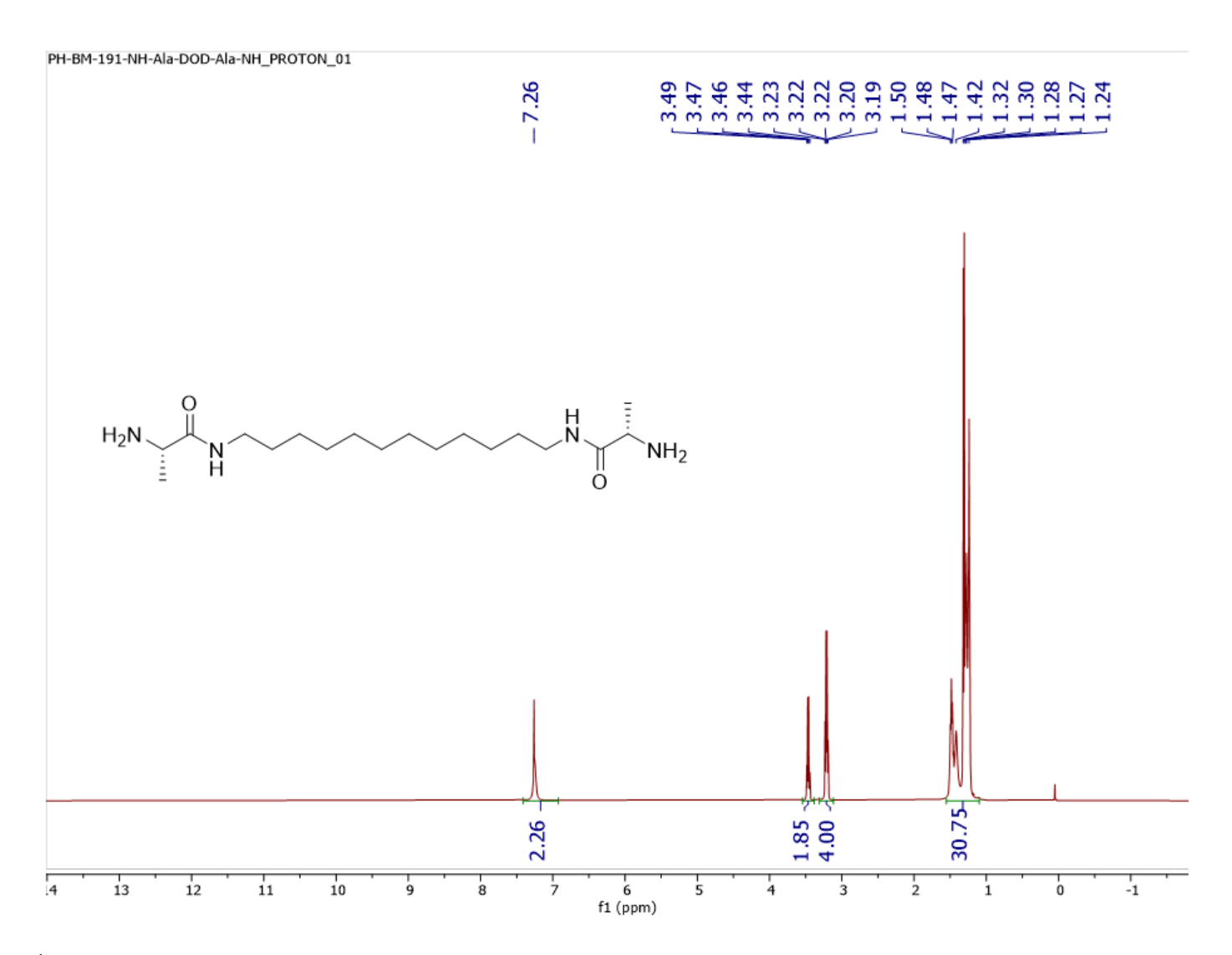


Figure A56. ¹H NMR spectrum of NH-Ala-C12-Ala-NH in CDCl₃.

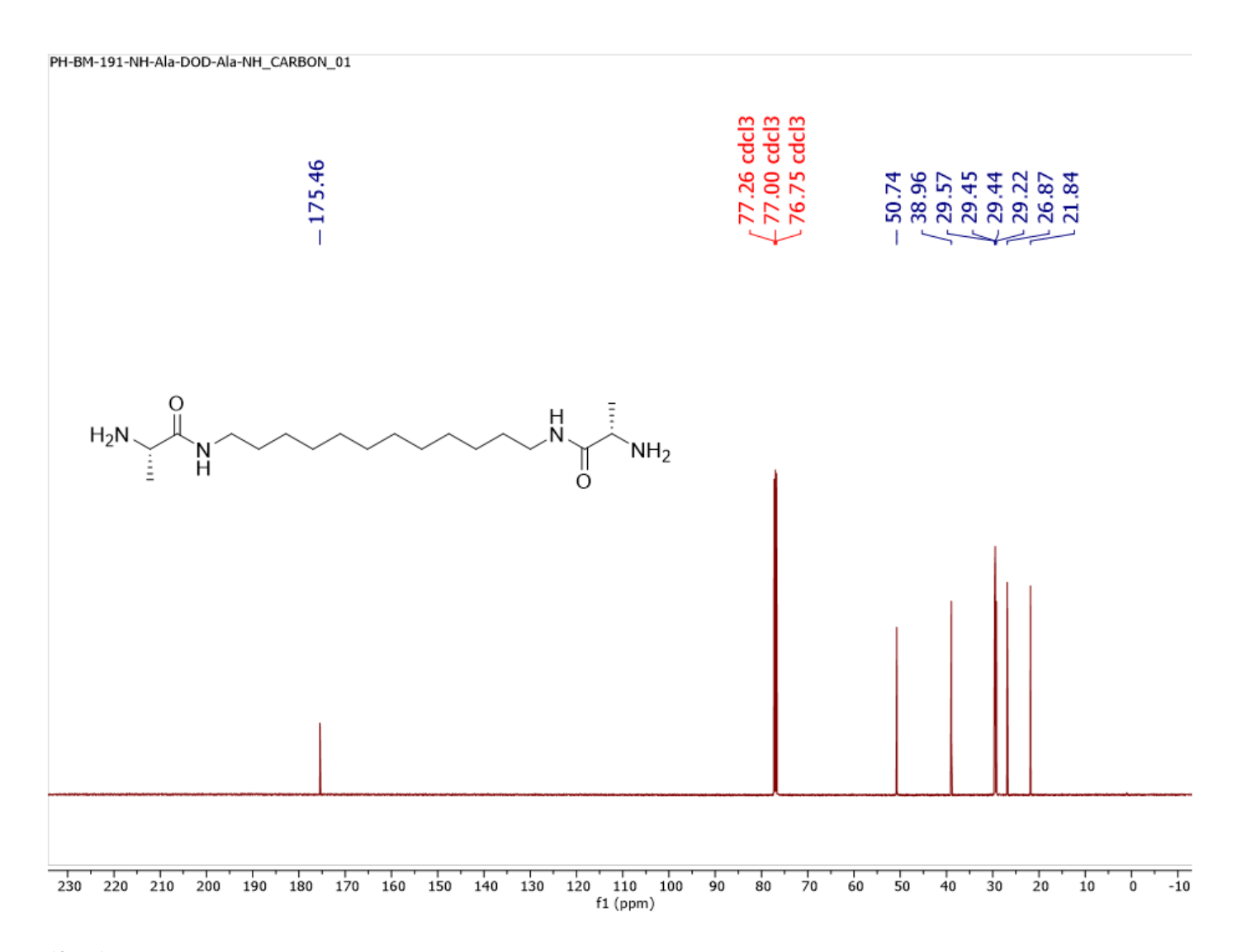


Figure A57. $^{13}C\{^{1}H\}$ NMR spectrum of NH-Ala-C12-Ala-NH in CDCl₃.

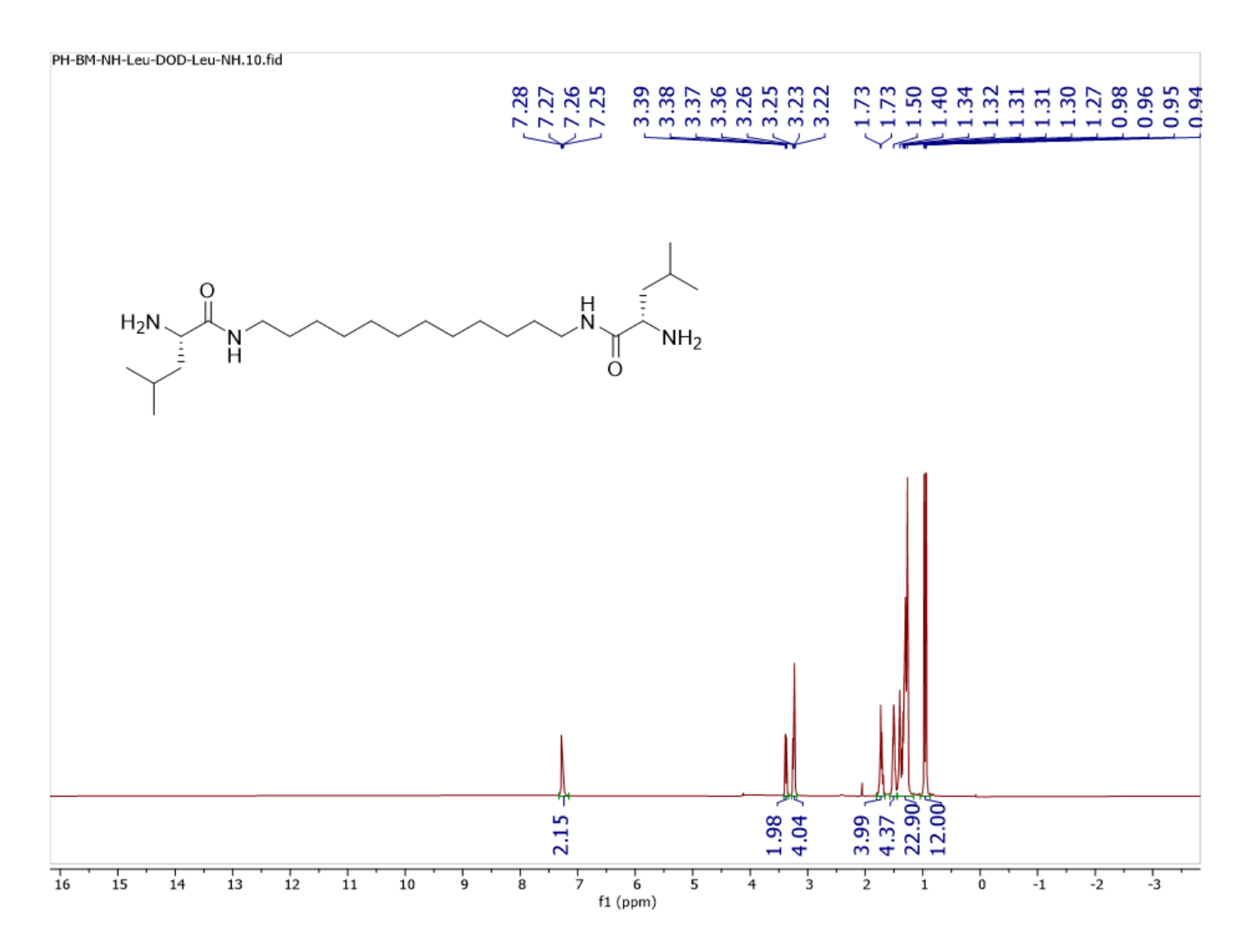


Figure A58. ¹H NMR spectrum of NH-Leu-C12-Leu-NH in CDCl₃.

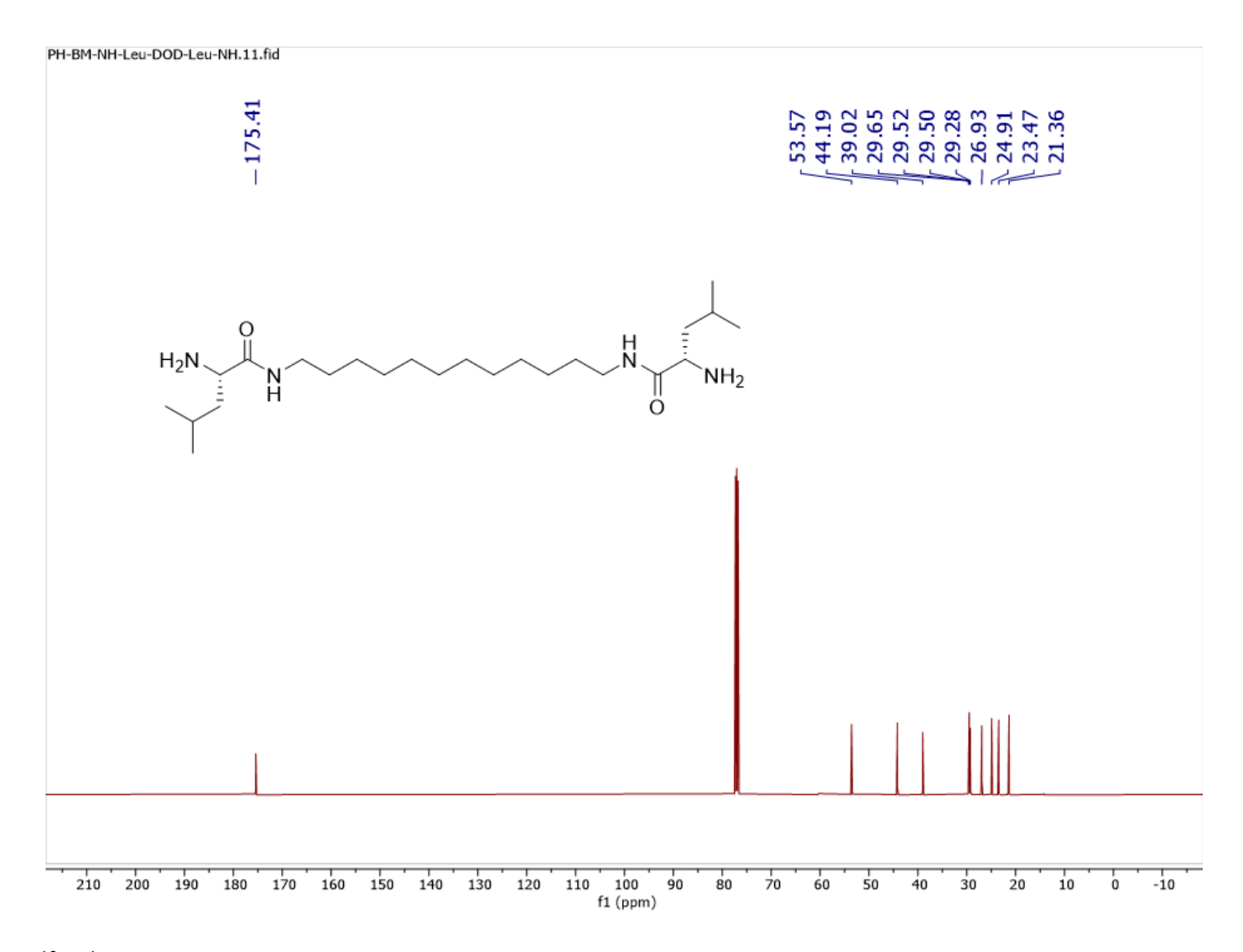


Figure A59. ¹³C{¹H} NMR spectrum of NH-Leu-C12-Leu-NH in CDCl₃.

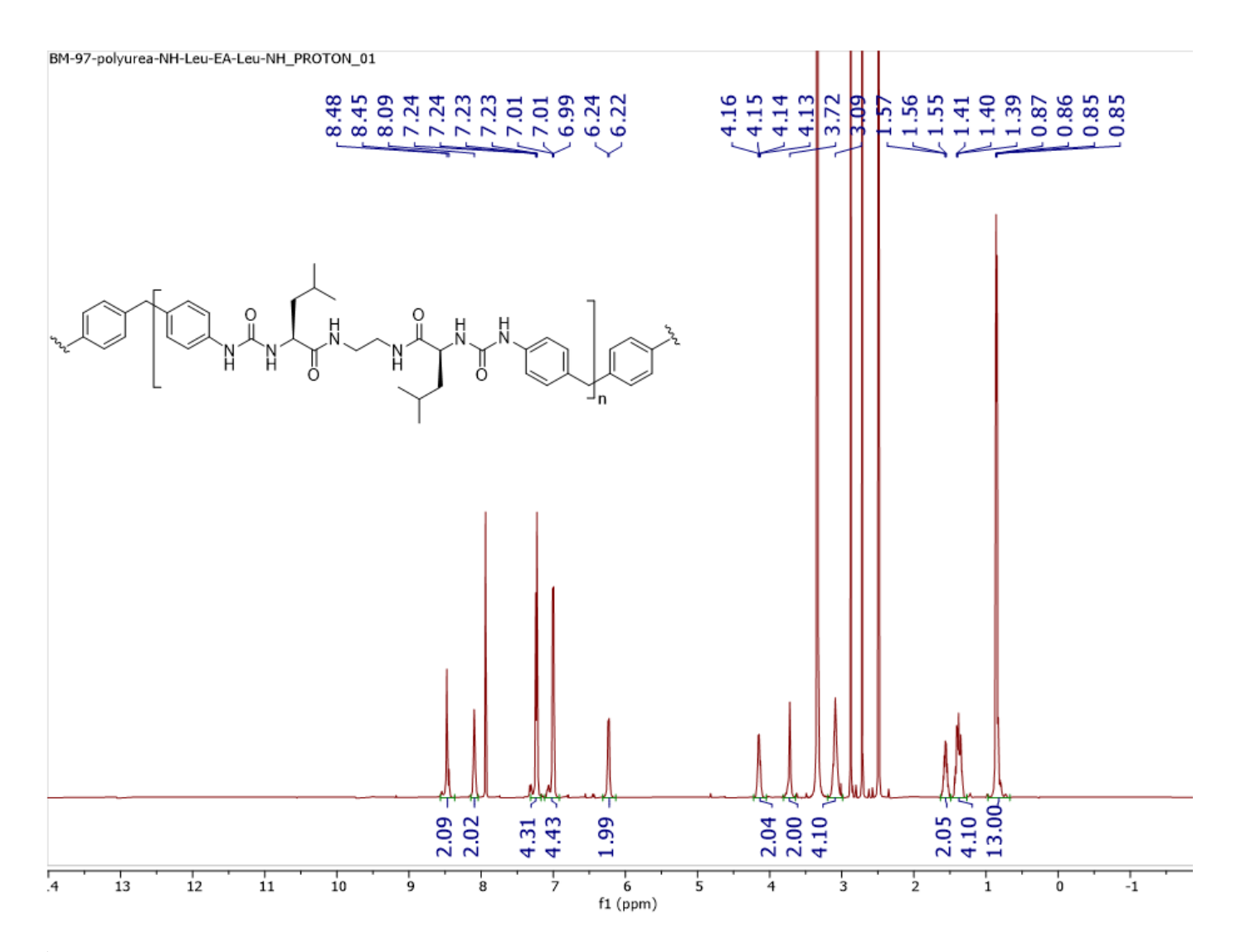


Figure A60. ¹H NMR spectrum of polyurea-NH-Leu-C2-Leu-NH in DMSO-*d*₆.

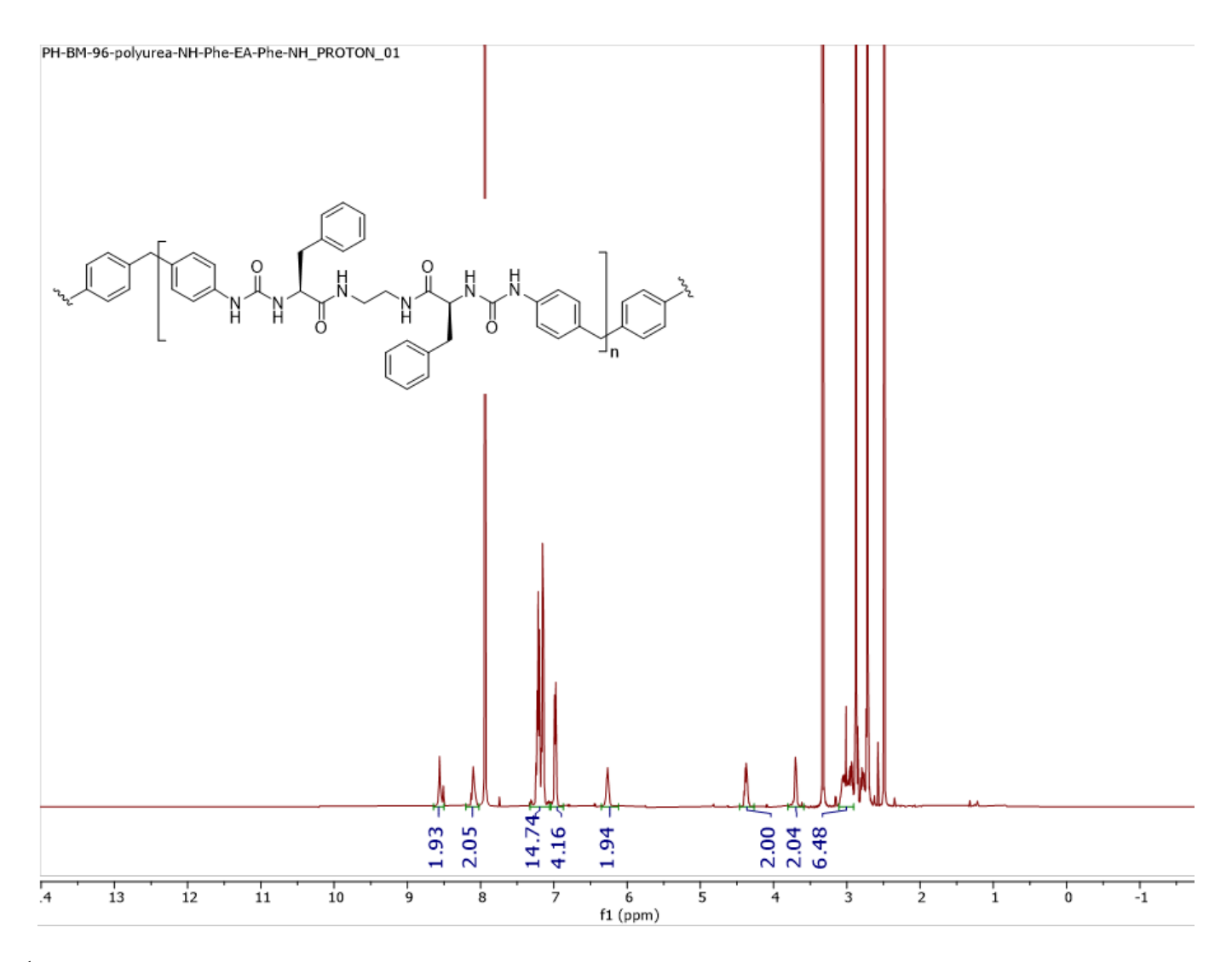


Figure A61. ¹H NMR spectrum of polyurea-NH-Phe-C2-Phe-NH in DMSO-*d*₆.

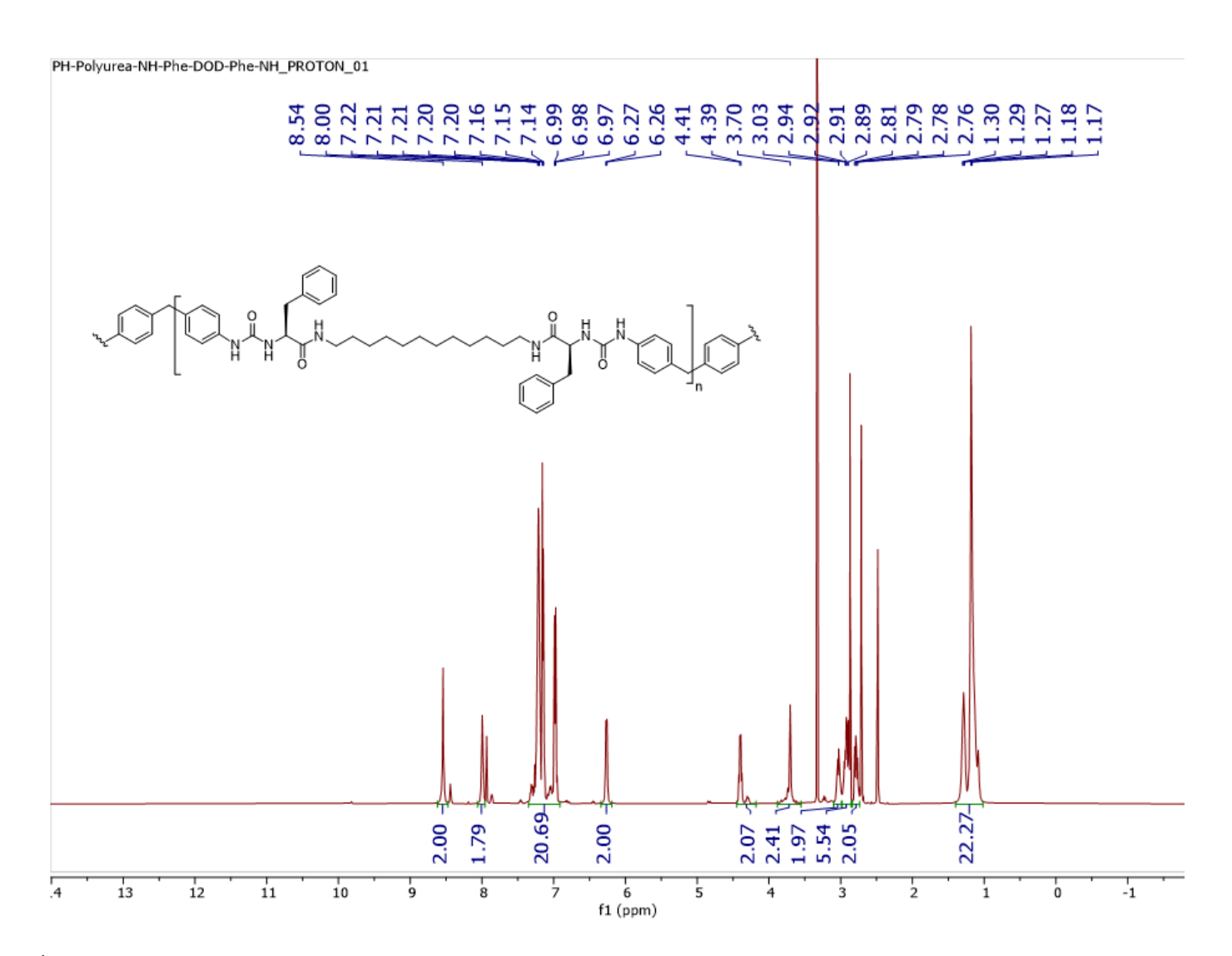


Figure A62. ¹H NMR spectrum of polyurea-NH-Phe-C12-Phe-NH in DMSO-*d*₆.

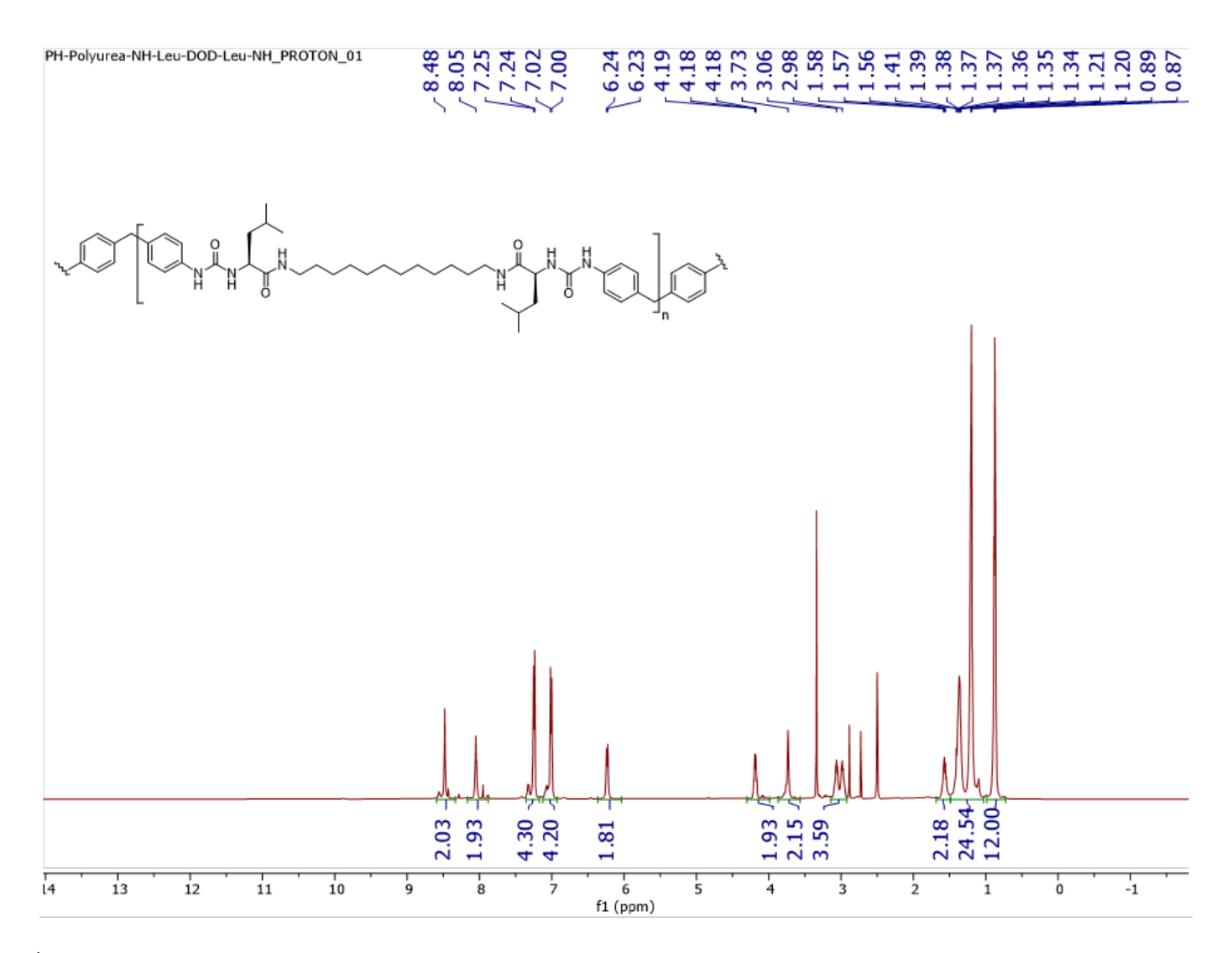


Figure A63. ¹H NMR spectrum of polyurea-NH-Leu-C12-Leu-NH in DMSO-*d*₆.

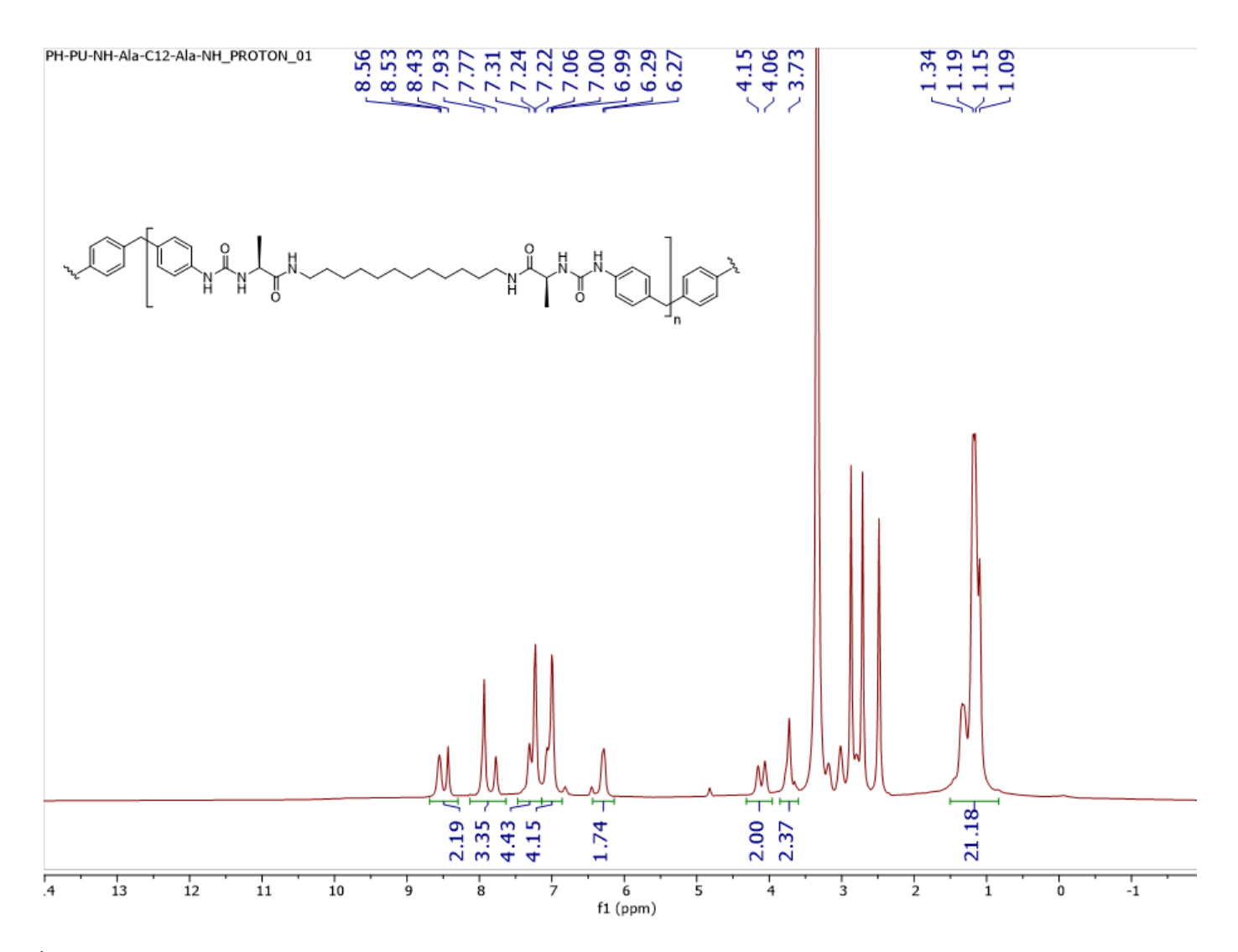


Figure A64. ¹H NMR spectrum of polyurea-NH-Ala-C12-Ala-NH in DMSO-*d*₆.

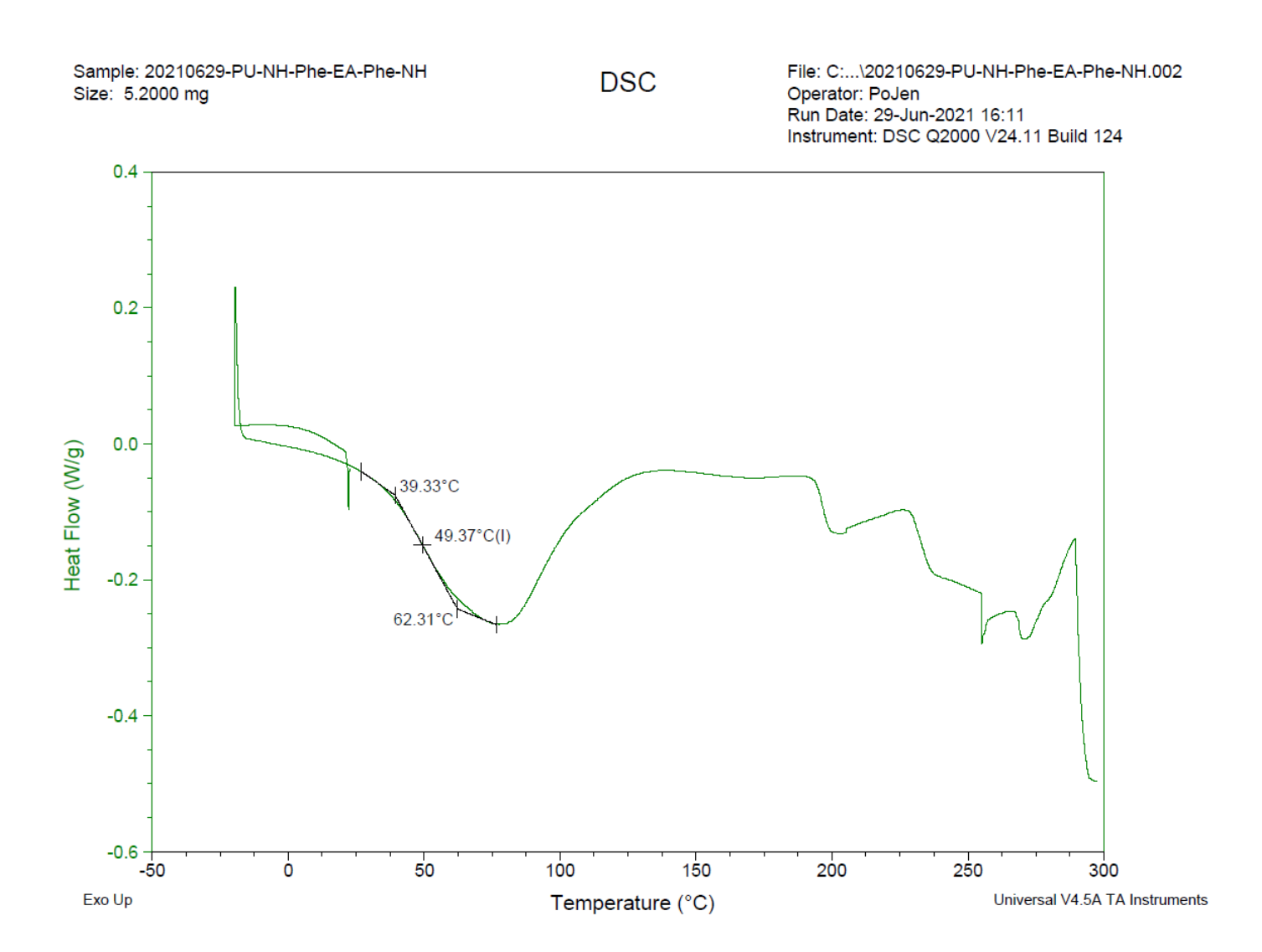


Figure A65. DSC data for polyurea-NH-Phe-C2-Phe-NH.

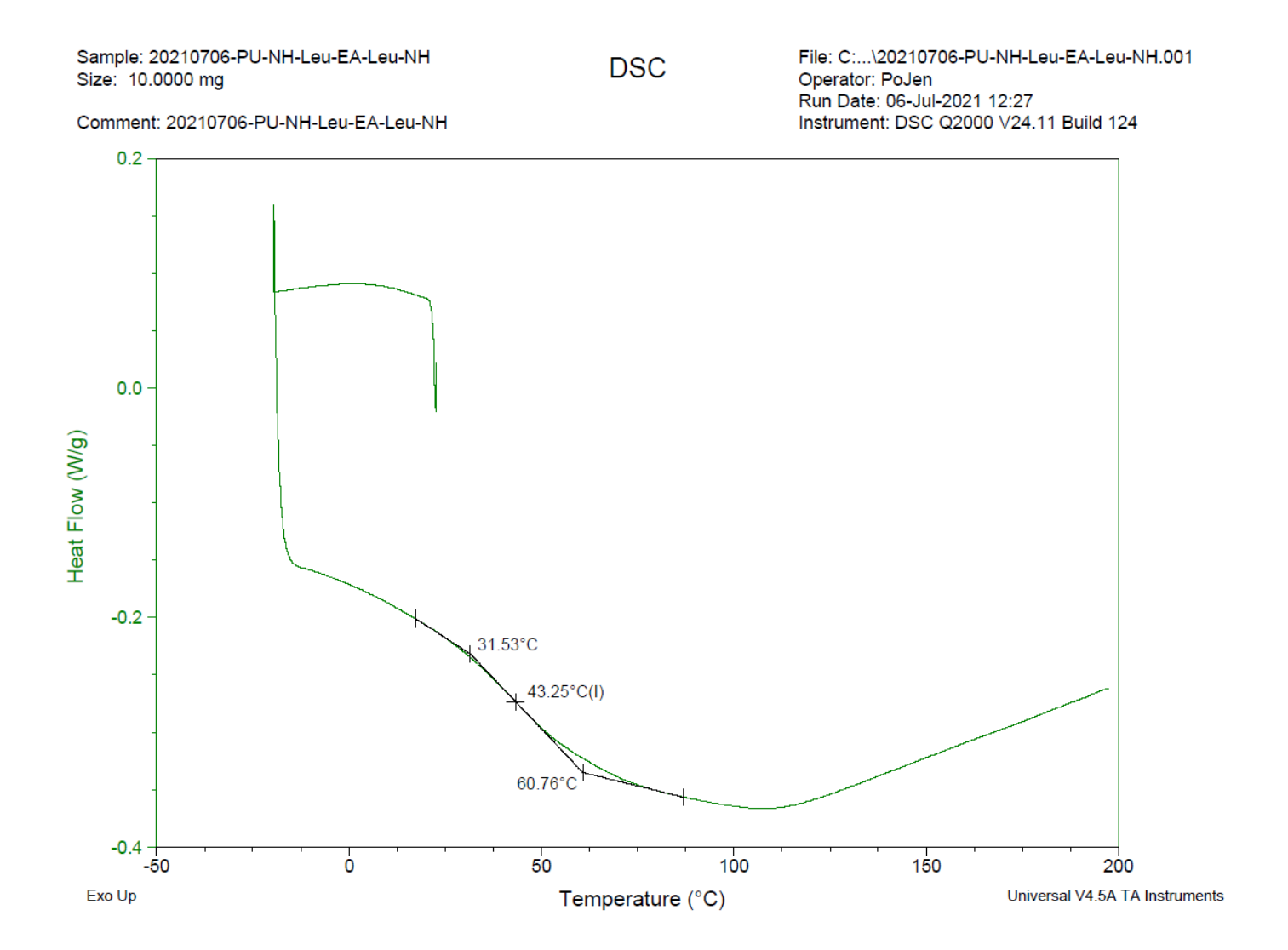


Figure A66. DSC data for polyurea-NH-Leu-C2-Leu-NH.

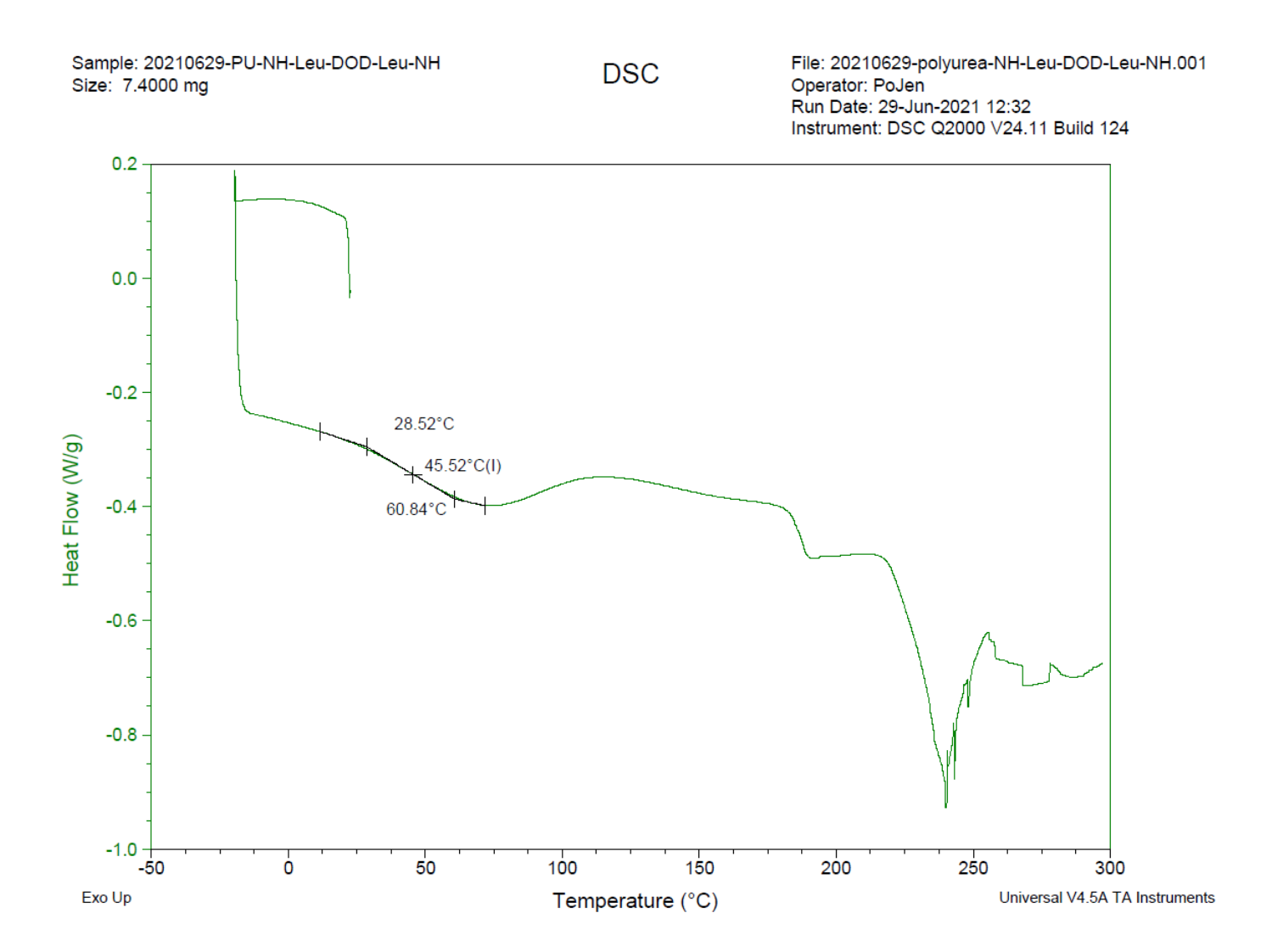


Figure A67. DSC data for polyurea-NH-Leu-C12-Leu-NH.

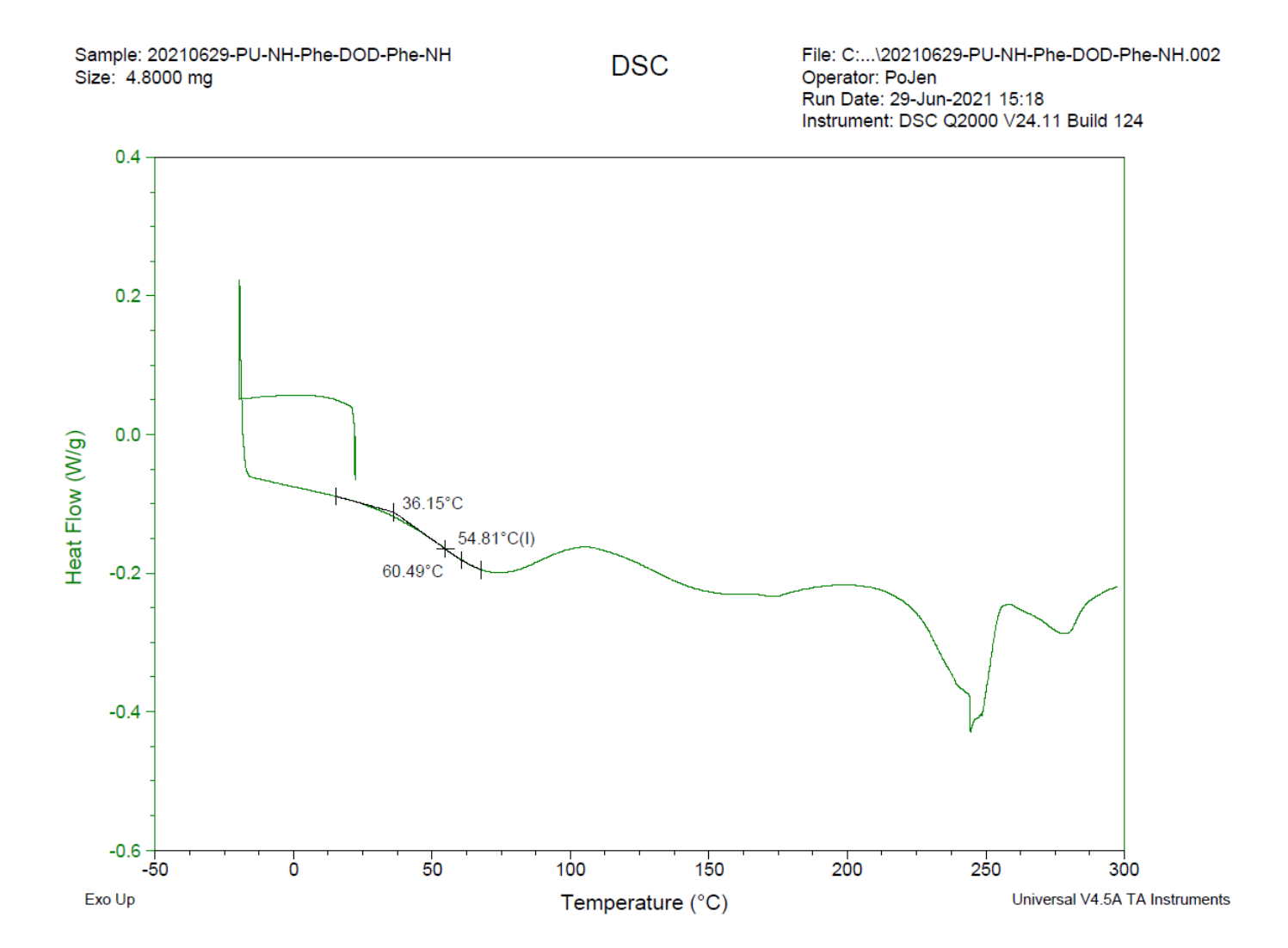


Figure A68. DSC data for polyurea-NH-Phe-C12-Phe-NH.

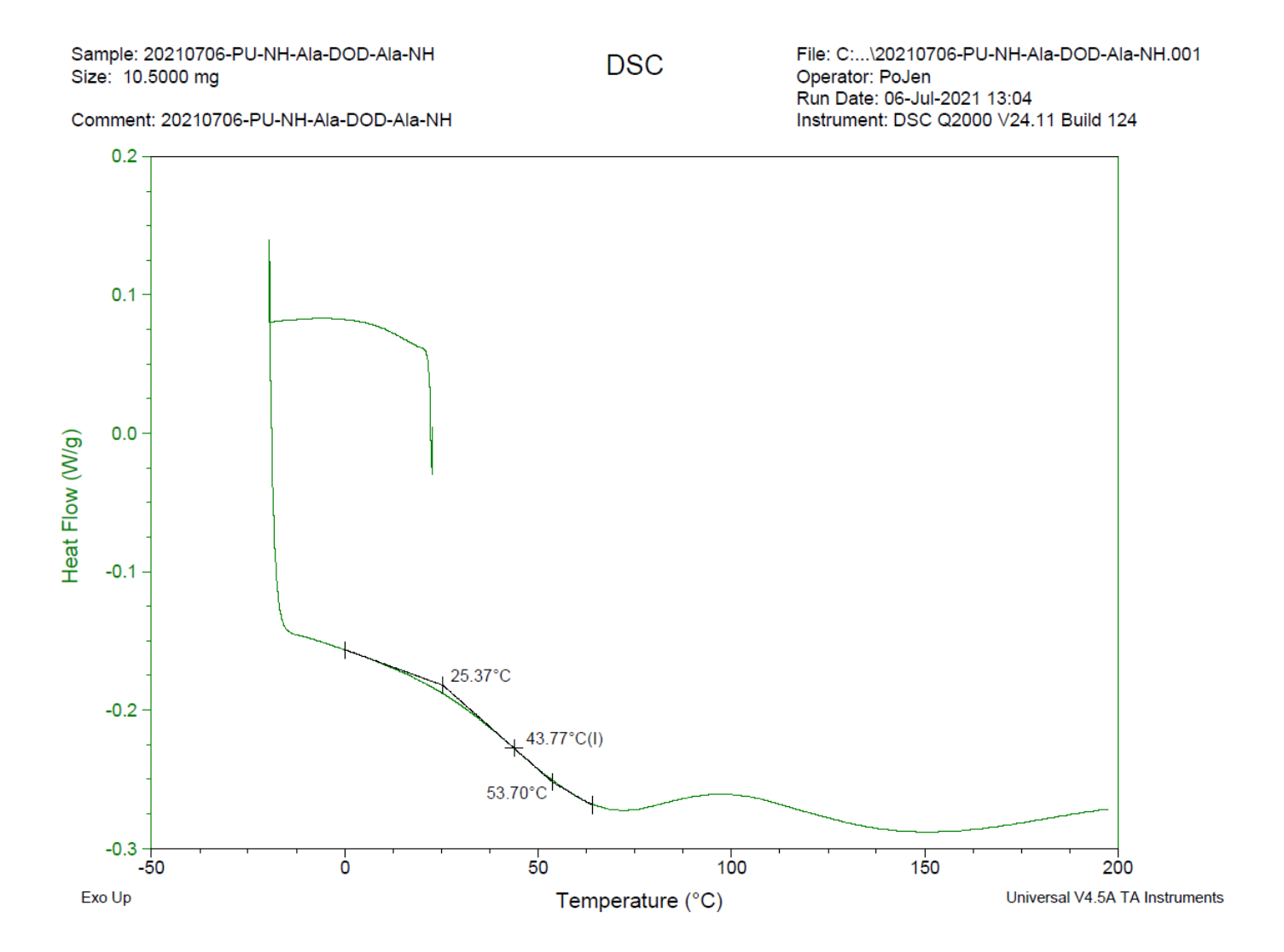


Figure A69. DSC data for polyurea-NH-Ala-C12-Ala-NH.

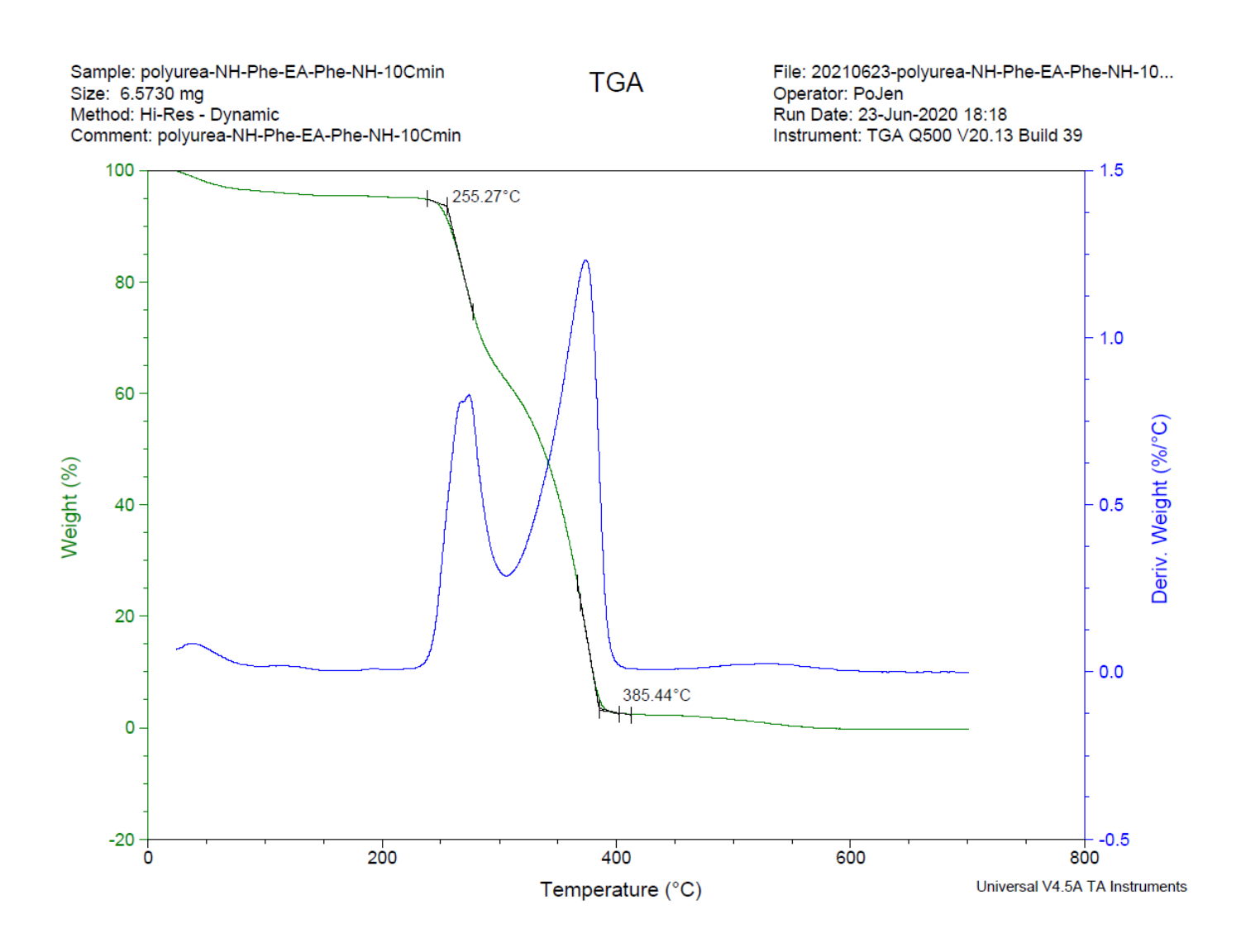


Figure A70. The thermogravimetric curve (green) and first derivative weight loss curve (blue) of polyurea-NH-Phe-C2-Phe-NH.

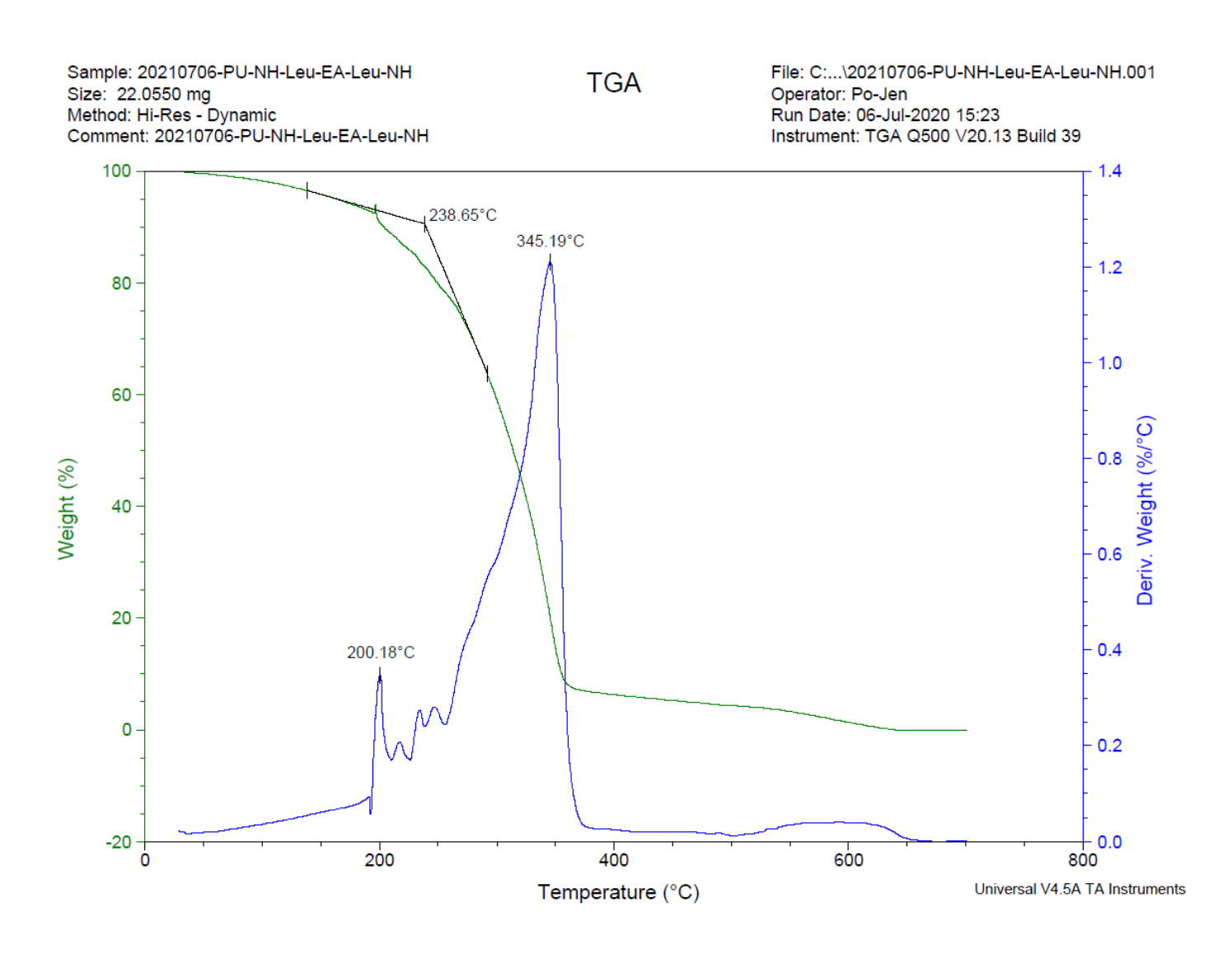


Figure A71. The thermogravimetric curve (green) and first derivative weight loss curve (blue) of polyurea-NH-Leu-C2-Leu-NH.

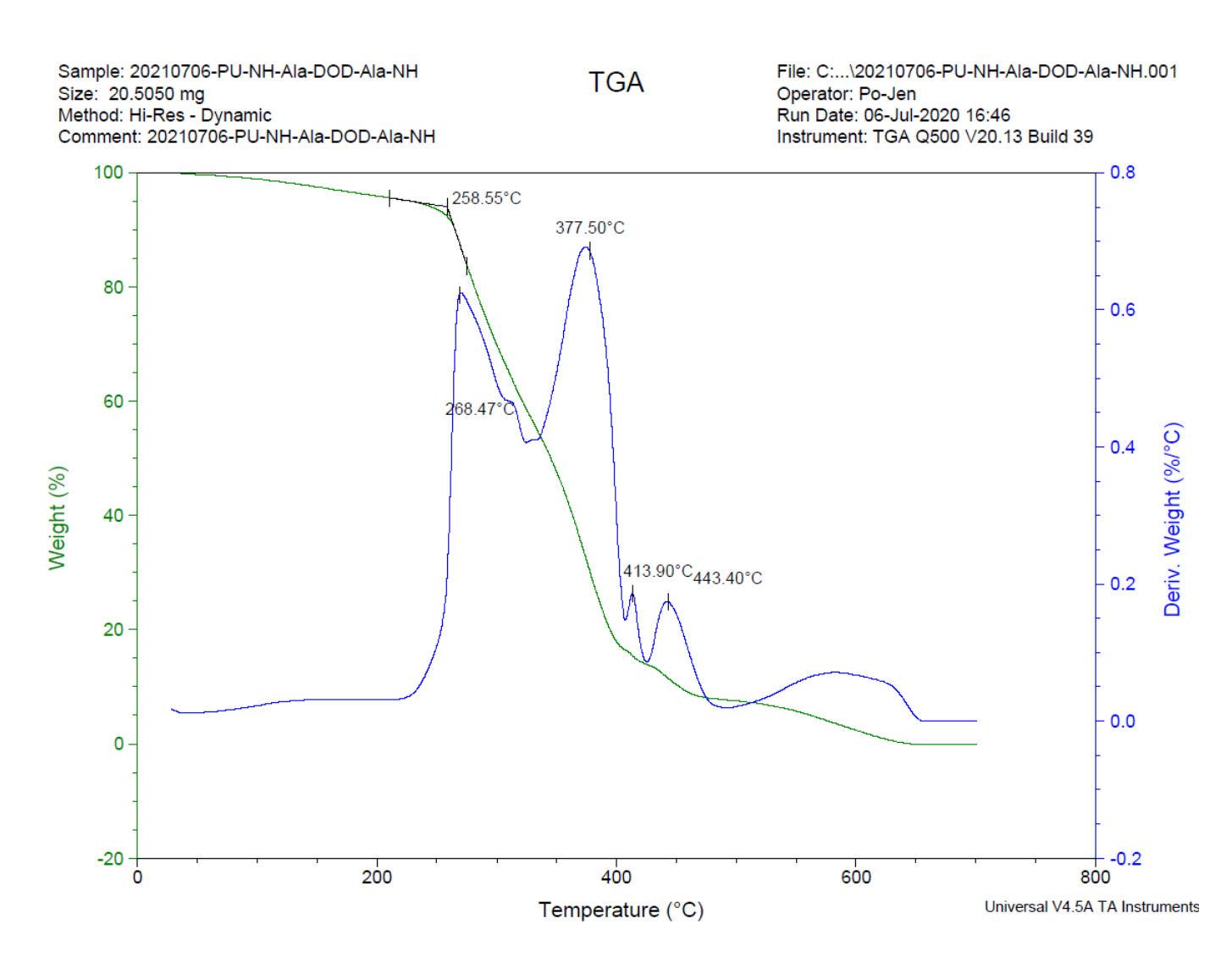


Figure A72. The thermogravimetric curve (green) and first derivative weight loss curve (blue) of polyurea-NH-Ala-C12-Ala-NH.

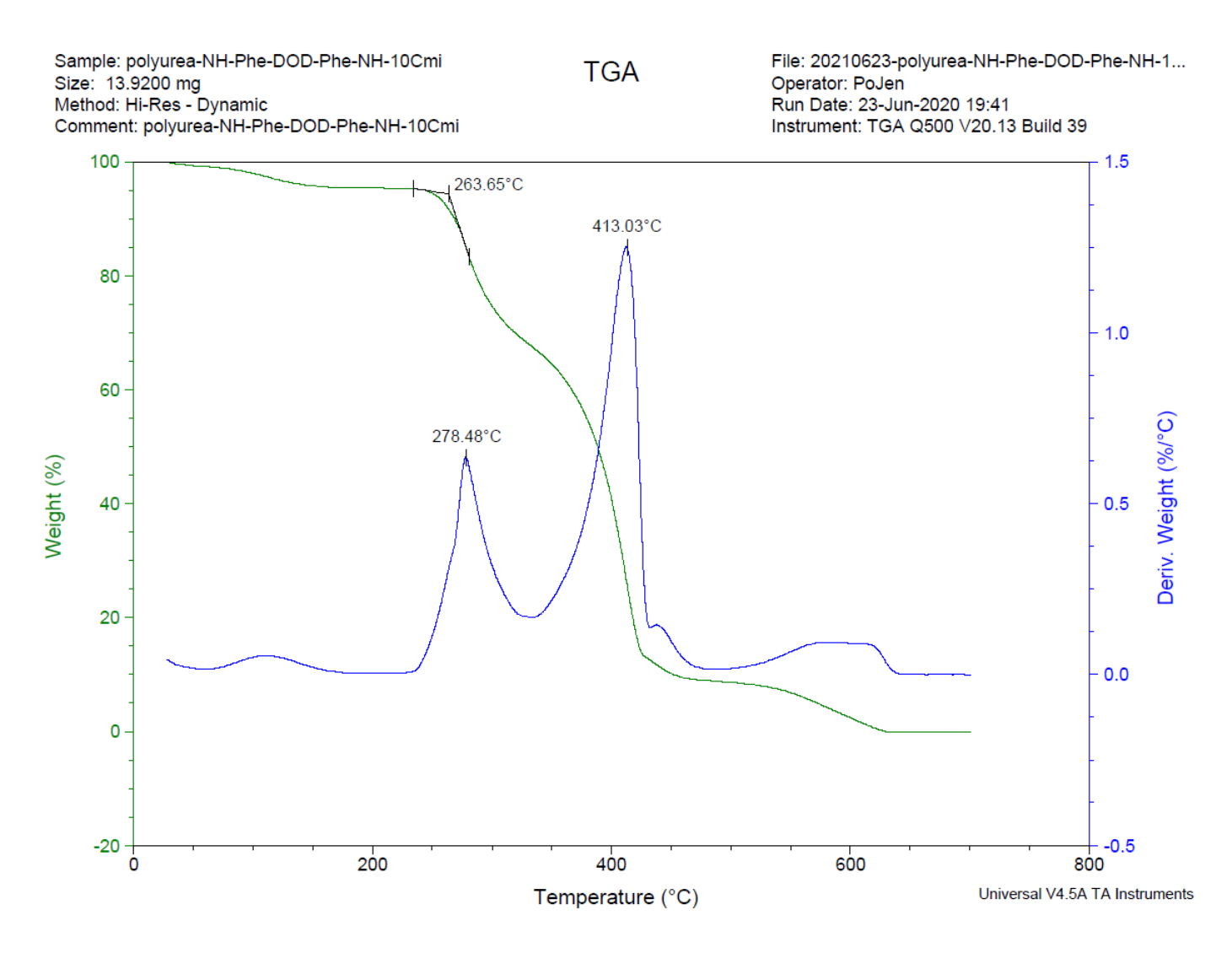


Figure A73. The thermogravimetric curve (green) and first derivative weight loss curve (blue) of polyurea-NH-Phe-C12-Phe-NH.

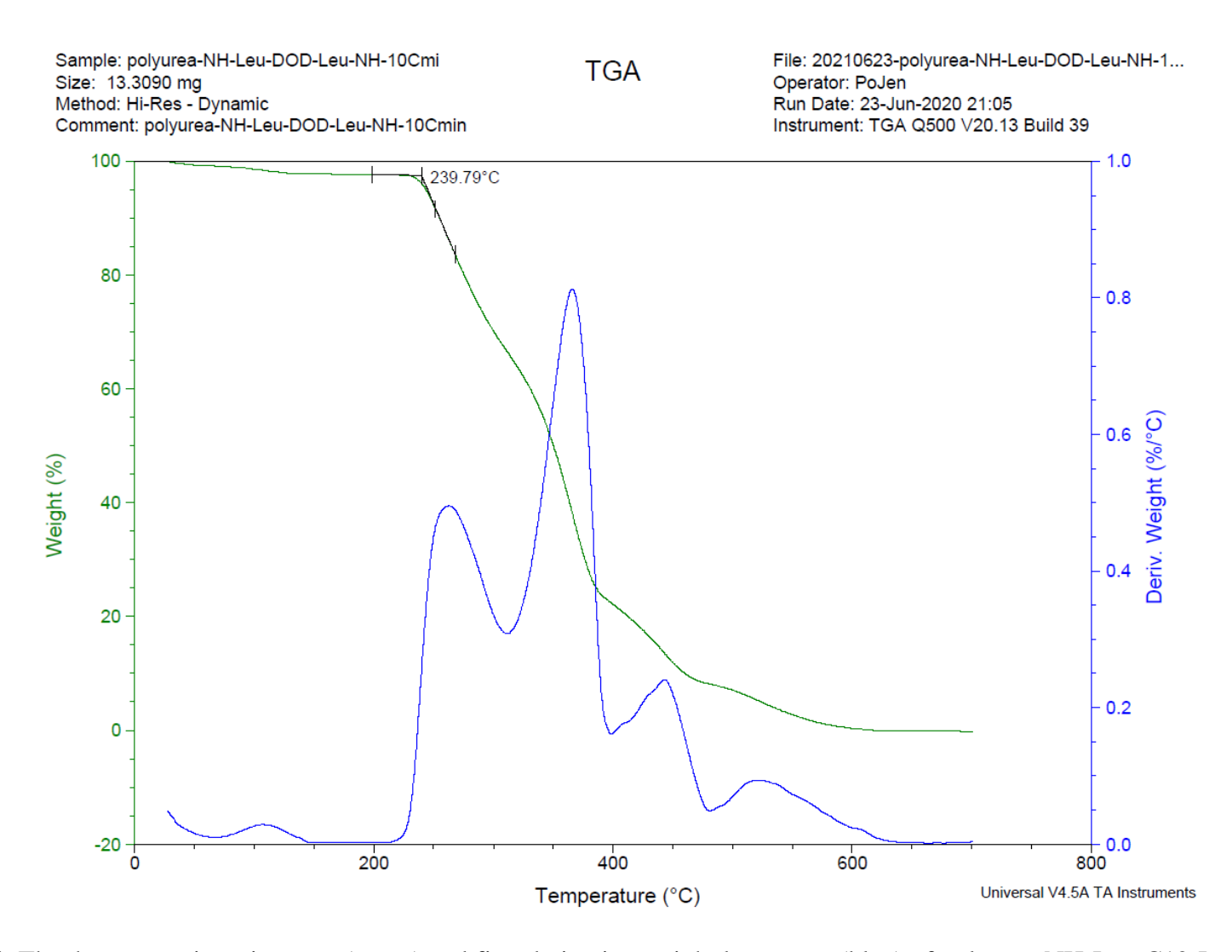


Figure A74. The thermogravimetric curve (green) and first derivative weight loss curve (blue) of polyurea-NH-Leu-C12-Leu-NH.

REFERENCES

REFERENCES

- (1) Kato, M.; Kamigaito, M.; Sawamoto, M.; Higashimura, T. Polymerization of Methyl Methacrylate with the Carbon Tetrachloride/Dichlorotris-(triphenylphosphine)ruthenium(II)/Methylaluminum Bis(2,6-Di-Tert Butylphenoxide) Initiating System: Possibility of Living Radical Polymerization. *Macromolecules* **1995**, 28 (5), 1721–1723.
- (2) Wang, J.-S.; Matyjaszewski, K. Controlled/"living" Radical Polymerization. Atom Transfer Radical Polymerization in the Presence of Transition-Metal Complexes. *J. Am. Chem. Soc.* **1995**, *117* (20), 5614–5615.
- (3) Tang, W.; Kwak, Y.; Braunecker, W.; Tsarevsky, N. V.; Coote, M. L.; Matyjaszewski, K. Understanding Atom Transfer Radical Polymerization: Effect of Ligand and Initiator Structures on the Equilibrium Constants. *J. Am. Chem. Soc.* **2008**, *130* (32), 10702–10713.
- (4) Matyjaszewski, K.; Paik, H.-J.; Zhou, P.; Diamanti, S. J. Determination of Activation and Deactivation Rate Constants of Model Compounds in Atom Transfer Radical Polymerization. *Macromolecules* **2001**, *34* (15), 5125–5131.
- (5) Tang, W.; Matyjaszewski, K. Effects of Initiator Structure on Activation Rate Constants in ATRP. *Macromolecules* **2007**, *40* (6), 1858–1863.
- (6) Coote, M. L.; Henry, D. J. Effect of Substituents on Radical Stability in Reversible Addition Fragmentation Chain Transfer Polymerization: An Ab Initio Study. *Macromolecules* **2005**, *38* (4), 1415–1433.
- (7) Horn, M.; Matyjaszewski, K. Solvent Effects on the Activation Rate Constant in Atom Transfer Radical Polymerization. *Macromolecules* **2013**, *46* (9), 3350–3357.
- (8) Matyjaszewski, K.; Patten, T. E.; Xia, J. Controlled/"Living" Radical Polymerization. Kinetics of the Homogeneous Atom Transfer Radical Polymerization of Styrene. *J. Am. Chem. Soc.* **1997**, *119* (4), 674–680.
- (9) Jakubowski, W.; Matyjaszewski, K. Activators Regenerated by Electron Transfer for Atom-Transfer Radical Polymerization of (meth)acrylates and Related Block Copolymers. *Angew. Chem. Int. Ed Engl.* **2006**, *45* (27), 4482–4486.
- (10) Matyjaszewski, K.; Mu Jo, S.; Paik, H.-J.; Gaynor, S. G. Synthesis of Well-Defined Polyacrylonitrile by Atom Transfer Radical Polymerization. *Macromolecules* **1997**, 30 (20), 6398–6400.

- (11) Teodorescu, M.; Matyjaszewski, K. Controlled Polymerization of (meth) Acrylamides by Atom Transfer Radical Polymerization. *Macromol. Rapid Commun.* **2000**.
- (12) Xia, J.; Zhang, X.; Matyjaszewski, K. Atom Transfer Radical Polymerization of 4-Vinylpyridine. *Macromolecules* **1999**, *32* (10), 3531–3533.
- (13) Fantin, M.; Isse, A. A.; Venzo, A.; Gennaro, A.; Matyjaszewski, K. Atom Transfer Radical Polymerization of Methacrylic Acid: A Won Challenge. *J. Am. Chem. Soc.* **2016**, *138* (23), 7216–7219.
- (14) Shi, H.; Zhao, Y.; Dong, X.; Zhou, Y.; Wang, D. Frustrated Crystallisation and Hierarchical Self-Assembly Behaviour of Comb-like Polymers. *Chem. Soc. Rev.* **2013**, *42* (5), 2075–2099.
- (15) Gao, H.; Matyjaszewski, K. Synthesis of Molecular Brushes by "Grafting onto" Method: Combination of ATRP and Click Reactions. *J. Am. Chem. Soc.* **2007**, *129* (20), 6633–6639.
- (16) Beers, K. L.; Gaynor, S. G.; Matyjaszewski, K.; Sheiko, S. S.; Möller, M. The Synthesis of Densely Grafted Copolymers by Atom Transfer Radical Polymerization. *Macromolecules* **1998**, *31* (26), 9413–9415.
- (17) Gauthier, M. A.; Gibson, M. I.; Klok, H.A. Synthesis of Functional Polymers by Post-Polymerization Modification. *Angew. Chem. Int. Ed.* **2009**, *48*, 48-58.
- (18) Díaz, D. D.; Punna, S.; Holzer, P.; McPherson, A. K.; Barry Sharpless, K.; Fokin, V. V.; Finn, M. G. Click Chemistry in Materials Synthesis. 1. Adhesive Polymers from Copper-Catalyzed Azide-Alkyne Cycloaddition. *Journal of Polymer Science Part A: Polymer Chemistry.* 2004, pp 4392–4403.
- (19) Tornøe, C. W.; Christensen, C.; Meldal, M. Peptidotriazoles on Solid Phase: [1,2,3]-Triazoles by Regiospecific Copper(I)-Catalyzed 1,3-Dipolar Cycloadditions of Terminal Alkynes to Azides. *The Journal of Organic Chemistry*. **2002**, pp 3057–3064.
- (20) Parrish, B.; Breitenkamp, R. B.; Emrick, T. PEG- and Peptide-Grafted Aliphatic Polyesters by Click Chemistry. *J. Am. Chem. Soc.* **2005**, *127* (20), 7404–7410.
- (21) Fournier, D.; Du Prez, F. "Click" Chemistry as a Promising Tool for Side-Chain Functionalization of Polyurethanes. *Macromolecules* **2008**, *41* (13), 4622–4630.
- (22) Luxenhofer, R.; Jordan, R. Click Chemistry with Poly(2-Oxazoline)s. *Macromolecules* **2006**, *39* (10), 3509–3516.

- (23) Tempelaar, S.; Barker, I. A.; Truong, V. X.; Hall, D. J.; Mespouille, L.; Dubois, P.; Dove, A. P. Organocatalytic Synthesis and Post-Polymerization Functionalization of Propargyl-Functional Poly(carbonate)s. *Polym. Chem.* **2013**, *4* (1), 174–183.
- (24) Englert, B. C.; Bakbak, S.; Bunz, U. H. F. Click Chemistry as a Powerful Tool for the Construction of Functional Poly(p-Phenyleneethynylene)s: Comparison of Preand Postfunctionalization Schemes. *Macromolecules* **2005**, *38* (14), 5868–5877.
- (25) Michinobu, T. Click Functionalization of Aromatic Polymers for Organic Electronic Device Applications. *Macromol. Chem. Phys.* **2015**, 216 (13), 1387–1395.
- (26) Sletten, E. M.; Bertozzi, C. R. Bioorthogonal Chemistry: Fishing for Selectivity in a Sea of Functionality. *Angew. Chem. Int. Ed Engl.* **2009**, *48* (38), 6974–6998.
- (27) Wolbers, F.; ter Braak, P.; Le Gac, S.; Luttge, R.; Andersson, H.; Vermes, I.; van den Berg, A. Viability Study of HL60 Cells in Contact with Commonly Used Microchip Materials. *Electrophoresis* **2006**, *27* (24), 5073–5080.
- (28) Carrea, G.; Riva, S. Properties and Synthetic Applications of Enzymes in Organic Solvents. *Angew. Chem. Int. Ed.* **2000**, *39*, 2226–2254.
- (29) Clouthierz, C. M.; Pelletier, J. N. Expanding the Organic Toolbox: A Guide to Integrating Biocatalysis in Synthesisw. *Chem. Soc. Rev. Chem. Soc. Rev* **2012**, *41*, 1585–1605.
- (30) Liu, J.; Yang, Q.; Li, C. Towards Efficient Chemical Synthesis via Engineering Enzyme Catalysis in Biomimetic Nanoreactors. *Chem. Commun.* **2015**, *51*, 13731–13739.
- (31) Zaks, A.; Klibanov, A. M. Enzymatic Catalysis in Nonaqueous Solvents. *J. Biol. Chem.* **1988**, 263, 3194–3201.
- (32) Zaks, A.; Klibanov, A. M. Enzyme-Catalyzed Processes in Organic Solvents. *Proc. Natl. Acad. Sci. U. S. A.* **1985**, 82 (10), 3192–3196.
- (33) Zacharis, E.; Halling, P. J.; Rees, D. G. Volatile Buffers Can Override the "pH Memory" of Subtilisin Catalysis in Organic Media. *Proc. Natl. Acad. Sci. U. S. A.* **1999**, *96* (4), 1201–1205.
- (34) Khmelnitsky, Y. L.; Welch, S. H.; Clark, D. S.; Dordick, J. S. Salts Dramatically Enhance Activity of Enzymes Suspended in Organic Solvents. *J. Am. Chem. Soc.* **1994**, *116*, 2647–2648.

- (35) Klibanov, A. M. Improving Enzymes by Using Them in Organic Solvents. *Nature* **2001**, *409*, 241–246.
- (36) Butler, L. G. Enzymes in non-aqueous solvents *Enzyme Microb. Technol.* **1979**, *1*, 253-259.
- (37) Pazhang, M.; Khajeh, K.; Ranjbar, B.; Hosseinkhani, S. Effects of water-miscible solvents and polyhydroxy compounds on the structure and enzymatic activity of thermolysin. *J. Biotechnol.* **2006**, *127*, 45–53.
- (38) Wubbolts, M. G.; Favre-Bulle, O.; Withold, B. Biosynthesis of synthons in two-liquid-phase media. *Biotechnol Bioeng.* **1996**, *52*, 301-308.
- (39) Dabulis, K.; Klibanov, A. M. Dramatic enhancement of enzymatic activity in organic solvents by lyoprotectants *Biotechnology and Bioengineering*. **1993**, *41*, 566-571.
- (40) Abuchowski, A.; McCoy, J. R.; Palczuk, N. C.; van Es, T.; Davis, F. F. Effect of Covalent Attachment of Polyethylene Glycol on Immunogenicity and Circulating Life of Bovine Liver Catalase. *J. Biol. Chem.* **1977**, 252 (11), 3582–3586.
- (41) Abuchowski, A.; van Es, T.; Palczuk, N. C.; Davis, F. F. Alteration of Immunological Properties of Bovine Serum Albumin by Covalent Attachment of Polyethylene Glycol. *J. Biol. Chem.* **1977**, 252 (11), 3578–3581.
- (42) Turecek, P. L.; Bossard, M. J.; Schoetens, F.; Ivens, I. A. PEGylation of Biopharmaceuticals: A Review of Chemistry and Nonclinical Safety Information of Approved Drugs. *J. Pharm. Sci.* **2016**, *105* (2), 460–475.
- (43) Yadav, G. D.; Jadhav, S. R. Synthesis of Reusable Lipases by Immobilization on Hexagonal Mesoporous Silica and Encapsulation in Calcium Alginate: Transesterification in Non-Aqueous Medium. *Microporous Mesoporous Mater.* **2005**, *86* (1), 215–222.
- (44) Liu, W.; Wang, L.; Jiang, R. Specific Enzyme Immobilization Approaches and Their Application with Nanomaterials. *Top. Catal.* **2012**, *55* (16), 1146–1156.
- (45) Zhen, G.; Falconnet, D.; Kuennemann, E.; Vörös, J.; Spencer, N. D.; Textor, M.; Zürcher, S. Nitrilotriacetic Acid Functionalized Graft Copolymers: A Polymeric Interface for Selective and Reversible Binding of Histidine-Tagged Proteins. *Adv. Funct. Mater.* **2006**, *16* (2), 243–251.
- (46) Abad, J. M.; Mertens, S. F. L.; Pita, M.; Fernández, V. M.; Schiffrin, D. J. Functionalization of Thioctic Acid-Capped Gold Nanoparticles for Specific

- Immobilization of Histidine-Tagged Proteins. J. Am. Chem. Soc. 2005, 127 (15), 5689–5694.
- (47) Wang, L.; Xu, R.; Chen, Y.; Jiang, R. Activity and Stability Comparison of Immobilized NADH Oxidase on Multi-Walled Carbon Nanotubes, Carbon Nanospheres, and Single-Walled Carbon Nanotubes. *J. Mol. Catal. B Enzym.* 2011, 69 (3), 120–126.
- (48) Weber, P. C.; Ohlendorf, D. H.; Wendoloski, J. J.; Salemme, F. R. Structural Origins of High-Affinity Biotin Binding to Streptavidin. *Science* **1989**, *243* (4887), 85–88.
- (49) You, C.; Bhagawati, M.; Brecht, A.; Piehler, J. Affinity Capturing for Targeting Proteins into Micro and Nanostructures. *Anal. Bioanal. Chem.* **2009**, *393* (6-7), 1563–1570.
- (50) Schatz, P. J. Use of Peptide Libraries to Map the Substrate Specificity of a Peptide-Modifying Enzyme: A 13 Residue Consensus Peptide Specifies Biotinylation in Escherichia Coli. *Biotechnology* **1993**, *11* (10), 1138–1143.
- (51) Chirra, H. D.; Sexton, T.; Biswal, D.; Hersh, L. B.; Hilt, J. Z. Catalase-Coupled Gold Nanoparticles: Comparison between the Carbodiimide and Biotin-Streptavidin Methods. *Acta Biomater.* **2011**, *7* (7), 2865–2872.
- (52) Zhang, Y.; Tang, Z.; Wang, J.; Wu, H.; Lin, C.-T.; Lin, Y. Apoferritin Nanoparticle: A Novel and Biocompatible Carrier for Enzyme Immobilization with Enhanced Activity and Stability. *J. Mater. Chem.* **2011**, *21* (43), 17468–17475.
- (53) Garcia, J.; Zhang, Y.; Taylor, H.; Cespedes, O.; Webb, M. E.; Zhou, D. Multilayer Enzyme-Coupled Magnetic Nanoparticles as Efficient, Reusable Biocatalysts and Biosensors. *Nanoscale* **2011**, *3* (9), 3721–3730.
- (54) Imam, H. T.; Marr, P. C.; Marr, A. C. Enzyme Entrapment, Biocatalyst Immobilization without Covalent Attachment. *Green Chem.* 2021, 23 (14), 4980–5005.
- (55) Campás, M.; Marty, J.-L. Encapsulation of Enzymes Using Polymers and Sol-Gel Techniques. In *Immobilization of Enzymes and Cells*; Guisan, J. M., Ed.; Humana Press: Totowa, NJ, 2006; pp 77–85.
- (56) Braun, S.; Rappoport, S.; Zusman, R.; Avnir, D.; Ottolenghi, M. Biochemically Active Sol-Gel Glasses: The Trapping of Enzymes. *Mater. Lett.* **1990**, *10* (1), 1–5.

- (57) Yamanaka, S. A.; Nishida, F.; Ellerby, L. M.; Nishida, C. R.; Dunn, B.; Valentine, J. S.; Zink, J. I. Enzymatic Activity of Glucose Oxidase Encapsulated in Transparent Glass by the Sol-Gel Method. *Chem. Mater.* **1992**, *4* (3), 495–497.
- (58) Demirel, G.; Özçetin, G.; Şahin, F.; Tümtürk, H.; Aksoy, S.; Hasirci, N. Semi-Interpenetrating Polymer Networks (IPNs) for Entrapment of Glucose Isomerase. *React. Funct. Polym.* **2006**, *66* (4), 389–394.
- (59) Yamak, O.; Kalkan, N. A.; Aksoy, S.; Altinok, H.; Hasirci, N. Semi-Interpenetrating Polymer Networks (semi-IPNs) for Entrapment of Laccase and Their Use in Acid Orange 52 Decolorization. *Process Biochem.* **2009**, *44* (4), 440–445.
- (60) Demirci, S.; Sahiner, M.; Yilmaz, S.; Karadag, E.; Sahiner, N. Enhanced Enzymatic Activity and Stability by in Situ Entrapment of α-Glucosidase within Super Porous p(HEMA) Cryogels during Synthesis. *Biotechnol Rep (Amst)* **2020**, 28, e00534.
- (61) Barnola, J.-M., D. Raynaud, C. Lorius, and N.I. Barkov. 2003. Historical CO₂ record from the Vostok ice core. In Trends: A Compendium of Data on Global Change. Carbon Dioxide Information Analysis Center, Oak Ridge National Laboratory, U.S. Department of Energy, Oak Ridge, Tenn., U.S.A.
- (62) Global Monitoring Laboratory. *Trends in Atmospheric Carbon Dioxide*. https://gml.noaa.gov/ccgg/trends/ (accessed 2021-11-13)
- (63) Sheffield, J.; Wood, E. F.; Roderick, M. L. Little Change in Global Drought over the Past 60 Years. *Nature* **2012**, *491* (7424), 435–438.
- (64) Dai, A. Recent Climatology, Variability, and Trends in Global Surface Humidity. *J. Clim.* **2006**, *19* (15), 3589–3606.
- (65) U.S. Environmental Protection Agency. *Sources of Greenhouse Gas Emissions*. <u>https://www.epa.gov/ghgemissions/sources-greenhouse-gas-emissions</u> (accessed 2021-09-02).
- (66) Sheffield, J.; Wood, E. F.; Roderick, M. L. Little Change in Global Drought over the Past 60 Years. *Nature* **2012**, *491* (7424), 435–438.
- (67) Cebrucean, D.; Cebrucean, V.; Ionel, I.; Post-combustion CO₂ capture technologies for coal-fired power plants. Proceedings of the 2nd International Conference "Ecology of Urban Areas 2012"; 2012.

- (68) Kang, D.; Park, S.; Jo, H.; Min, J.; Park, J. Solubility of CO₂ in Amino-Acid-Based Solutions of (Potassium Sarcosinate), (Potassium Alaninate + Piperazine), and (Potassium Serinate + Piperazine). *J. Chem. Eng. Data* **2013**, 58 (6), 1787–1791.
- (69) Ramezani, R.; Mazinani, S.; Di Felice, R. State-of-the-Art of CO₂ Capture with Amino Acid Salt Solutions. *Rev. Chem. Eng.* **2020** DOI: 10.1515/revce-2020-0012.
- (70) Song, H.-J.; Lee, S.; Park, K.; Lee, J.; Chand Spah, D.; Park, J.-W.; Filburn, T. P. Simplified Estimation of Regeneration Energy of 30 Wt % Sodium Glycinate Solution for Carbon Dioxide Absorption. *Ind. Eng. Chem. Res.* **2008**, *47* (24), 9925–9930.
- (71) Williams, P. J. le B.; Laurens, L. M. L. Microalgae as Biodiesel & Biomass Feedstocks: Review & Analysis of the Biochemistry, Energetics & Economics. *Energy Environ. Sci.* **2010**, *3* (5), 554–590.
- (72) Li, Y.; Horsman, M.; Wu, N.; Lan, C. Q.; Dubois-Calero, N. Biofuels from Microalgae. *Biotechnol. Prog.* **2008**, *24* (4), 815–820.
- (73) Sumerlin, B. S.; Tsarevsky, N. V.; Louche, G.; Lee, R. Y.; Matyjaszewski, K. Highly Efficient "Click" Functionalization of Poly(3-Azidopropyl Methacrylate) Prepared by ATRP. *Macromolecules* **2005**, *38* (18), 7540–7545.
- (74) Li, Y.; Yang, J.; Benicewicz, B. C. Well-Controlled Polymerization of 2-Azidoethyl Methacrylate at near Room Temperature and Click Functionalization. *J. Polym. Sci. A Polym. Chem.* **2007**, *45* (18), 4300–4308.
- (75) Tsarevsky, N. V.; Bencherif, S. A.; Matyjaszewski, K. Graft Copolymers by a Combination of ATRP and Two Different Consecutive Click Reactions. *Macromolecules* **2007**, *40* (13), 4439–4445.
- (76) Feng, A.; Tang, H.; Luan, Y. Reversible Addition-Fragmentation Chain Transfer Polymerization of 2-Chloroethyl Methacrylate and Post-Polymerization Modification. *Macromol. Res.* **2019**, *27* (7), 686–692.
- (77) Gan, W.; Shi, Y.; Jing, B.; Cao, X.; Zhu, Y.; Gao, H. Produce Molecular Brushes with Ultrahigh Grafting Density Using Accelerated CuAAC Grafting-Onto Strategy. *Macromolecules* **2017**, *50* (1), 215–222.
- (78) Ishizone, T.; Uehara, G.; Hirao, A.; Nakahama, S. Anionic Polymerization of Monomers Containing Functional Groups, 11. Anionic Polymerizations of Alkynyl Methacrylates. *Chemistry and Physics* **1998**, 1827–1834.

- (79) Bertrand, A.; Stenzel, M.; Fleury, E.; Bernard, J. Host–guest Driven Supramolecular Assembly of Reversible Comb-Shaped Polymers in Aqueous Solution. *Polym. Chem.* **2012**, *3* (2), 377–383.
- (80) Gou, Y.; Slavin, S.; Geng, J.; Voorhaar, L.; Haddleton, D. M.; Becer, C. R. Controlled Alternate Layer-by-Layer Assembly of Lectins and Glycopolymers Using QCM-D. *ACS Macro Lett.* **2012**, *1* (1), 180–183.
- (81) Nasrullah, M. J.; Vora, A.; Webster, D. C. Block Copolymer Synthesis via a Combination of ATRP and RAFT Using Click Chemistry. *Macromol. Chem. Phys.* **2011**, *212* (6), 539–549.
- (82) Zarafshani, Z.; Akdemir, Ö.; Lutz, J.-F. A "click" Strategy for Tuning in Situ the Hydrophilic–hydrophobic Balance of AB Macrosurfactants. *Macromol. Rapid Commun.* **2008**, 29 (12-13), 1161–1166.
- (83) Gao, H.; Matyjaszewski, K. Synthesis of Star Polymers by a Combination of ATRP and the "Click" Coupling Method. *Macromolecules* **2006**, *39* (15), 4960–4965.
- (84) Tsarevsky, N. V.; Bencherif, S. A.; Matyjaszewski, K. Graft Copolymers by a Combination of ATRP and Two Different Consecutive Click Reactions. *Macromolecules* **2007**, *40* (13), 4439–4445.
- Ladmiral, V.; Mantovani, G.; Clarkson, G. J.; Cauet, S.; Irwin, J. L.; Haddleton, D.
 M. Synthesis of Neoglycopolymers by a Combination of "Click Chemistry" and Living Radical Polymerization. J. Am. Chem. Soc. 2006, 128 (14), 4823–4830.
- (86) Johnson, J. A.; Lewis, D. R.; Díaz, D. D.; Finn, M. G.; Koberstein, J. T.; Turro, N. J. Synthesis of Degradable Model Networks via ATRP and Click Chemistry. J. Am. Chem. Soc. 2006, 128 (20), 6564–6565.
- (87) Ishizone, T.; Uehara, G.; Hirao, A.; Nakahama, S. Anionic Polymerization of Monomers Containing Functional Groups, 11. Anionic Polymerizations of Alkynyl Methacrylates. *Chemistry and Physics* 1998, 1827–1834.
- (88) Matyjaszewski, K.; Patten, T. E.; Xia, J. Controlled/"Living" Radical Polymerization. Kinetics of the Homogeneous Atom Transfer Radical Polymerization of Styrene. J. Am. Chem. Soc. 1997, 119 (4), 674–680.
- (89) Magenau, A. J. D.; Kwak, Y.; Matyjaszewski, K. ATRP of Methacrylates Utilizing CuIIX2/L and Copper Wire. *Macromolecules* **2010**, *43* (23), 9682–9689.

- (90) Williams, V. A.; Ribelli, T. G.; Chmielarz, P.; Park, S.; Matyjaszewski, K. A Silver Bullet: Elemental Silver as an Efficient Reducing Agent for Atom Transfer Radical Polymerization of Acrylates. *J. Am. Chem. Soc.* **2015**, *137* (4), 1428–1431.
- (91) Williams, V. A.; Matyjaszewski, K. Expanding the ATRP Toolbox: Methacrylate Polymerization with an Elemental Silver Reducing Agent. *Macromolecules* **2015**, 48 (18), 6457–6464.
- (92) Matyjaszewski, K.; Coca, S.; Gaynor, S. G.; Wei, M.; Woodworth, B. E. Zerovalent Metals in Controlled/"Living" Radical Polymerization. *Macromolecules* **1997**, *30* (23), 7348–7350.
- (93) Jakubowski, W.; Matyjaszewski, K. Activator Generated by Electron Transfer for Atom Transfer Radical Polymerization. *Macromolecules* **2005**, *38* (10), 4139–4146.
- (94) Min, K.; Gao, H.; Matyjaszewski, K. Use of Ascorbic Acid as Reducing Agent for Synthesis of Well-Defined Polymers by ARGET ATRP. *Macromolecules* **2007**, *40* (6), 1789–1791.
- (95) Liarou, E.; Whitfield, R.; Anastasaki, A.; Engelis, N. G.; Jones, G. R.; Velonia, K.; Haddleton, D. M. Copper-Mediated Polymerization without External Deoxygenation or Oxygen Scavengers. *Angew. Chem. Int. Ed Engl.* 2018, 57 (29), 8998–9002.
- (96) Beuermann, S.; Buback, M. Rate Coefficients of Free-Radical Polymerization Deduced from Pulsed Laser Experiments. *Prog. Polym. Sci.* **2002**, 27, 191–254.
- (97) Chen, H.; Liu, D.; Song, Y.; Qu, R.; Wang, C. ARGET ATRP of Acrylonitrile with Ionic Liquid as Reaction Media and 1,1,4,7,7-Pentamethyldiethylenetriamine as Both Ligand and Reducing Agent in the Presence of Air. *Polym. Adv. Technol.* **2011**, 22 (11), 1513–1517.
- (98) Geng, J.; Mantovani, G.; Tao, L.; Nicolas, J.; Chen, G.; Wallis, R.; Mitchell, D. A.; Johnson, B. R. G.; Evans, S. D.; Haddleton, D. M. Site-Directed Conjugation of "Clicked" Glycopolymers To Form Glycoprotein Mimics: Binding to Mammalian Lectin and Induction of Immunological Function. *Journal of the American Chemical Society.* 2007, pp 15156–15163.
- (99) Yhaya, F.; Binauld, S.; Kim, Y.; Stenzel, M. H. Shell Cross-Linking of Cyclodextrin-Based Micelles via Supramolecular Chemistry for the Delivery of Drugs. *Macromol. Rapid Commun.* **2012**, *33* (21), 1868–1874.
- (100) Lum, K.; Chandler, D.; Weeks, J. D. Hydrophobicity at Small and Large Length Scales. *J. Phys. Chem. B* **1999**, *103* (22), 4570–4577.

- (101) Chandler, D. Hydrophobicity: Two Faces of Water. *Nature* **2002**, *417* (6888), 491.
- (102) Boyer, R. F. Concept in Biochemistry third Ed.; John Wiley & Sons, 2005; pp 242-245.
- (103) Wilhelm, M.; Zhao, C. L.; Wang, Y.; Xu, R.; Winnik, M. A.; Mura, J. L.; Riess, G.; Croucher, M. D. Poly(styrene-Ethylene Oxide) Block Copolymer Micelle Formation in Water: A Fluorescence Probe Study. *Macromolecules* **1991**, *24* (5), 1033–1040.
- (104) Hussain, H.; Busse, K.; Kressler, J. Poly(ethylene Oxide)- and Poly(perfluorohexylethyl Methacrylate)-Containing Amphiphilic Block Copolymers: Association Properties in Aqueous Solution. *Macromol. Chem. Phys.* **2003**, *204* (7), 936–946.
- (105) Castro, E.; Taboada, P.; Barbosa, S.; Mosquera, V. Size Control of Styrene Oxide-Ethylene Oxide Diblock Copolymer Aggregates with Classical Surfactants: DLS, TEM, and ITC Study. *Biomacromolecules* **2005**, *6* (3), 1438–1447.
- (106) Rodionov, V. O.; Fokin, V. V.; Finn, M. G. Mechanism of the Ligand-Free Cul-Catalyzed Azide-Alkyne Cycloaddition Reaction. *Angew. Chem. Int. Ed Engl.* **2005**, *44* (15), 2210–2215.
- (107) Worrell, B. T.; Malik, J. A.; Fokin, V. V. Direct Evidence of a Dinuclear Copper Intermediate in Cu(I)-Catalyzed Azide-Alkyne Cycloadditions. *Science* **2013**, *340* (6131), 457–460.
- (108) Venderbosch, B.; Oudsen, J.-P. H.; van der Vlugt, J. I.; Korstanje, T. J.; Tromp, M. Cationic Copper Iminophosphorane Complexes as CuAAC Catalysts: A Mechanistic Study. *Organometallics* **2020**, *39* (19), 3480–3489.
- (109) (a) Braunecker, W. A.; Pintauer, T.; Tsarevsky, N. V.; Kickelbick, G.; Matyjaszewski, K. Towards Understanding Monomer Coordination in Atom Transfer Radical Polymerization: Synthesis of [CuI (PMDETA)(π -M)][BPh4](M= Methyl Acrylate, Styrene, 1-Octene, and Methyl Methacrylate) and Structural Studies by FT-IR and 1H NMR Spectroscopy and X-Ray Crystallography. J. Organomet. Chem. 2005, 690 (4), 916-924. (b) Braunecker, W. A.; Tsarevsky, N. V.; Pintauer, T.; Gil, R. R.; Matyjaszewski, K. Quantifying Vinyl Monomer Coordination to CuI in Solution and the Effect of Coordination on Monomer Reactivity in Radical Copolymerization. Macromolecules 2005, 38 (10), 4081–4088.

- (110) Onogi, S.; Kobayashi, T.; Kojima, Y.; Taniguchi, Y. Non-Newtonian Flow of Concentrated Solutions of High Polymers. *J. Appl. Polym. Sci.* **1963**, *7* (3), 847–859.
- (111) Döhler, D.; Michael, P.; Binder, W. H. Autocatalysis in the Room Temperature Copper(I)-Catalyzed Alkyne–Azide "Click" Cycloaddition of Multivalent Poly(acrylate)s and Poly(isobutylene)s. *Macromolecules* **2012**, *45* (8), 3335–3345.
- (112) Ganta, S.; Devalapally, H.; Shahiwala, A.; Amiji, M. A Review of Stimuli-Responsive Nanocarriers for Drug and Gene Delivery. *J. Control. Release* **2008**, *126* (3), 187–204.
- (113) Bordat, A.; Boissenot, T.; Nicolas, J.; Tsapis, N. Thermoresponsive Polymer Nanocarriers for Biomedical Applications. *Adv. Drug Deliv. Rev.* **2019**, *138*, 167–192.
- (114) Hatefi, A.; Amsden, B. Biodegradable Injectable in Situ Forming Drug Delivery Systems. *J. Control. Release* **2002**, *80* (1-3), 9–28.
- (115) Ward, M. A.; Georgiou, T. K. Thermoresponsive Polymers for Biomedical Applications. *Polymers* **2011**, *3* (3), 1215–1242.
- (116) Heskins, M.; Guillet, J. E. Solution Properties of Poly(N-Isopropylacrylamide). *Journal of Macromolecular Science: Part A - Chemistry* **1968**, *2* (8), 1441–1455.
- (117) Lien, Y. L. Poly(ethylene glycol) tailored polymers: nanomicelles with tunable lower critical solution temperature behavior. Michigan State University, **2018**.
- (118) Sambasiva Rao, P.; Kurumurthy, C.; Veeraswamy, B.; Santhosh Kumar, G.; Shanthan Rao, P.; Pamanji, R.; Venkateswara Rao, J.; Narsaiah, B. Synthesis of Novel 2-Alkyl Triazole-3-Alkyl Substituted Quinoline Derivatives and Their Cytotoxic Activity. *Bioorg. Med. Chem. Lett.* **2013**, *23* (5), 1225–1227.
- (119) Younis, M.; Darcos, V.; Paniagua, C.; Ronjat, P.; Lemaire, L.; Nottelet, B.; Garric, X.; Bakkour, Y.; El Nakat, J. H.; Coudane, J. MRI-Visible Polymer Based on Poly(methyl Methacrylate) for Imaging Applications. *RSC Adv.* **2016**, *6* (7), 5754–5760.
- (120) (a) Evans, K. L.; Crowder, J.; Miller, E. S. Subtilisins of Bacillus Spp. Hydrolyze Keratin and Allow Growth on Feathers. *Can. J. Microbiol.* **2000**, *46* (11), 1004–1011.

- (b) Peters, K.; Pauli, D.; Hache, H.; Boteva, R. N.; Genov, N. C.; Fittkau, S. Subtilisin DY—Kinetic Characterization and Comparison with Related Proteinases. *Curr. Microbiol.* **1989**, *18* (3), 171–177.
- (121) Reimann, A.; Robb, D. A.; Halling, P. J. Solvation of CBZ-Amino Acid Nitrophenyl Esters in Organic Media and the Kinetics of Their Transesterification by Subtilisin. *Biotechnol. Bioeng.* **1994**, *43* (11), 1081–1086.
- (122) Egwim, I. O. C.; Gruber, H. J. Spectrophotometric Measurement of Mercaptans with 4,4′-Dithiodipyridine. *Anal. Biochem.* **2001**, 288 (2), 188–194.
- (123) Cummings, C. S.; Murata, H.; Matyjaszewski, K.; Russell, A. J. Polymer-Based Protein Engineering Enables Molecular Dissolution of Chymotrypsin in Acetonitrile. *ACS Macro Lett.* **2016**, *5* (4), 493–497.
- (124) Cutshaw, A.; Daiek, C.; Zheng, Y.; Frost, H.; Marks, A.; Clements, D.; Uludag-Demirer, S.; Verhanovitz, N.; Pavlik, D.; Clary, W.; Liu, Y.; Liao, W. A Long-Term Pilot-Scale Algal Cultivation on Power Plant Flue Gas Cultivation Stability and Biomass Accumulation. *Algal Research* **2020**, *52*, 102115.
- (125) Pavlik, D.; Zhong, Y.; Daiek, C.; Liao, W.; Morgan, R.; Clary, W.; Liu, Y. Microalgae Cultivation for Carbon Dioxide Sequestration and Protein Production Using a High-Efficiency Photobioreactor System. *Algal Research* 2017, 25, 413–420.
- (126) Caplow, M. Kinetics of carbamate formation and breakdown. *J. Am. Chem. Soc.* **1968**, *90* (24), 6795–6803.
- (127) Danckwerts, P. V. The Reaction of CO₂ with Ethanolamines. *Chem. Eng. Sci.* **1979**, 34 (4), 443–446.
- (128) Blauwhoff, P. M. M.; Versteeg, G. F.; Van Swaaij, W. P. M. A Study on the Reaction between CO₂ and Alkanolamines in Aqueous Solutions. *Chem. Eng. Sci.* **1983**, *38* (9), 1411–1429.
- (129) Clarke, J. K. A. Kinetics of Absorption of Cardon Dioxide in Monoethanolamine Solutions at Short Contact Times. *Ind. Eng. Chem. Fundam.* **1964**, *3* (3), 239–245.
- (130) Emmert, R. E.; Pigford, R. L. Gas Absorption Accompanied by Chemical Reaction: A Study of the Absorption of Carbon Dioxide in Aqueous Solutions of Monoethanolamine. *AIChE J.* **1962**, 8 (2), 171–175.
- (131) Donaldson, T. L.; Nguyen, Y. N. Carbon Dioxide Reaction Kinetics and Transport in Aqueous Amine Membranes. *Ind. Eng. Chem. Fundam.* **1980**, *19* (3), 260–266.

- (132) McCann, N.; Phan, D.; Wang, X.; Conway, W.; Burns, R.; Attalla, M.; Puxty, G.; Maeder, M. Kinetics and Mechanism of Carbamate Formation from CO₂(aq), Carbonate Species, and Monoethanolamine in Aqueous Solution. *J. Phys. Chem. A* **2009**, *113* (17), 5022–5029.
- (133) Bentley, T. W. Nucleophilicity Parameters for Amines, Amino Acids and Peptides in Water. Variations in Selectivities for Quinone Methides. *Org. Biomol. Chem.* **2011**, *9* (19), 6685–6690.
- (134) Shen, S.; Yang, Y.-N.; Bian, Y.; Zhao, Y. Kinetics of CO₂ Absorption into Aqueous Basic Amino Acid Salt: Potassium Salt of Lysine Solution. *Environ. Sci. Technol.* **2016**, *50* (4), 2054–2063.
- (135) Gupta, M.; Svendsen, H. F. Understanding Carbamate Formation Reaction Thermochemistry of Amino Acids as Solvents for Postcombustion CO₂ Capture. *J. Phys. Chem. B* **2019**, *123* (40), 8433–8447.
- (136) Majchrowicz, M. E.; Kersten, S.; Brilman, W. Reactive Absorption of Carbon Dioxide in L-Prolinate Salt Solutions. *Ind. Eng. Chem. Res.* **2014**, *53* (28), 11460–11467.
- (137) Li, Y.; Duan, X.; Song, W.; Ma, L.; Jow, J. Reaction Mechanisms of Carbon Dioxide Capture by Amino Acid Salt and Desorption by Heat or Mineralization. *Chem. Eng. J.* **2021**, *405*, 126938.
- (138) Ciftja, A. F.; Hartono, A.; Svendsen, H. F. ¹³C NMR as a Method Species Determination in CO₂ Absorbent Systems. *Int. J. Greenhouse Gas Control* **2013**, *16*, 224–232.
- (139) Ciftja, A. F.; Hartono, A.; Svendsen, H. F. Amine Neutralized Amino Acid as CO₂ Absorbents: A Quantitative ¹³C NMR Study. *Int. J. Greenhouse Gas Control* **2014**, 27, 169–177.
- (140) Ciftja, A. F.; Hartono, A.; Svendsen, H. F. Selection of Amine Amino Acids Salt Systems for CO₂ Capture. *Energy Procedia* **2013**, *37*, 1597–1604.
- (141) Harris, D. Quantitative Chemical Analysis, 7th ed.; W. H. Freeman and Company, 2007.
- (142) Al-Terkawi, A.-A.; Lamaty, F.; Métro, T.-X. Efficient CO₂ Sequestration by a Solid–Gas Reaction Enabled by Mechanochemistry: The Case of L-Lysine. *ACS Sustainable Chem. Eng.* **2020**, 8 (35), 13159–13166.

- (143) Picture is downloaded from Wilmad labglass.com (https://sp-wilmadlabglass.com/product/stem-coaxial-inserts/).
- (144) Hatada, K.; Terawaki, Y.; Okuda, H. Quantitative Analysis by Nuclear Magnetic Resonance Using Precision Coaxial Tubing. *Organic Magnetic* **1977**.
- (145) Fulton, D. B.; Sayer, B. G.; Bain, A. D.; Malle, H. V. Detection and Determination of Dilute, Low Molecular Weight Organic Compounds in Water by 500 MHz Proton Nuclear Magnetic Resonance Spectroscopy. *Anal. Chem.* **1992**, *64* (4), 349–353.
- (146) Henderson, T. J. Quantitative NMR Spectroscopy Using Coaxial Inserts Containing a Reference Standard: Purity Determinations for Military Nerve Agents. *Anal. Chem.* **2002**, *74* (1), 191–198.
- (147) Sartori, G.; Savage, D. W. Sterically Hindered Amines for Carbon Dioxide Removal from Gases. *Ind. Eng. Chem. Fundam.* **1983**, 22 (2), 239–249.
- (148) Hook, R. J. An Investigation of Some Sterically Hindered Amines as Potential Carbon Dioxide Scrubbing Compounds. *Ind. Eng. Chem. Res.* **1997**, *36* (5), 1779–1790.
- (149) Hiemenz, P. C.; Lodge, T. P. Polymer Chemistry, 2nd ed.; CRC Press, 2007.
- (150) Swapna, V. P.; Abhisha, V. S.; Stephen, R. 9 Polymer/polyhedral Oligomeric Silsesquioxane Nanocomposite Membranes for Pervaporation. In *Polymer Nanocomposite Membranes for Pervaporation*; Thomas, S., George, S. C., Jose, T., Eds.; Elsevier, 2020; pp 201–229.
- (151) Caruso, S.; Foti, S.; Maravigna, P.; Montaudo, G. Mass Spectral Characterization of Polymers. Primary Thermal Fragmentation Processes in Polyureas. *J. Polym. Sci. Polym. Chem. Ed.* **1982**, *20* (7), 1685–1696.
- (152) Tena-Solsona, M.; Angulo-Pachón, C. A.; Escuder, B.; Miravet, J. F. Mechanistic Insight into the Lability of the Benzyloxycarbonyl (Z) Group inN-Protected Peptides under Mild Basic Conditions. *European J. Org. Chem.* **2014**, *2014* (16), 3372–3378.
- (153) Nakamura, M.; Yamaguchi, M.; Sakai, O.; Inoue, J. Exploration of Cornea Permeable Calpain Inhibitors as Anticataract Agents. *Bioorg. Med. Chem.* **2003**, *11* (7), 1371–1379.
- (154) Becerril, J.; Bolte, M.; Burguete, M. I.; Galindo, F.; García-España, E.; Luis, S. V.; Miravet, J. F. Efficient Macrocyclization of U-Turn Preorganized Peptidomimetics:

- The Role of Intramolecular H-Bond and Solvophobic Effects. *J. Am. Chem. Soc.* **2003**, *125* (22), 6677–6686.
- (155) Becerril, J.; Burguete, M. I.; Escuder, B.; Galindo, F.; Gavara, R.; Miravet, J. F.; Luis, S. V.; Peris, G. Self-Assembly of Small Peptidomimetic Cyclophanes. *Chemistry* **2004**, *10* (16), 3879–3890.